UNIVERSITÀ
DEGLI STUDI
DI PADOVA

Sede Amministrativa: Università degli Studi di Padova

Dipartimento di Astronomia

Scuola di dottorato di ricerca in: Astronomia

Indirizzo: Stellare-Galattico

Ciclo XXII

HIGH-PRECISION ASTROMETRY AND PHOTOMETRY OF STAR CLUSTERS FROM *HST* AND GROUND-BASED TELESCOPES

Direttore della scuola: Ch.mo Prof. Giampaolo Piotto

Supervisore: Ch.mo Prof. Giampaolo Piotto

Dottorando: Andrea Bellini

Dipartimento di Astronomia

Facoltà di Scienze Matematiche Fisiche Naturali

Università di Padova

788° Anno Accademico

HIGH-PRECISION ASTROMETRY AND PHOTOMETRY OF STAR CLUSTERS FROM *HST* AND GROUND-BASED TELESCOPES

Thesis submitted by

Andrea Bellini

as a requirement for the degree of

Philosophy Doctor in Astronomy Science

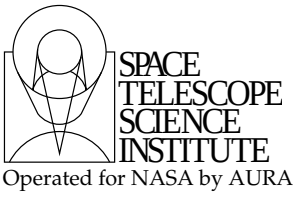

July 26, 2010

Thesis supervisors:

- Prof. Giampaolo Piotto
  Dipartimento di Astronomia, Università di Padova, Italy, EU
- Dr. Luigi "Rolly" Bedin
  Space Telescope Science Institute, Baltimore, MD, USA
- Dr. Jay Anderson
  Space Telescope Science Institute, Baltimore, MD, USA

Examination date: September 17th, 2010

Part of this work has been carried out at the *Space Telescope Science Institute*, 3700 San Martin Drive, Baltimore, MD, 21210 USA, under the *"2008 Graduate Research Assistantship"* program (coordinator of the program: Dr. Ronald Allen).

Some of the material included in this document has been already published (or will be published soon) in *Astronomy & Astrophysics*, *Publications of the Astronomical Society of the Pacific*, *The Astrophysical Journal* and *The Astronomical Journal*.

External Examiner:

Dr. Peter B. Stetson

Committe Members:

Prof. Francesco Ferraro

Prof. Young Wook Lee

Prof. Antonio Aparicio

Prof. Ivan R. King

Prof. Scilla degl'Innocenti

Prof. Roberto Buonanno

Supply Members:

Dr. Raffaele Gratton

Dr. Angela Bragaglia

Contents

Introduction **1**

1 Introduction to astrometry and wide-field imagers **3**
1.1 Brief history of astrometry . . . 3
1.2 Differential and absolute astrometry . . . 5
1.3 Astrometric projects . . . 6
1.3.1 Ground-based projects . . . 6
1.3.2 Space-based projects . . . 7
1.4 The wide-field imagers . . . 8

2 Geometric distortion correction of the LBC at the prime focus of the LBT **13**
2.1 Introduction . . . 13
2.2 The Large Binocular Camera Blue . . . 14
2.3 The data-set . . . 15
2.4 Auto-calibration . . . 17
2.4.1 Deriving a self-consistent solution . . . 18
2.4.2 The GD solution . . . 23
2.4.3 Accuracy of the GD Solution . . . 24
2.4.4 GD correction for the *B* filter . . . 26
2.5 Relative positions of the chips . . . 27
2.6 Stability of the solution . . . 29
2.7 Conclusions . . . 31
2.8 Appendix . . . 33

3 Geometric distortion correction of the WFC3/UVIS on board the *HST* **35**
3.1 Introduction, Data set, Measurements . . . 35
3.2 The Geometric Distortion Solutions . . . 36
3.3 Interchip transformations . . . 43
3.4 Average Absolute Scale relative to ACS/WFC . . . 45
3.5 Conclusions . . . 45

3.6 Appendix 49

Applications **51**

4 Proper-motions of faint sources in the field of the open cluster M 67 **53**
4.1 Observations 53
4.1.1 Large Binocular Telescope data set 54
4.1.2 Canada-France-Hawaii Telescope data set 54
4.2 Photometry of LBC@LBT data set 55
4.2.1 First-passage photometry 56
4.2.2 Second-passage photometry 61
4.2.3 Aperture photometry 69
4.3 Photometry of the UH8K@CFHT data set 70
4.3.1 First-passage photometry 70
4.3.2 Second-passage photometry 72
4.4 Photometric calibration 73
4.5 Proper-motion measurements 75
4.6 Applications 77
4.7 Introduction 79
4.8 Observations 79
4.9 Measurements and Selections 80
4.9.1 First step 80
4.9.2 Second step 82
4.9.3 Third step 83
4.9.4 Proper motions 84
4.9.5 Completeness 87
4.10 Comparison with previous studies 87
4.11 Comparison with theory 89
4.12 Discussion 93

5 Absolute proper motion of the open cluster M 67 **97**
5.1 Introduction 97
5.2 Observations, data reduction, proper motions 97
5.3 The Galactic orbit of M 67 104

6 WFI@2.2m proper-motions of the globular cluster ω Centauri. **109**
6.1 Introduction 109
6.2 Observations 110
6.3 Photometry, astrometry and calibration 112
6.3.1 Photometric reduction 112
6.3.2 Sky-concentration correction 113
6.3.3 Instrumental $UBVR_CI_C$-Hα photometric catalog 119

6.3.4 Photometric calibration . . . 120
6.3.5 Zero-point residuals . . . 121
6.4 Proper-motion measurements . . . 121
6.4.1 Cluster CMD decontamination . . . 123
6.4.2 Differential chromatic refraction (DCR) . . . 123
6.4.3 Astrometric calibration . . . 126
6.4.4 Comparison with other ω Cen proper-motion catalogs . . . 128
6.5 Membership probability . . . 129
6.6 Applications . . . 132
6.6.1 The proper motion of the RGB sub-populations . . . 132
6.6.2 Membership probability of published ω Cen variable stars . . . 134
6.7 Summary . . . 135
6.7.1 Electronic catalog . . . 137

7 Radial distribution of the multiple stellar populations in ω Centauri 143
7.1 Introduction . . . 143
7.2 Observations and data reductions . . . 145
7.2.1 *HST*: ACS/WFC inner 3×3 mosaic . . . 146
7.2.2 *HST*: ACS/WFC outer field . . . 146
7.2.3 *HST*: WFPC2 field . . . 147
7.2.4 VLT: eight FORS1 fields . . . 148
7.2.5 WFI@2.2*m* . . . 150
7.2.6 The astrometric and photometric reference frame . . . 150
7.2.7 The deep color-magnitude diagrams . . . 152
7.2.8 The *angular* radial distance: r^* . . . 153
7.3 MS subpopulations . . . 153
7.3.1 Straightened main sequences . . . 153
7.3.2 Dual-Gaussian fitting . . . 156
7.3.3 The Radial Gradient of $N_{\rm bMS}/N_{\rm rMS}$ . . . 159
7.3.4 Artificial star tests . . . 162
7.4 Radial gradients in the RGB subpopulations . . . 166
7.4.1 Defining the RGB-MP, RGB-MInt, and RGB-a subsamples . . . 166
7.4.2 Relative radial distributions of RGB stars . . . 167
7.5 Discussion . . . 168
7.6 Bibliography . . . 170

8 New *HST* WFC3/UVIS observations of ω Centauri 173
8.1 Introduction . . . 173
8.2 Observations, Measurements and Selections . . . 174
8.3 Color-Magnitude Diagrams . . . 176
8.3.1 The triple main sequence . . . 177
8.3.2 The intrinsic broadening of the rMS . . . 179
8.3.3 The MS-a. . . . 182

8.3.4 The sub-giant and lower red giant branches . . . 184
8.3.5 The horizontal branch . . . 188
8.4 Electronic catalog . . . 189

Future projects **191**

9 Future projects **193**
9.1 The VISTA VVV survey . . . 193
9.1.1 The telescope+camera system . . . 193
9.1.2 The survey . . . 193
9.1.3 Our science with VISTA . . . 194
9.2 Tidal tails of Galactic globular clusters . . . 195
9.3 Absolute motion of Galactic globular clusters . . . 196
9.4 Exporting our techniques to other wide-field imagers . . . 197
9.4.1 HAWK-I@VLT . . . 198

Introduction

1

Introduction to astrometry and wide-field imagers

Astrometry is one of the oldest subfields of Astronomy, born to provide positions, and by extension, the dimensions and shapes of celestial bodies. Because these quantities vary with time, one of the first purposes of astrometry is to describe the motion of these celestial bodies.

During the first half of the last century, astrometric accuracy reached the physical limitations of the instruments, and astrometry was neglected for almost 50 years. Recently, the role played by astrometry is again becoming very important thanks to space-based telescopes. Astrometry is fundamental to the study of kinematics and the physical origin of the Solar System and the Milky Way: the first steps in understanding the Universe.

For stellar observers (like me!), high-precision astrometry is a precious, essential tool to measure proper motions and provide bona-fide star-cluster members in order to infer star and cluster properties, which in turn can be used to constrain stellar-evolution models.

1.1 Brief history of astrometry

Measuring stellar distances, their three-dimensional distribution and their space motions, remains a difficult task even within our solar neighborhood. Astrometry began with the first naked-eye observations of the sky. These observations led to the discovery of *wanderers* (planets) among the stars, knowledge of the cycles of days and years, predictions of eclipses, the concept of almanacs and calendars, and the catalogs of observations. The naked eye limited both the faintness of objects and accuracies of the positions observed, but still the observations of phenomena, such as eclipses and occultations, along with the location on Earth of the observer are rather accurate observations from ancient times.

From the beginning, astrometric observations were the basis for theories and discoveries. Around 190 BC Hipparchus took advantage of previous observations of Spica, made by his predecessor Timocharis and Aristillus, to discover the Earth's precession. Hipparchus himself is thought to have prepared the first star catalog (with the brightness scale still in use today), but Ptolemy's star catalog (circa 150 AD), as

in his *Almagest*, is the oldest passed down from ancient times. This catalog includes star positions with a precision of around 20′. Ptolemy also developed theoretical explanations of the motions of the planets around the Earth, who was then accepted by the growing Cristian Church at that time.

During the middle ages, Europe underwent a rather long period of science obscurantism, perpetrated by the Church itself. Improvements and discoveries regarding astronomy and astrometry at that time were carried out by scientists of the Islamic empire. al-Sufi (960) produced a catalog of positions, magnitudes and color for stars using armillary spheres, while Ibn Yunus compiled more than 10 000 Sun's positions with an astrolabe. His observations were still used many years later by Newcomb and Laplace. In the 15$^{\text{th}}$ century Ulugh Beg compiled the *Zij-i-Sultani*, with 1 019 star positions measured with a huge sextant, with a precision of the order of around 10′.

With the advent of the Renaissance, Europe finally came out from its long dark age and with a renewed enthusiasm, new ideas started to flourish also in the field of astrometry. In the 16$^{\text{th}}$ century, Tycho Brahe used improved instruments to measure star positions with an average precision of within 2′ (Verbunt & van Gent 2010), while Taqi al-Din improved the measurements of right ascension of stars using the "observational clock" he invented. However, even these improved observations were unable to measure stellar parallaxes, and this raised questions about the Copernican theory. On the other side, the observations of Mars led Kepler to develop his laws of motion, which in turn led to Newton's Universal Law of Gravity. The invention of the telescope permitted Galileo to discover the satellites of Jupiter and make astrometric observations of those objects, the first astrometric observations made with a telescope.

The application of astrometry for navigation and time-keeping led, between the 17$^{\text{th}}$ and the 18$^{\text{th}}$ century, to the establishment of national observatories in Paris, Greenwich, Berlin, St. Petersburg, and Padova. At the Greenwich observatory, the Astronomer Royal Flamsteed produced the *Historiae Coelestis* (1725), the first star catalog based on telescopic observations. Halley, Flamsteed's successor as Astronomer Royal, discovered that some bright stars, Aldebaran, Sirius, and Arcturus, were displaced by several arcmin from their positions as reported from ancient catalogs. This proved that stars are not "fixed", but they move on the celestial plane by proper motions. Another Astronomer Royal, Bradley, successor of Halley, discovered the aberration of light (1728) and the nutation (which effect is as small as 9.″2), in 1748. Bradley's star catalog of 3332 stars was refined in 1807 by Bessel, one of the fathers of modern astrometry.

Improvements in the precision of astrometric observations were sufficient enough that around 1840 Bessel, Struve, and Henderson independently announced observations with a precision within few tenths of arcsec. In particular, in 1838 Bessel made the first measurement of a stellar parallax: 0.3″ for the binary star 61 Cygni, proving once forever the truth of the Copernican theory. Being very difficult to measure, only about 60 stellar parallaxes had been obtained by the end of the 19$^{\text{th}}$ century, mostly by use of the filar micrometer. Bessel himself, in 1844 discovered stellar companions of Procyon and Sirius by the variation in their proper motions.

For most of the 20$^{\text{th}}$ century, the primary instrument for wide-angle astrometry was the meridian (or transit) circle, introduced by Troughton in 1806. The observations from transit circles were at the basis for positions and proper motions in the compilation of the Catalogue of Fundamental Stars, a series of six astrometric catalogs of high-precision positional data for stars, to define a celestial reference frame.

While the transit circle was good for accurate measurements of individual stars on the hour circle of the instrument all over the sky, the photographic plate could observe many stars in a small field-of-

view (FoV). The first international photographic survey of the sky, the *Carte du Ciel*, coordinated by the International Astrophotographic Congress in Paris in 1887, was able to reach a visual magnitude limit of about 12, while subsequent photographic surveys using Schmidt telescopes have gone as deep as 21st magnitude.

Long-focus refractors were being used at the end of the 19th century in small fields for observations of double stars, asteroids and satellites. The advantage of long-focus astrometry is that it provides a large scale on the plate, proportional to the focal length. At the beginning of the 20th century, Schlensinger and Allegheny began using photographic plates on long-focus refractors to determine parallaxes.

Automated plate-measuring machines and more sophisticated computer technology of the 1960s allowed more efficient compilation of star catalogs. In the 1980s, charge-coupled devices (CCDs) replaced photographic plates, starting a revolution in astrometry and reducing optical uncertainties to the order of 1 mas or better. The advent of space missions (Hipparcos, *Hubble Space Telescope*, SIM, GAIA, ...), optical interferometers and radio astrometry, further pushed up the accuracy of astrometric measurements, reaching precisions of fractions of mas.

Finally, the era of detecting exoplanets, i.e. planets outside our solar system which orbit around other stars, by astrometric means has just begun. Astrometric "wobbles" will be observed by space missions which are already being constructed. This is similar to detecting orbital motions of invisible components of certain double stars, which for example lead to the discovery of stellar companions by Bessel in 1844. The astrometric method is the only way to determine the masses of those components which could either be stars or planets except when a pair of objects is seen transiting each other (the orbital plane is along our line of sight).

1.2 Differential and absolute astrometry

The projection of the real space motion of a celestial object (with respect to our solar system) on to the celestial sphere is the *proper motion*, which is an angular velocity. The corresponding linear velocity is the tangential velocity. When the distance to an object is known, the tangential velocity can be calculated from its angular velocity. The third component of the 3-dimensional space motion of a celestial object is the motion along the line of sight, which is called the radial velocity. It is measured by spectroscopic methods and is not a topic of astrometry.

There is another important motion of the stars: the apparent, annual parallactic motion. A nearby star seems to move along a small elliptical pattern with respect to distant stars over the course of a year, due to the motion of the Earth around the Sun. Half the diameter of this parallactic motion is called the parallax, p, of a star. It is related to the distance, d, of the star by $d = p^{-1}$, where p is measured in arcsec and d in parsec. The closest star beyond our Sun belongs to the α Centauri system with $d = 1.3$ pc and $p = 0.77$ arcsec. All other stars have smaller parallaxes.

Another important area of astrometry is the research of double and multiple stars. Astrometric observations and determination of orbits is the only way to directly measure the masses of stars. The mass of a star is the fundamental quantity which determines the evolution and appearance of a star throughout its life. Orbital motion of course complicates the determination of parallax and proper motions. Fortunately (from the point of view of deriving masses) and unfortunately (from the point of view of using "clean" fiducial points of light for astrometric-reference frame work) most stars belong to a double or multiple star system.

Proper motions and parallaxes were typically measured over long periods of time with large (high magnification or large-plate scale) telescopes on photographic plates. This is the domain of narrow-field, small-angle, *differential* astrometry. However, the Hipparcos satellite and other future projects are capable of measuring small, local position changes like parallax and proper motions from large angle, global, *absolute*, observations. On the other hand, proper motions for most of the millions of faint stars are still known today from differential comparisons of pairs of photographic plates taken of the same area of the sky decades apart. Differential observations measure the positions of celestial objects in a small area of the sky relative to other objects. This is technically easier than absolute, large-angle measures and often yields higher precision than the wide-angle measures.

1.3 Astrometric projects

There are several important astrometric projects, both from ground-based and space-based telescopes. The most complete, ground-based projects made use of all the available information collected over the years, from photographic plates to modern CCD detectors. Their advantage is the available wide time baseline with which to compute accurate proper motions, and to compensate for the measurement errors introduced by atmospheric effects. On the other hand, space-based projects are relatively short in time (a few years), but they take advantage of being in space, with no atmosphere or gravity limitations.

1.3.1 Ground-based projects

The most accurate position observations within our solar system, used to support ephemerides and space navigation, are laser and radar ranging techniques. They directly measure the distance to spacecrafts, the Moon and nearby asteroids, superseding traditional astrometric observations performed with transit circles and photography. However, for most minor planets (asteroids) and for the outer and trans-Neptunian planets, astrometric observations are essential. Pioneering in the automated observation of solar system objects was the Naval Observatory Flagstaff Station (NOFS) 8-inch-telescope scanning transit circle, still in operation. One of the most productive projects in this area is the LINEAR program which discovered hundreds of thousands of asteroids. Ephemerides of natural satellites are being improved by new reductions and scanning of photographic plates taken over decades with state-of-the-art plate measure machines like the DAMIN (Royal Observatory Belgium).

Looking at nearby stars, the 4^{th} edition of the Yale Trigonometric Parallaxes Catalog summarizes the standard over the last century of observations, superseded in number of stars only recently by the Hipparcos Catalog and the NOFS 61-inch program. However, the best ground-based parallaxes are of comparable or even better accuracy (0.5 mas) than the Hipparcos parallaxes. The most active parallax observing program today is the RECONS project utilizing the 0.9 m Cerro Tololo Interamerican (CTIO) telescope in Chile, targeting in particular nearby ($\lesssim 25$ pc) but faint dwarf stars.

The Tycho-2 catalog of the 2.5 million brightest stars is the first step in the identification of the net of reference stars beyond the Hipparcos Catalogue. Tyhco-2 is 99% complete to $V \sim 11.0$ and 9% complete to $V \sim 11.5$. It is based on the star-mapper data obtained on board the Hipparcos satellite, combined with over 140 ground-based star catalogs to obtain proper motions on the 2 mas yr^{-1} level. Several scanning transit circle programs (Bordeaux, Carlsberg, San Fernando) produced zone catalogs of different areas of the sky with millions of stars.

The United States Naval Observatory (USNO) CCD Astrograph Catalog (UCAC) project covered the whole sky to about 16^{th} magnitude with positional errors of 20 to 70 mas for about 80 million stars providing accurate reference stars beyond the Tycho-2 limit. Based on all applicable Schmidt telescopes sky survey plates, the USNO-B catalog contains over 10^9 objects. In August 2009 a new version of the UCAC catalog (UCAC3) was released, providing the first all-sky coverage of the series (Zacharias et al. 2009).

The Yale University and the University of San Juan, Argentina, covered the sky south of Dec. = −20° with the Southern Proper Motion survey (SPM4) catalog of just over 100 million objects with absolute proper motions and positions to magnitude 18 and accuracies of 2 to 5 mas yr^{-1} and 20 to 100 mas, respectively. The Naval Observatory Merged Astrometric Dataset (NOMAD) combines most of the above star catalogs.

The new era of ground-based projects will probably be carried out by automated small telescopes, like SkyMapper, a state-of-the-art automated wide-field survey telescope, representing a new vehicle for scientific discovery. Sited in Australia, SkyMapper's mission is to robotically create the first comprehensive digital survey of the entire southern sky. Proper motions will be determined thanks to a total of 36 visits to each patch of the sky.

1.3.2 Space-based projects

Concerning differential astrometry, the Fine Guidance Sensors (FGS) aboard the *HST* have been used for a limited number of very accurate astrometric observations (sub-mas) of the open cluster M 35 (as an astrometric calibration area) and precise distance and mass determinations of selected bright stars and binaries. Direct imaging with various *HST* CCD instruments provided high accuracy proper motions of faint stars in selected areas of the sky.

However, the real power of space-based projects is the possibility to perform large-angle astrometry with unprecedented accuracy with respect to ground-based telescopes. Indeed, measurements from the ground have to face insurmountable barriers to improvements in accuracy, especially for large-angle measurements and systematic terms (see also Monet 1988). Problems are dominated by the effects of the Earth's atmosphere, but are compounded by complex optical terms, thermal and gravitational instrument flexures, and the absence of all-sky visibility. In this perspective, the European Space Agency (ESA) Hipparcos mission boosted the field of astrometry by orders of magnitude, providing an all-sky catalog of over 118 000 stars with positions, proper motions and parallaxes on the 1 mas (1 mas yr^{-1}) level. The biggest impact on science was achieved by the enormous number of highly accurate parallaxes, while the positions of the stars already have degraded to about 20 mas due to accumulation of errors in the proper motions. A new reduction of the catalog (van Leeuwen 2007) provided an improvement by a factor 2.2 in the total weight compared to the original catalog, released in 1997, and provides much improved data for a wide range of studies on stellar luminosities and local galactic kinematics.

A new series of space-based projects is scheduled to start in the new few years. The Joint Milliarcsecond Pathfinder Survey (J-MAPS) mission aims at Hipparcos-like accuracies but for millions of stars to about 14^{th} magnitude. In combination with Hipparcos data, proper motions near 0.1 mas yr^{-1} accuracy are expected for the bright stars. This mini-satellite is expected to launch in 2012.

The next big step in space astrometry will be the ESA GAIA mission. The goal is to observe about 10^9 stars in our Galaxy and throughout the Local Group to 20^{th} magnitude with accuracies of 0.01 to

0.2 mas for position, proper motions and parallaxes. GAIA is an ambitious mission to chart a three-dimensional map of the Milky Way, in the process revealing the composition, formation and evolution of the Galaxy. Combined with astrophysical information for each star, provided by on-board multi-color photometry, these data will have the precision necessary to quantify the early formation, and subsequent dynamical, chemical and star formation evolution of the Milky Way Galaxy. Additional scientific products include detection and orbital classification of tens of thousands of extra-solar planetary systems, a comprehensive survey of objects ranging from huge numbers of minor bodies in our Solar System, through galaxies in the nearby Universe, to some 500 000 distant quasars. It will also provide a number of stringent new tests of general relativity and cosmology. Launch of GAIA is expected in 2012 and the final catalog should become available in 2020.

Finally, the SIM-Lite mission will be able to observe astrometric wobbles on the 1 microarcsec (μas) level and thus be capable of discovering earth-like planets around nearby stars. SIM Lite is a pointed, astrometric mission which will observe about 20 000 selected targets down to $20^{\rm th}$ magnitude in the post-GAIA era. A large variety of science questions will be addressed by SIM Lite in addition to planet hunting, ranging from outer solar system objects to binary black holes at cosmological distances.

1.4 The wide-field imagers

Besides specific dedicated projects, there are other ways to obtain high-precision astrometric measurements. A keystone in studies of the stellar clusters of the Milky Way is represented by wide-field imagers, as we will see in the following. Hereafter we will consider both ground-based and space-based wide-field imagers likewise[1].

Recent investigations have shown that imaging from the cameras on board *HST* can provide high-precision astrometry for point-like sources (Anderson & King 2000). There are several factors which make imaging astrometry much more accurate from space than from the ground. First, the absence of atmospheric effects allows us to obtain diffraction-limited images, with a point-spread function (PSF) which is nearly constant in time and therefore amenable to detailed modeling. Also, space-based observatories are free of differential-refraction effects, which plague ground-based images not taken at the zenith. Finally, the weightless environment means that telescope flexure does not lead to large changes in the distortion solution, which means that it is possible to model the solution to much higher accuracy.

However, despite all the benefits of imaging astrometry from space, there are some significant limitations as well. First, the need to download all the data taken to the ground puts a major limit on how much data can be collected by *HST* per hour. For this reason, both *HST* wide-field cameras [the wide-field channel (WFC) of the Advance Camera for Surveys (ACS) and the ultraviolet-visible channel (UVIS) of the Wide-field Camera 3 (WFC3)] are made of 4096×4096 pixels, and are undersampled in order to get the maximum sky coverage for the limited number of pixels.

Ground-based telescopes suffer no such limitations. They can be made up of dozens of CCDs and can collect terabytes of information every night. Furthermore, each exposure can cover over up to 400 times more than the biggest *HST* FoV. In addition, the fact that *HST* is undersampled introduces a significant

[1]Note that the ratio between the full width at half maximum and the linear size in pixel for ground-based mosaic CCDs – for instance the 8k×8k pixel WFI@ESO2.2m – and for *HST* wide-field channels (either ACS/WFC or WFC3/UVIS) is comparable, being $\sim 5/10000 \simeq 5{\cdot}10^{-4}$ for the formers, and $\sim 2/4000 \simeq 5{\cdot}10^{-4}$ for the latter. This means that these ground- and space-based wide-field imagers have around the same number of resolution elements.

complexity to the data analysis. Special care must be taken to derive exquisitely accurate PSFs (see Anderson & King 2000), so that the positions measured with them will be free from bias. Ground-based detectors can afford to oversample the stellar image, so that sampling will not be a limitation or complication for high accuracy. Finally, the fact that time on *HST* is scarce means that it is hard to get space-based observations. By contrast, there are many ground-based observatories.

Even with its sampling and FoV limitations, the phenomenal astrometric precision possible with *HST* has allowed us to undertake projects that were simply impossible before, such as:

- the geometrical determination of the globular cluster (GC) distance scale by comparison of the internal proper motions with radial velocity dispersion obtained from the ground (Bedin et al. 2003a; Anderson & van der Marel 2010; van der Marel & Anderson 2010);
- the study of the low-mass Main Sequence (MS) down to the hydrogen burning limit (King et al. 1998, 2005; Bedin et al. 2001; Richer et al. 2008);
- the proper motions of the Galactic star clusters and nearby galaxies; (Bedin et al. 2003b, 2006; Milone et al. 2006; Richer et al. 2008; Anderson et al. 2009);
- the Galactic dynamic measurements (Bedin et al. 2003b);
- the cluster rotation on the plane of the sky (Anderson & King 2003; Milone et al. 2006).

Nonetheless, even given the clear advantages of *HST*, there are a number of cluster studies that are better suited to ground-based observations. For instance, studying the outskirts of clusters requires large areal coverage but does not require a telescope with the resolution of *HST*. Many aspects of cluster evolution can only be understood by putting together surveys done in the cluster core with more extended surveys of the outer regions. Therefore, large FoV ground-based studies are very much complementary to the core studies possible only with *HST*. These large-FoV studies will tend to probe the clusters in the outskirts where the density is low relative to the field, so proper-motion cleaning will play an essential role in constructing a pure cluster sample, as it has in many *HST* projects.

High-precision astrometry significantly improves high-precision photometry. Specifically, (i) it allows to derive PSFs at the second order of accuracy thanks to the improved ability to determine star centroids; (ii) it provides additional selection criteria to isolate well-measured stars (i.e., the QFIT parameter, Anderson et al. 2008, see Chapter 4.2.1); (iii) it enables to derive precise transformations to bring each individual exposure on to the master frame reference system, so that it is possible to collect, for a given star, all the information contained in all the exposures at once (i.e., the "second-passage" photometry, Anderson et al. 2008, see also Chapter 4.2.2). Several projects take advantage of these indirect aspects of astrometry, some of them already published:

- the double MS in ω Centauri (Bedin et al. 2004);
- the anomalous white dwarf (WD) cooling sequence (CS) in the open cluster NGC 6791 (Bedin et al. 2005, 2008a, 2008b);

- the bottom of the WD CS in the old open cluster NGC 2158 (Bedin et al. 2010) and in the GC M 4 (Bedin et al. 2009);
- the discovery of a triple MS in the globular cluster NGC 2808 (Piotto et al. 2007);
- the discovery of a split sub-giant branch (SGB) in the GC NGC 1851 (Milone et al. 2008), and its sub-population radial distribution (Milone et al. 2009a);
- split SGBs in other Milky Way GCs (47 Tuc, Anderson et al. 2009; NGC 6752, Milone et al. 2010; and several others, Piotto 2009), and in intermediate-age GCs of the Large Magellanic Cloud (Milone et al. 2009b).

Our interest in the above applications, in particular in the proper-motion aspects, has stimulated the effort to transfer what we have learned by measuring high-accuracy positions on *HST* images to wide-field, ground-based data. Much attention has been devoted over the years to software that can extract good photometry from ground-based images (DAOPHOT, ROMAPHOT, ...), but thus far very little attention has been devoted to astrometry. Photometry and astrometry make very different demands on PSF analysis. Photometry concerns itself more with sums of pixels, whereas astrometry keys off of differences between nearby pixel values, but there is no reason that with a good PSF we cannot measure both good fluxes and positions.

Over the last few years, several Wide Field Imagers (WFIs) have come on-line at large ground-based telescopes (MPI-ESO 2.2 m, AAT 4 m, CFHT 3.6 m, UKIRT 3.8 m, SUBARU 8.2 m, LBT 2×8.4 m), and their number and their FoV are continuously increasing (VST 2.5 m, VISTA 4 m, LSST 8.4 m, ...). These WFIs allow us to map completely any open or globular cluster in our Galaxy and their tidal tails, and to get accurate photometry for an enormous numbers of stars.

One of the most promising (and still quite largely unexplored) opportunities presented by wide-field images involves astrometry. Accurate astrometry over wide fields is important for a variety of reasons. To begin with, an accuracy of 0.2 arcsec or better is usually required to position point-like sources in the increasing number of multi-slit and multi-fiber spectroscopic facilities. But the most promising astrometric applications lie in the ability to measure proper-motions for a large number of stars. In principle, the ground-based WFIs should allow astrometric measurements with an accuracy far better than the nominal 0.2 arcsec. As we will show in Chapters 4 and 6, with a baseline of just a few years, images collected with modern WFIs can provide proper motions more accurate than those obtainable with old plates with a baseline of several decades (see also Anderson et al. 2006). (Note, however, that these plates will still remain valuable for long-term non-linear astrometry, such as the determination of the orbit of long-period visual binaries, and of course for long-term variation in the light curves.)

There are clearly some things that only *HST* can do, namely astrometry and photometry of extremely faint stars or stars in crowded regions, where there truly is no substitute for high resolution (i.e., Chapters 7, 8). Nevertheless, we will show in this thesis that many scientifically interesting projects can now be carried out with ground-based imagers, such as the Large Binocular Camera mounted at the prime focus of the LBT (Chapters 4, 4.6, 5), or the WFI@2.2m (Chapters 6, 7).

Bibliography

Anderson, J., & King, I. R. 2000, PASP, 112, 1360

Anderson, J. & King, I. R. 2003, AJ, 126, 772
Anderson, J., Bedin, L. R., Piotto, G., Yadav, R. S., & Bellini, A. 2006, A&A, 454, 1029
Anderson, J. et al. 2008, AJ, 135, 2055
Anderson, J., Piotto, G., King, I. R., Bedin, L. R., & Guhathakurta, P. 2009, ApJL, 697, L58
Anderson, J., & van der Marel, R. P. 2010, ApJ, 710, 1032
Bedin, L. R., Anderson, J., King, I. R., Piotto, G. 2001, ApJL, 560, L75
Bedin, L. R., Piotto, G., Anderson, J., & King, I. R. 2003, New Horizons in Globular Cluster Astronomy, ASP Conf. Ser., 296, 360 (2003a)
Bedin, L. R., Piotto, G., King, I. R., & Anderson, J. 2003, AJ, 126, 247 (2003b)
Bedin, L. R. et al. 2004 ApJL, 605, L125
Bedin, L. R. et al. 2005 ApJL, 624, L45
Bedin, L. R., Piotto, G., Carraro, G., King, I. R., & Anderson, J. 2006, A&A, 460, L27
Bedin, L. R., King, I. R., Anderson, J., Piotto, G., Salaris, M., Cassisi, S., & Serenelli, A. 2008, ApJ, 678, 1279 (2008a)
Bedin, L. R., Salaris, M., Piotto, G., Cassisi, S., Milone, A. P., Anderson, J., & King, I. R. 2008, ApJL, 679, L29 (2008b)
Bedin, L. R., Salaris, M., Piotto, G., Anderson, J., King, I. R., & Cassisi, S. 2009, ApJ, 697, 965
Bedin, L. R., Salaris, M., King, I. R., Piotto, G., Anderson, J., & Cassisi, S. 2010, ApJL, 708, L32
King, I. R., Anderson, J., Cool, A. M., Piotto, G. 1998, ApJL, 492, L37
King, I. R., Bedin, L. R., Piotto, G., Cassisi, S., Anderson, J. 2005, AJ, 130, 626
Milone, A. P., Villanova, S., Bedin, L. R., Piotto, G., Carraro, G., Anderson, J., King, I. R., & Zaggia, S. 2006, A&A, 456, 517
Milone, A. P., Villanova, S., Bedin, L. R., Piotto, G., Carraro, G., Anderson, J., King, I. R., & Zaggia, S. 2006, A&A, 456, 517
Milone, A. P., et al. 2008, ApJ, 673, 241
Milone, A. P., Stetson, P. B., Piotto, G., Bedin, L. R., Anderson, J., Cassisi, S., & Salaris, M. 2009, A&A, 503, 755 (2009a)
Milone, A. P., Bedin, L. R., Piotto, G., & Anderson, J. 2009, A&A, 497, 755 (2009b)
Milone, A. P., et al. 2010, ApJ, 709, 1183
Monet, D. G. 1988, ARA&A, 26, 413
Richer, H. B., et al. 2008, AJ, 135, 2141
van der Marel, R. P., & Anderson, J. 2010, ApJ, 710, 1063
van Leeuwen, F. 2007, A&A, 474, 653
Verbunt, F., & van Gent, R. H. 2010, arXiv:1003.3836
Zacharias, N., et al. 2009, VizieR Online Data Catalog, 1315, 0

2

Geometric distortion correction of the LBC at the prime focus of the LBT

The first step to achieve high-precision astrometry is to derive an accurate geometric-distortion (GD) solution. In this Chapter we describe our GD correction technique and its application to the Blue Camera of the Large Binocular Telescope, which enables a relative astrometric accuracy of ∼15 mas for the $B_{\rm Bessel}$ and $V_{\rm Bessel}$ broad-band filters.

Material contained in this Chapter has been accepted for publication in *Astronomy & Astrophysics* (Bellini & Bedin 2010).

2.1 Introduction

Modern wide-field imagers (WFI) equipped with CCD detectors began their operations at the end of the last century, however – after more than 10 years – their astrometric potential still remains somehow unexploited (see Anderson et al. 2006, hereafter Paper I). It is particularly timely to begin exploring their full potential now that WFI start to appear also at the focus of the largest available 8m-class telescopes.

In this work we present a correction for the GD of the Blue prime-focus Large Binocular Camera (LBC), at the Large Binocular Telescope (LBT). Unlike in Paper I, in which we corrected the GD of the WFI at the focus of the 2.2m MPI/ESO telescope (WFI@2.2m) with a look-up table of corrections, for the LBC@LBT we will adopt the same technique described in Anderson & King (2003, hereafter AK03), and successfully applied to the new Wide field Camera 3/UV-Optical channel on board the *Hubble Space Telescope* (Bellini & Bedin 2009, hereafter BB09; see also Chapter 3).

This Chapter is organized as follows: Section 2 briefly describes the telescope/camera set up; Section 3 presents the data set used. In section 4, we describe the steps which allowed us to obtain a solution of the GD, for each detector separately, while in Section 5 we presents a (less accurate) inter-chip solution. Distortion stability is analyzed in Section 6, and a final Section summarizes our results.

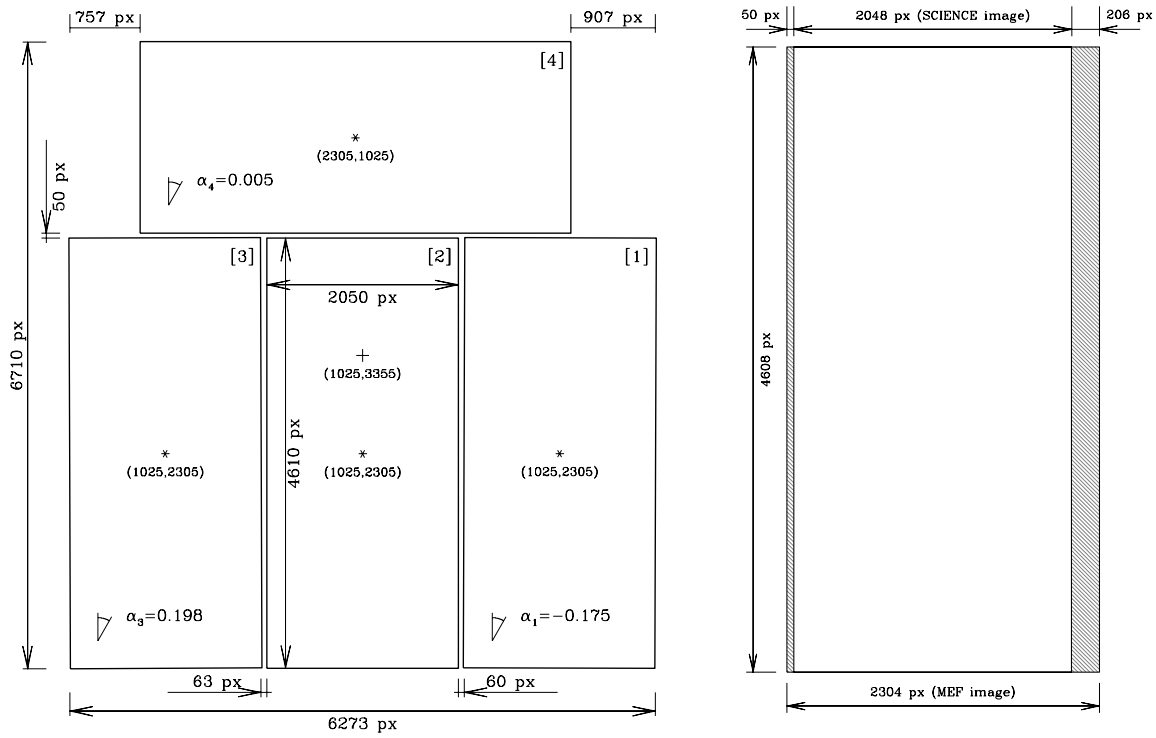

FIGURE 2.1— (*Left*): LBC-Blue mosaic layout; "∗" marks the center for each chip (see Sect. 2.3 for the operative definition of centers and chips), while "+" marks the here defined center of the mosaic. (*Right*): Each MEF file consists of 4 images. Each image is composed by one scientific region and two overscan regions, covering the first 50 and the last 206 pixel columns (shaded).

2.2 The Large Binocular Camera Blue

The LBT is a large optical/infrared telescope that utilizes two mirrors, each having a diameter of 8.4 meters[1]. The focal ratio of the LBT primary mirrors ($F/1.14$) and its large diameter are factors that require a careful development of the corrector for a prime-focus camera. The blue channel of the LBC (LBC-Blue) is mounted at the prime focus of the first LBT unit. The corrector, consisting of three lenses, is designed to correct spherical aberration, coma, and field curvature, according to the design by Wynne (1996). The last two of these three lenses are sub-divided in two elements each, with the last one being the window of the cryostat (Ragazzoni et al. 2000, 2006; Giallongo et al. 2008). The final LBC-Blue focal-ratio is $F/1.46$.

The LBC-Blue employs an array of four 16-bit e2v 42-90 (2048×4608) chips, with a reference pixel-scale of $0\farcs2297\,\mathrm{pix}^{-1}$, providing a total Field of View (FoV) of $\sim 24' \times 25'$. The four chips are mounted on the focal plane in such a way as to maximize the symmetry of the field, with three chips contiguous longside, and the fourth one rotated 90 degrees anti-clockwise, and centered above the others. The LBC-Blue layout is shown on the left hand of Fig. 2.1. Row estimates of the intra-chip gaps are expressed as the nearest integer pixel. Numbers between square brackets are chip identification numbers, as read from the raw Multi Extension Fits (MEF) file. Average rotation angles are given with respect to chip # 2, chosen as reference (we will see in Section 2.5 how to bring positions from each chip into a common corrected meta-chip system). On the right hand of Fig. 2.1 we show, in

[1] `www.lbt.it`; `medusa.as.arizona.edu/lbto/`.

TABLE 2.1— Log of M 67 data used here.

Date	**Filter**	**#Images×Exp. time** (s)	**Airmass** (sec z)	**Image Quality** (arcsec)
Feb 22, 2007	$V_{\rm Bessel}$	$1\times15{,}1\times330{,}17\times110$	1.07-1.13	0.62-1.31
Feb 27, 2007	$V_{\rm Bessel}$	25×100	1.07-1.10	0.84-1.26
Mar 16, 2007	$B_{\rm Bessel}$	25×180	1.07-1.14	0.84-1.08

units of raw pixel coordinates, the dimensions of each chip, which consists of the scientific image in between two overscan regions (shaded areas Fig. 2.1, which cover the first 50 and the last 206 pixel columns).

During the optical design phase, GD (of pin-cushion type) was not considered as an aberration, since it may be corrected at post-processing stages. The GD is found to be always below the 1.75% level (Giallongo et al. 2008). This is translated in offsets as large as 50 pixels (∼11 arcsec) from corner to corner of the LBC-Blue FoV. Obviously, the correction of such a large GD is of fundamental importance for high precision astrometric measurements. Note that in the following, with the term "geometric distortion" we are lumping together several effects: the optical field-angle distortion introduced by camera optics, light-path deviations caused by the filters (in this case $B_{\rm Bessel}$ and $V_{\rm Bessel}$), non-flat CCDs, alignment errors of CCDs on the focal plane, etc.

Raw data images are contained in a single MEF file with four extensions, one for each chip, constituted by 2304×4608 pixels, containing overscan regions. The scientific area of these chips is located within pixel (51, 1) and pixel (2098, 4608) (i.e. 2K×4.5K pixels, see right panel of Fig. 2.1). For reasons of convenience, we added an extra pixel (flagged at a value of −475) to define the borders of the 2048×4608 pixel scientific regions, and we will deal exclusively with 2050×4610 arrays (*work-images*). Again for reasons of convenience, since chip # [4] is stored along the same physical dimensions as the other three in the raw MEF file, we decided to rotate it by 90 degrees anti-clockwise.

Hereafter, when referring to x and y positions, we will refer to the raw pixel coordinates measured on these work-images, and – unless otherwise specified – we will refer to the work-image of the chip # [k], simply as [k]. Transformation equations to convert from the raw pixel coordinates of the archive MEF file $(x_k^{\rm MEF}, y_k^{\rm MEF})$ to the pixel coordinates of the work-images (x, y) are as follows:

$$k = 1,2,3: \begin{cases} x = x_k^{\rm MEF} - 49 \\ y = y_k^{\rm MEF} + 1 \end{cases}$$

$$k = 4: \begin{cases} x = 4610 - y_k^{\rm MEF} \\ y = x_k^{\rm MEF} - 49. \end{cases}$$

[For clarity, every LBC-Blue image is a MEF file, from which we define 4 *work-images*. Moreover, we will treat every chip of each image independently.]

2.3 The data-set

During LBT science-demonstration time, between February and March 2007, we obtained (under the Italian guaranteed time) about four hours to observe the old, metal-rich open cluster M 67 ($\alpha = 08^{\rm h}51^{\rm m}23^{\rm s}.3$, $\delta = +11^\circ49'02''$,

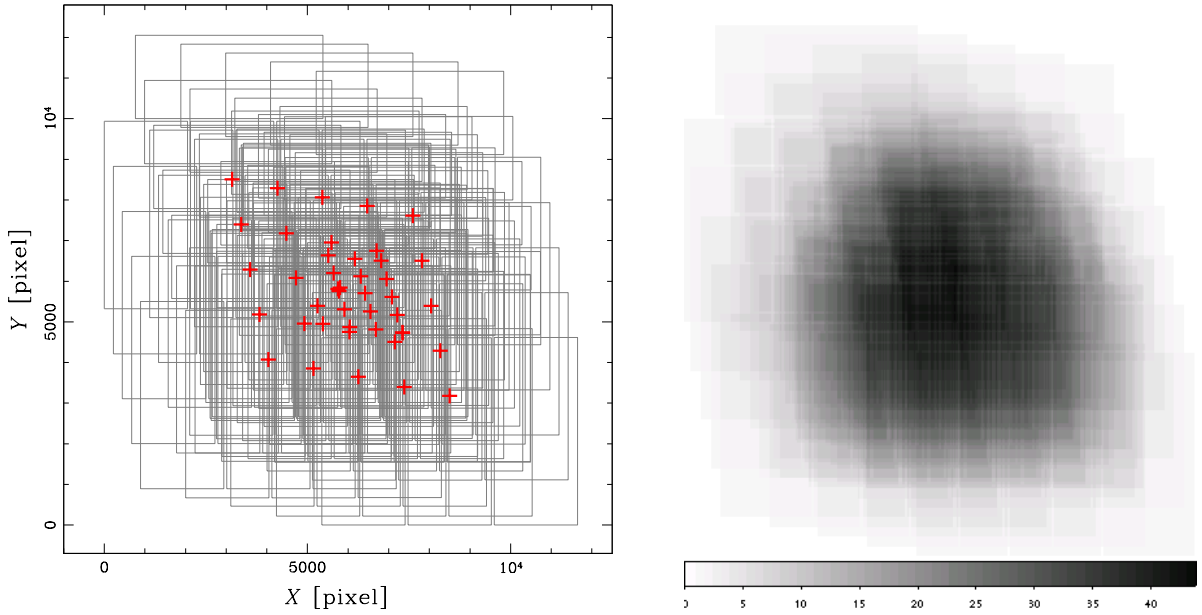

FIGURE 2.2— *(Left)*: Dither pattern, in pixel units, of the *V* images used to solve for the geometric distortion. We used both small and large dithers to adequately sample the GD. Red crosses mark the center of LBC-Blue mosaic, (1025, 3355) position in the coordinate system of chip # [2], as defined in Fig. 2.1). The original pattern was designed to be a rhomboidal array of 5×5 pointings (see text). Unfortunately some of the images with the small dither pattern were not usable. *(Right):* Depth-of-coverage map for the same images.

J2000.0, Yadav et al. 2008, hereafter Paper II). The aim of the project is to reach the end of the DA white dwarf (WD) cooling sequence (CS) in the two filters $V_{\rm Bessel}$ and $B_{\rm Bessel}$ (hereafter simply *V* and *B*). In addition, we want to compute proper motions for a sample of objects in the field by combining these LBC@LBT exposures with archival images collected 10 years before at the Canada France Hawaii Telescope (CFHT). The pure sample of WD members will serve to better understand the physical processes that rule the WD cooling in metal-rich clusters. A necessary first step to get accurate proper motions is to solve the GD for the LBC-Blue. The results of the investigation on the WD CS of M 67, and its absolute proper motion, are presented in Chapters 4.6 and 5 (see also Bellini et al. 2010a, 2010b); here we will focus on the GD of LBC-Blue, providing a solution that might be useful to a broader community of LBC-Blue users.

The observing strategy had to arrange both the scientific goals of the project and the need to solve for the geometric distortion. As an educated guess, the adopted procedure to solve for the geometric distortion is the auto-calibration described in great detail in Paper I, which still represents the state of the art in ground-based CCD astrometry with wide-field imagers.

With the idea to map the same patch of the sky in different locations on the same chip, as well as on different chips, we chose a particular pointing set up, constituted by an array of 5×5 observations, dithered in such a way that a star never falls two times on the same gap between the chips. All 25 exposures of a given dither sequence were executed consecutively. The 5×5 dither pattern is repeated adopting small (∼100″) and large (∼200″) steps in filter *V*, and only small steps in the *B* filter. Figure 2.2 shows the dither pattern and the depth-of-coverage map for all our *V* exposures. Table 2.1 gives the log of observations for both *B* and *V* exposures. All the images were collected in service mode.

Unfortunately, not all the exposures met the desired specifications of our proposal (dark-night conditions and seeing better than 0.″8). In particular, all the *V* images with large dithers are affected by anomalously high background values (up to ∼20 000 counts for a 100 s exposure, thus limiting us at the faint magnitudes). Moreover, 6 out of the 25 *V* images taken with small dithers have an image quality well above 1.″5 (probably related to guide-star system problems). These images are of no use for our purpose, and were not considered in this study.

Our GD solution will be first obtained for the *V* filter images, and later tested, and eventually re-derived, for the *B* filter ones. To measure star positions and fluxes, we developed a reduction method that is mostly based on the software img2xym_WFI (Paper I). This new software (img2xym_LBC) similarly generates a list of positions, fluxes, and a quality of the PSF-fit values (see Anderson et al. 2008) for each of the measured objects in each of the four chips. Details of the PSF-fitting software img2xym_LBC and the final M 67 astro-photometric catalog will be presented in Chapter 4 (which will also deal with photometric zero point variations and PSF variability).

2.4 Auto-calibration

The most straightforward way to solve for the GD would be to observe a field where there is a prior knowledge of the positions of all the stars in a distortion-free reference frame. [A distortion-free reference frame is a system that can be transformed into any another distortion-free frame by means of *conformal transformations*[2].] GD would then show itself immediately as the residuals between the observed relative positions of stars and the ones predicted by the distortion-free frame (on the basis of a conformal transformation). Unfortunately, such an "astrometric flat-field" with the right magnitude interval, source density, and accuracy, is difficult to find and astronomers are often left with the only option of auto-calibration.

The basic principle of auto-calibration is to observe the same stars in as many different locations on the detector as possible, and to compute their average positions once they are transformed onto a common reference frame[3]. Ideally, a star should be observed from corner to corner in the FoV. This means that the total dither has to be as large as the FoV itself (see Fig. 2.2).

If the observations are taken with a symmetric dither pattern, the systematic errors will have a random amplitude, and the stars' averaged position will provide a better approximation of their true position in a distortion-free frame (the master frame). This master frame – as defined by the averaged position of the sources in the FoV – will then serve as a first guess for the construction of an astrometric flat-field, which in turn can be used (as we will see in detail below) to compute star-position residuals (hereafter simply residuals), necessary to obtain a first estimate of the GD for each chip. Single chips are then individually corrected with these preliminary GD solutions (one for each chip) and the procedure of deriving the master frame is repeated. With the new-derived master frame, new (generally smaller) residuals are computed, and the procedure is iteratively repeated until convergence is reached (see below).

The overall distortion of LBC-Blue is large enough (∼50 pixels) that – to facilitate the cross-correlation of positions of objects observed in different locations on the detector – it becomes very convenient to perform a preliminary (although crude) correction.

As a first guess for the master frame, we used the best astrometric flat-field available in the literature for the M 67 field: the astro-photometric catalog recently published in Paper II. This catalog was obtained with images taken with the WFI@2.2m; it is deeper with respect to other wide-field catalogs (i.e., UCAC2, USNO-A2, and 2MASS), has *V* photometry, and its global astrometric accuracy is of the order of ∼50 mas. Nevertheless, this

[2] A conformal transformation between two catalogs of positions is a four-parameter linear transformation, specifically: rigid shifts in the two coordinates, one rotation, and one change of scale, i.e. the shape is preserved.

[3] We want to make clear that we had at our disposal only ∼4 hours of telescope time during the science-demonstration time, to be used both for the science and the calibration project. With the minimum exposure time needed to have a good signal to noise ratio for the target stars (∼100 s), and taking into account overheads for the necessarily large dithers for GD correction, the optimal solution was to observe 25 dithered exposures with the aim of calibrating the LBC distortion.

catalog is far from ideal; even the faintest – poorly measured – stars of Paper II are close to saturation in our LBC-Blue images, and the total number of usable (even if saturated) objects was never above ∼250 per chip (among which less than ∼40 per chip were unsaturated). We also chose to re-scale the pixel coordinates of the Paper II catalog (with an assumed WFI@2.2m pixel-scale of 238 mas, Paper I) to the average pixel-scale of LBC-Blue, adopting for it the median value of 225.4 mas/pixel (as derived by Giallongo et al. 2008). Since the scale is a free parameter in deriving GD correction, choosing a particular scale value will not invalidate the solution itself. Later we will derive the average scale of [2] in its central pixel (1025,2305), and we will determine the absolute value of our master-frame plate scale by comparison with objects in the Digital Sky Survey, and study the average inter-chip scale variations with time and conditions.

Once this first-guess solution is obtained, it is easier to cross-correlate the star catalogs from each LBC-Blue work-image with respect to a common reference frame, in order to perform the auto-calibration procedure, as described in detail in the following subsections.

2.4.1 Deriving a self-consistent solution

We closely followed the auto-calibration procedures described in detail – and used with success – in AK03 to derive the GD correction for each of the four detectors of WFPC2. The auto-calibration method consists of two steps: 1) deriving the master frame, and 2) solving for the GD for each chip, individually. These two steps are then repeated interactively, until both the geometric distortion solutions and the positions in the master-list converge.

The master-list

As aforementioned, only during the very first iteration did we use the Paper II catalog as a master frame to get the preliminary best guess of the GD for each chip. In all the subsequent iterations, the master frame was obtained from all the available LBC work-images (i. e., the master-list is made with images taken within few days). Conformal transformations are used to bring star positions, as measured in each work-image, into the reference system of the current master frame. We used only well-measured, unsaturated objects with a stellar profile. The final master-list contains 2374 uniformly spread stars (see Fig. 2.3), with coordinates $(X^{\rm master}, Y^{\rm master})_i$, with $i = 1, \ldots, 2374$, that were observed, at each iteration, in at least 3 different images. As we can see on the right panel of Fig. 2.2, stars falling in the center of our FoV can be observed up to 44 times in the *V*-filter, i. e. the maximum overlap among the *V* exposures. We have at most 25 observations for a given star in the case of the *B*-filter exposures.

Modeling the geometric distortion

As in AK03 and in BB09, we represent our solution with two third-order polynomials. Indeed, we found that with two third-order polynomials our final GD correction has a precision level of ∼0.04 pixel in each coordinate (∼10 mas), and higher orders were unnecessary, with this precision level (as we will see) being well within the instrument stability. We performed tests with fourth- and fifth-order polynomials, obtaining comparable results in term of GD-solution accuracy, but at the expense of using a large number of degrees of freedom in modeling the GD solution.

Having an independent solution for each chip, rather than one that uses a common center of the distortion for the whole FoV, allows a better handle on individual detector effects, such as a different relative tilt of the chip surfaces, etc. We chose a pixel close to the physical center of each chip as reference position, with respect to solve for the GD, regardless of its relative position with respect to the principal axes of the optical system. The adopted centers of our solution are the locations $(x_\circ, y_\circ)_{k=1,2,3} = (1025, 2305)$ for chips [1], [2], [3], and the $(x_\circ, y_\circ)_4 = (2305, 1025)$ for chip [4], all in the raw pixel coordinates of the work-images.

For each *i*-star in each *k*-chip of each *j*-MEF file, the distortion corrected position $(x^{\rm corr}_{i,j,k}, y^{\rm corr}_{i,j,k})$ is the observed

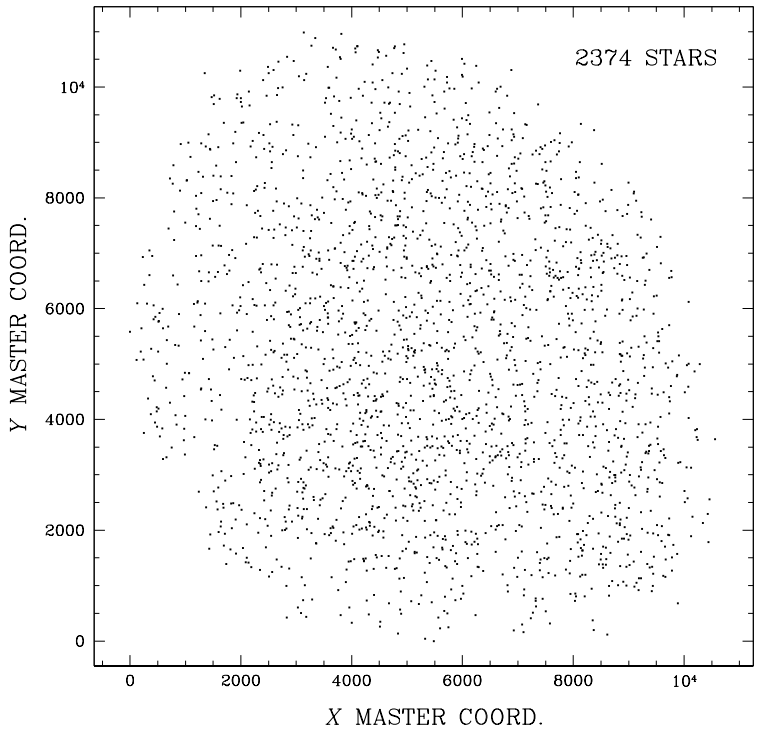

FIGURE 2.3— The master star-list map.

position plus the distortion correction $(\delta x_{i,j,k}, \delta y_{i,j,k})$:

$$\begin{cases} x^{\rm corr}_{i,j,k} = x_{i,j,k} + \delta x_{i,j,k}(\tilde{x}_{i,j,k}, \tilde{y}_{i,j,k}) \\ y^{\rm corr}_{i,j,k} = y_{i,j,k} + \delta y_{i,j,k}(\tilde{x}_{i,j,k}, \tilde{y}_{i,j,k}), \end{cases}$$

where $\tilde{x}_{i,j,k}$ and $\tilde{y}_{i,j,k}$ are the normalized positions, defined as:

$$\begin{cases} \tilde{x}_{i,j,k} = \dfrac{x_{i,j,k} - (x_\circ)_k}{(x_\circ)_k} \\ \tilde{y}_{i,j,k} = \dfrac{y_{i,j,k} - (y_\circ)_k}{(y_\circ)_k}. \end{cases}$$

[Normalized positions make it easier to recognize the magnitude of the contribution given by each solution term, and their numerical round-off.]

The final distortion correction, for each star in each work-image, is given by the following two third-order polynomials (we omitted here i, j, k indexes for simplicity):

$$\begin{cases} \delta x &= a_1\tilde{x} + a_2\tilde{y} + a_3\tilde{x}^2 + a_4\tilde{x}\tilde{y} + a_5\tilde{y}^2 + a_6\tilde{x}^3 + a_7\tilde{x}^2\tilde{y} \\ &\quad + a_8\tilde{x}\tilde{y}^2 + a_9\tilde{y}^3 \\ \delta y &= b_1\tilde{x} + b_2\tilde{y} + b_3\tilde{x}^2 + b_4\tilde{x}\tilde{y} + b_5\tilde{y}^2 + b_6\tilde{x}^3 + b_7\tilde{x}^2\tilde{y} \\ &\quad + b_8\tilde{x}\tilde{y}^2 + b_9\tilde{y}^3. \end{cases}$$

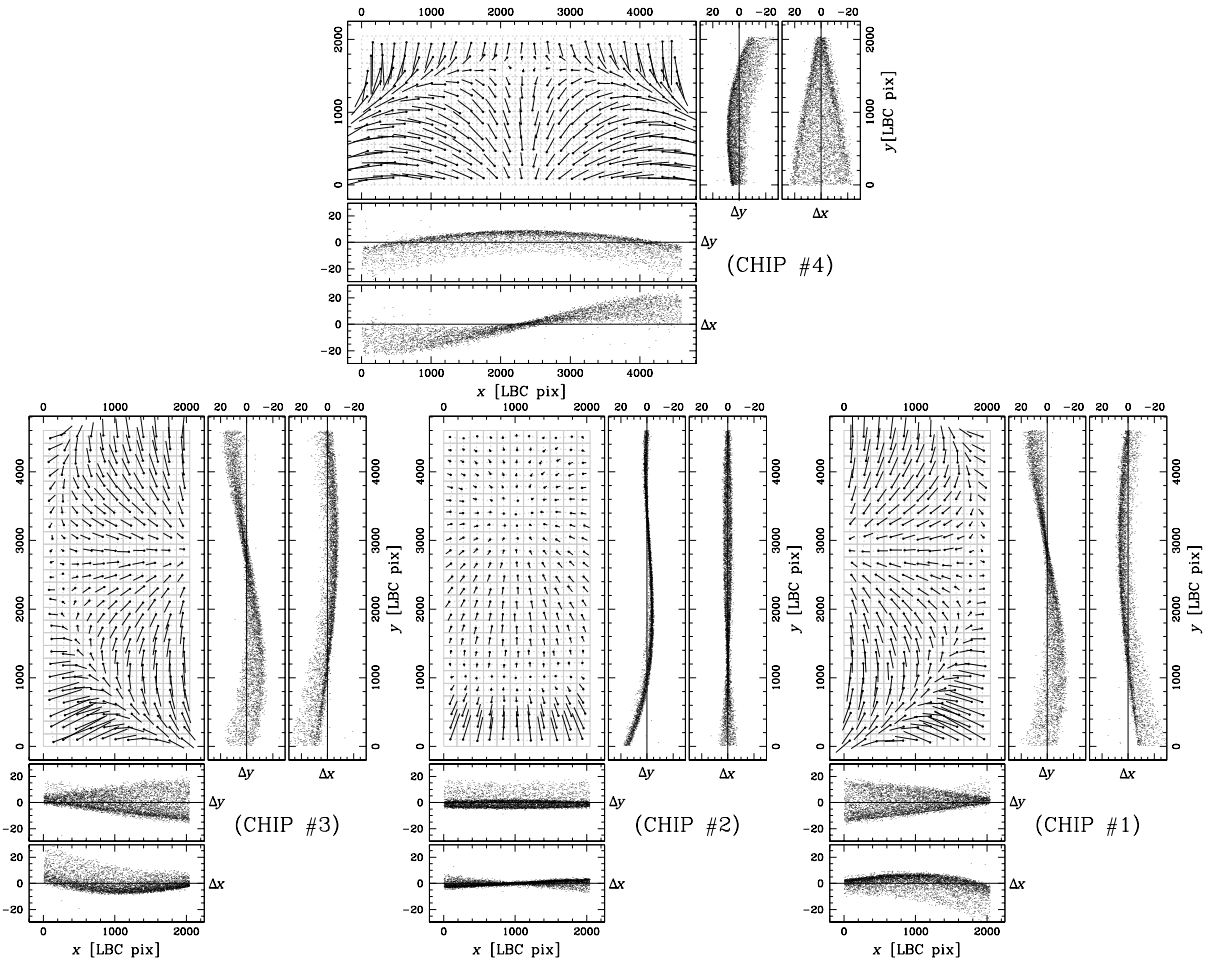

FIGURE 2.4— Residual trends for the four chips when we use uncorrected star positions. The size of the residual vectors is magnified by a factor of 25. For each chip, we also plot the single residual trends along the x and y axes. Units are expressed as LBC-Blue raw pixels.

Our GD solution is thus fully characterized by 18 coefficients: $a_1, \ldots, a_9$, $b_1, \ldots, b_9$. As done in AK03 and BB09, we imposed $a_{1,k} = 0$ and $a_{2,k} = 0$ to constrain the solution so that, at the center of the chip, it will have its x-scale equal to the one at the location $(x_\circ, y_\circ)$, and the corrected axis $y_{\rm corr}$ aligned with its y-axis at the same location. On the other hand, $b_{1,k}$ and $b_{2,k}$ must be free to assume whatever values fit best, to account for differences in scale and perpendicularity of detector's axes. Therefore, we only have to compute 16 coefficients (for each chip) to derive our GD solution.

Building the Residuals

Each i-star in the master frame is conformally transformed into each k-work-image/j-file, and cross-identified with the closest source. We indicate such transformed positions with $(X_i^{\rm master})^{T_{j,k}}$ and $(Y_i^{\rm master})^{T_{j,k}}$. Each of such

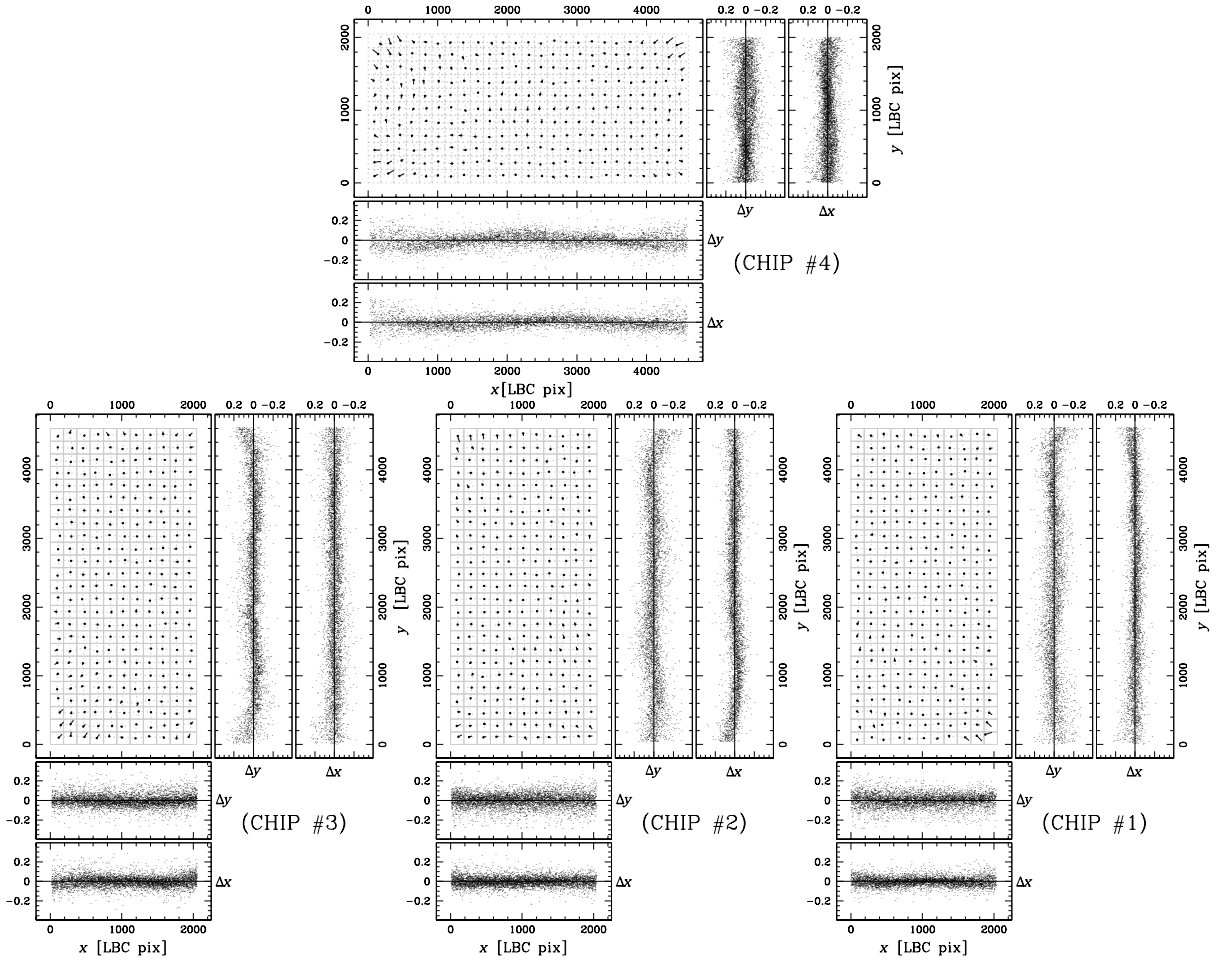

FIGURE 2.5— Same as Fig. 2.4, but for our corrected star positions. The size of the residual vectors is now magnified by a factor of 500.

cross-identifications, when available, generates a pair of positional residuals:

$$\begin{cases} \Delta x_{i,j,k} &= x^{\rm corr}_{i,j,k} - (X^{\rm master}_i)^{T_{j,k}} \\ \Delta y_{i,j,k} &= y^{\rm corr}_{i,j,k} - (Y^{\rm master}_i)^{T_{j,k}}, \end{cases}$$

which reflect the residuals in the GD (with the opposite sign), and depend on where the i-star fell on the k/j work-image/file (plus random deviations due to non-perfect PSF-fitting, photon noise, and errors in the transformations). [Note that, at the first iteration, $(x^{\rm corr}, y^{\rm corr})_{i,j,k}=(x,y)_{i,j,k}$.] In each chip we have typically 120-130 high-signal stars in common with the master frame, leading to a total of ~5500 residual pairs per chip.

These residuals were then collected into a look-up table made up of 11×25 elements, each related to a region of 186.4×184.4 pixels (25×11 elements of 184.4×186.4 for chip [4]). We chose this particular grid setup because it offers the best compromise between the need of an adequate number of grid points to model the GD (the larger, the better) and an adequate sampling of each grid element (we required to have at least 10 pairs of residuals in

each grid element). For each grid element, we computed a set of five 3σ-clipped[4] quantities: $\overline{x}_{m,n,k}$, $\overline{y}_{m,n,k}$, $\overline{\Delta x}_{m,n,k}$, $\overline{\Delta y}_{m,n,k}$, and $P_{m,n,k}$; where $\overline{x}_{m,n,k}$ and $\overline{y}_{m,n,k}$ are the average positions of all the stars within the grid element (m,n) of the k-chip, $\overline{\Delta x}_{m,n,k}$ and $\overline{\Delta y}_{m,n,k}$ are the average residuals, and $P_{m,n,k}$ is the number of stars that were used to calculate the previous quantities. These $P_{m,n,k}$ will also serve in associating a weight to the grid cells when we fit the polynomial coefficients.

Iterations

To obtain the 16 coefficients describing the two polynomials ($a_{q,k}$ with $q = 3,\ldots,9$, and $b_{q,k}$ with $q = 1,\ldots,9$) that represent our GD solution in each chip, we perform a linear least square fit of the N=m×n=11×25=275 cells (hereafter we will use the notation p=1,…,N, instead of the two m=1,…,11 and n=1,…,25). In the linear least square fit, we can safely consider the errors on the average positions $\overline{x}_{p,k}$, $\overline{y}_{p,k}$ (i.e., $\overline{x}_{m,n,k}$, $\overline{y}_{m,n,k}$) negligible with respect to the uncertainties on the average residuals $\overline{\Delta x}_{p,k}$, $\overline{\Delta y}_{p,k}$ (i.e., $\overline{\Delta x}_{m,n,k}$, $\overline{\Delta y}_{m,n,k}$). Thus, for each chip, we can compute the average distortion correction in each cell ($\overline{\delta x}_{p,k}$, $\overline{\delta y}_{p,k}$) with N relations of the form:

$$k = 1,\ldots,4;\ p = 1,\ldots,N: \begin{cases} \overline{\delta x}_{p,k} = \sum_{q=3}^{9} a_{q,k} t_{q,p,k} \\ \overline{\delta y}_{p,k} = \sum_{q=1}^{9} b_{q,k} t_{q,p,k} \end{cases}$$

(where $t_{1,p,k} = \overline{\tilde{x}}_{p,k}$, $t_{2,p,k} = \overline{\tilde{y}}_{p,k}$, …, $t_{9,p,k} = \overline{\tilde{y}}^{3}_{p,k}$), concerning the 16 unknown quantities – or fitting parameters – $a_{q,k}$ and $b_{q,k}$, for each chip.

In order to solve for $a_{q,k}$ and $b_{q,k}$, we defined, for each chip, one 9×9 matrix $\mathcal{M}_k$ and two 9×1 column vectors $\mathcal{V}_{a,k}$ and $\mathcal{V}_{b,k}$:

$$\mathcal{M}_k = \begin{pmatrix} \sum_p P_{p,k} t_{1,p,k}^2 & \sum_p P_{p,k} t_{1,p,k} t_{2,p,k} & \cdots & \sum_p P_{p,k} t_{1,p,k} t_{9,p,k} \\ \sum_p P_{p,k} t_{2,p,k} t_{1,p,k} & \sum_p P_{p,k} t_{2,p,k}^2 & \cdots & \sum_p P_{p,k} t_{2,p,k} t_{9,p,k} \\ \vdots & \vdots & \ddots & \vdots \\ \sum_p P_{p,k} t_{9,p,k} t_{1,p,k} & \sum_p P_{p,k} t_{9,p,k} t_{2,p,k} & \cdots & \sum_p P_{p,k} t_{9,p,k}^2 \end{pmatrix};$$

$$\mathcal{V}_{a,k} = \begin{pmatrix} \sum_p P_{p,k} t_{1,p,k} \overline{\Delta x}_{p,k} \\ \sum_p P_{p,k} t_{2,p,k} \overline{\Delta x}_{p,k} \\ \vdots \\ \sum_p P_{p,k} t_{9,p,k} \overline{\Delta x}_{p,k} \end{pmatrix}; \quad \mathcal{V}_{b,k} = \begin{pmatrix} \sum_p P_{p,k} t_{1,p,k} \overline{\Delta y}_{p,k} \\ \sum_p P_{p,k} t_{2,p,k} \overline{\Delta y}_{p,k} \\ \vdots \\ \sum_p P_{p,k} t_{9,p,k} \overline{\Delta y}_{p,k} \end{pmatrix}.$$

The solution is given by two 9×1 column vectors $\mathcal{A}_k$ and $\mathcal{B}_k$, containing the best fitting values for $a_{q,k}$ and $b_{q,k}$, obtained as:

$$\mathcal{A}_k = \begin{pmatrix} a_{1,k} \\ a_{2,k} \\ \vdots \\ a_{9,k} \end{pmatrix} = \mathcal{M}_k^{-1} \mathcal{V}_{a,k}; \qquad \mathcal{B}_k = \begin{pmatrix} b_{1,k} \\ b_{2,k} \\ \vdots \\ b_{9,k} \end{pmatrix} = \mathcal{M}_k^{-1} \mathcal{V}_{b,k}.$$

[4]The clipping procedure is performed as follow: first we compute the median value of the positional residuals of all the stars within a given grid element (m,n), then we estimate the σ as the 68.27 percentile of the distribution around the median. Outliers for which residuals are larger than 3σ are rejected iteratively. We note that the process converge after 2–3 iterations, and that most of the outliers are poorly measured stars, or mismatches, as at the very first steps the GD could be as large as 20 pixels, and only later (as the GD improves) these stars are correctly matched.

TABLE 2.2— Coefficients of the third-order polynomial in each chip used to represent our geometric distortion in the final solution for the *V* filter.

Term(q)	Polyn.	$a_{q,[1]}$	$b_{q,[1]}$	$a_{q,[2]}$	$b_{q,[2]}$	$a_{q,[3]}$	$b_{q,[3]}$	$a_{q,[4]}$	$b_{q,[4]}$
1	$\tilde{x}$	+0.000	+6.388	+0.000	+0.164	+0.000	−6.286	+0.000	+1.024
2	$\tilde{y}$	+0.000	+20.205	+0.000	−2.788	+0.000	+20.202	+0.000	−16.577
3	$\tilde{x}^2$	−7.194	+0.606	−0.103	+0.692	+7.218	+0.690	+0.971	−15.787
4	$\tilde{x}\tilde{y}$	+3.280	−10.700	+3.611	−0.222	+3.526	+10.544	−13.820	+0.354
5	$\tilde{y}^2$	−12.203	+11.332	−0.317	+11.737	+12.129	+11.781	+0.085	−9.097
6	$\tilde{x}^3$	−1.142	−0.014	−1.161	+0.017	−1.066	+0.020	−13.195	+0.021
7	$\tilde{x}^2\tilde{y}$	−0.156	−2.531	−0.020	−2.513	+0.146	−2.608	+0.160	−5.493
8	$\tilde{x}\tilde{y}^2$	−5.717	−0.375	−5.734	−0.171	−5.884	+0.281	−2.397	+0.032
9	$\tilde{y}^3$	−0.274	−12.671	+0.009	−12.495	+0.119	−13.191	+0.088	−0.956

With the first set of calculated coefficients $a_{q,k}$ and $b_{q,k}$ we computed the corrections $\delta x_{i,j,k}$ and $\delta y_{i,j,k}$ to be applied to each *i*-star of the *k*-chip in each *j*-MEF file, but actually we corrected the positions only by half of the recommended values, to guarantee convergence. With the new improved star positions, we start-over and recalculated new residuals. The procedure is iterated until the difference in the average corrections from one iteration to the following one – for each grid point – became smaller than 0.001 pixels. Convergence was typically reached after ∼20–30 iterations.

2.4.2 The GD solution

Once new corrected star positions have been obtained for all the images, we can derive a new master frame, and consequently improve our GD solution for each chip, simply by repeating the procedure used to determine the polynomial coefficients. At the end of each iteration, star positions in the newly derived master frame are closer than before to the ones of a distortion-free frame, and provide a better reference on which to calculate the GD correction. After 15 such iterations, we were able to reduce star-position residuals from the initial average of ∼4 pixels down to 0.085 pixels (∼20 mas) (or ∼15 mas for each single coordinate). [A further iteration proved to give no significant improvements to our solution.]

In Fig. 2.4 we show – for each chip – the residual of uncorrected star positions versus the predicted positions of our final master frame, which is representative of our GD solution. For each chip, we plot the 11×25 cells used to model the GD, each with its distortion vector magnified by a factor of 25. Residual vectors go from the average position of the stars belonging to each grid cell $(\overline{x},\overline{y})$ to the corrected one. We also show the overall trend of residuals Δx, Δy along x and y directions. Note the symmetric shape of the geometric distortion around the center of the FoV. In Fig. 2.5 we show, in the same way, the remaining residuals after our GD solution is applied. This time we magnified the distortion vectors by a factor of 500. [Note that, close to chip edges, remaining residuals are larger that the average. We suggest to exclude those regions for high precision astrometry.] The coefficients of the final solution for the four chips are given in Table 2.2.

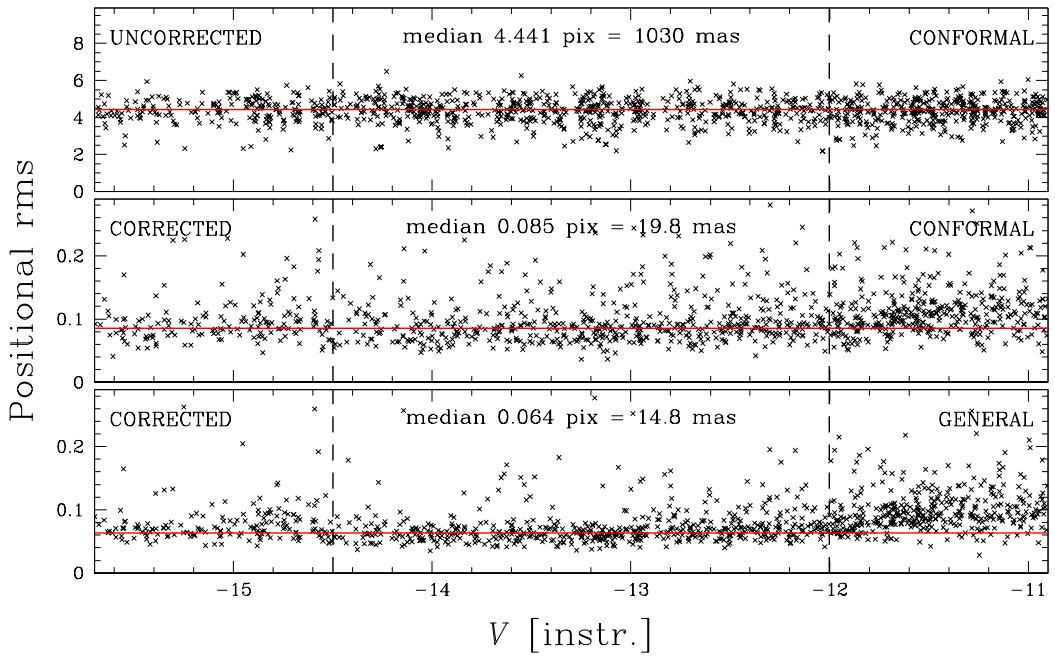

FIGURE 2.6— (*Top*): Positional rms as a function of the instrumental V magnitude without GD correction. (*Middle*): Same plot, but with GD correction. Corrected catalogs are transformed into the reference frame using a conformal transformation. (*Bottom*): Same plot, but using the most general linear transformations (6 parameters) to bring the corrected catalogs into the reference frame, instead of a conformal transformation (4 parameters). Vertical dashed lines mark the magnitude interval used to calculate median values for the positional rms

2.4.3 Accuracy of the GD Solution

The best estimate of the true errors in our GD solution is given by the size of the rms of the position residuals observed in each work-image, which have been GD-corrected, and transformed into the reference frame ($X_{i,j,k}$, $Y_{i,j,k}$). Since each star has been observed in several work-images and in different regions of the detectors, the consistency of these star positions, once transformed in the coordinate system of the distortion-free reference frame ($X_i^{\rm master}$, $Y_i^{\rm master}$), immediately quantifies how well we are able to put each image into a distortion-free system.

In the top panel of Fig. 2.6 we show the size of these rms versus the instrumental V magnitude, before GD correction is applied – *at all* – to the observed positions, before transforming them into the master-frame using a conformal transformation. The instrumental magnitude ($m_{\rm instr.}$) has been computed as the sum of the pixel's digital numbers (DNs) under the best fitted PSF (i.e. $m_{\rm instr.}=-2.5\log[\Sigma({\rm DNs})]$). For reference, in images with a seeing of $0\farcs6$, saturation begins at $m_{\rm instr.}=-14.1$, while if the seeing is $\sim1\farcs0$, the saturation level can reach $m_{\rm instr.}=-15.2$. (This simply means that in these two cases, the brightest pixels contain ∼12% or ∼4% of the flux, respectively, enabling to collect more or fewer photons before saturation is reached in the brightest pixel.)

The rms are computed from the values $\sqrt{[(X_i^{\rm master})^{T_{j,k}}-X_i^{\rm master}]^2+[(Y_i^{\rm master})^{T_{j,k}}-Y_i^{\rm master}]^2}$. Only stars in the master-list observed in at least 9 images, and within ∼2.5 magnitudes below the saturation level (between the dashed lines) were considered to test the accuracy of the GD solution, because faint stars are dominated by random errors. Note, however, that we applied our GD solution to all the sources in our catalogs. We can see that if no GD correction is applied, the positional rms exceed 4.4 pixels (i.e. a whole arcsec). In some locations on the chips

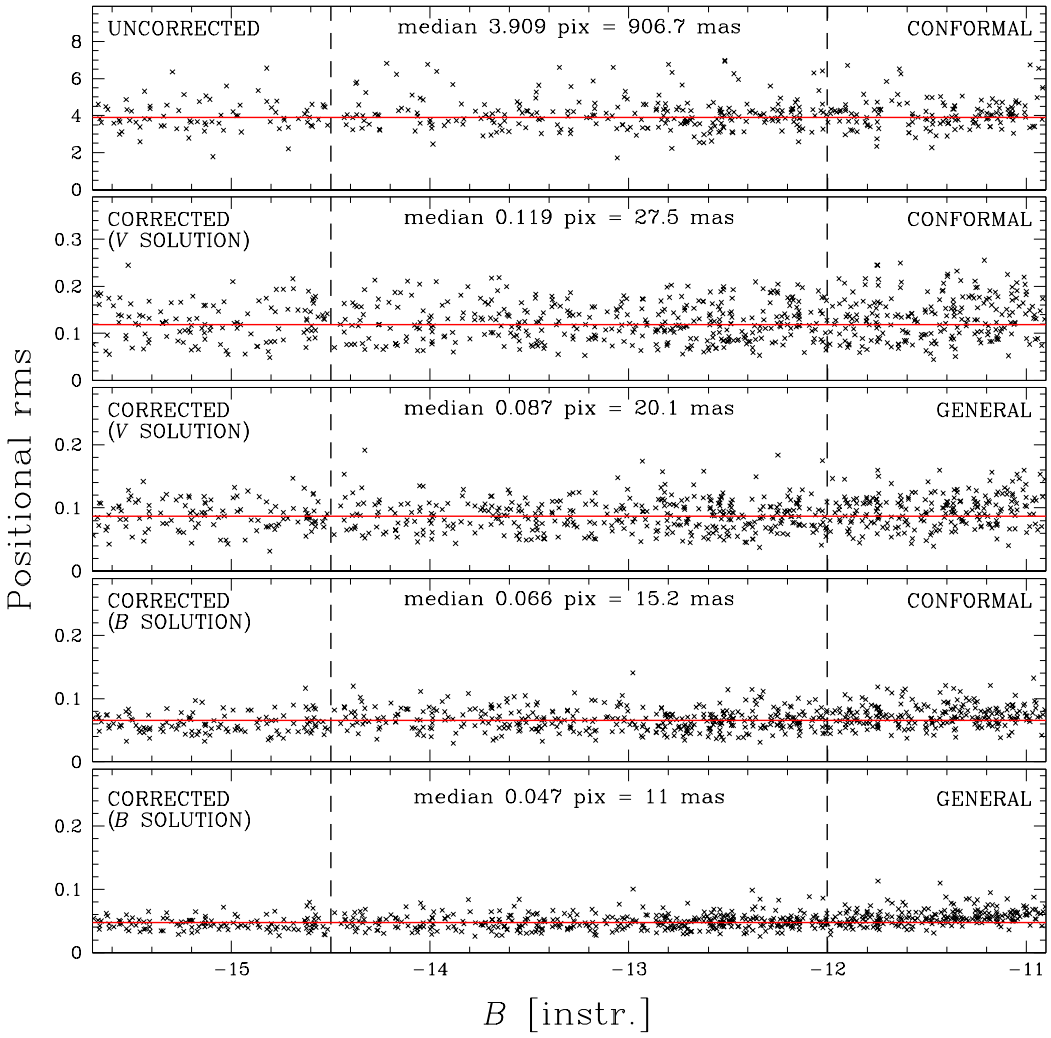

FIGURE 2.7— (*From Top to Bottom*): Positional rms as function of the instrumental *B* magnitude when no GD correction is applied at all. (*Next*): Same plot, but after the *V*-derived GD correction applied, and using conformal transformations to transform corrected catalogs into the reference frame. (*Next*): Same plot, but using the most general linear transformations (6 parameters). (*Next*): Positional rms after the GD correction obtained from *B* images is applied, and using conformal transformations. (*Bottom*): Same as above but using a general linear transformations. Vertical dashed lines mark the magnitude interval used to calculate median values for the positional rms

individual displacements can exceed 20 pixels (5 arcsec), see Fig. 2.4.

Middle panel of Fig. 2.6 shows that, once our GD correction is applied, the positional rms reach an accuracy of ~20 mas for high signal-to-noise ratio (S/N) stars. It is worth noting that saturated stars ($V_{\rm instr.}$<−14.5) are also reasonably well measured. When a 6-parameter linear transformation (the most general possible linear transformation, hereafter simply *general* transformation) is applied, most of the residuals introduced by variation of the telescope+optics system (due to thermal or gravity-induced flexure variation, and/or differential atmospheric

TABLE 2.3— Our distortion coefficients for the *B* filter.

Term(q)	Polyn.	$a_{q,[1]}$	$b_{q,[1]}$	$a_{q,[2]}$	$b_{q,[2]}$	$a_{q,[3]}$	$b_{q,[3]}$	$a_{q,[4]}$	$b_{q,[4]}$
1	$\tilde{x}$	+0.000	+6.340	+0.000	+0.004	+0.000	−5.962	+0.000	+1.263
2	$\tilde{y}$	+0.000	+20.810	+0.000	−2.506	+0.000	+20.397	+0.000	−16.597
3	$\tilde{x}^2$	−7.186	+0.585	−0.076	+0.646	+7.102	+0.601	+1.037	−15.841
4	$\tilde{x}\tilde{y}$	+3.438	−10.926	+3.607	−0.260	+3.445	+10.517	−13.733	+0.311
5	$\tilde{y}^2$	−12.162	+11.485	+0.039	+11.649	+12.440	+11.490	+0.085	−8.907
6	$\tilde{x}^3$	−1.055	−0.038	−1.204	+0.009	−1.067	+0.008	−13.094	−0.021
7	$\tilde{x}^2\tilde{y}$	−0.195	−2.424	+0.010	−2.610	+0.076	−2.536	+0.059	−5.388
8	$\tilde{x}\tilde{y}^2$	−5.632	−0.326	−5.961	+0.043	−5.765	+0.246	−2.362	−0.010
9	$\tilde{y}^3$	−0.304	−13.267	−0.089	−13.347	+0.068	−13.350	+0.035	−0.960

refraction) are absorbed, and the rms further reduces to 0.064 pixels (∼15 mas, see bottom panel of Fig. 2.6). Note that when at least a dozen of high S/N stars are present in the field, this kind of transformation should always be preferred for relative astrometry. The corners of the FoV, however, show systematic residuals larger than the rms (see also Fig. 2.4 and 2.5), indicating problems of stability of the geometric distortion solution over the 6-day period of observations.

If the stellar density in the field is high enough, and if relative astrometry is the goal of the investigation, these residual systematic errors could be further reduced with a local transformation approach (Bedin et al. 2003; Paper I, II, and in Bellini et al. 2009, hereafter Paper III, see also Chapter 6).

2.4.4 GD correction for the *B* filter

Every LBC-Blue filter constitutes a different optical element which could slightly change the optical path and introduce – at some level – changes in the GDs. To test the filter-dependency of our GD solution derived for the *V* filter, we corrected the positions measured on each *B* images with our *V*-filter-derived GD solution and studied the positional rms.

Analogously to Fig. 2.6, we show in the top panel of Fig. 2.7 the positional rms as a function of the instrumental *B* magnitude when no GD correction is applied to the observed positions, and where conformal transformations were used to bring each catalog into the reference frame. In the following second panel we show the positions corrected with the GD-solution obtained from *V* images, again using conformal transformations. In the third panel, we show the same rms once the corrected positions are transformed with a general (linear) transformation.

Since we found these rms significantly larger (>20 mas) than the ones obtained for the *V* filter, we decided to independently solve for the GD also for the *B* images. We repeated the procedure described in the previous sections, but this time using our *V* filter GD correction as a first guess. Table 2.3 contains the coefficients derived for our GD solution using only images in the *B* filter. The values of the coefficients are consistent with those obtained for the *V* filter, but different at a level of few percent.

In the fourth panel of Fig. 2.7 we show that the positional rms (now corrected with the *B*-derived GD solution and conformally transformed into the reference frame) are significantly smaller, down to ∼ 0.07 pixels. Finally, a general linear transformation further reduces these values to less than ∼0.05 pixels, i.e. ∼11 mas (∼8 mas in each coordinate, see bottom panel of Fig. 2.7).

TABLE 2.4— Inter-chip transformation parameters, with formal errors. The absolute x-scale factor of chip [2] in its reference pixel is 229.7±0.1 mas. The values for θ are expressed in degrees.

Parameter	k =[1]	k =[2]	k =[3]	k =[4]
$\alpha_k/\alpha_{[2]}$	1.01482 ±0.00006	1.00000	1.01445 ±0.00006	1.0073 ±0.0001
$\theta_k-\theta_{[2]}$	−0.175 ±0.003	0.000	0.198 ±0.04	0.005 ±0.003
$(x^{\rm corr}_{[2]})_k$	3135.0 ±0.1	1025.00	−1088.1 ±0.1	948.36 ±0.08
$(y^{\rm corr}_{[2]})_k$	2311.2 ±0.1	2305.00	2307.4 ±0.1	5684.9 ±0.2

It might seem that the GD solution derived from images collected with the B filter is even better than the one derived from the V one, but that would be a wrong interpretation. Indeed, these smaller rms are due to the fact that the chip inter-comparison is not complete, having at our disposal only small dithers for the B filter.

2.5 Relative positions of the chips

Now that we are able to correct each of the four catalogs (one per chip) of every LBC image for GD, we want to put them into a common distortion-free system. This can be done in a way conceptually very similar to the one used to solve for the GD within each chip.

We could then simply conformally transform the corrected positions of chip k into the distortion-corrected positions of chip [2], using the following relations:[5]

$$\begin{pmatrix} x^{\rm corr}_{[2]} \\ y^{\rm corr}_{[2]} \end{pmatrix} = \frac{\alpha_{[2]}}{\alpha_k}\begin{bmatrix} \cos(\theta_{[2]}-\theta_k) & \sin(\theta_{[2]}-\theta_k) \\ -\sin(\theta_{[2]}-\theta_k) & \cos(\theta_{[2]}-\theta_k) \end{bmatrix}\begin{pmatrix} x^{\rm corr}_k-(x_\circ)_k \\ y^{\rm corr}_k-(y_\circ)_k \end{pmatrix}+ + \begin{pmatrix} (x^{\rm corr}_{[2]})_k \\ (y^{\rm corr}_{[2]})_k \end{pmatrix};$$

where – following the formalism in AK03 – we indicate the scale factor as α_k, the orientation angle as θ_k, and the positions of the center of the chip $(x_\circ, y_\circ)_k$ in the corrected reference system of chip [2] as $(x^{\rm corr}_{[2]})_k$ and $(y^{\rm corr}_{[2]})_k$. Of course, for k=2, corrected and uncorrected values of $(x_\circ, y_\circ)_{[2]}$ are identical. The values of the interchip transformation parameters are given in Table 2.4.

In Figure 2.8 we show our calculated quantities for chip [1], [3], and [4], relative to chip [2], using all V-images (numbered from 1 to 44, in chronological order). Top panels show all the values for the relative scale $\alpha_k/\alpha_{[2]}$. The panels in the second row show the variations of the relative angle $\theta_k-\theta_{[2]}$, while the panels in the third and fourth row show the relative offsets $(x^{\rm corr}_{[2]})_k$ and $(y^{\rm corr}_{[2]})_k$, respectively.

[5]Chip [2] occupies a central position within the LBC-Blue layout (see Fig. 2.1), therefore we chose to adopt it as the reference chip with respect to which we compute relative scales, orientations, and shifts of the other chips.

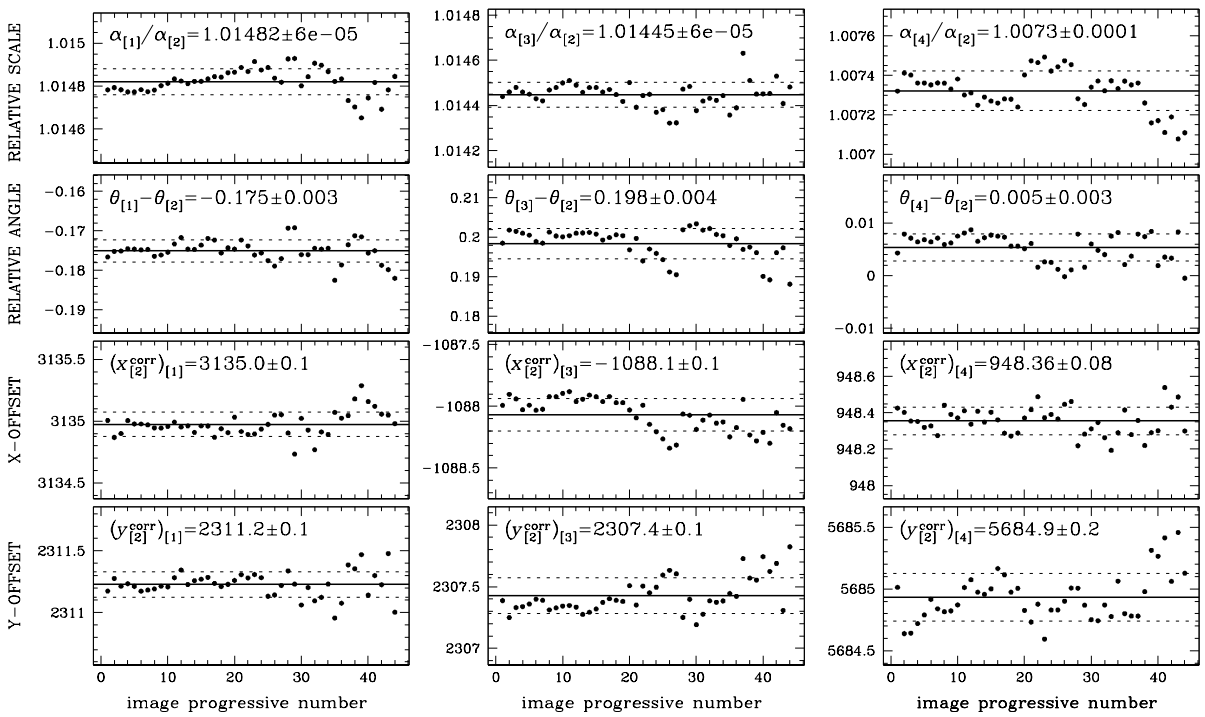

FIGURE 2.8— For all the 44 *V* images (sorted by chronological order) we show the variation of the linear quantities of chips [1], [3], and [4], relative to those of chip [2]. From top to bottom: *(i)* the relative scale $\alpha_k/\alpha_{[2]}$; *(ii)* the relative position angle $\theta_k-\theta_{[2]}$, in degrees; *(iii)* the offset $(x^{corr}_{[2]})_k$ of the central pixel of chips [1], [3], [4] with respect to the corrected pixel-coordinate system of chip [2]; and *(iv)* the same for the offset $(y^{corr}_{[2]})_k$. Images from number 20 to 44 are those affected by an anomalously high background value, and present larger scatters. Horizontal dot-dashed lines show the mean values, while short-dashed lines mark $\pm1\sigma$ (rms).

The differences in scale observed among the chips merely reflect the different distances of the respective (arbitrarily adopted) reference pixels from the principal axes of the optical system, roughly at the center of the LBC-Blue FoV (see Fig. 2.1). This is also the reason why the values of the relative scales for [1] and [3] are similar.

Finally, we inter-compared star positions in the Digital Sky Surveys with those of our reference frame, and derived an absolute *x*-scale factor for chip [2] in its reference point $(x_\circ, y_\circ)_{[2]}$. We found a value for $\alpha_{[2]}$= 229.7±0.1 mas (≡1 pixel on the LBC-Blue chip [2]); the error reflects the scale stability under the limited conditions explored (see next Section).

As a further test on our GD-correction solution (and its utility for a broader community), we reduced two dithered images with independent, commonly-used software (DAOPHOT, Stetson 1987) and applied (step by step) the procedure given in the previous Sections to the obtained raw-pixel coordinates. We verified that our solution is able to bring the two images (four chips each) into a common distortion-free system with an average error $\lesssim$ 20 mas, i. e. within the positioning single-star error of an independent code.

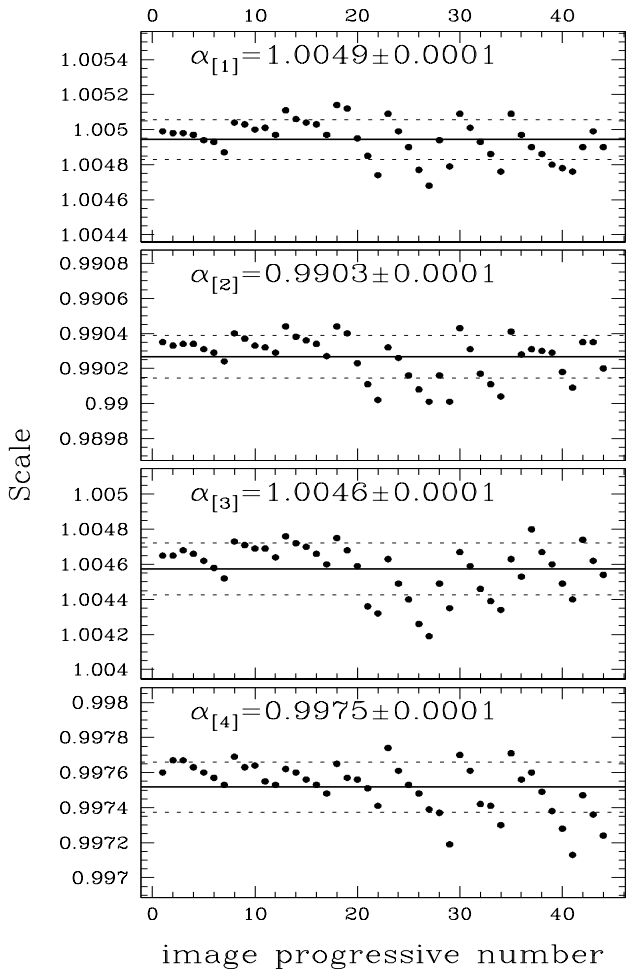

FIGURE 2.9— Scale factor α_k with formal errors, relative to the scale of the master frame (0.″2319) [note, not $\alpha_{[2]}$], for all the 44 *V* images (in chronological order). Solid lines mark the average values, while, dashed lines mark $\pm1\sigma$ (rms).

2.6 Stability of the solution

In this section we explore the stability of our derived GD solution on the limited time baseline and condition samplings offered by our observations.

Table 2.1 shows us that for *V* images we can explore only a time baseline of the order of an hour, and at two different epochs separated by roughly a week. Moreover, we have already described in Sect. 2.4.4 how *B* images provide a somewhat different GD correction with respect to the *V*-derived GD solution. It has to be noted, however, that the *V*-derived GD solution is obtained from data collected ~2 weeks before the *B*-filter one, therefore we can not assess if the observed dependencies of the GD solution on the filter are really due to an effective influence of a different element in the optical path, or to a filter-independent temporal variation of the GD.

In Figure 2.9 we show the variation of the individual (corrected) work-image scale α_k, with respect to the master frame (note that here the reference scale is the one of the master frame, by definition identically equal to 1, and not the one of chip[2]), as a function of the progressive image number. Scale-values show fluctuations with

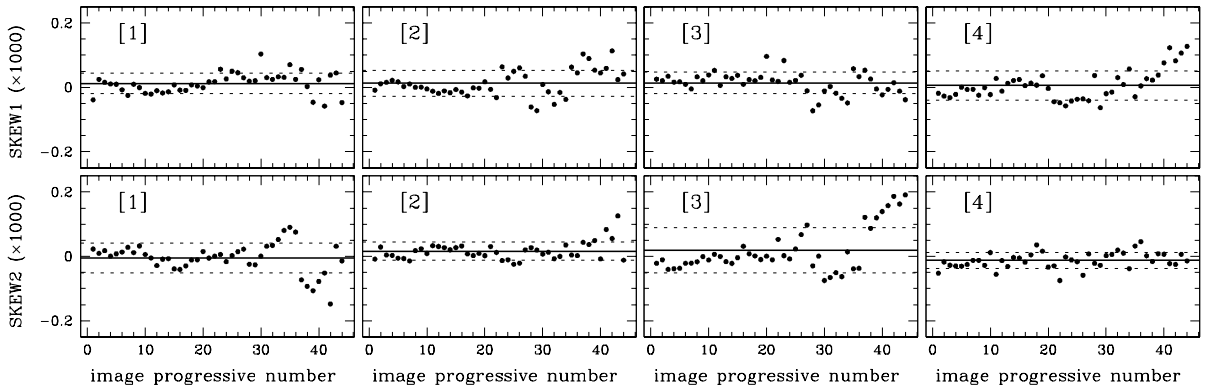

FIGURE 2.10— As in Fig. 2.9, but this time for the observed variations in SKEW1 and SKEW2, magnified by a factor of 1000 (see text).

amplitudes up to 5 parts in 10 000, even within the same night (although the run lasted only about an hour). We also note a clear path of about five consecutive exposures within each observing block (OB). Indeed, every OB was meant not to last for more than ∼20 minutes, after which the focus of the telescope needs to be readjusted (and therefore the scale changes). [This is totally expected for a prime-focus camera with such a short focal ratio and large FoV; as different pointings cause different gravity-induced flexures of the large LBT+LBC structure.] Solid lines mark the average values, while, dashed lines mark $\pm 1\sigma$ (rms). This seems to suggest that positional astrometry – *which completely relies on our GD solution* – could have systematics as large as 250 mas (∼1 pixel) within a given chip, or up to 0.″5 (∼2 pixels) in the meta-chip system, although it could be even worse because of the limited observing conditions explored. At any rate, one should never rely on the absolute values of the linear terms provided by our GD corrections for precise *absolute* astrometry (more in the conclusions).

Then, we explore the variations of the skew terms: SKEW1, and SKEW2: SKEW1 indicate whether or not there is a lack of perpendicularity between axes, while SKEW2 gives information about the scale differences along the two directions. These quantities are defined for each k-chip as:

$$\begin{aligned} \mathrm{SKEW1}_k &= (A_k - D_k)/(2\alpha_k) \\ \mathrm{SKEW2}_k &= (B_k + C_k)/(2\alpha_k), \end{aligned}$$

where $A_k, B_k, C_k, D_k, X_{\circ,k}, Y_{\circ,k}$ are the values of a general 6-parameter linear transformation of the form:

$$\begin{cases} X^{\mathrm{master}} = A_k x_k^{\mathrm{corr}} + B_k y_k^{\mathrm{corr}} + X_{\circ,k} \\ Y^{\mathrm{master}} = C_k x_k^{\mathrm{corr}} + D_k y_k^{\mathrm{corr}} + Y_{\circ,k}. \end{cases}$$

In Figure 2.10 we show, for each different chip, the variation of SKEW1 and SKEW2 parameters (magnified by a factor of 1000).

As expected (because compared with their average, i.e. the master frame), the average values of the two skew terms are consistent with zero, although they show some significant well defined trend with time. [For example, images with progressive number from 20 to 44 (those affected by the anomalously high background, Feb. 27$^{\mathrm{th}}$), show a trend and a larger scatter with respect to the previous ones (Feb. 22$^{\mathrm{nd}}$)]. Solid lines mark the average values, while, dashed lines mark $\pm 1\sigma$ (rms).

It is interesting to check – at this point – if the observing parameters correlate, or not, with temporal variations of the measured inter-chip transformation parameters. Figure 2.11, shows the variation of $\alpha_k/\alpha_{[2]}$ (left panels) and $\theta_k - \theta_{[2]}$ (right panels) with respect to airmass and image quality. Full circles mark images obtained on Feb. 22$^{\mathrm{nd}}$,

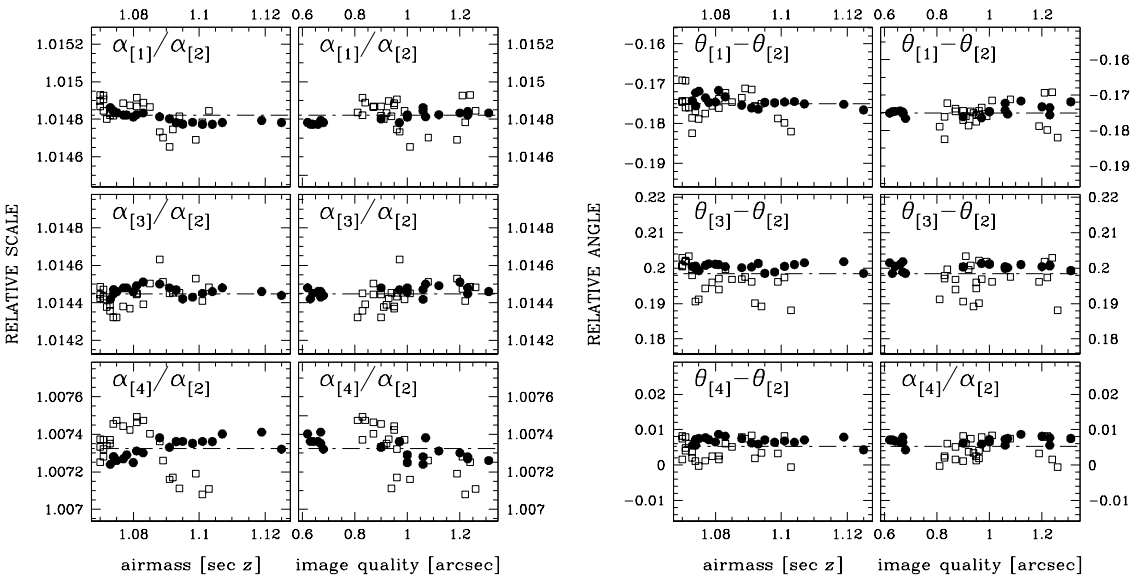

FIGURE 2.11— *(Left:)* Variation of the relative scale $\alpha_k/\alpha_{[2]}$ with respect to airmass and image quality. Full circles are images obtained on Feb. 22nd, while open squares are those of Feb. 27th. *(Right:)* The same, but for the relative angle $\theta_k - \theta_{[2]}$, in degrees. Horizontal lines mark the mean values.

while open squares are those of Feb. 27th (affected by high background values). The relative scale $\theta_k - \theta_{[2]}$, and the relative angle $\alpha_k/\alpha_{[2]}$ both present larger scatter in observations collected on Feb. 27th, than those of Feb. 22nd. Again, solid lines mark the average values, while, dashed lines mark $\pm 1\sigma$ (rms).

2.7 Conclusions

By using a large number of well dithered exposures we have found a set of third-order-correction coefficients for the geometric distortion solution of each chip of the LBC-Blue, at the prime focus of the LBT.

The use of these corrections removes the distortion over the entire area of each chip to an accuracy of ∼0.09 pixel (i.e. ∼20 mas), the largest systematics being located in the 200-400 pixels closest to the boundaries of the detectors. Therefore, we advise the use of the inner parts of the detectors for high-precision astrometry. The limitation that has prevented us from removing the distortion at even higher level of accuracies – in addition to atmospheric effects and to the relatively sparsity of the studied field – is the dependency of the distortion on the scale changes that result from thermal and/or gravitational induced variations of the telescope+optical structure.

If a dozen (or more) well distributed high S/N stars are available within the same chip, a general 6-parameter linear transformation could register relative positions in different images down to about 15 mas. If the field is even more densely populated, then a local transformation approach [as the one adopted in Bedin et al. (2003), from space, or in Paper I, II, III) from ground] can further reduce these precisions to the mas level. [Indeed, using these techniques and this very same data-set we were able to reach a final precision of ∼1 mas yr^{-1} (Bellini et al. 2010b, see also Chapter 5)].

These are the precisions and accuracies with which we can hope to bring one image into another image by adopting: *conformal*, *general*, or *local* transformations. In the case of absolute astrometry, however, the accuracies are much lower. During the available limited number of nights of observations (and atmospheric conditions), we observed scale-variations up to 5 parts in 10 000, even during the same night. This implies that astrometric accuracy – which completely relies on our GD solution – can not be better than ∼250 mas (∼1 pixel) within a

given chip (from center to corners), and can be as large as 0.″5 (∼2 pixels) in the meta-chip system. This value is in-line with the meta-chip stability observed in other ground-based WFI (Paper I), and absolutely excellent for a ground-based prime-focus instrument with such a small focal ratio and large FoV.

Thankfully, several stars from astrometric catalogs such as the UCAC-2, GSC-2, 2MASS, will be always available within any given LBC-Blue large FoV. These stars, in addition to provide a link to absolute astrometry (as done for example in Rovilos et al. 2009), will enable constrains of linear terms in our GD solution, and to potentially reach an absolute astrometric precision of 20 mas. The fact that we are able to reach good astrometric precision also for saturated stars will make the comparison between these catalogs and the sources measured in the – generally deeper – LBC images, even easier.

For the future, more data and a longer time-baseline are needed to better characterize the GD stability of LBC@LBT detectors on the medium and long time term. This could make it possible to: (1) determine a multi-layer model of the distortion which would properly disentangle the contributions given by optical field-angle distortion, light-path deviations caused by filters and windows, non-flat CCDs, CCDs artifacts, alignment errors of the CCD on the focal plane, etc.; and (2) allow for time-dependent and/or mis-alignments of mirrors, filters/windows, and CCDs.

Bibliography

Anderson, J., & King, I. R. 2003, PASP, 115, 113 (AK03)
Anderson, J., Bedin, L. R., Piotto, G., Yadav, R. S., & Bellini, A. 2006, A&A, 454, 1029 (Paper I)
Anderson, J., et al. 2008, AJ, 135, 2114
Bedin, L. R., Piotto, G., King, I. R., & Anderson, J. 2003, AJ, 126, 247
Bellini, A., et al. 2009, A&A, 493, 959 (Paper III)
Bellini, A., & Bedin, L. R. 2009, PASP, 121, 1419 (BB09)
Bellini A., & Bedin L. R. 2010, A&A in press, arXiv:1005.0848
Bellini, A., et al. 2010, A&A, 513, A50 (2010a)
Bellini, A., Bedin, L. R., Pichardo, B., Moreno, E., Allen, C., Piotto, G., & Anderson, J. 2010, A&A, 513, A51 (2010b)
Giallongo, E., et al. 2008, A&A, 482, 349
Ragazzoni, R., et al. 2000, Proc. SPIE, 4008, 439
Ragazzoni, R., et al. 2006, Proc. SPIE, 6267, 33
Rovilos, E., et al. 2009, A&A, 507, 195
Wynne, C. G. 1996, MNRAS, 280, 555
Yadav, R. K. S., et al. 2008, A&A, 484, 609 (Paper II)

2.8 Appendix

Log of M 67 observations obtained during the Commissioning Time of LBC-blue camera and used in this work.

Filename	R.A. (^{h} ^{m} ^{s})	Decl. ($^\circ$ $'$ $''$)	Exp. time (s)	Filter	Airmass (sec z)	Seeing ($''$)
		FEBRUARY 22nd 2007				
lbcb.20070222.044829.fits	08:51:18.2	+11:48:00.37	15	$V_{\rm Bessel}$	1.125	0.68
lbcb.20070222.045224.fits	08:50:53.7	+11:43:59.23	330	$V_{\rm Bessel}$	1.119	0.67
lbcb.20070222.050155.fits	08:50:53.8	+11:44:00.59	110	$V_{\rm Bessel}$	1.107	0.62
lbcb.20070222.050431.fits	08:50:55.6	+11:45:39.96	110	$V_{\rm Bessel}$	1.104	0.66
lbcb.20070222.050707.fits	08:50:57.8	+11:47:20.59	110	$V_{\rm Bessel}$	1.101	0.64
lbcb.20070222.050943.fits	08:50:59.8	+11:49:00.29	110	$V_{\rm Bessel}$	1.098	0.67
lbcb.20070222.051228.fits	08:51:01.9	+11:50:39.96	110	$V_{\rm Bessel}$	1.095	0.63
lbcb.20070222.051516.fits	08:51:03.9	+11:44:20.29	110	$V_{\rm Bessel}$	1.093	0.97
lbcb.20070222.051753.fits	08:51:05.9	+11:46:00.56	110	$V_{\rm Bessel}$	1.091	0.90
lbcb.20070222.052035.fits	08:51:08.0	+11:47:40.01	110	$V_{\rm Bessel}$	1.088	1.07
lbcb.20070222.052735.fits	08:51:10.0	+11:49:19.27	110	$V_{\rm Bessel}$	1.083	1.20
lbcb.20070222.053021.fits	08:51:12.0	+11:50:59.99	110	$V_{\rm Bessel}$	1.081	1.12
lbcb.20070222.053314.fits	08:51:14.1	+11:44:39.99	110	$V_{\rm Bessel}$	1.080	1.00
lbcb.20070222.053557.fits	08:51:16.2	+11:46:20.42	110	$V_{\rm Bessel}$	1.078	1.00
lbcb.20070222.053839.fits	08:51:18.3	+11:48:00.19	110	$V_{\rm Bessel}$	1.077	1.23
lbcb.20070222.054120.fits	08:51:20.4	+11:49:40.00	110	$V_{\rm Bessel}$	1.075	1.31
lbcb.20070222.054401.fits	08:51:22.2	+11:51:20.15	110	$V_{\rm Bessel}$	1.074	1.06
lbcb.20070222.054648.fits	08:51:24.4	+11:44:59.62	110	$V_{\rm Bessel}$	1.074	1.23
lbcb.20070222.054928.fits	08:51:26.3	+11:46:40.11	110	$V_{\rm Bessel}$	1.073	1.06
		FEBRUARY 27th 2007				
lbcb.20070227.050501.fits	08:51:35.2	+11:48:49.98	100	$V_{\rm Bessel}$	1.085	0.87
lbcb.20070227.050745.fits	08:51:38.7	+11:52:59.97	100	$V_{\rm Bessel}$	1.083	0.84
lbcb.20070227.051028.fits	08:51:42.0	+11:57:09.94	100	$V_{\rm Bessel}$	1.081	0.87
lbcb.20070227.051322.fits	08:51:45.4	+11:41:20.13	100	$V_{\rm Bessel}$	1.081	0.83
lbcb.20070227.051603.fits	08:51:48.8	+11:45:30.10	100	$V_{\rm Bessel}$	1.079	0.95
lbcb.20070227.051842.fits	08:51:52.4	+11:49:39.30	100	$V_{\rm Bessel}$	1.077	0.95
lbcb.20070227.052114.fits	08:51:55.7	+11:53:49.87	100	$V_{\rm Bessel}$	1.075	0.81
lbcb.20070227.052344.fits	08:51:59.1	+11:57:59.67	100	$V_{\rm Bessel}$	1.074	0.90
lbcb.20070227.053705.fits	08:51:04.6	+11:51:19.99	100	$V_{\rm Bessel}$	1.071	1.21
lbcb.20070227.053938.fits	08:51:07.9	+11:55:30.00	100	$V_{\rm Bessel}$	1.070	1.24
lbcb.20070227.054236.fits	08:51:11.4	+11:39:40.05	100	$V_{\rm Bessel}$	1.072	0.91
lbcb.20070227.054515.fits	08:51:14.8	+11:43:49.98	100	$V_{\rm Bessel}$	1.071	0.99
lbcb.20070227.054753.fits	08:51:18.2	+11:47:59.97	100	$V_{\rm Bessel}$	1.071	0.96
lbcb.20070227.055030.fits	08:51:21.5	+11:52:10.06	100	$V_{\rm Bessel}$	1.070	0.93
lbcb.20070227.055301.fits	08:51:25.0	+11:56:20.05	100	$V_{\rm Bessel}$	1.070	0.90
lbcb.20070227.055554.fits	08:51:28.3	+11:40:30.20	100	$V_{\rm Bessel}$	1.073	0.83
lbcb.20070227.055831.fits	08:51:31.9	+11:44:39.90	100	$V_{\rm Bessel}$	1.073	0.92

Continues on next page

Continues from prev. page

Filename	R.A. (^{h} ^{m} ^{s})	Decl. ($^\circ$ $'$ $''$)	Exp. time (s)	Filter	Airmass (sec z)	Seeing ($''$)
lbcb.20070227.062533.fits	08:50:37.3	+11:37:59.54	100	$V_{\rm Bessel}$	1.088	0.97
lbcb.20070227.062805.fits	08:50:40.8	+11:42:10.67	100	$V_{\rm Bessel}$	1.089	1.08
lbcb.20070227.063042.fits	08:50:44.1	+11:46:19.85	100	$V_{\rm Bessel}$	1.091	1.01
lbcb.20070227.063312.fits	08:50:47.6	+11:50:29.85	100	$V_{\rm Bessel}$	1.092	0.96
lbcb.20070227.063550.fits	08:50:50.9	+11:54:39.59	100	$V_{\rm Bessel}$	1.094	0.94
lbcb.20070227.063843.fits	08:50:54.4	+11:38:50.85	100	$V_{\rm Bessel}$	1.099	1.19
lbcb.20070227.064120.fits	08:50:57.8	+11:42:58.99	100	$V_{\rm Bessel}$	1.101	1.22
lbcb.20070227.064357.fits	08:51:01.1	+11:47:09.96	100	$V_{\rm Bessel}$	1.103	1.26
		MARCH 16th 2007				
lbcb.20070316.031311.fits	08:50:53.5	+11:43:59.94	180	$B_{\rm Bessel}$	1.139	0.93
lbcb.20070316.031702.fits	08:50:55.5	+11:45:39.95	180	$B_{\rm Bessel}$	1.132	0.93
lbcb.20070316.032052.fits	08:50:57.6	+11:47:19.91	180	$B_{\rm Bessel}$	1.126	0.92
lbcb.20070316.032440.fits	08:50:59.6	+11:48:59.98	180	$B_{\rm Bessel}$	1.121	0.98
lbcb.20070316.032829.fits	08:51:01.7	+11:50:39.96	180	$B_{\rm Bessel}$	1.115	0.83
lbcb.20070316.033228.fits	08:51:03.7	+11:44:19.99	180	$B_{\rm Bessel}$	1.111	0.86
lbcb.20070316.033624.fits	08:51:05.7	+11:45:59.98	180	$B_{\rm Bessel}$	1.106	0.88
lbcb.20070316.034021.fits	08:51:07.8	+11:47:40.01	180	$B_{\rm Bessel}$	1.101	0.88
lbcb.20070316.034842.fits	08:51:09.8	+11:49:19.99	180	$B_{\rm Bessel}$	1.093	0.96
lbcb.20070316.035236.fits	08:51:11.9	+11:51:00.01	180	$B_{\rm Bessel}$	1.089	1.04
lbcb.20070316.035641.fits	08:51:13.9	+11:44:39.99	180	$B_{\rm Bessel}$	1.087	0.94
lbcb.20070316.040031.fits	08:51:16.0	+11:46:19.97	180	$B_{\rm Bessel}$	1.084	0.92
lbcb.20070316.040417.fits	08:51:18.0	+11:48:00.01	180	$B_{\rm Bessel}$	1.081	1.08
lbcb.20070316.040809.fits	08:51:20.0	+11:49:40.00	180	$B_{\rm Bessel}$	1.079	1.06
lbcb.20070316.041157.fits	08:51:22.1	+11:51:19.99	180	$B_{\rm Bessel}$	1.076	1.06
lbcb.20070316.041603.fits	08:51:24.1	+11:45:00.02	180	$B_{\rm Bessel}$	1.075	0.98
lbcb.20070316.041955.fits	08:51:26.2	+11:46:40.02	180	$B_{\rm Bessel}$	1.074	0.95
lbcb.20070316.042838.fits	08:51:28.2	+11:48:19.99	180	$B_{\rm Bessel}$	1.071	0.79
lbcb.20070316.043229.fits	08:51:30.3	+11:49:59.99	180	$B_{\rm Bessel}$	1.071	0.87
lbcb.20070316.043610.fits	08:51:32.3	+11:51:39.94	180	$B_{\rm Bessel}$	1.070	0.92
lbcb.20070316.044017.fits	08:51:34.3	+11:45:19.98	180	$B_{\rm Bessel}$	1.071	0.92
lbcb.20070316.044406.fits	08:51:36.4	+11:46:59.96	180	$B_{\rm Bessel}$	1.071	0.91
lbcb.20070316.044755.fits	08:51:38.4	+11:48:39.93	180	$B_{\rm Bessel}$	1.071	0.80
lbcb.20070316.045140.fits	08:51:40.5	+11:50:19.93	180	$B_{\rm Bessel}$	1.072	0.84
lbcb.20070316.045528.fits	08:51:42.5	+11:51:59.93	180	$B_{\rm Bessel}$	1.073	0.87

3

Geometric distortion correction of the WFC3/UVIS on board the *HST*

Our GD-correction technique can be used to obtain an accurate GD solution in many different telescope/camera combinations. In this Chapter we will describe how we derived a GD solution for the new *Wide-Field Planetary camera 3, UV/Optical* (WFC3/UVIS) on board the *H*ubble Space Telescope (*HST*), that enables a relative astrometric accuracy of ∼1 mas (in each axis for well exposed stars) in three broad-band ultraviolet filters (F225W, F275W, and F336W). More data and a better understanding of the instrument are required to constrain the solution to a higher level of accuracy.

This Chapter contains results published in *Publications of the Astronomical Society of the Pacific* (Bellini & Bedin 2009).

3.1 Introduction, Data set, Measurements

The accuracy and the stability of the geometric distortion (GD) correction of an instrument is at the basis of its use for high precision astrometry. The particularly advantageous conditions of the *Hubble Space Telescope (HST)* observatory make it ideal for imaging-astrometry of (faint) point sources. The point-spread functions (PSFs) are not only sharp and (essentially) close to the diffraction limit – which directly results in high precision positioning – but also the observations are not plagued by atmospheric effects (such as differential refraction, image motion, differential chromatic refraction, etc), which severely limit ground-based astrometry. In addition to this, *HST* observations do not suffer from gravity-induced flexures on the structures of the telescope (and camera), which add (relatively) large instabilities in the GD of ground-based images, and make its corrections more uncertain.

On May 14th 2009, the brand-new *Wide Field Camera 3* (WFC3) was successfully installed during the *Hubble Servicing Mission 4* (SM4, May 12–24 2009). After a period of intense testing, fine-tuning, and basic calibration, on September 9th 2009 the first calibration- and science-demonstration images were finally made public.

Our group is active in bringing *HST* to the *state of the art* of its astrometric capabilities, that we used for a number of scientific applications (e.g. from King et al. 1998, to Milone et al. 2010, first and last accepted papers). Now that the *"old"* ACS/WFC is successfully repaired, and that the new instruments are installed, our first step is to extend our astrometric tools to the new instruments (and to monitor the old ones). This chapter is focused on the geometric distortion correction of the *UV/Optical (UVIS)* channel of the WFC3. Since the results of these efforts might have some immediate public utility (e.g. relative astrometry in general, stacking of images, UV-identification

of X-counterparts such as pulsars and cataclysmic variables in globular clusters, etc.), we made our results available to the WFC3/UVIS user-community.

We immediately focused our attention on a deep UV-survey of the core of the Galactic globular cluster ω Centauri (NGC 5139), where some well dithered images were collected. The dense – and relatively flat – stellar field makes the calibration particularly suitable for deriving and monitoring the GD on a relatively small spatial scale. In addition, while most of the efforts to derive a GD correction will be concentrated on relatively redder filters, we undertook a study to determine the GD solutions of the three bluest broad-band filters (with the exception of F218W): F225W, F275, and F336W.

The WFC3/UVIS layout is almost indistinguishable from that of ACS/WFC[1]: two E2V thinned, backside illuminated and UV optimized 2k×4k CCDs contiguous on the long side of the chip, and covering a Field of View (FoV) of $\sim$ 160×160 arcsec^2. The ω Cen data set used here consists of 9×350 s exposures in each of the filters F225W, F275W, and F336W. The nine images follow a squared 3×3 dither-pattern with a step of about 40 arcsec (i.e. ∼1000 pixels), and were all collected on July 15, 2009 (PID 11452).

We downloaded the standard pipe-line reduced FLT files from the archive. The FLT images are de-biased and flat-field corrected, but *no* pixel-resampling is performed on them. The FLT files are multi-extension fits (MEF) on which the first slot contains the image of what – hereafter – we will call chip 1 (or simply [1]). The second chip, instead, is stored in the fourth slot of the MEF, and we will refer to it as chip 2 (or [2]). [Note that others might choose a different notation]. Our GD corrections refer to the raw pixel coordinates of these images.

The fluxes and positions were obtained from a code mostly based on the software img2xym_WFI by Anderson et al. (2006). This is essentially a spatially variable PSF-fitting method. We were pleased to see that for the WFC3/UVIS images of this data set the PSFs were only marginally undersampled. Left panel of Figure 3.1 shows a preliminary color-magnitude diagram in the three filters for the bright stars in the WFC3/UVIS data set.

3.2 The Geometric Distortion Solutions

The most straightforward way to solve for the GD would be to observe a field where there is a-priori knowledge of the positions of all the stars in a distortion-free reference frame. [A distortion-free reference frame is a system that can be transformed into any other distortion-free frame by means of *conformal transformations*[2].] Geometric distortion would then show itself immediately as the residuals between the observed relative positions of stars and the ones predicted by the distortion-free frame (on the basis of a conformal transformation).

Thankfully, we possess such an "astrometric flat-field", moreover with the right magnitude interval, source density, and accuracy. This reference frame is the mosaic of 3×3 *Wide Field Channel (WFC)* of the *Advanced Camera for Surveys (ACS)* fields collected – at the end of June 2002 – under the program GO-9442 (PI: Cool) reduced by Jay Anderson and published in Villanova et al. (2007). This reference frame was obtained from a total of 18 short and 90 long ACS/WFC exposures in the filters: F435W, F625W, and F658N (see Villanova et al. 2007 for details). The entire field covers an area of 10×10 arcmin^2, and can be considered distortion-free at the ∼0.5 mas level. The catalog contains more than 2 million sources, and we will refer to it as *master frame*, and to the coordinates of each *i*-source in it with the notation ($X_i^{\rm master}$,$Y_i^{\rm master}$). A color-magnitude diagram for the stars in the master frame is shown on the right panel of Figure 3.1.

To derive the WFC3/UVIS GD corrections we closely follow the procedures described in Anderson & King (2003, hereafter AK03, see also Chapter 2) used to correct the GD for each of the four detectors of WFPC2. We represent our solution with a third-order polynomial, which is able to provide our final GD correction to the ∼0.025 pixel level in each coordinate (∼1 mas). Higher orders proved to be unnecessary.

Having a separate solution for each chip, rather than one that uses a common center of the distortion in the FoV, allows a better handle of potential individual detector effects (such as a different relative tilt of the chip surfaces,

[1] http://www.stsci.edu/hst/wfc3

[2] A conformal transformation between two catalogs of positions is a four-parameter linear transformation, specifically: rigid shifts in the two coordinates, one rotation, and one change of scale, i.e. the shape is preserved.

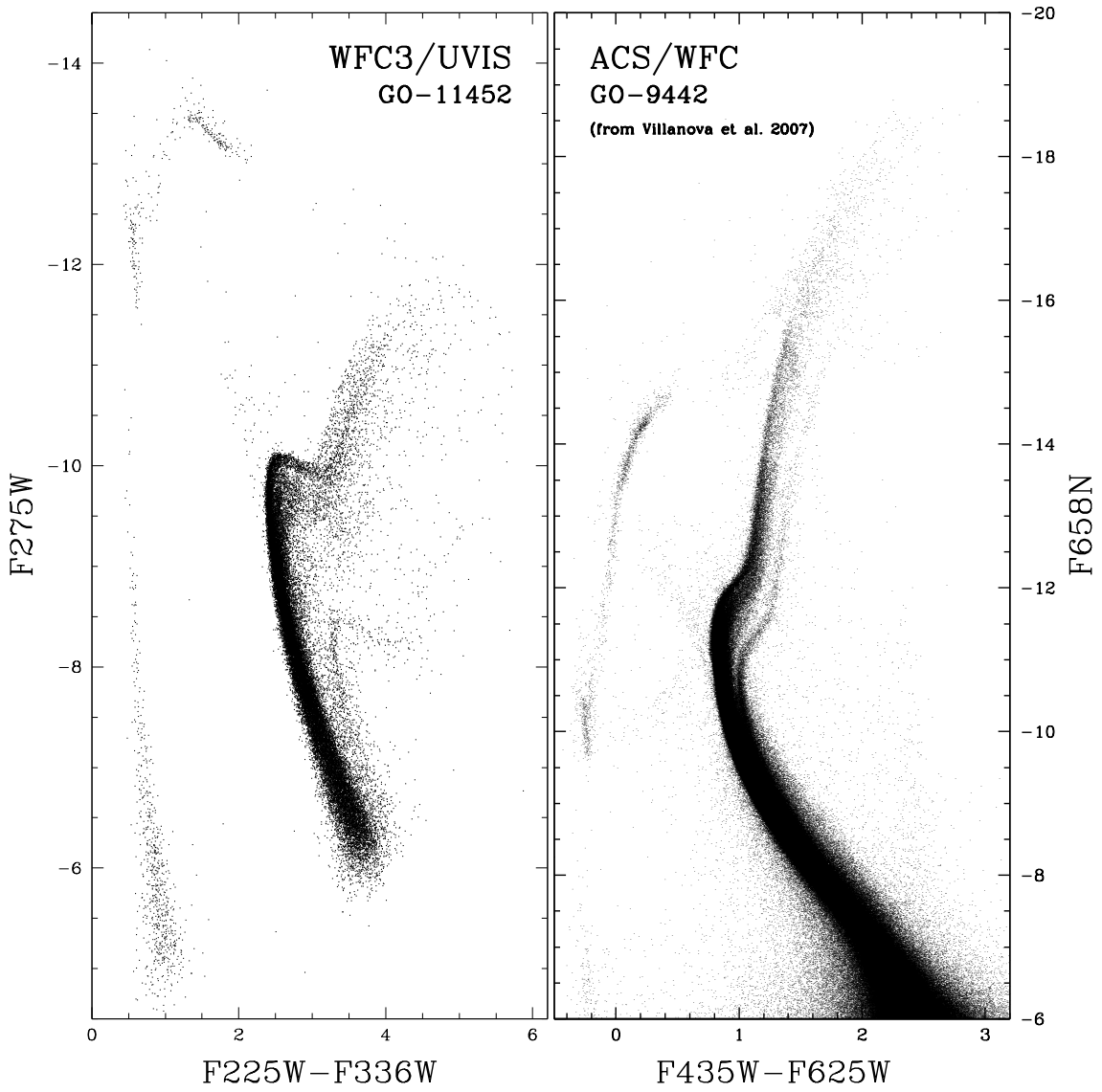

FIGURE 3.1— *Left:* Preliminary color-magnitude diagram of the bright stars in the new WFC3/UVIS data set (fluxes are neither pixel-area- nor L-flat-corrected). *Right:* Color-magnitude diagram of the stars in our ACS/WFC master frame (from Villanova et al. 2007). Both plots are in instrumental magnitudes.

relative motions, etc.). We adopted as the center of our solution, for each chip, the point $(x_\circ, y_\circ)_{k=1,2} = (2048, 1025)$ [in the raw pixel coordinates, to which we will refer hereafter as (x, y)].

For each *i*-star of the master list, in each *k*-chip of each *j*-MEF-file, the distortion *corrected* position $(x^{\rm corr}, y^{\rm corr})$

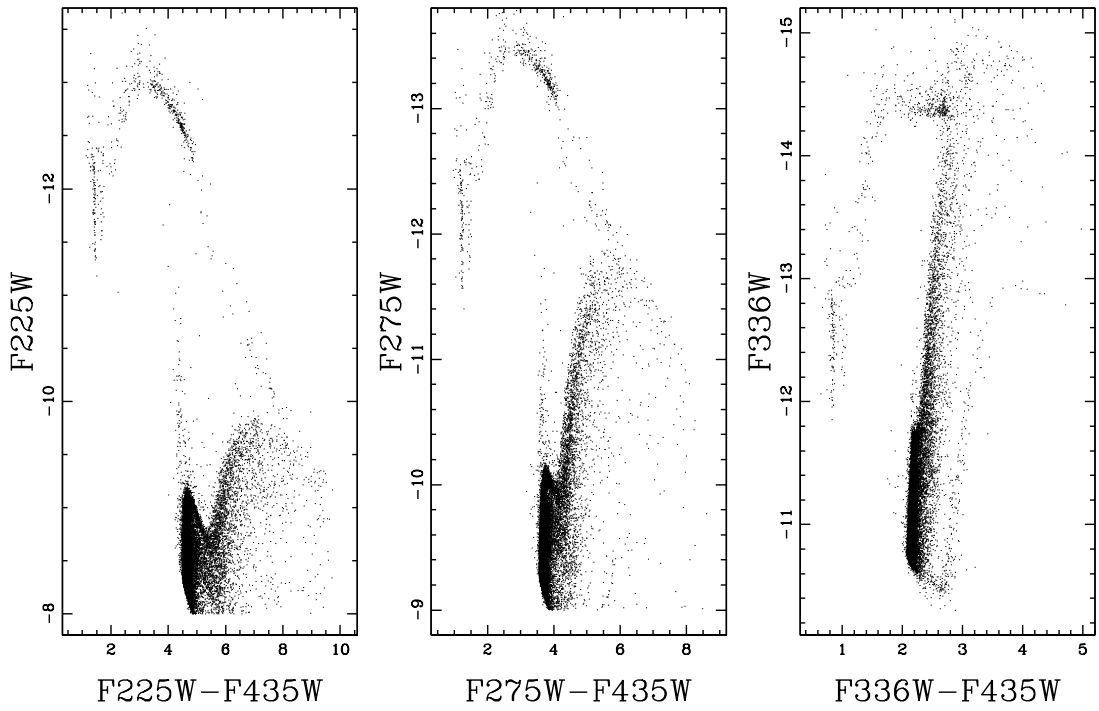

FIGURE 3.2— *Left:* Color-magnitude diagrams of the high S/N stars in common with the ACS/WFC master frame (F435W), actually used to derive the geometric distortion correction, for each of the WFC3/UVIS filters (F225W, F275W, and F336W).

is the observed position (x, y) plus the distortion correction $(\delta x, \delta y)$:

$$\begin{cases} x^{\rm corr}_{i,j,k} = x_{i,j,k} + \delta x_{i,j,k}(\tilde{x}_{i,j,k}, \tilde{y}_{i,j,k}) \\ y^{\rm corr}_{i,j,k} = y_{i,j,k} + \delta y_{i,j,k}(\tilde{x}_{i,j,k}, \tilde{y}_{i,j,k}), \end{cases}$$

where $\tilde{x}_{i,j,k}$ and $\tilde{y}_{i,j,k}$ are the normalized positions, defined as:

$$\begin{cases} \tilde{x}_{i,j,k} = \dfrac{x_{i,j,k} - (x_\circ)_k}{(x_\circ)_k} \\ \tilde{y}_{i,j,k} = \dfrac{y_{i,j,k} - (y_\circ)_k}{(y_\circ)_k}. \end{cases}$$

Normalized positions make it easier to recognize the magnitude of the contribution given by each solution term, and their numerical round-off.

The final GD correction for each star, in each chip/image, is given by these two third-order polynomials (we omitted here i, j, k indexes for simplicity):

$$\begin{cases} \delta x &= a_1\tilde{x} + a_2\tilde{y} + a_3\tilde{x}^2 + a_4\tilde{x}\tilde{y} + a_5\tilde{y}^2 + a_6\tilde{x}^3 + a_7\tilde{x}^2\tilde{y} + a_8\tilde{x}\tilde{y}^2 + a_9\tilde{y}^3 \\ \delta y &= b_1\tilde{x} + b_2\tilde{y} + b_3\tilde{x}^2 + b_4\tilde{x}\tilde{y} + b_5\tilde{y}^2 + b_6\tilde{x}^3 + b_7\tilde{x}^2\tilde{y} + b_8\tilde{x}\tilde{y}^2 + b_9\tilde{y}^3. \end{cases}$$

Our GD solution is thus fully characterized by 18 coefficients: $a_1, \ldots, a_9$, $b_1, \ldots, b_9$. However, as done in AK03, we constrained the solution so that, at the center of the chip, it will have its x-scale equal to the one at

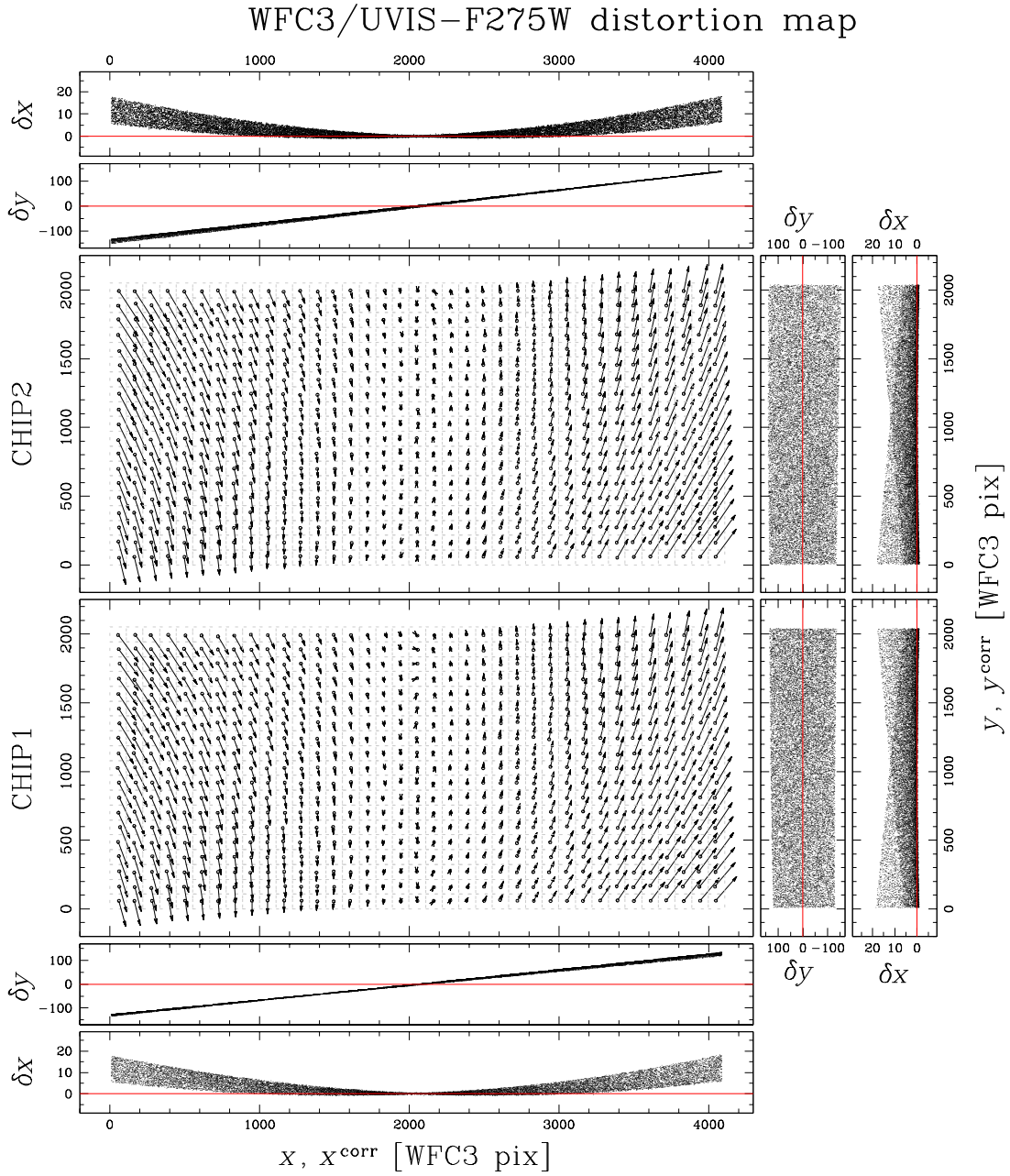

FIGURE 3.3— Predicted vs. uncorrected positions. The size of the residual vectors is magnified by a factor of ×8 in x and ×1.5 in y. For each chip we plot also individual residuals as function of x and y axes. Units are expressed WFC3/UVIS pixels in the reference positions $(x_\circ, y_\circ)$. For clarity only a random 40% of the residuals is plotted.

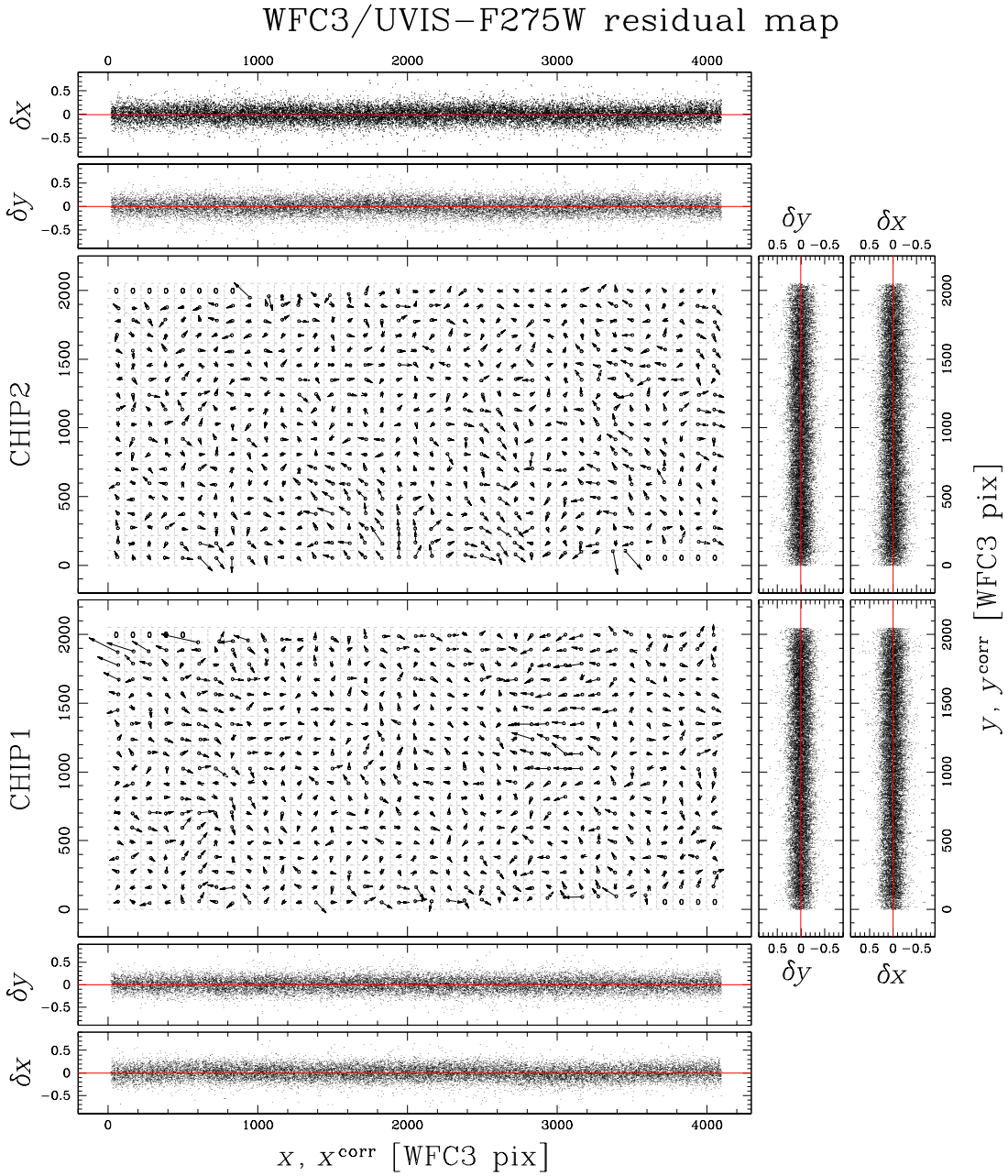

FIGURE 3.4— Same as Fig. 3.3 after the correction was applied. The size of the residuals is now magnified by a factor of 1500.

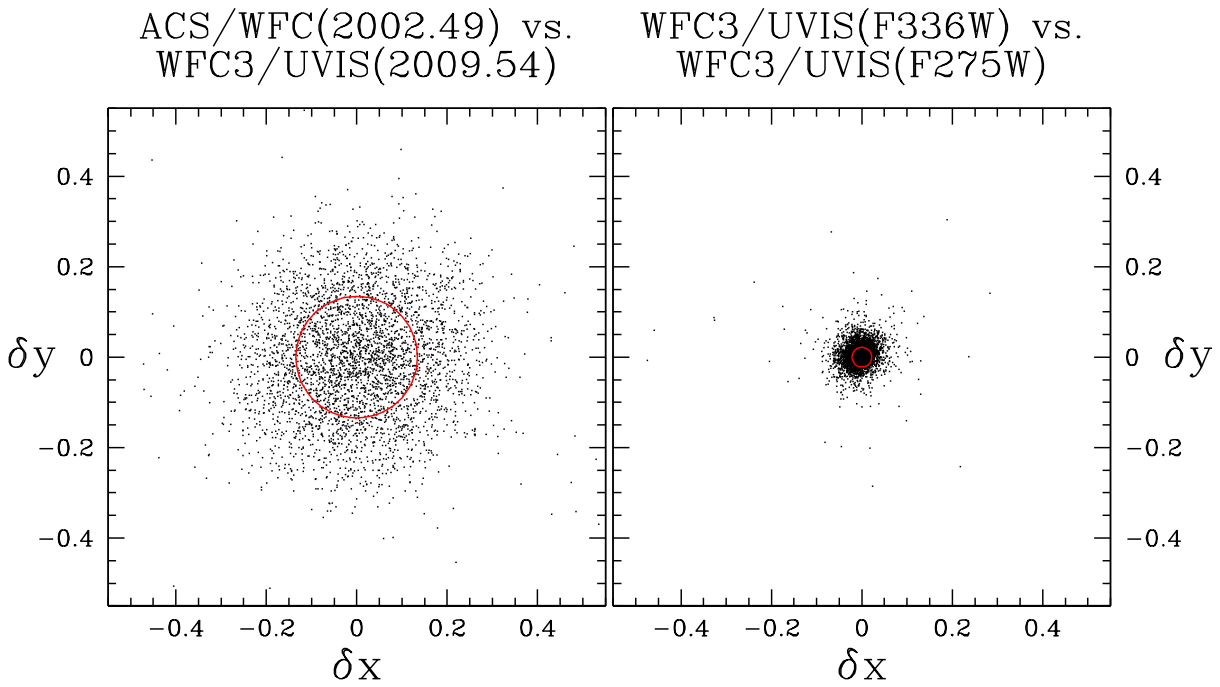

FIGURE 3.5— *Left:* Vector-point diagram of displacements for the stars in common between the ACS/WFC epoch of the master catalog, and the average of the corrected WFC3/UVIS new data in filter F275W. The internal motions of ω Cen dominate the observed dispersions, but do not prevent a GD solution accurate to ~0.025 WFC3 pixels. *Right:* Vector-point diagram of displacements for the stars in common between the corrected WFC3/UVIS data in filter F336W, and those corrected for F275W. The images are collected at the same epoch, and no sizable internal motions are present. In this case, the dispersion reflects our errors. The red circles, in both panels, indicate the 1-dimensional dispersion of the residuals, and all quantities are expressed in units of WFC3/UVIS pixels.

the location $(x_\circ, y_\circ)$, and the corrected axis $y^{\rm corr}$ has to be aligned with its y-axis at the location $(x_\circ, y_\circ)$. This is obtained by imposing $a_{1,k} = 0$ and $a_{2,k} = 0$. Since the detector axes do not necessarily have the same scales nor are perpendicular to each other, $b_{1,k}$ and $b_{2,k}$ must be free to assume whatever values fit best. Therefore, we have to compute in fact only 16 coefficients (for each chip) to derive our GD solution.

Each i-star in the master frame is conformally transformed into each k-chip/j-image, and cross-identified with the closest source. We indicate such transformed positions with $(X_i^{\rm master})^{T_{j,k}}$ and $(Y_i^{\rm master})^{T_{j,k}}$. Each of such cross-identifications, when available (of course not all the red sources in the master list were available in the WFC3 UV-filters), generates a pair of positional residuals:

$$\begin{cases} \Delta x_{i,j,k} &= x^{\rm corr}_{i,j,k} - (X_i^{\rm master})^{T_{j,k}} \\ \Delta y_{i,j,k} &= y^{\rm corr}_{i,j,k} - (Y_i^{\rm master})^{T_{j,k}}, \end{cases}$$

which reflect the residuals in the GD (with the opposite sign), and depend on where the i-star fell on the k/j-chip/image (plus random deviations due to non-perfect PSF-fitting and photon noise). Note that our calibration process is an iterative procedure, and that necessarily, at the first iteration, we have to impose $(x^{\rm corr}, y^{\rm corr})_{i,j,k} = (x, y)_{i,j,k}$. In each chip/image we have typically ~5500 high-signal unsaturated stars in common with the master frame, leading to a total of ~50 000 residual pairs per chip. [A color-magnitude diagram of the stars actually used

to compute the GD solution is shown, for each filter, in Fig.3.2.]

For each chip, these residuals were then collected into a look-up table made up of 37×19 elements, each related to a region of 110×110 pixels. We chose this particular grid setup because it offers the best compromise between the need for an adequate number of grid points to model the GD, and an adequate sampling of each grid element, containing at least 60 pairs of residuals. For each grid element, we computed a set of five 3σ-clipped quantities: $\overline{x}_{m,n,k}$, $\overline{y}_{m,n,k}$, $\overline{\Delta x}_{m,n,k}$, $\overline{\Delta y}_{m,n,k}$, and $P_{m,n,k}$; where $\overline{x}_{m,n,k}$ and $\overline{y}_{m,n,k}$ are the averaged positions of all the stars within the grid element (m, n) of the k-chip, $\overline{\Delta x}_{m,n,k}$ and $\overline{\Delta y}_{m,n,k}$ are the average residuals, and $P_{m,n,k}$ is the number of stars that were used to calculate the previous quantities. These $P_{m,n,k}$ will also serve in associating a weight to the grid cells when we fit the polynomial coefficients.

To obtain the 16 coefficients describing the two polynomials ($a_{q,k}$ with $q = 3, \ldots, 9$, and $b_{q,k}$ with $q = 1, \ldots, 9$), which represent our GD solution in each chip, we perform a linear least-square fit of the $N = m \times n = 37 \times 19 = 703$ data points. Thus, for each chip, we can compute the average distortion correction in each cell ($\overline{\delta x}_{p,k}$, $\overline{\delta y}_{p,k}$) with N relations of the form:

$$k = 1, 2;\ p = 1, \ldots, N: \begin{cases} \overline{\delta x}_{p,k} = \sum_{q=3}^{9} a_{q,k} t_{q,p,k} \\ \overline{\delta y}_{p,k} = \sum_{q=1}^{9} b_{q,k} t_{q,p,k} \end{cases}$$

(where $t_{1,p,k} = \overline{\overline{x}}_{p,k}$, $t_{2,p,k} = \overline{\overline{y}}_{p,k}$, …, $t_{9,p,k} = \overline{\tilde{y}^3}_{p,k}$), and where the 16 unknown quantities – $a_{q,k}$ and $b_{q,k}$ – are our fitting parameters (16 for each chip) .

In order to solve for $a_{q,k}$ and $b_{q,k}$, we formed, for each chip, one 9×9 matrix $\mathcal{M}_k$ and two 9×1 column vectors $\mathcal{V}_{a,k}$ and $\mathcal{V}_{b,k}$:

$$\mathcal{M}_k = \begin{pmatrix} \sum_p P_{p,k} t_{1,p,k}^2 & \sum_p P_{p,k} t_{1,p,k} t_{2,p,k} & \cdots & \sum_p P_{p,k} t_{1,p,k} t_{9,p,k} \\ \sum_p P_{p,k} t_{2,p,k} t_{1,p,k} & \sum_p P_{p,k} t_{2,p,k}^2 & \cdots & \sum_p P_{p,k} t_{2,p,k} t_{9,p,k} \\ \vdots & \vdots & \ddots & \vdots \\ \sum_p P_{p,k} t_{9,p,k} t_{1,p,k} & \sum_p P_{p,k} t_{9,p,k} t_{2,p,k} & \cdots & \sum_p P_p t_{9,p,k}^2 \end{pmatrix};$$

$$\mathcal{V}_{a,k} = \begin{pmatrix} \sum_p P_{p,k} t_{1,p,k} \overline{\Delta x}_{p,k} \\ \sum_p P_{p,k} t_{2,.,p,k} \overline{\Delta x}_{p,k} \\ \vdots \\ \sum_p P_{p,k} t_{9,p,k} \overline{\Delta x}_{p,k} \end{pmatrix}; \qquad \mathcal{V}_{b,k} = \begin{pmatrix} \sum_p P_{p,k} t_{1,p,k} \overline{\Delta y}_{p,k} \\ \sum_p P_{p,k} t_{2,p,k} \overline{\Delta y}_{p,k} \\ \vdots \\ \sum_p P_{p,k} t_{9,p,k} \overline{\Delta y}_{p,k} \end{pmatrix}.$$

The solution is given by two 9×1 column vectors $\mathcal{A}_k$ and $\mathcal{B}_k$, containing the best fitting values for $a_{q,k}$ and $b_{q,k}$, obtained as:

$$\mathcal{A}_k = \begin{pmatrix} a_{1,k} \\ a_{2,k} \\ \vdots \\ a_{9,k} \end{pmatrix} = {\mathcal{M}_k}^{-1} \mathcal{V}_{a,k}; \qquad \mathcal{B}_k = \begin{pmatrix} b_{1,k} \\ b_{2,k} \\ \vdots \\ b_{9,k} \end{pmatrix} = {\mathcal{M}_k}^{-1} \mathcal{V}_{b,k}.$$

With the first set of calculated coefficients $a_{q,k}$ and $b_{q,k}$ we computed the corrections $\delta x_{i,j,k}$ and $\delta y_{i,j,k}$ to be applied to each i-star of the k-chip in each j-MEF file, but actually we corrected the positions only by half of the recommended values, to guarantee convergence. With the new improved star positions, we start-over and re-calculated new residuals. The procedure is iterated until the difference in the average correction from one iteration to the following one – for each grid point – became smaller than 0.001 pixels. Convergence was reached after ~ 100 iterations. The coefficients of the final GD solutions for the two chips, and for the three different filters, are given in Table 3.1.

In Figure 3.3 we show for the intermediate filter F275W the total residuals of uncorrected star positions vs. the predicted positions of the master frame, which is representative of our GD solutions. For each chip, we plot the 37×19 cells used to model the GD, each with its distortion vector magnified (by a factor of $\times 8$ in x, and by a factor of $\times 1.5$ in y). Residual vectors go from the average position of the stars belonging to each grid cell $(\overline{x}, \overline{y})$ to the corrected one $(\overline{x^{\rm corr}}, \overline{y^{\rm corr}})$. Side panels show the overall trends of the individual residuals δx, δy along x and y directions (where for clarity we plot only a 40% sub-sample, randomly selected). It immediately strikes the large linear terms in y, reaching up to $\sim$140 pixels.

In Figure 3.4 we show, in the same way, the remaining residuals after our GD solution is applied. This time we magnified the distortion vectors by a factor $\times 1500$ in both axes.

At this point it is very interesting to examine the rms of these remaining residuals, that show a rather large $\sim$0.15 pixels dispersion. We will see, in the following, that this dispersion can be interpreted as the effect of the internal motions of the cluster stars on the time baseline of $\sim$7 years between the ACS/WFC observations of the reference frame, and the new WFC3/UVIS data set. Indeed, assuming 1) a distance of 4.7 kpc for ω Cen (van der Marel & Anderson 2009), 2) an internal velocity dispersion of $\sim$18 km s^{-1} in our fields (van de Ven et al. 2006), and 3) an isotropic velocity distribution for stars, we would expect to observe in $\sim$7 years a dispersion of the displacements of $\sim$5.5 mas. This dispersion, assuming a pixel scale of $\sim$40 mas for WFC3/UVIS, corresponds to a displacement of $\sim$0.14 pixels (also in good agreement with the recent measurements by Anderson & van der Marel 2009).

To show this more clearly we intercompare the average positions of the nine WFC3/UVIS corrected catalogs in the filter F275W, with those in the F336W, for the stars in common between the two filters. All these images were taken at the same epoch, and so positions of stars are not affected by internal motion effects. The 1-dimension dispersion should reflect our accuracy, and indeed the observed residuals – in this case – have a dispersion of $\sim$0.025 pixels (i.e. $\sim$1 mas). Figure 3.5 illustrates the two situations. On the left-panel we plot the displacements between the ACS/WFC epoch of the reference frame and the new WFC3/UVIS epoch, while on the right-panel we show the displacements between our corrected position in filter F275W and the corrected positions in F336W. On the left-panel the internal motions of ω Cen dominate the dispersion, while on the right-panel, there are no internal motions at all, and what we are left with are our errors only.

Unfortunately the WFC3/UVIS images were either not enough, or not well dithered to perform a pure auto-calibration, and we had to use the ACS/WFC reference frame. Nevertheless, even a dispersion of 0.15 pixel within a given cell should be reduced to less than 0.02 pixels if averaged over more than 60 residuals. And this should be regarded as an upper limit, since we are using 703 grid points to constrain 16 parameters.

For this reason, the estimated 0.025 pixel accuracy is larger than we would have expected. We can not exclude that these residuals could be due to a deviation from an isotropic distribution of the internal motion of ω Cen (i.e. at the level of $\lesssim 3$ km s^{-1}), or simply by unexpectedly large errors in the adopted ACS/WFC astrometric flat-field (the master frame). Another possibility is that there could be some unexpected (and so far undetected) manufacturing artifact in the WFC3/UVIS detectors which could affect the positions (such as those identified on WFPC2 CCDs, and characterized by Anderson & King 1999, or those of ACS/WFC found by Anderson 2002). Finally, it could simply be a higher frequency spatial variation which can not be properly represented by a polynomial of a reasonable order, but rather by a residual table as done in Anderson (2006) for ACS/WFC. Surely, more data are needed to further improve the GD solutions presented here, as well as a better time-baseline for the understanding of its variations. We want to end this section by pointing out that the detection of the internal motions among the stars of a Galactic globular cluster is a rather challenging measurement, and it could well be one of the best demonstrations of the goodness of our derived geometric distortion solutions.

3.3 Interchip transformations

For many applications it would be useful to transform the GD corrected positions of each chip into a common distortion-free reference frame. We could then, simply conformally transform the corrected positions of chip [k]

TABLE 3.1— The coefficients of the third-order polynomial for each chip and filter.

Term(w)	Polyn.	$a_{w,[1]}$	$b_{w,[1]}$	$a_{w,[2]}$	$b_{w,[2]}$
		WFC3/UVIS FILTER F225W			
1	$\tilde{x}$	0.000	129.230	0.000	140.270
2	$\tilde{y}$	0.000	1.935	0.000	−4.215
3	$\tilde{x}^2$	12.120	0.591	12.021	0.773
4	$\tilde{x}\tilde{y}$	−6.279	5.553	−6.057	5.496
5	$\tilde{y}^2$	0.064	−3.227	0.001	−3.058
6	$\tilde{x}^3$	0.176	0.029	0.149	0.156
7	$\tilde{x}^2\tilde{y}$	−0.057	0.033	0.022	−0.009
8	$\tilde{x}\tilde{y}^2$	0.004	−0.041	0.061	−0.026
9	$\tilde{y}^3$	0.035	−0.023	0.032	0.028
		WFC3/UVIS FILTER F275W			
1	$\tilde{x}$	0.000	129.270	0.000	140.285
2	$\tilde{y}$	0.000	1.925	0.000	−4.221
3	$\tilde{x}^2$	12.102	0.581	12.016	0.781
4	$\tilde{x}\tilde{y}$	−6.284	5.547	−6.040	5.493
5	$\tilde{y}^2$	0.061	−3.241	0.001	−3.048
6	$\tilde{x}^3$	0.178	0.033	0.144	0.163
7	$\tilde{x}^2\tilde{y}$	−0.056	0.054	0.026	0.007
8	$\tilde{x}\tilde{y}^2$	0.005	−0.041	0.051	−0.025
9	$\tilde{y}^3$	0.033	−0.012	0.032	0.020
		WFC3/UVIS FILTER F336W			
1	$\tilde{x}$	0.000	129.438	0.000	140.315
2	$\tilde{y}$	0.000	1.786	0.000	−4.322
3	$\tilde{x}^2$	12.091	0.676	11.994	0.672
4	$\tilde{x}\tilde{y}$	−6.188	5.565	−6.135	5.476
5	$\tilde{y}^2$	0.065	−3.155	0.004	−3.152
6	$\tilde{x}^3$	−0.062	0.004	−0.151	0.189
7	$\tilde{x}^2\tilde{y}$	−0.097	0.034	0.074	−0.027
8	$\tilde{x}\tilde{y}^2$	0.016	−0.061	0.040	0.005
9	$\tilde{y}^3$	0.033	0.016	0.033	0.014

into the distortion corrected positions of chip [1], using the following relations:

$$\begin{pmatrix} x^{\rm corr}_{[1]} \\ y^{\rm corr}_{[1]} \end{pmatrix} = \frac{\alpha_{[1]}}{\alpha_{[k]}} \begin{bmatrix} \cos(\theta_{[1]}-\theta_{[k]}) & \sin(\theta_{[1]}-\theta_{[k]}) \\ -\sin(\theta_{[1]}-\theta_{[k]}) & \cos(\theta_{[1]}-\theta_{[k]}) \end{bmatrix} \begin{pmatrix} x^{\rm corr}_{[k]} - 2048 \\ y^{\rm corr}_{[k]} - 1025 \end{pmatrix} + \begin{pmatrix} (x^{[k]}_{\circ})^{\rm corr}_{[1]} \\ (y^{[k]}_{\circ})^{\rm corr}_{[1]} \end{pmatrix};$$

TABLE 3.2— Interchip transformation parameters. Chip [1] parameters are indicated only for clarity. For chip [2] formal errors are given.

k-chip	$\alpha_{[k]}/\alpha_{[1]}$	$\theta_{[k]}-\theta_{[1]}$	$(x_\circ^{[k]})_{[1]}^{\rm corr}$	$(y_\circ^{[k]})_{[1]}^{\rm corr}$
	[number]	[°]	[pixel]	[pixel]
[1]	1.00000	0.0000	2048.00	1025.00
[2]	1.00595 ±2/100 000	0.0654 ±0.001	2046.00 ±0.03	3098.34 ±0.03

where – following the formalism in AK03 – we indicate the scale factor as as $\alpha_{[k]}$, the orientation angle with $\theta_{[k]}$, and the positions of the center of the chip $(x_\circ, y_\circ)$ in the corrected reference system of chip [1] as $(x_\circ^{[k]})_{[1]}^{\rm corr}$ and $(y_\circ^{[k]})_{[1]}^{\rm corr}$. Of course, for $k = 1$, we end up with the identity. The values of the interchip transformation parameters are given in Table 3.2, and shown for individual images in Figure 3.6.

3.4 Average Absolute Scale relative to ACS/WFC

The final step is to link, for each filter, the WFC3/UVIS chip [1] to an absolute plate scale in mas. To this purpose we adopt an average plate scale for our ACS/WFC master frame of 49.7248 mas ACS/WFC-pixel^{-1} (from van der Marel et al. 2007), and multiplied it by the – measured – scale factor between the WFC3/UVIS chip [1] and the master frame (which is expressed in ACS/WFC pixels). The results for the individual images and the averages for each filter, are shown in Figure 3.7, while Table 3.3 gives the average values in mas pixel^{-1}. We believe that the differences in the relative values for the three filters are significant. The fact that the plate scales correlate with the wavelength suggests that refraction introduced by either the filters, or by the two fused-silica windows of the dewar, could have some role.

Concerning their absolute values, instead, we have to consider that the velocity of *HST* around the Earth (±7 km s^{-1}) causes light aberration which induces plate-scale variations up to 5 parts in 100 000 (Cox & Gilliland 2002)[3], and that our master frame (from Villanova et al. 2007) was not corrected for it.

The ACS/WFC plate scale for the Anderson's (2006, 2007) GD solution – once corrected for the temporal variations of the linear terms – has proved to be stable at a level of accuracy better than these velocity aberration variations (van der Marel et al. 2007). However, since we are not attempting to correct for this effect on our adopted ACS/WFC master frame, we simply limit the accuracy of the here derived WFC3/UVIS plate-scale absolute values to these accuracies, i.e. 12 parts in 100 000.

3.5 Conclusions

By using a limited (but best available) number of exposures with large dithers, and an existing ACS/WFC astrometric flat field, we have found a set of third-order correction coefficients to represent the geometric distortion of

[3]If we sum to this the Earth velocity around the Sun the plate-scale variations can reach up to 12 parts in 100 000 (Cox & Gilliland 2002).

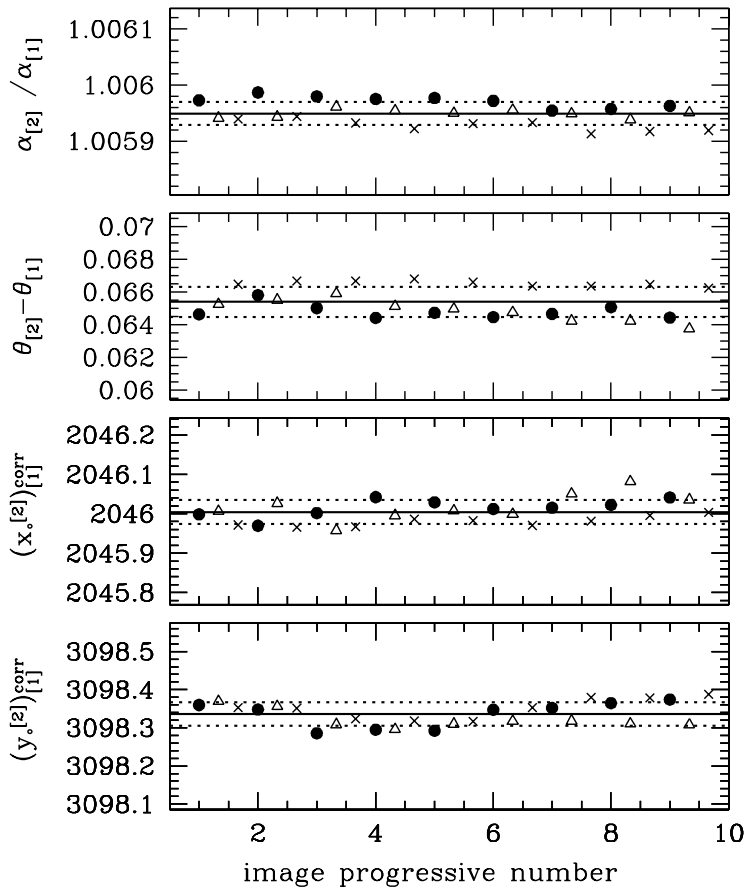

FIGURE 3.6— Interchip transformation parameters as obtained from individual images. Data points from F225W are indicated with filled-circles, F275W with triangles, and F336W with crosses. The averages are indicated with solid lines, while the dashed-lines give the formal uncertainties.

TABLE 3.3— Average absolute plate scale of WFC3/UVIS in mas pixel^{-1}. Accuracy is 12 parts in 100 000.

[mas pixel^{-1}]	F225W	F275W	F336W
$\alpha_{[1]}$	39.760	39.764	39.770

WFC3/UVIS in three broad-band ultraviolet filters. The solution was derived independently for each of its two CCDs.

The use of these corrections removes the distortion over the entire area of each chip to an average accuracy of

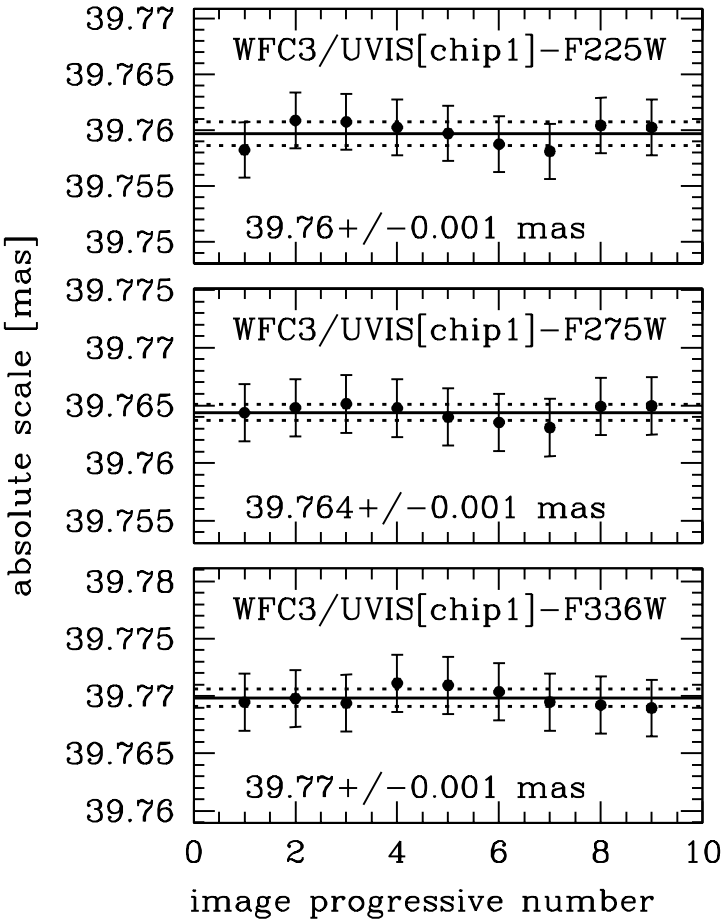

FIGURE 3.7— Absolute scales relative to the one adopted for our ACS/WFC master frame expressed in mas. Each panel shows individual images, for different filters. As in the previous figure, the average values are indicated with solid lines, while the dashed-lines give the formal uncertainties. For reference, we show with error-bars the on-orbit maximum systematic errors introduced by the velocity aberration on the plate scale, i.e. for a velocity of ±7 km s^{-1}. However, since our master frame has not been corrected for scale variation induced by velocity aberration, these values can not be considered more accurate – in absolute sense – than 12 parts in 100 000.

∼0.025 pixel (i.e. ∼1 mas), the largest systematics being located in the ∼200 pixels closest to the boundaries of the detectors (and never exceeding 0.06 pixels). We advise the use of the inner parts of the detectors for high-precision astrometry. The limitation that has prevented us from removing the distortion at an even higher level of accuracy is the lack of enough observations collected at different roll-angles and dithers which could enable us to perform an auto-calibration.

Nevertheless, the comparison of the mid-2002 ACS/WFC positions with the new WFC3 observations corrected with our astrometric solutions are good enough to clearly show the internal motions of ω Centauri. These proved to be in perfect agreement with the most recent determinations.

We also derived the average absolute scale of the detector with an accuracy limited by the uncertainties in the

plate-scale variations induced by the velocity aberration of the telescope motion in the Earth-Sun system.

For the future, more data with a longer time-baseline are needed to better characterize the GD stability of *HST* WFC3/UVIS detectors in the medium and long term.

Bibliography

Anderson, J., & King, I. R. 1999, PASP, 111, 1095
Anderson, J. 2002, The 2002 *HST* Calibration Workshop: Hubble after the Installation of the ACS and the NICMOS Cooling System, 13
Anderson, J., & King, I. R. 2003, PASP, 115, 113
Anderson, J. 2006, The 2005 *HST* Calibration Workshop: Hubble After the Transition to Two-Gyro Mode, 11
Anderson, J., Bedin, L. R., Piotto, G., Yadav, R. S., & Bellini, A. 2006, A&A, 454, 1029
Anderson, J. 2007, , Instrument Science Report ACS 2007-08, 12 pages, 8
Anderson, J., & van der Marel, R. P. 2010, ApJ, 710, 1032 Bellini A., & Bedin L. R. 2009, PASP, 121, 1419
Cox, C., & Gilliland, R. L. 2002, The 2002 *HST* Calibration Workshop : Hubble after the Installation of the ACS and the NICMOS Cooling System, 58
King, I. R., Anderson, J., Cool, A. M., & Piotto, G. 1998, ApJL, 492, L37
Milone, A. P., et al. 2010, ApJ, 709, 1183
van de Ven, G., van den Bosch, R. C. E., Verolme, E. K., & de Zeeuw, P. T. 2006, A&A, 445, 513
van der Marel, R. P., Anderson, J., Cox, C., Kozhurina-Platais, V., Lallo, M., & Nelan, E. 2007, Instrument Science Report ACS 2007-07, 22 pages, 7
van der Marel, R. P., 2003, Instrument Science Report ACS 2003-10, 21 pages, 10
van der Marel, R. P., & Anderson, J. 2010, ApJ, 710, 1063
Villanova, S., et al. 2007, ApJ, 663, 296

3.6 Appendix

We reduced WFC3/UVIS images of 47 Tuc (PID 11444 and 11452), to solve GD also for F438W, F606W and F814W filters, using the same technique described here. We then determined proper motions for all the objects in the field using as first epoch star positions from the MEMBER.RIGID.XYM catalog (Anderson, J., ISR 2007-08), and the local-transformation approach that will be described in Chapters 4–6.

In Fig. 3.8 we plotted the CMD F814W vs. F438W-F814W (instrumental magnitudes) for all the well-measured stars. Cluster members are drawn in black, stars belonging to the Small Magellanic Cloud (SMC) are plotted in red, and field stars are in azure. The sequence of stars in the bottom-left corner are 47 Tuc white dwarfs. The inset in the top-right corner shows the vector-point diagram (VPD) for the same objects. The two circle define the criteria used to select 47 Tuc and SMC members. There is an almost perfect separation between 47 Tuc and SMC stars. Note that 47 Tuc stars have a larger internal motion with respect to SMC ones, as we can see from their larger dispersion in the VPD.

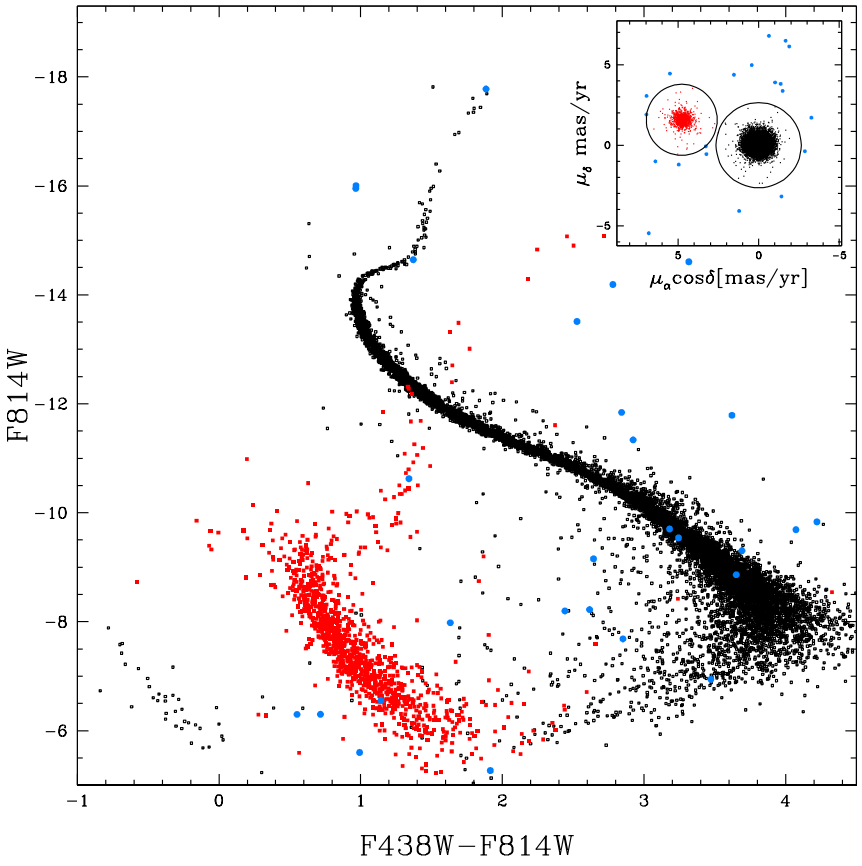

FIGURE 3.8— CMD F814W vs. F438W-F814W (instrumental magnitudes). Cluster members are drawn in black, stars belonging to the SMC are plotted in red, and field stars are in azure. The vector-point diagram for all the plotted objects is shown in the top-right panel. The two circle highlight the selection criteria adopted to define 47 Tuc and SMC members.

Applications

4

Proper-motions of faint sources in the field of the open cluster M 67

Once we have at our disposal an accurate geometric distortion (GD) correction (see Chapter 2), we can start to analyze images taken at different epochs, and compute proper motions for objects in the field of view (FoV) of our targets (open or globular clusters). This process is necessary to isolate field stars from cluster members, and it will lead to several different scientific applications, e.g. to infer cluster and stellar parameters, to derive stellar spatial distributions and radial gradients, to provide bona-fide targets for spectroscopic follow-up, and so on.

Computing proper motions that are both precise and accurate is, anyway, a very delicate matter. Indeed we have to:

- derive a *Point-Spread Function* (PSF) which is able to mimic the variability of star profiles all over the camera;
- carefully measure star positions in each image of each epoch via PSF fitting;
- compare position differences (displacements) from one epoch to the other, using a local-transformation approach to minimize GD residuals and other systematic sources of error.

This chapter is focused in describing all these steps. We will apply our astro-photometric techniques to two different telescope/camera systems: the Large Binocular Camera (LBC) mounted at the prime focus of the Large Binocular Telescope (LBT), and the University of Hawaii 8K×8K pixels mosaic camera (UH8K) at the Canada-France-Hawaii Telescope (CFHT), to obtain a proper-motion catalog of the faint stars of open cluster M 67, which will be used in Chapters 4.6–5 to study the white dwarf cooling sequence of the cluster and its absolute proper motion, respectively.

4.1 Observations

We made use of two different cameras on two different telescopes: the LBC@LBT and the UH8K@CFHT. In the following, we will address each data set individually.

4.1.1 Large Binocular Telescope data set

The LBT is a large optical/infrared telescope that utilizes two mirrors, each having a diameter of 8.4 meters[1]. The LBCs (Giallongo et al. 2008) are mounted at the prime foci of the LBT arms. One camera is optimized for blue filters, the other for red ones. Here we present results obtained with the LBT blue arm. The LBC-blue (hereafter simply LBC) is made by an array of four E2V 42-90 chips (2048×4608 pixel each), with an average pixel-scale of 232 mas (Chapter 2, see also Bellini & Bedin 2010, hereafter Paper IV). The four chips are installed on the focal plane in such a way as to maximize the symmetry of the FoV: three chips are aligned longside and the fourth, rotated 90 degrees, is located on top of them. The total FoV is ∼24′×26′.

During the LBT science-demonstration time (SDT), between February and March 2007, we obtained ∼4 hours (to be used both for science and calibration purposes) to observe the old, metal-rich open cluster M 67 ($\alpha = 08^{\rm h}51^{\rm m}23\overset{\rm s}{.}3$, $\delta = +11^\circ49'02''$, J2000.0, Yadav et al. 2008, Paper II) through $V_{\rm Bessel}$ and $B_{\rm Bessel}$ filters.

For long science exposures (180 s for each of the $B_{\rm Bessel}$ images, and 110 s for each of the $V_{\rm Bessel}$ ones), we chose a relatively small dithering scheme (spacing ∼140″), while all the 100 s $V_{\rm Bessel}$ exposures were devoted to calibrate the GD and have a larger dither scheme (spacing ∼280″). In the following, we will refer to LBC filters simply with *B* and *V*. A set of short exposures (10 each filter) were also taken in order to recover photometry for stars otherwise saturated in the long exposures.

Unfortunately, not all the images agreed with the scheduled requirements (dark time, seeing<0.8″). All the large dithered ones are affected by anomalously high background values (up to over 20 000 counts, in fact limiting the total dynamical range, and lowering the achievable magnitude faint limit of at least one magnitude), and some others have image quality above 1.″5 (caused mostly by guide-star system problems) harming PSF shapes, and again limiting the achievable magnitude faint limit[2]. Moreover, all the short exposures are affected by bad image quality (up to 5″). Some exposures were repeated trying to match the observational requirements (see Table 4.1), and we got two bonus *V* images, of 15 s and 330 s exposure time.

4.1.2 Canada-France-Hawaii Telescope data set

With the aim of identify (and separate) M 67 cluster members from field stars and background galaxies, we retrieved from the CADC on-line archive[3] a set exposures obtained from December 1996 to January 1997, taken with the UH8K camera mounted at the prime focus of the 3.6m CFHT[4].

The UH8K camera consists of a mosaic of eight 3-edge-buttable CCDs arranged in a 4×2 array, each chip of 2048×4096 pixels (pixel scale of 0.″21 pixel), giving a total FoV is ∼29′×29′. The UH8K layout closely resembles the one of the Wide-Field Imager (WFI) mounted on the ESO2.2m telescope (hereafter WFI@E2.2m), for which we have already developed a high-precision photometric and astrometric reduction software (Anderson et al. 2006, Paper I).

Long exposures consist of 15×1200 s through $V_{\rm Johnson}$ filter and 11×1200 s through $I_{\rm Cousins}$ filter, centered on M 67 center, with a small dither steps (typically ∼21″). A set of short exposures in both filters were also acquired, to recover photometry for the brightest stars otherwise saturated in long exposures. Thanks to this data set, that we used as first epoch, we will derive proper motions with more than 10 years of time baseline.

See Table 4.1 for the complete log of observations with both the instruments.

---

[1] `http://www.lbt.it/`; `http://medusa.as.arizona.edu/lbto/`.

[2] Because the measured seeing in these images is the sum of different factors besides the seeing itself (e.g., the mentioned guide-star problems and/or focus problems) we will use in the following the term “image quality”.

[3] `http://www2.cadc-ccda.hia-iha.nrc-cnrc.gc.ca/cadcbin/cfht/wdbi.cgi/cfht/wfi/form`.

[4] `http://www.cfht.hawaii.edu/`.

TABLE 4.1— Log of M 67 data used here, in temporal order. (1) and (2) mark images used as first and second epoch, respectively.

Date	Filter	#Images×Exp. time (s)	Airmass ($\sec z$)	Image Quality (arcsec)
		UH8K@CFHT		
Dec. 10, 1996	$V_{\rm Johnson}$	1×20	1.09	1.01
	$I_{\rm Cousins}$	1×20	1.10	1.02
Jan. 10, 1997	$V_{\rm Johnson}$	1×4, $4\times1200^{(1)}$	1.02–1.34	0.90–1.37
	$I_{\rm Cousins}$	1×3, $3\times1200^{(1)}$	1.02–1.58	0.75–1.12
Jan. 11, 2007	$V_{\rm Johnson}$	$11\times1200^{(1)}$	1.05–1.50	0.74–1.13
Jan. 12, 2007	$I_{\rm Cousins}$	$2\times1200^{(1)}$	1.26–1.50	0.87–0.95
Jan. 13, 2007	$I_{\rm Cousins}$	$6\times1200^{(1)}$	1.03–1.70	0.80–1.26
		LBC@LBT		
Feb. 18, 2007	$B_{\rm Bessel}$	$8\times180^{(2)}$	1.10–1.38	1.39–1.65
Feb. 19, 2007	$B_{\rm Bessel}$	$9\times180^{(2)}$	1.09–1.13	1.46–1.88
Feb. 21, 2007	$B_{\rm Bessel}$	$8\times180^{(2)}$	1.08–1.11	1.11–1.37
Feb. 22, 2007	$V_{\rm Bessel}$	1×15, $17\times110^{(2)}$, $1\times330^{(2)}$	1.07–1.12	0.62–1.31
Feb. 26, 2007	$V_{\rm Bessel}$	17×100	1.07–1.09	1.90–2.77
Feb. 27, 2007	$V_{\rm Bessel}$	10×1, $25\times100^{(2)}$	1.07–1.30	0.81–3.09
	$B_{\rm Bessel}$	10×2	1.20–1.30	1.28–5.12
Mar. 11, 2007	$B_{\rm Bessel}$	$8\times180^{(2)}$	1.12–1.18	1.40–1.68
Mar. 16, 2007	$B_{\rm Bessel}$	1×5, $25\times180^{(2)}$	1.07–1.15	0.79–1.08

4.2 Photometry of LBC@LBT data set

Due to the inhomogeneous quality of this data set, we were forced to develop different reduction methods. To measure bright-star positions and fluxes in deep exposures with image quality $\lesssim1\farcs6$, we used img2xym_LBC, a software directly derived from img2xym_WFI (Paper I), specifically optimized for LBC. We will refer to this method as *"first-passage photometry"*. A total of 56×180 s *B* exposures and 25×100 + 25×110 + 1×330 s *V* ones

were reduced with this method. In order to obtain a good photometry also for the faintest objects, for all these images we developed specific software tools, closely following the prescriptions given in Anderson et al. (2008). We will refer to this method as *"second-passage photometry"*. Finally, for all the short exposures, and for long exposures with image quality $\gtrsim 1\farcs6$, we simply performed aperture photometry. In the following subsections we will describe each of the different reduction procedures separately.

4.2.1 First-passage photometry

The WFI@2.2m software package discussed in Paper I has been designed to be easily adapted to other CCD mosaics. Anyway, in order to fully take advantage of this, we had to properly prepare raw LBC images. These images are contained in a single Multi-Extension Fits (MEF) file with four extensions (one per chip). In each chip the first 50 and the last 206 columns are constituted by overscan regions. The scientific area is located within pixel (51, 1) and pixel (2098, 4608), giving a total of 2048×4608 pixels. For reasons of convenience, after the extraction of the scientific regions, we added a frame of 1 pixel size (flagged at a value of -475 counts, see also Paper IV) to define their borders. Hereafter, when referring to LBC chips, we will refer to these 2050×4610 pixel areas.

We performed standard pre-reduction procedures (de-bias, de-flat) on all the images. Cosmic rays and bad-column corrections were also applied. LBC detectors work in 16 bit mode, so digital saturation starts at 65 535 counts. We safely adopted a saturation limit of 55 000 counts to minimize deviations from linearity close to the saturation regime and flat-field effects. Every pixel which counts exceed this saturation limit was never used, nor for the derivation of the PSFs, neither during the PSF fitting.

We applied the pixel-area correction to each chip using the GD coefficients published in Paper IV, for both for the $B_{\rm Bessel}$ and the $V_{\rm Bessel}$ filter images. Indeed, GD affects not only the position in which photons fall on the detector, but also the pixel collecting area itself. The corrected flux to be assigned to each pixel is the raw pixel flux multiplied by the corrected pixel area the pixel has in a distortion-free system.

Finally, again for reasons of convenience, for every LBC exposure we created a single fits file (hereafter, the work-image) in which we put the four pre-reduced single-chip images, all aligned longside and separated by gaps of 50 pixels. Specifically we put, from left to right, chip # 3, 2, 1 (to preserve their orientation in the sky), 4 (chip numbers reflect their storage positions in the MEF file). Our work-images are therefore constituted by 8350×4610 pixels. Note that work-images have no physical meaning: we will use them only for convenience to measure star positions and fluxes. Once the reduction procedure is completed, we will have single-chip individual catalogs.

Derivation of the PSF

To compute PSFs models, we developed the software img2psf_LBC, derived from the WFI@2.2m reduction package. As done in Paper I, our PSF models are completely empirical. They are represented by an array of 201×201 grid points, super-sampling the PSF grid by a factor of 4 with respect to the image pixels. The fraction of flux contained in the central pixel is given by the central grid point at position (101,101). A bi-cubic spline is used to interpolate the value of the PSF in between the grid points.

The value of a given pixel $P_{i,j}$ in the vicinity of a star of total flux z_*, located at position (x_*, y_*) is:

$$P_{i,j} = z_* \cdot \psi(i - x_*, i - y_*) + s_*, \tag{4.1}$$

where $\psi(\Delta x, \Delta y)$ is the instrumental PSF, specifically, the fraction of light (per unit pixel area) that falls on the detector at a point offset $(\Delta x, \Delta y) = (i - x_*, j - y_*)$ from the star's center, and s_* is the local sky background value. For each star we have an array of pixels that we can fit to solve for the triplet of parameters: x_*, y_*, and z_*. The local sky s_* is calculated as the 2.5σ-clipped median of the counts in the annulus between 21 and 24 pixels from the location where the star's center falls, where σ is the rms of the residuals around the median.

Equation (4.1) can be inverted (having a set of positions and fluxes for a star) to solve for the PSF:

$$\psi(\Delta x, \Delta y) = \frac{P_{i,j} - s_*}{z_*}. \tag{4.2}$$

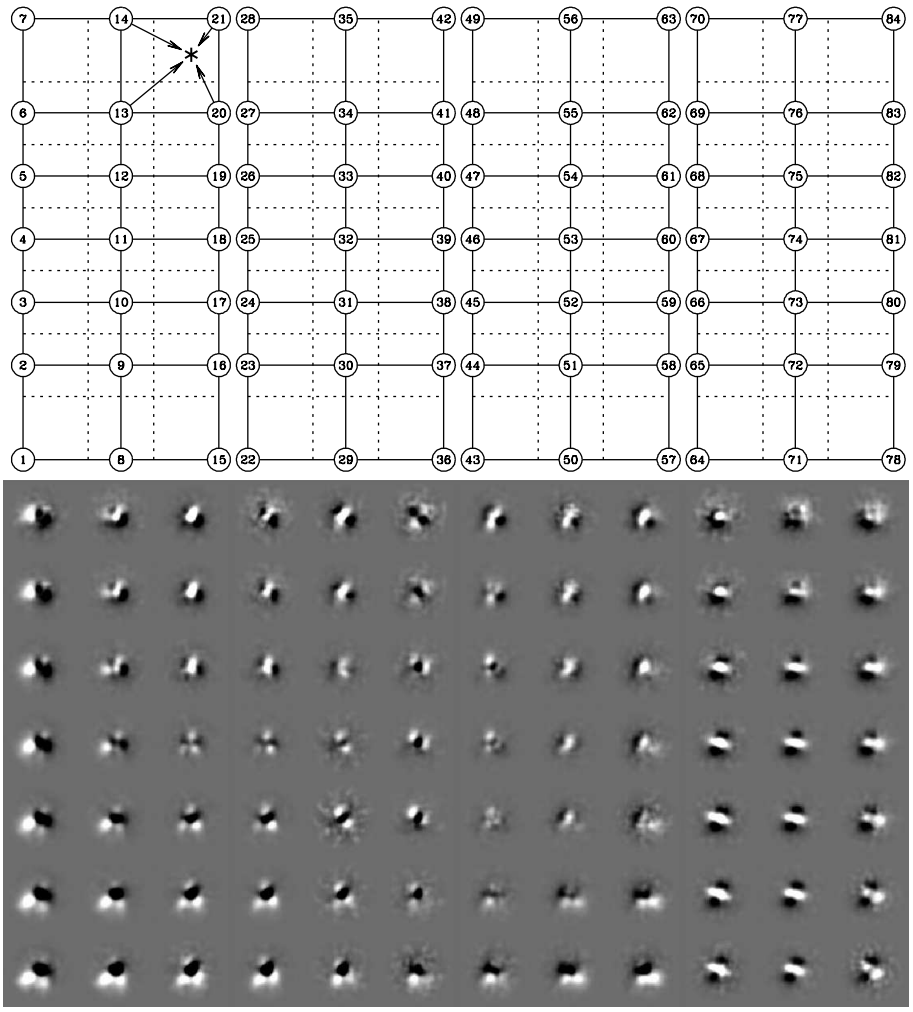

FIGURE 4.1— (*Top*): locations of the 84 fiducial PSFs on the work-image. The arrows show the process of interpolation to find a PSF at a particular point on the chip ("$*$"). Dotted lines separate the regions whom stars are used to solve each PSF. (*Bottom*): Difference between the local PSF and the average PSF over the entire FoV. White stands for a flux excess in the local PSF.

Equation (4.2) puts in relation a pixel in the star's image with an estimate of the bi-dimensional PSF function at the location $(\Delta x, \Delta y)$. By combining the array of sampling from many stars we can construct a reliable PSF model. Due to the nature of the so-defined PSF itself, its derivation is an iterative procedure. Indeed, without an accurate PSF, we cannot derive good positions and fluxes. On the other hand, without good positions and fluxes, we cannot derive and accurate PSF.

The software img2psf_LBC thus iterates in order to improve both the PSF model and stellar parameters. The starting point is given by simple centroid positions and aperture-based fluxes. The procedure consists of a two-step iteration (the same as in Paper I): first, the software builds the PSF model using star profiles. Then, it derives a better estimate of the star centroids with the PSF model.

We imposed some constraints to ensure a reasonable PSF;

1. We smoothed the PSF with a quadratic smoothing kernel (as done in Paper I, see also Anderson & King 2000), in such a way as to use the largest smoothing kernel that was consistent with the star images.
2. We wanted our PSF to be centered on the grid. To do so, we fit the inner 11×11 PSF grid points with a paraboloid to estimate the center of the PSF and, if it is not coincident with the center of the grid, we used a bi-cubic interpolation to re-sample the PSF at the locations where the grid points should be, and replaced the PSF with the properly centered one.
3. The last constraint we applied is normalization: we normalized the PSF to have a volume of unity within 6 pixels (1.″4). For normal image-quality and sky-background conditions, unsaturated stars are lost in the sky noise beyond ∼8 pixels. Our routine derives PSFs out to 25 pixels using the wings of saturated stars, but it is more accurate within 8 pixels, where it uses well-measured bright unsaturated stars. We chose this particular radius, 6 pixels, so that our normalization would not be affected by uncertainties related to saturation.

As in the case of the WFI@2.2m (Paper I), also for LBC@LBT the PSF shape is quite different from one chip to the other, and also from side to side within the same chip (the flux in the PSF core can vary up to 10%). To fully take into account for this spatial variation, we decided to solve for an array of 21 PSFs per chip (3 across and 7 high). This way, we can model an independent PSF at each of the locations shown in the left panel of Fig. 4.1. Dotted lines mark the regions used to determine each of the 84 PSFs. A bi-linear interpolation is used to construct a model for the PSF in between these fiducial points (represented by a "$*$"), as shown by the arrows. The right panel of Fig. 4.1 shows the difference of the 84 fiducial PSFs and the average PSF of the whole FoV, obtained with a deep (110 s) $V_{\rm Bessel}$ exposure (archive name lbcb.20070222.050155, image quality $\sim 0.''7$).

To model PSFs, we have to use only stars with high signal-to-noise (S/N) ratio in both the core and in the wings. This is obtained by creating a list of stars with a flux of at least 1500–2000 digital numbers (DNs) above the local sky in their inner 3×3 pixels, and with no nearby (within 15 pixels) brighter neighbors. Moreover, we don't want to include in our list objects that are clearly not stars: for sparse star fields like the one of the M 67, most of the faint point-like sources are actually background galaxies. These objects are blurred and, for a given total flux, their light is distributed more in the wings than in the core, with respect to the stars' light.

To avoid including galaxies in our PSF list, we requested that, in case a candidate star is found, centered on pixel (i, j), the sum of the flux of the 8 surrounding pixels [$f_{\rm in} = (\sum_{k=i-1}^{i+1} \sum_{l=j-1}^{j+1} P_{k,l}) - P_{i,j}$] has to be lower then $\mathcal{G}$ times the sum of the flux of the 16 pixels that lay outside them [$f_{\rm out} = (\sum_{k=i-2}^{i+2} \sum_{l=j-2}^{j+2} P_{k,l}) - f_{\rm in} - P_{i,j}$]:

$$f_{\rm in} < \mathcal{G} \cdot f_{\rm out}.$$

The parameter $\mathcal{G}$ (a sort of crude galaxy-shape parameter) is a function of both the image quality and the used filter. It is smaller for point-like sources, and bigger for more spread ones. Due to the wide variety of different image qualities in our data set, it was possible to properly tabulate $\mathcal{G}$ for both the B and V filters. We look at each of our images to verify that only stars were included in our PSF lists.

After some tests, we found that a single PSF model is well constrained if at least 50 stars are used to model it. Unfortunately, in sparse fields (or in short exposures, or with bad image quality) there could be not enough stars to use for modeling the PSFs. In these cases, we would prefer to model a smaller number of fiducial PSFs, in order to increase the number of stars designed to derive each of them. For this reason, the program img2psf_LBC has been set to allow the determination of: $(3 \times 7) \times 4$(= 84 PSFs), $(3 \times 4) \times 4$(= 48 PSFs), $(3 \times 3) \times 4$(= 36 PSFs), $(2 \times 4) \times 4$(= 32 PSFs), $(2 \times 3) \times 4$(= 24 PSFs), $(2 \times 2) \times 4$(= 16 PSFs), or $(1) \times 4$(= 4 PSFs) to cover the whole area of the detector.

Choosing the best solution (i.e., less, well sampled PSFs that might not be able to properly take into account for the PSF space variation or, on the other hand, more PSFs but worse constrained) is indeed a delicate matter. In order to obtain the best results we investigated, for every single exposure, whether it was better to have more or less PSFs. The chosen criterion to select the best solution is to directly inspect the produced PSFs, and to analyze

the trend of the quality-of-fit parameter (QFIT, see next subsection for details) across the work-image. Better PSF models provide smaller QFIT values.

Fitting star positions and fluxes

Once PSF models are computed, we can use them to measure all the stars in the image. To do so, we developed the software img2xym_LBC (mostly based on img2xym_WFI, Paper I). It requires two input arguments: (i) the threshold flux of the faintest star to be found, in its centermost 3×3 pixels above the local sky, (ii) how many pixels a star can be close to brighter neighbors.

To disentangle and measure overlapping stellar profiles is, once again, an iterative procedure. The program therefore performs seven iterations (enough to find and measure all the significant sources), each of them subdivided into the following tasks;

1. Creation of the convolved image, by convolving the current subtracted image with the PSF. Of course at the first iteration the subtracted image is the work-image itself;
2. Searching for significant peaks on the convolved image. Using the convolved image in fact makes it easier to find real peaks, i.e. pixels brighter than their eight surrounding pixels. At the first iteration the program finds all the saturated stars and those being 10× brighter than the threshold value with no brighter sources within 15 pixels. In the subsequent iterations, the program will gradually find fainter peaks, and closer to brighter neighbors, up to reach the threshold requirements given as input parameters.
3. PSF fitting to measure fluxes for all the found sources (for the saturated stars, the software uses only their unsaturated pixels, i.e. the stars' wings) on the subtracted image. As a consequence, the fits for two nearby stars can quickly converge upon an accurate position and flux for each. For unsaturated stars, we found that a fitting radius of 3.5 pixels offers the best results (i.e., for a given star measured in several exposures, to have the smallest rms of the magnitude residuals around its median).
4. Subtraction of all the unsaturated, measured sources from the work-image. Saturated stars are not subtracted because the PSF is generally not reliable out in the wings, and that would make the subtracted image less useful than the original one.

At the end of the iteration process, the software produces four catalogs of position and fluxes for all the detected sources, one per chip. These catalogs contain the following information for every measured source: raw and GD corrected coordinates (in pixel, see next subsection for details); instrumental magnitude (defined as $-2.5 \cdot \log[\mathrm{DNs}]$); total flux in DNs; QFIT; and the iteration number at which a source is detected.

The QFIT is defined as the sum, for each pixel of a star within the fitting radius (3.5 pixels), of the absolute value of the difference between the pixel values $P_{i,j}$ and the predicted ones, normalized with respect to the $P_{i,j}$. Specifically:

$$\mathrm{QFIT} = \sum_{i,j} \left(\frac{|P_{i,j} - z_* \cdot \psi(i - x_*, j - y_*)|}{P_{i,j}} \right).$$

QFIT is close to zero for well-measured stars, and close to unity for the badly-measured (or not star-like) ones. We found that typically $\mathrm{QFIT} < 0.1$ for well-measured stars in our images.

Top-left panel of Fig. 4.2 shows QFIT values versus instrumental magnitudes, for exposure lbcb.20070222.050155 (110 s, *V* filter, image quality $\sim 0\farcs7$). The vertical dotted line marks the magnitude saturation limit. Even for barely saturated stars, the QFIT parameter is comparable to that of well-measured stars ($\mathrm{QFIT} \lesssim 0.1$), because only unsaturated pixels have been used to fit the PSF to saturated sources[5]. Albeit well-measured stars have a $\mathrm{QFIT} \lesssim 0.1$,

[5]For severely saturated stars (instrumental magnitude $\lesssim -17$), the QFIT parameter rapidly increases because, even if we used only pixels in the unsaturated wings of the star's profile to fit the PSF, for such bright objects these pixels are located at a radial distance from the star's center for which the PSF model starts to be unreliable.

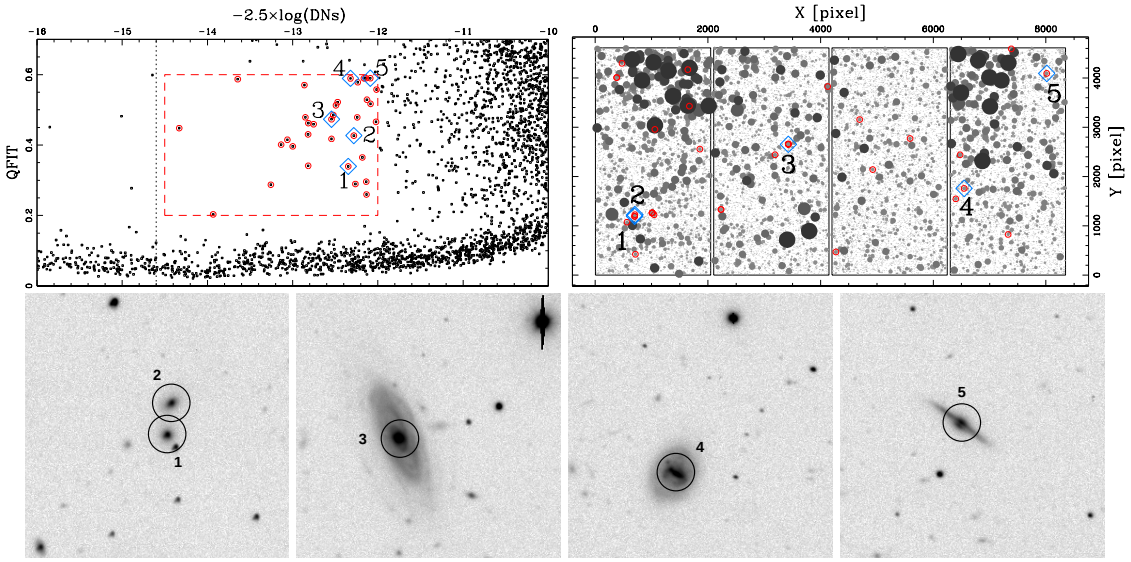

FIGURE 4.2— *(Top left:)* QFIT parameter versus the instrumental magnitude for exposure lbcb.20070222.050155. Saturation limit is marked by the vertical dotted line. We highlighted with open circles a sample of bright objects (S/N>100 in their central pixel) with a higher QFIT values with respect to well-measured stars of the same luminosity. *(Top right:)* Dark circles show all the measured sources on the work-image (the bigger and darker the circle, the brighter the source). Red symbols mark the position of selected high QFIT objects. These objects are randomly placed on the FoV. If some of the derived PSFs were bad sampled, these objects would have been brought closer to each other, in the same regions where the bad PSFs were derived. We select five of these objects (blue open squares), located in different parts of the work-image, numbered according to their increasing QFIT value. *(Bottom panels:)* A region of ∼64 arcsec^2 around these five sources. All of them are galaxies: number 1 and 2 are elliptical galaxies with bright sharp nuclei, number 3 is a spiral, number 4 is a barred spiral, and number 5 is an edge-on one.

there is an increasing number of objects, going to fainter magnitudes, with higher QFIT values. These objects could be: *i*) background galaxies (the vast majority); *ii*) blends; *iii*) stars too close to chip edges, bleeding or bad columns, or *iv*) uncorrected cosmic rays. We highlighted, with open red circles, a sample of bright objects (S/N>100) with a higher QFIT with respect to well-measured stars at the same luminosity. On the top-right panel of Fig. 4.2 we plotted with black circles the location of all the measured sources in the work-image. The bigger the circle, the brighter the source. Selected high-QFIT objects (marked again with red open circles) are randomly distributed across the work-image; if they were to be more concentrated at a particular region of the work-image, it would suggest some kind of problems, related for instance to our PSF models around that region. We chose five of these objects (blue open squares), distributed all around the work-image and having a similar luminosity, and we numbered them according to their increasing QFIT value (see left panel). On the bottom panels of Fig. 4.2 we show a region of ∼280×280 pixels (∼64 arcsec^2) around these five sources. They reveal to be all galaxies, in particular: (1) and (2) are elliptical galaxies; (3) a spiral galaxy with sharp nuclei; (4) a barred spiral; and (5) an edge-on spiral. It is clear that the QFIT parameter is a good indicator of how close the profile of a source is with respect to the PSF one.

Finally, raw *x* and *y* positions in the catalogs are referred to the raw pixel coordinates on each individual chip. [Note that we rotated chip # 4 counter-clockwise of 90 degrees, so that its *x* and *y* axes are parallel to R.A. and Dec., respectively, as it is for the other chips.] Transformation equations to convert *i*-star raw positions from the

work-image reference frame $(x_i, y_i)_{\text{w.i.}}$ to the k-chip reference frame are:

$$k = 1,2,3 : \begin{cases} x_{i,k} &= x_{i,\text{w.i.}} - (3-k)\cdot 2100 \\ y_{i,k} &= y_{i,\text{w.i.}} \end{cases}$$

$$k = 4 : \begin{cases} x_{i,k} &= 4610 - y_{i,\text{w.i.}} \\ y_{i,k} &= x_{i,\text{w.i.}} - k\cdot 2100. \end{cases}$$

Geometric distortion correction

Star positions are corrected for GD as described in Chapter 2 (see also Paper IV). The same technique has been successfully applied also to the case of the Wide-Field Camera 3, on board the *Hubble space telescope* (Bellini & Bedin 2009, see also Chapter 3).

In a nutshell, we modeled the GD with a third-order polynomial for each LBC chip, independently. For each i-star in each k-chip, the distortion corrected position $(x^{\text{corr}}_{i,k}, y^{\text{corr}}_{i,k})$ is obtained as the observed position $(x_{i,k}, y_{i,k})$ plus the distortion correction $(\delta x_{i,k}, \delta y_{i,k})$:

$$\begin{cases} x^{\text{corr}}_{i,k} &= x_{i,k} + \delta x_{i,k}(\tilde{x}_{i,k}, \tilde{y}_{i,k}) \\ y^{\text{corr}}_{i,k} &= y_{i,k} + \delta y_{i,k}(\tilde{x}_{i,k}, \tilde{y}_{i,k}), \end{cases}$$

where $\tilde{x}_{i,k}$ and $\tilde{y}_{i,k}$ are normalized positions with respect to the center $(x_\circ, y_\circ)_k$ of the k-chip, and $(\delta x_{i,k}, \delta y_{i,k})$ are given as:

$$\begin{cases} \delta x &= a_1\tilde{x}+a_2\tilde{y}+a_3\tilde{x}^2+a_4\tilde{x}\tilde{y}+a_5\tilde{y}^2+a_6\tilde{x}^3+a_7\tilde{x}^2\tilde{y}+a_8\tilde{x}\tilde{y}^2+a_9\tilde{y}^3 \\ \delta y &= b_1\tilde{x}+b_2\tilde{y}+b_3\tilde{x}^2+b_4\tilde{x}\tilde{y}+b_5\tilde{y}^2+b_6\tilde{x}^3+b_7\tilde{x}^2\tilde{y}+b_8\tilde{x}\tilde{y}^2+b_9\tilde{y}^3 \end{cases}$$

(we omitted here the subscript "i,k" for simplicity).

The GD solution is therefore fully characterized by 18 coefficients: $a_1, \ldots, a_9$, $b_1, \ldots, b_9$. We constrained the solution so that, at the center of the chip, it will have its x-scale equal to the one at the location $(x_\circ, y_\circ)$, and the corrected axis y^{corr} has to be aligned with its y-axis at the location $(x_\circ, y_\circ)$. This is obtained by imposing $a_{1,k} = 0$ and $a_{2,k} = 0$, so we are left with only 16 coefficients. Our average correction enables a relative astrometric accuracy of ∼10 mas per coordinate in both filters. The values of the GD-solution coefficients are tabulated in Chapter 2 (see also Bellini & Bedin 2010).

Figure 4.3 shows the color-magnitude diagram (CMD) for the stars found in this way. Dotted lines mark the saturation limit for exposures with the best and the worst image quality. The cluster main sequence (MS) is well defined even above the saturation limits. The equal-mass binary sequence is also evident. At $(B-V) \simeq 1.4$ there is an effect, due to the saturation of the color index, that makes the MS almost vertical. The majority of objects gathered together in the lower left side of the CMD is constituted by blue faint galaxies. It is possible to foresee the white dwarf (WD) cooling sequence (CS) on the left hand of the CMD (mixed with field stars and blue galaxies).

4.2.2 Second-passage photometry

While bright stars can be easily identified in almost every exposure, faint stars may not stand out above the noise in some images. To find and measure even the faintest sources, the first step consists in analyzing the relatively bright stars, in order to establish astrometric and photometric transformations from each exposure into a reference frame (master frame). We will then use these transformations to measure star fluxes in all the exposures at once.

Transformation between images

In building the master frame, we need to choose an exposure/chip to start with. We chose the first deep B exposure of March 16 (archive name lbcb.20070316.031311) simply because it is the first one of a good-image-quality run. Moreover, we started with its chip # 2, given its central location among the LBC chips. [Note also that during SDT

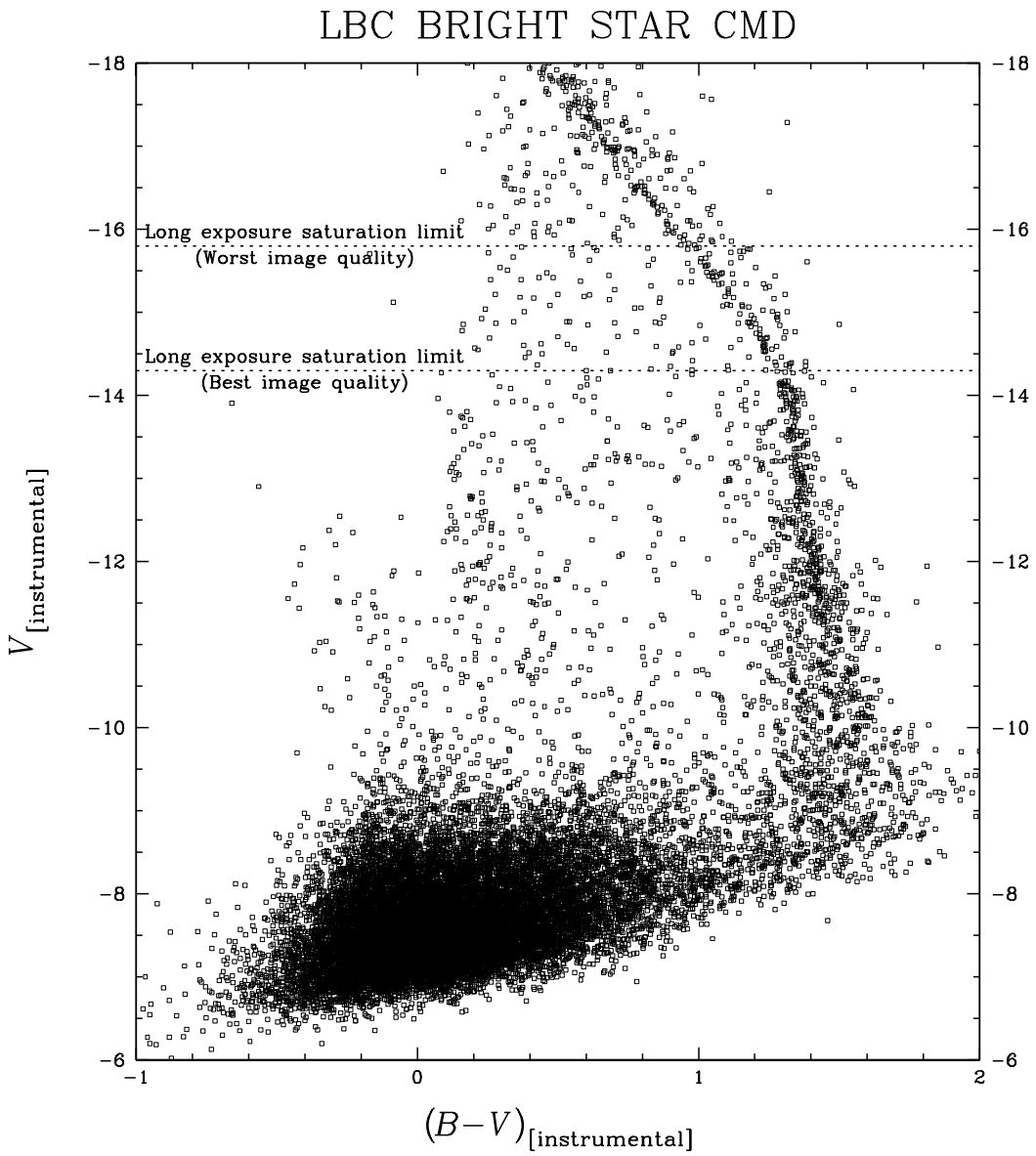

FIGURE 4.3— CMD obtained with the first-passage photometry technique. The cluster main sequence is narrow and well defined even for slightly saturated stars. We expect the white dwarf cooling sequence to be deeply merged with background galaxies and field stars. The equal-mass binary sequence, parallel to the main sequence, is also well visible.

chip # 2 had been used to put into focus the whole camera.] We preferred to use *B* images for the construction of the master frame with respect to *V* ones because, with the available data set, they allow us to detect the WDs in M 67 (being this the scientific goal of our LBT SDT). We selected only bright, unsaturated stars (~130 objects with

instrumental magnitude <-11[6] and QFIT<0.1) to build a master list of positions in order to specify orientation, scale, and zero point of the master frame.

We identified stars in common between each chip list and the master list, and used their coordinates in the two systems to define general six-parameter linear transformations to transform from the distortion-corrected frame of each exposure's chip into the master frame. We then derived a new, improved master frame, in which now each star position is calculated as the the median of the positions of that star in each exposure's chip, once transformed into the master frame. Only stars found in at least three different chip lists were used to derive the new master frame.

Of course, not all the chips contain a region in common with the master frame. The construction of the master frame is again an iterative process, in which at every step more chips can be matched with the master frame in a progressive way. First we started with chips # 2 only (to fix also the photometric zero point). Once we have obtained a master frame from them, we started to gradually add the other chips. In this way, we also registered the photometric zero points of all the different chips to the one of chip # 2.

For bright stars, the root mean square (rms) of the residuals around their average positions on the master frame were less then 0.035 pixels (∼8 mas) in each coordinate, while photometric rms residuals were about 0.01 mag for the well-exposed stars. These small residuals confirm that now we can transform transparently from individual-exposure chips into the master frame, and vice versa. We repeated the same procedure also for the *V* filter images, using the *B* filter master frame as a reference for star positions. Again, we started with chip # 2, and we successively added the other chips. As for the *B* filter case, only sources found in at least three individual exposures were added to the master frame. Photometry and astrometry collected in these lists are essentially the best that can be done for the brighter stars, since we can fit for both their position and flux in individual exposures.

Image stacks

It is useful to construct stacks so that we could examine the images of stars and galaxies that are hard to see clearly in individual exposures. The stacks (one each filter) are invaluable in helping us discriminate between real objects the software should classify as star or galaxies, and objects that should be rejected as PSF artifacts or peaks of noise.

Because LBC is not undersampled, there is no need to supersample our stack images, as done in Anderson et al. (2008). We used the positional transformations found in the previous subsection to determine where each pixel in each exposure mapped into the stack image. The value of these pixels (sky subtracted) were properly scaled to match the photometric zero point of the master frame. Therefore, for a generic pixel of the *k*-chip of the *l*-image mapping a pixel (i, j) on the stack image, its proper-scaled value is

$$P^{\rm stack}_{i,j,k,l} = P_{i,j} \cdot 10^{-0.4 \cdot {\rm zp}_{k,l}},$$

where $\mathrm{zp}_{k,l}$ is the photometric zero point correction for the *k*-chip of the *l*-image.

For a given pixel of the stack image, we can dispose of several such mapping pixels $P^{\rm stack}_{i,j,k,l}$. We assigned to a stack pixel the 3σ-clipped median of its $k\times l$ mapping pixels. There was no need to iterate this procedure, as done in Anderson et al. (2008), because we are not supersampling the stack.

On the left panel of Fig. 4.4 we show our stack image made with the deep *B* filter exposures. The FoV is $\sim 36\times 34$ arcmin^2. A region, located $\sim 9'$ south from M 67 center has been imaged with ACS/WFC through F775W filter (2 exposures with 970 s of total integration time, GO-9984, P.I. Rhodes), and it is highlighted by the trapezoid. A close view of this region in common is show on the right panels. on the top one there is the ACS/WFC stack image obtained following the prescriptions given in Anderson et al. 2008). On the bottom one we show the LBC counterpart. In particular, this region is mapped by 56 single LBC exposures, providing a total integration time of

[6]For most of this chapter we will keep our photometry in the instrumental system, since it is a more natural system for evaluating photometric quality in term of S/N. We will calibrate the photometry in Sect. 4.4.

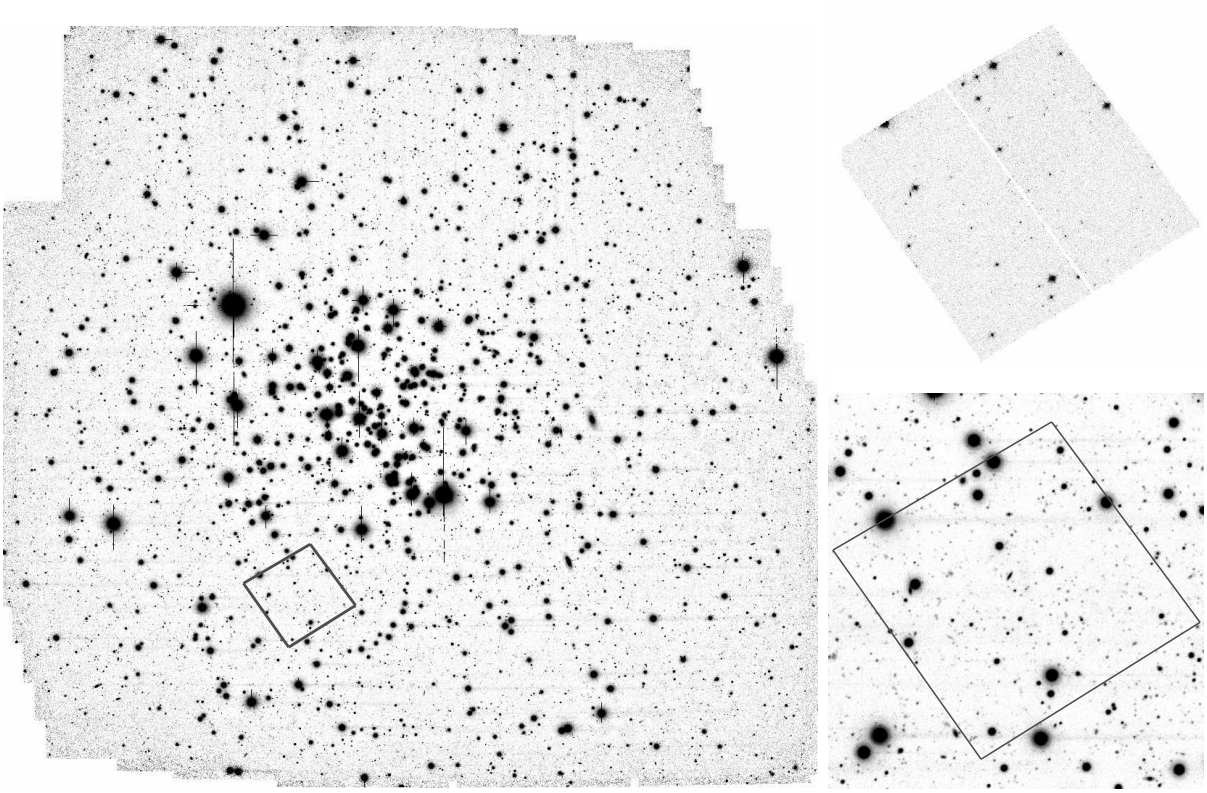

FIGURE 4.4— *(Left:)* The FoV offered by the stack image in the *B* filter (~36×34 arcmin^2). A portion of the field, highlighted by the trapezoid, has been imaged with ACS/WFC (GO-9984, P.I. Rhodes). *(Top right:)* The stack image made with the ACS/WFC (two exposures through F775W filter, total time 970 s). *(Bottom right:)* the same zoomed region as imaged by LBC.

$2^h\,42^m$ in *B* (i.e., 10× the ACS/WFC in F775W filter). The central object is an edge-on galaxy, that falls in the gap between the two ACS/WFC chips. We can safely affirm that our stack can reveal the same number of detail as the ACS/WFC one.

Figure 4.5 compares a closer view (~350×370 pixels, ~80×92 arcsec^2) of the centermost region showed on the right panels of Fig. 4.4: on the left panel as imaged by the work-image lbcb.20070316.031311 (180 s exposure, *B* filter, image quality ~0.″9); on the right panel by the *B* filter stack image. Typically, the sky background for a 180 s *B* filter exposure is ~3000 DNs, giving a Poisson noise of ~50 counts. All the faint sources are lost in this noise in a single exposure, but they are able to stand out in the stack image, where the noise is reduced to ~7 counts (i.e., $50/\sqrt{56-1}$).

The peak map

The next step is to set up the most-complete list of positions for sources in the master frame, in order to find and measure even the faintest ones. At this point, it is worthwhile to consider what effects a barely detectable star will have on this data set. Unlike *Hubble Space Telescope* (*HST*) cameras, that concentrate most of a source light in its centermost pixel, in the case of the LBC only a small fraction is stored in the central pixel (typically ~4–6% for the used images), and the sky noise is definitely higher. Therefore it is even harder, for a faint star in a single exposure, to be able to push its central pixel value above the noise. However, if this source can generate a local

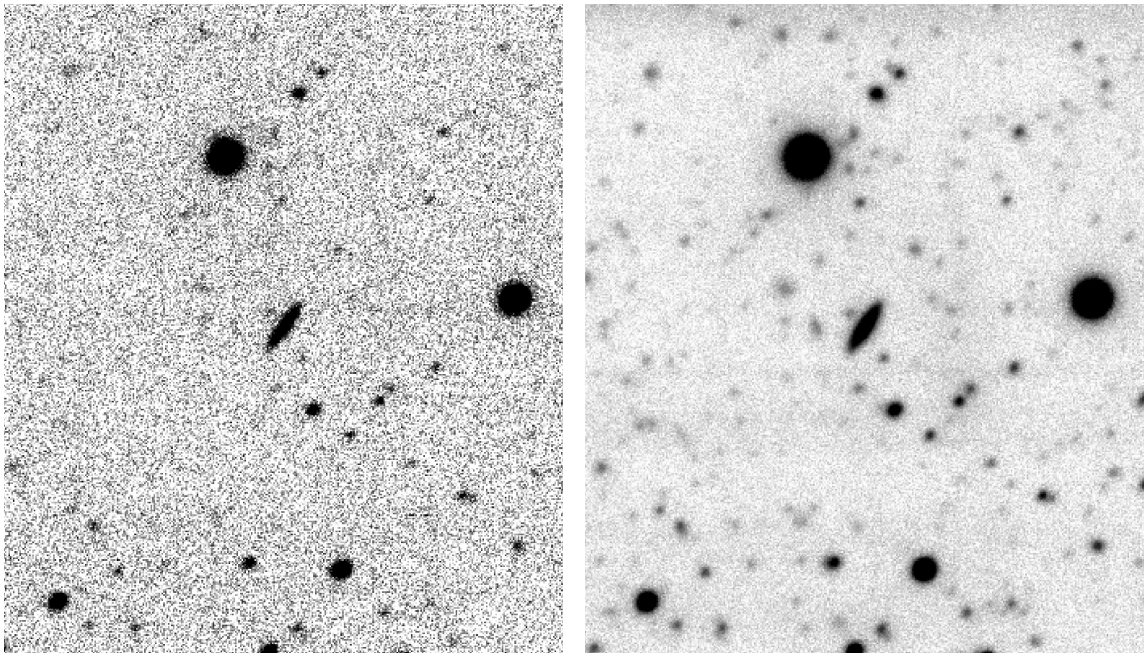

FIGURE 4.5— *(Left:)* A region of ~350×400 pixels (~80×92 arcsec^2) in the *B* exposure we used as starting point to construct the master frame (lbcb.20070316.031311, 180 s, image quality ~0.″93). *(Right:)* the same region in the stacked image. This region is mapped by 56 individual exposures. Color code and scale are the same for both panels. A considerable amount of details – lost in the background noise of the single exposure – is now clearly visible in the stack image.

maximum in a statistically significant number of images, then we have some chance of detecting it.

We began by defining a local maximum (peak) as any pixel which flux is strictly higher than any of its eight surrounding neighbors in the convolved image. We used convolved images because it is easier to identify peaks on the them with respect of the work-images, because sky noise is smoother. The adopted procedure to identify local maxima finds an enormous amount of peaks – on average one pixel over nine in any region dominated by background noise – but if a local maximum occurs in the "sample place" (i.e., within 1.5 pixels) in many exposures, it is an indication of the presence of a faint source.

To identify these candidate sources, we constructed what we call peak maps, i.e. maps of how often a local maximum occurred at a particular location in the field. To construct the peak maps (one per filter), we went through each of the 56 *B*-filter exposures, and each of the 44 *V*-filter ones, pixel by pixel. Each time we found a pixel housing a local maximum, we used positional transformations to calculate its corresponding location on the master frame, and added 1 count to the closest peak-map pixel. As done for the stack image, we did not supersample our peak-map pixels.

A faint star does not make a local peak in every image, and random peaks add a background level which we found to be (in a region mapped by all the 56 images) around 2.2 counts. Hadn't we used convolved images, the background level should be, in that case, $56/9 \gtrsim 6$ counts. The ~2.2 background value (i.e., $56/(9 \times \sqrt{9-1})$) we found means that, on average, convolved (smoothed) images provide a local random maximum every ~20 pixels. As a consequence, the S/N is enhanced.

At this point, we need a way of analyzing the peak map that would allow us to collect nearly all of the genuine sources. As in Anderson et al. (2008) we found that, by overbinning the peak map by 3×3 (just like a box-car smoothing but without dividing the sum by 9), we are able to optimally highlight the signal from the faintest

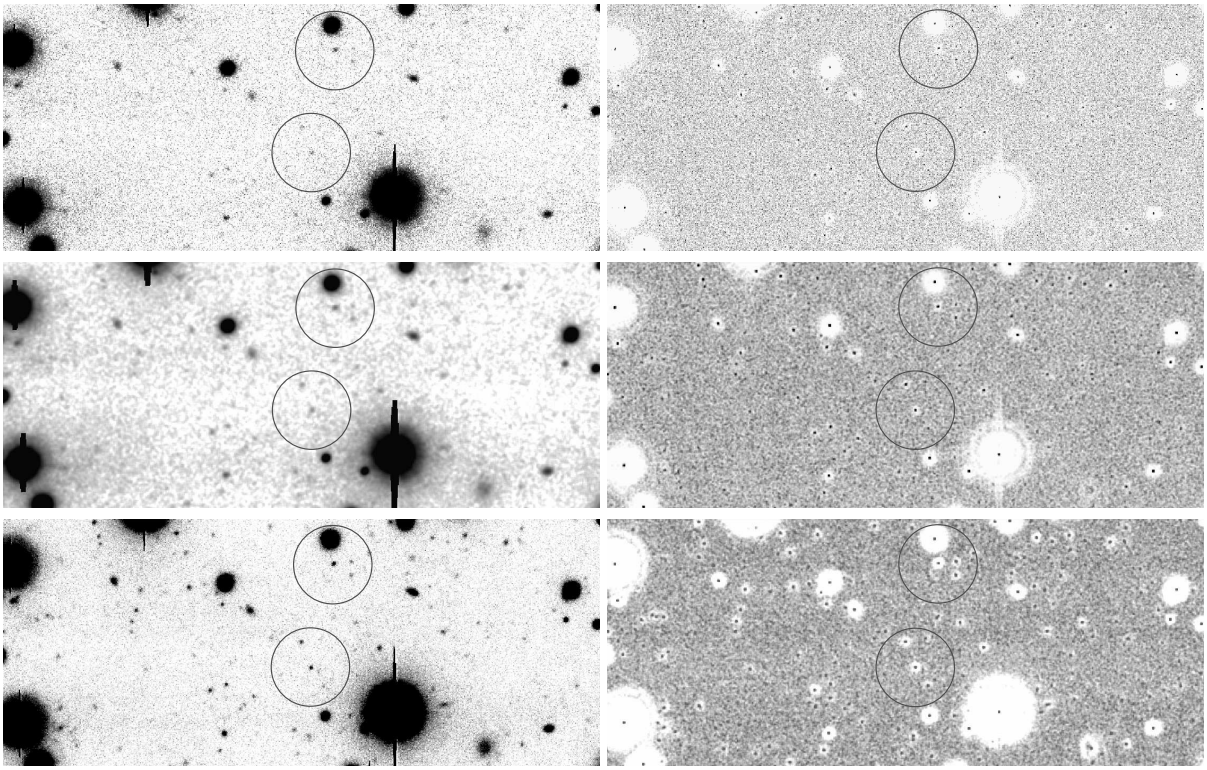

FIGURE 4.6— *(Left, top to bottom:)* (1) A region (300×750 pixel^2, 69×172 arcsec^2) of the work-image lbcb.20070222.052035 (110 s, *V* filter, image quality 1″); (2) its convolved image; (3) the *V* stack image (mapped by 36 exposures). *(Right, top to bottom:)* (4) the peak map; (5) the 3×3 overbinned peak map; and (6) the 3×3 overbinned *B*-filter peak map. This region contains two M 67 white dwarfs (marked with circles in all the panels). The centermost white dwarf has a calibrated *V* magnitude of 24.1, and marks the end of the white-dwarf cooling sequence. It generates a peak in 31/36 exposures in the *V* filter, and in 49/56 exposures in the *B* filter.

objects. This overbinning is necessary because very faint sources do not always fall in the same pixels on the peak map (in other words it can happen that, due to noise fluctuations, the brightest pixel of a faint source might not be the at the location predicted by the PSF, but instead in one of its neighbors).

In Fig. 4.6 we show a region of the FoV (~300×750 pixel^2, ~69×172 arcsec^2) as imaged by, from top to bottom: (1) the work-image lbcb.20070222.052035 (110 s, *V* filter, image quality 1″); (2) its convolved image (clearly smoothed with respect to the work-image); (3) the *V* filter stack image (this particular region is mapped by 36 individual exposures); (4) the peak map; (5) the 3×3 overbinned peak map for the *V* filter; and (6) the the 3×3 overbinned peak map for the *B* filter, showed for completeness (for the *B* filter, this region is mapped by 56 individual exposures). It is clear that, thanks to the 3×3 overbinning, in both peak maps the faintest sources are better highlighted with respect to the peak map alone. The two sources marked with open circles are M 67 white dwarfs, and the centermost one, with a calibrated *V* magnitude of 24.1, marks the end of the WD CS. These two stars are barely visible in the single exposure, but they are easily detectable in the 3×3 peak maps. The faintest white dwarf is able to generate a peak in 31/36 *V* exposures and in 49/56 in the case of the *B* exposures.

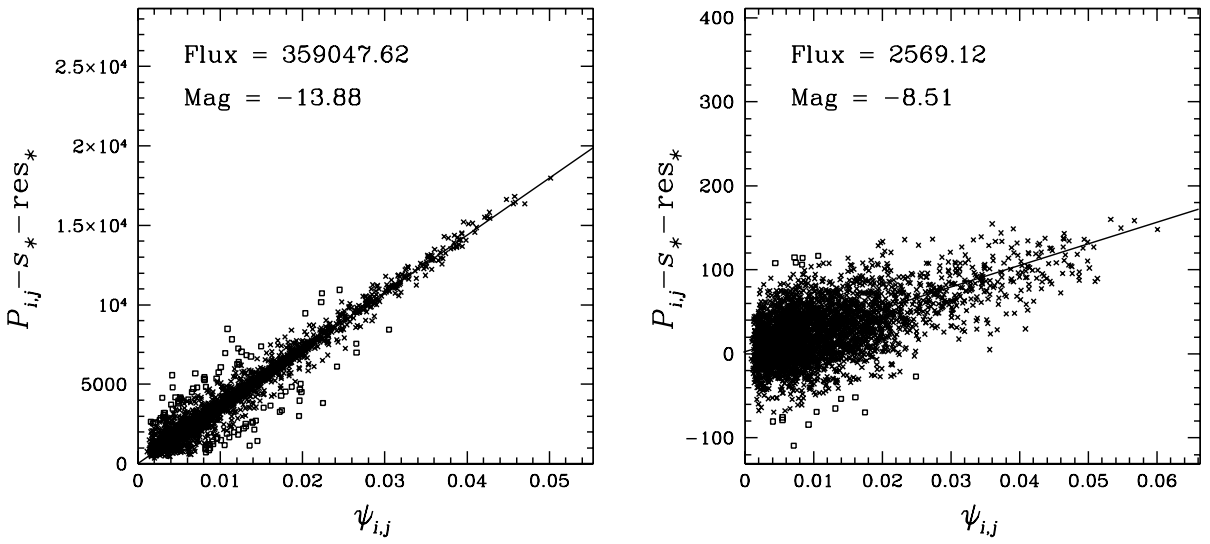

FIGURE 4.7— *(Left:)* A plot of observed pixel values (sky and background-residual subtracted) against PSF values ($\psi_{i,j}$) for a bright star of instrumental *B* magnitude −13.88. The slope of the fit provides the source flux. Open squares are the points that were rejected from the fit. *(Right:)* Same for a faint WD (instrumental magnitude -8.51). See the text for details.

Analyzing the peak map

It is clear from Fig. 4.6 that the 3×3 peak maps, especially the *B* filter one, are able to highlight very faint objects in individual exposures, therefore we used this *B*-filter overbinned peak map to generate our faint-source list.

We adopted a two-parameters algorithm. In order to be included in our initial list, a source has to (1) generate a peak which value representing at least a 3.2σ detection, where σ is the local sky noise, and (2) be at least 5 pixels away from any more significant source. These parameters were carefully chosen as a balance between including the highest possible number of genuine sources, without including too many artifacts. Moreover, we also wanted to reject a peak if it is found at a location mapped by less then 10 individual exposures.

With a background of ∼19.6 counts in the central part of the overbinned peak map (mapped by 56 exposures), a 3.2σ detection means that a peak needs has to have no less than 34 counts in order to be included in our list. In other words, that peak generates a local maximum in ∼60% its mapping images. Lowering this threshold would dramatically increase the noise contribution to our sample. The second condition naturally rejects PSF artifacts found around bright stars.

The above strategy resulted in a list of 131 657 sources. For each source, we have a position in the reference frame, based on the centroid of the found peaks. All of these peaks went forward to the photometry stage. Note that we explored also different ways of deriving the above source list (as done in Anderson et al. 2008), but we found the use of the peak map to be the best solution.

Raster photometry

We initially tried doing photometry on the stacked images, but the combination of images, with such different image-quality conditions and PSF shapes, used to construct the stacks resulted in a CMD with broader (i.e., with larger photometric errors) M 67 sequences with respect to the ones obtained with the first passage photometry. We therefore made all our final measurements on the individual work-images.

To measure sources that were too faint to see in a single exposure, we collected all the information for a given

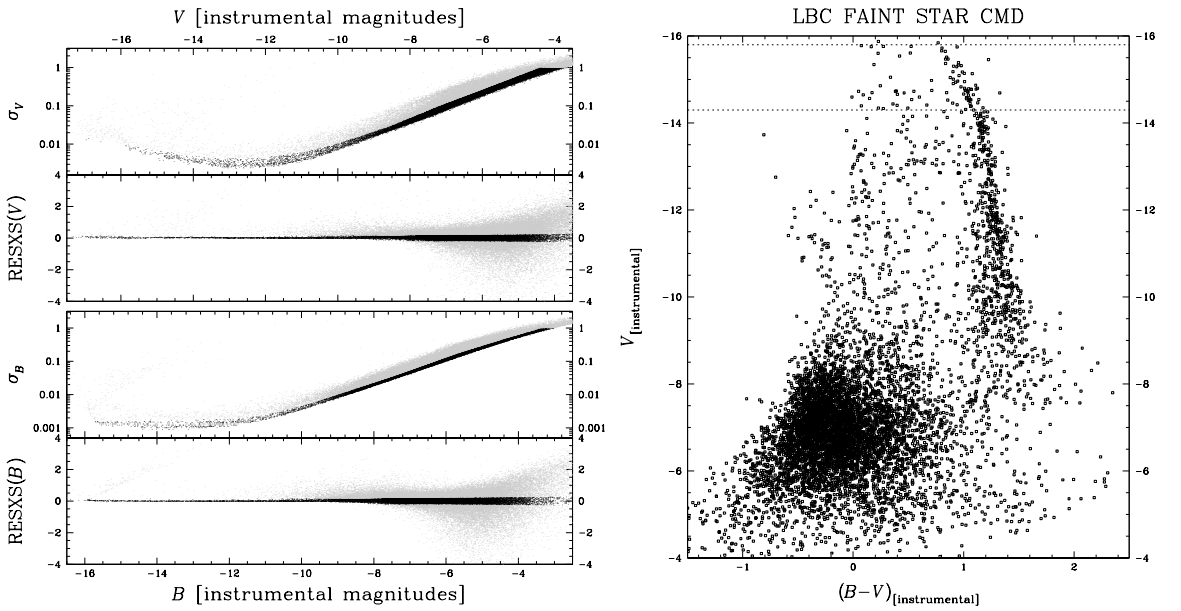

FIGURE 4.8— *(Left:)* σ_V and RESXS(V) versus V magnitude (on top). Selected stars, according to their photometric quality and shape parameter, are marked in black. We show the same for B magnitude in the bottom panels. *(Right:)* CMD of all the sources found in our peak-based finding scheme: the selected ones with open black squares, the rejected ones with grey dots. Horizontal lines mark saturation limits for the best and the worst exposure (as in Fig. 4.3).

source, individually in each of the two filters, as follows. We used positional transformations to calculate the GD corrected position of the source in each individual exposure, and extracted a 11×11 array of pixels (raster) around its centermost one. Because the four chips have different zero points, and the image quality is different from one image to the other, we corrected each raster (sky subtracted) to the photometric zero point of the master frame. Each saturated pixel was flagged and not used. Out of the 121 raster pixels of each exposure, we used only the 79 within r=5 pixels from the central pixel. Therefore, we have 79×56=4424 such pixel values in the best case of maximum image coverage for the B filter (3476 in the case of the V filter), down to 79×10=790 values for the worst case scenario.

As seen in Sect. 4.2.1, our PSF model tells us the fraction of the star's light that is expected to fall in a pixel centered at an offset $(\Delta x, \Delta y)$ from the star's center. The flux in each pixel (i, j) in each exposure n is therefore described by:

$$P_{i,j,n} - s_{*,n} = f_* \cdot \psi_{i,j,n} \tag{4.3}$$

where f_* is the star's flux, $s_{*,n}$ is the sky value (as calculated in Sect. 4.2.1), and $\psi_{i,j,n}$ is the fraction of light that should fall in that pixel, according to the PSF model. [Note that the PSF is defined at each spatial location of each individual exposure.] This is the equation of a straight line with slope f_* and a null intercept (note that our rasters are already sky subtracted).

We fit the flux f_* for each star by a least-square fit to all the pixels, taking into account the expected noise in each pixel. We iteratively rejected the points that were more than 3σ discordant with the best-fitting model.

Unlike Anderson et al. (2008), we did not calculate a further local sky value prior to solve for f_* in equation 4.3; indeed, with a central normalized pixel value of only ∼0.05, star's light is spread all over the raster. Instead, we performed an additional procedure. After we had the first-guess f_* value, we went back into every single raster and we subtracted the quantity $f_* \cdot \psi_{i,j}$ from each pixel $P_{i,j}$. We used the 3σ-clipped average of the 40 pixels between

r=3.5 and r=5 to estimate the background residual res_*. We subtracted from each pixel of raster the corresponding res_*. Finally, we recalculated the star's flux f_* by solving the new equation

$$f_* = \frac{P_{i,j,n} - s_{*,n} - \mathrm{res}_{*,n}}{\psi_{i,j,n}}. \tag{4.4}$$

The formal error of the calculated slope, σ_{f_*} is obtained as:

$$\sigma_{f_*} = \sqrt{\frac{\sum_k (P_{i,j,n} - s_{*,n} - \mathrm{res}_{*,n} - f_* \cdot \psi_{i,j,n})^2}{\sum_k (k-1) \cdot \sum_k \psi^2_{i,j,n}}}$$

where k stands for any available pixel for the fit.

We defined the quantity RESXS (RESidual eXceSs) as the difference between the first-guess and the final determination of f_*, once transformed into instrumental magnitude values. For a given source, RESXS>0 implies either that its light distribution is more spread with respect to a point-light source, or that there is a not negligible light contamination from close sources[7]), while RESXS<0 means that the source's light is more concentrated than expected, and it could probably be a noise peak.

Fig. 4.7 shows how the set of pixels for a star is fit by the PSF model. The tight linear relation for the bright star (instrumental magnitude −13.88) on the left panel shows that our PSF model is very accurate and also that our astrometric and photometric transformations are able to properly relate each pixel in each exposure to the model[8]. This demonstrably good fit for the bright stars means that we can trust our model to measure accurate fluxes for the fainter stars. The star on the right is a M 67 faint white dwarf (instrumental magnitude −8.51).

Left panel on Fig. 4.8 shows σ_V and RESXS(V) versus the raster photometry in the V magnitude (top two panels), while σ_B and RESXS(B) versus the B magnitude are shown in the bottom two panels. We drew cutting lines (by eye) to isolate best measured sources (plotted in black). Rejected sources are drawn in grey. The right panel of Fig. 4.8 shows the V vs. $B-V$ CMD of all the so-selected sources. Horizontal lines mark saturation limits for the best and the worst exposure (same as in Fig. 4.3). It is clear from the CMD on Fig. 4.8 that, thanks to the second passage photometry, we were able to recover reliable photometry down to instrumental magnitude $V\sim-6$. Moreover, it seems to be almost possible to follow M 67 main sequence down to its end, i.e. down to the hydrogen-burning limit.

In our selections (left panel of Fig. 4.8), we tried to keep only the best-measured star-like sources. Still, a huge number of objects (mostly blue galaxies) are collected together in the CMD in the same location of the faint WDs. These sources are small enough to be almost unresolved (given the pixel/scale of 0.″231 of LBC), therefore selections based on photometric properties are not enough to be able to get rid of them (as done in Anderson et al. 2008). We will show later (Sect. 4.5) how, thanks to high-quality proper motion measurements, we can do an excellent job in isolating all the non-cluster members.

4.2.3 Aperture photometry

As we anticipated at the beginning of Sect. 4.2, in order to measure fluxes also for images with very poor image quality, we performed simple aperture photometry, using an aperture radius of 1.5× the value of the image quality.

We linked star positions and photometric zero points to our master frame. In Fig. 4.9 we show the CMD obtained with short exposures only. Saturation limit is marked by an horizontal dotted line. Despite having images with only 1 s of exposure time for the V filter, and being the star's light seriously blurred (due to poor image quality), M 67 evolved stellar population is mostly saturated.

[7]Note that the second passage photometry does not perform neighbor subtraction.

[8]The points in Fig. 4.7 show a wider spread around the best-fit line, with respect to Fig. 5 of Anderson et al. (2008). Note that here we are dealing with ground-based images affected by a wide range of image-quality conditions, together with a necessarily lesser accuracy in our PSF models and geometric distortion solutions. Therefore, each single pixel contains much less information about the star than in the *HST* case.

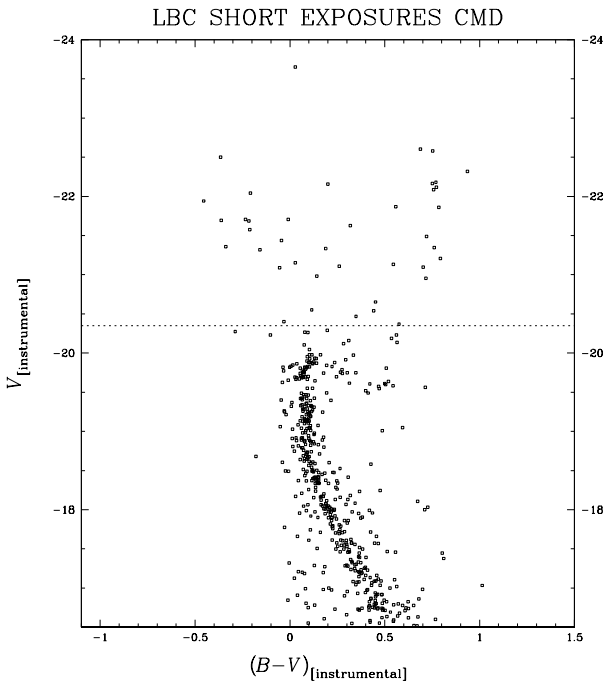

FIGURE 4.9— CMD obtained with short exposures. The horizontal dotted line marks the saturation limit for the *V* filter.

4.3 Photometry of the UH8K@CFHT data set

Photometric reduction of the UH8K data set employed the same techniques developed for the LBC one. For this reason, in the following we will mostly focus on the differences between UH8K and LBC photometric reductions.

As done for the LBC data set, we performed two different reduction methods: (1) the first-passage photometry using img2xym_UH8K (directly derived from img2xym_WFI with very few modifications; and (2) the second-passage photometry, using the same technique developed for the LBC case.

Note that we reduced the UH8K data set mainly to derive proper motions. Because we are focused on recovering star positions and fluxes for the faintest sources (achievable only with the second-passage photometry technique), we asked img2xym_UH8K to measure photometry only for unsaturated stars. Their positions (GD corrected) will be successively used to derive positional transformations from each UH8K exposure/chip to our LBC master frame.

4.3.1 First-passage photometry

The UH8K chip size (2K×4K pixels) and the 4×2 mosaic layout makes it straightforward to adapt the img2xym_WFI software for the UH8K case. There are though some differences. To start, chip ID position in the focal place is different with respect to WFI. From left to right and from top to bottom they are: 2, 3, 5, 4, 0 ,1, 7, 6 (for comparison, in the case of the WFI@2.2m they are: 1, 2, 3, 4, 8, 7, 6, 5). Moreover, chips 2, 3, 5, 4 appear "upside down" as compared to chips 0, 1, 7, 6. Some chips has a digital saturation limit of $\sim 2^{15}$ counts. For convenience (since we are not interested to bright stars), we adopted a saturation-limit value of 30 000 counts for the whole mosaic.

Note that chip # 2 and chip # 4 are seriously affected by charge-transfer inefficiency (CTI), that causes pixel charges to be captured in traps, and slowly released in different locations along the pixel-reading column during the read-out process. The main effect of CTI is to smear source light along the *y* axis, making their precise position

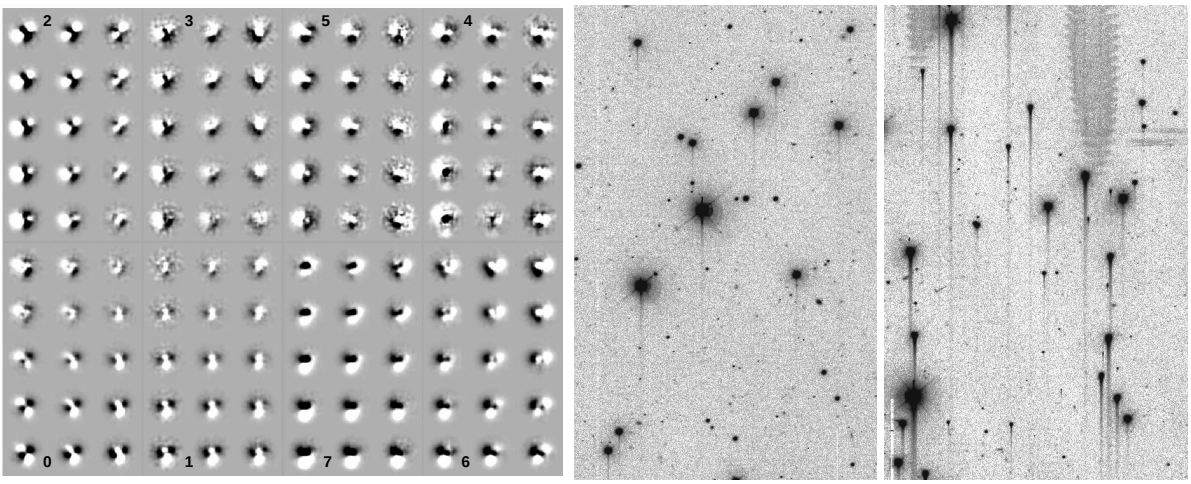

FIGURE 4.10— *(Left panel:)* Difference between the local PSF and the average PSF over the entire FoV (as Fig. 4.1). Chip identification numbers are also shown, reflecting their storage position in the original MEF file. *(Right panels:)* Example of CTI for chip # 2 and # 4, respectively. Enlargement, color code, and scale are the same for the two chips. Note that chip # 4 looks also somehow scratched.

(and flux) harder to measure.

Standard pre-reduction procedures were applied, as done for the LBC data set, as well as pixel-area correction, for which we used UH8K GD correction obtained by mean of the same technique adopted the LBC case. Specifically, we derived a set third-order polynomials for each filter and for each UH8K chip individually, using our LBC master frame as distortion-free reference frame. [Note that the UH8K exposures have small dithers, making it impossible to autocalibrate a GD correction.] Our relative solution is accurate enough (~0.05 pixels in each coordinate) to univocally link each measured source to the master frame using general six-parameters linear transformations. Finally, we put the pre-reduced chips into a meta-fits file, of 8500×8500 pixels, as done for WFI in Paper I.

The derivation of the PSFs has been performed on the deep exposures (1200 s) of both filters, following the prescription of Paper I, and explained in details for the LBC data set (see Sect. 4.2.1). We kept the same PSF-modeling scheme of WFI, with 3×5 PSFs each chip, for a total of 120 PSFs. As done for LBC, we carefully avoided to use galaxies in modeling PSFs. Left panel of Fig. 4.10 shows the differences of the 120 fiducial PSFs with respect to the average PSF of the whole FoV, in the case of the best available 1200 s *V* exposure (archive name 382368o, image quality 0.″74). Chip-identification numbers, from 0 to 7, are also shown. Right two panels of Fig. 4.10 show a portion of chip # 2 and chip # 4, respectively. Note the effects of CTI, especially on chip # 4.

Star positions and fluxes were measured with img2xym_WFI (Paper I). This software works in the same way as img2xym_LBC (Sect. 4.2.1), and it is fully documented in Paper I. We asked the software to measure every source with at least 10 counts (sky subtracted) in its inner 3×3 pixels, at least 4 pixels away from brighter neighbors. Because the aim of the UH8K data set is to provide proper motions for faint objects, we did not required the software to extract photometry also for saturated stars.

At the end of the iteration process, the software produces a catalog of position and fluxes for all the detected sources, individually for each chip of each exposure, containing the following information for every measured source: raw and GD corrected coordinates; instrumental magnitude; total flux in DNs; QFIT; and the iteration number at which a source is detected.

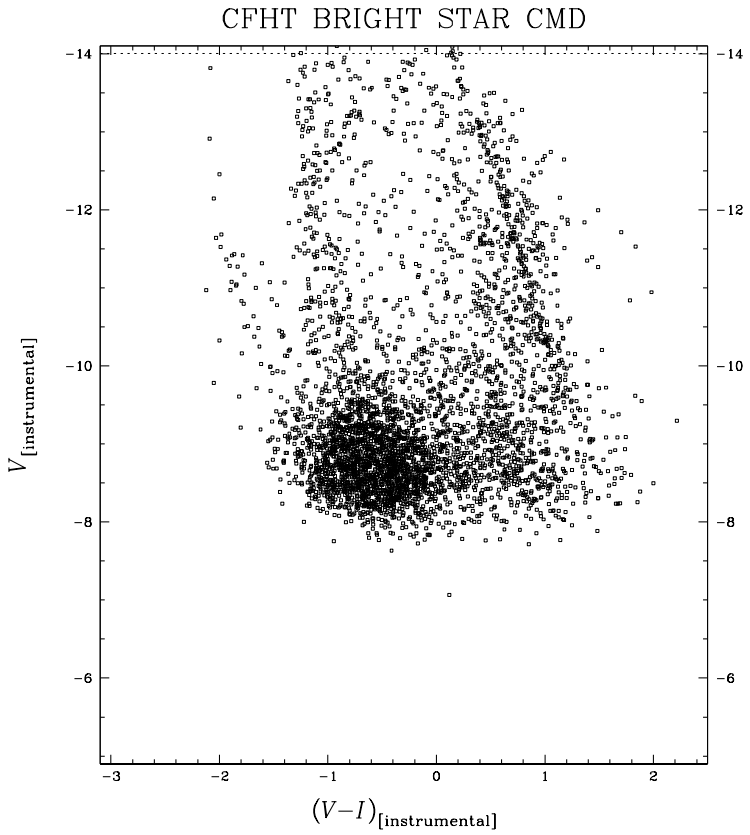

FIGURE 4.11— CFHT V vs. $V-I$ CMD from the first passage photometry. Saturation starts at $V\sim-14$ (dotted line).

4.3.2 Second-passage photometry

Once we possess a list of source positions for every chip/exposure, we can use them to derive general six-parameters linear transformations between each chip list and the LBC master frame. UH8K V exposures were linked to the master frame, each chip individually, in order to to register also the photometric zero points to the same photometric LBC V reference frame. For I-filter exposures, photometric zero points of each UH8K chip were registered to the Paper II I-filter photometric catalog, while we linked astrometric positions of all the detected sources to our LBC master frame.

Fig. 4.11 shows the CMD obtained for the bright sources, collected in our UH8K master lists. Saturation limit (dotted line) starts at instrumental magnitude $V\sim-14$. As for the LBT bright CMD (Fig. 4.3), also in the case of the bright CFHT CMD there is a conspicuous number of objects collected along the lower part of the WD CS. Moreover, the cluster MS is overimposed to field MS stars.

Raster photometry (each filter individually) on the UH8K data set has been performed in the very same way as for the LBT data set. For every source in the list obtained from the LBT B-filter peak map (see Sect. 4.2.2), and for each chip/exposure individually, we extracted a 11×11 pixels raster around its centermost pixel. As for LBC rasters, we corrected each raster pixel (sky subtracted) with the respective zero point of its chip. We then used the proper PSF to calculate pixel fluxes for each raster of each source, in order to solve for equation 4.3. We subtracted the quantity $f_* \cdot \psi_{i,j}$ from each pixel of each raster, to estimate the background residual res_*. Finally, we solved equation 4.4 to get source fluxes, with their formal errors, and derived RESXS as the difference between the fluxes

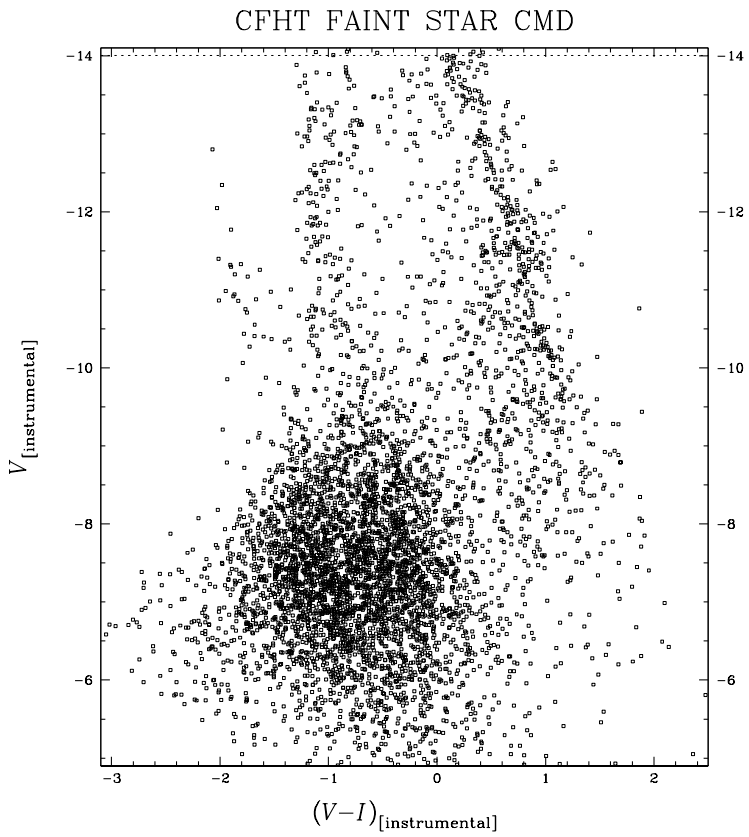

FIGURE 4.12— As in Fig. 4.11, but for the second-passage photometry. Note that the y-axis scale is the same as in Fig. 4.11.

obtained from equation 4.3 and 4.4.

Fig. 4.12 shows the CMD obtained with the second-passage photometry. A dotted line marks the V saturation limit. It is clear from the figure that our second-passage photometry succeeds to recover almost all the faintest M 67 stars also for the UH8K data set.

4.4 Photometric calibration

Photometric calibration was performed using the stars in the Paper II photometric catalog as secondary standards. To register LBC *BV*-Bessel instrumental photometry onto the *BV*-Johnson system of Paper II is not a simple procedure. We can't simply use linear photometric equations (like in Paper III, see their Fig. 4). Indeed, we found that photometric differences (in both bandpasses) with respect to the calibrated $B - V$ color, can be interpolated with third-order polynomials.

In Fig. 4.13 we show these polynomial fits. We considered only unsaturated, well-exposed stars in common between our instrumental catalog and the Paper II one. From top to bottom, the three panels in Fig. 4.13 show, for such common stars, the magnitude differences: $B_{\rm PaperII} - B_{instr.}$, $B_{\rm instr.} - V_{instr.}$ and $V_{\rm PaperII} - V_{instr.}$ with respect to their calibrated $B - V$ color, with error bars.

Polynomial fits were performed by mean of weighted-least-square fits, using photometric errors to estimate weights. For the $B_{\rm instr.} - V_{instr.}$ and $V_{\rm PaperII} - V_{instr.}$ case, the curve is monotonic in the color interval of interest,

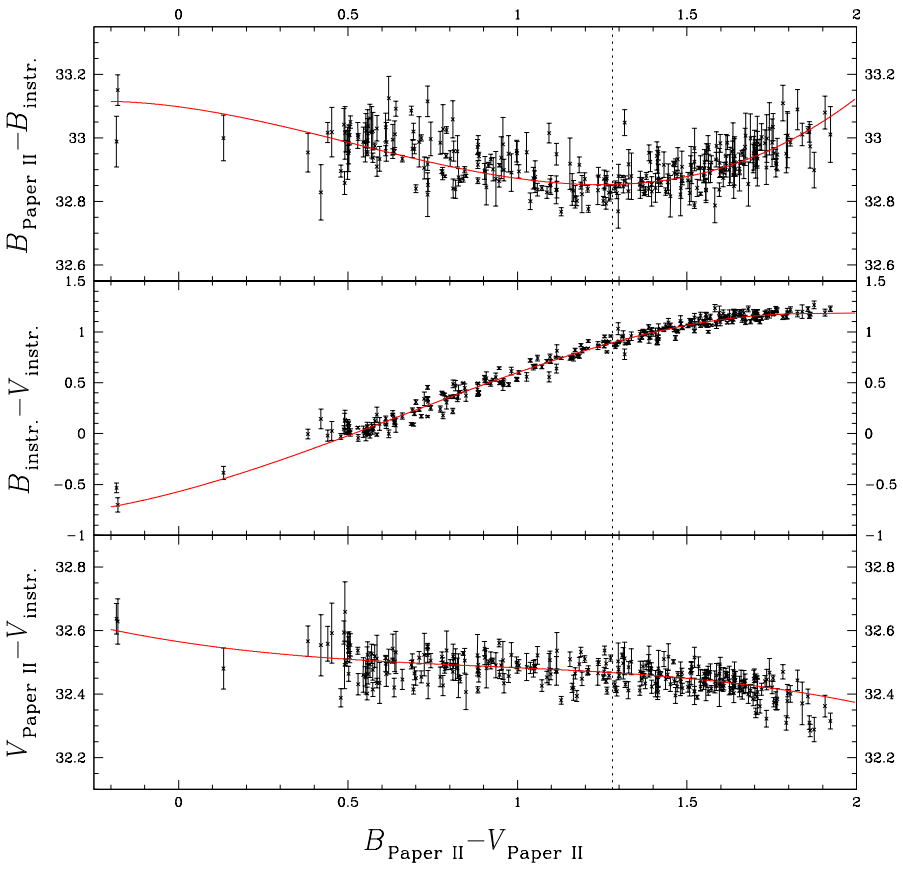

FIGURE 4.13— Calibration fits used to bring LBC $B_{\rm Bessel}$ and $V_{\rm Bessel}$ instrumental magnitudes onto the *BV* Johnson photometric system. See the text for details.

while at $B-V$=1.28 the curve present a minimum for the $B_{\rm PaperII}-B_{instr.}$ case. To avoid color degeneracy during the calibration process, we treated stars with $B-V\leq$1.28 and $B-V>$1.28 separately.

Once polynomial coefficients are obtained, for all the three curves shown in Fig. 4.13, we can calibrate our instrumental magnitudes in the following two-step procedure: for each star, we started with its instrumental color, and we found the respective calibrated one (middle panel). We then calculated the proper ΔB and ΔV magnitude with which to correct instrumental B and V photometry (top and bottom panels). Now that we have a first-guess-calibrated photometry, we iterated the second of this two-step procedure four, in order to improve our estimates of B and V in the calibrated Johnson system. We note that the magnitude differences between the magnitude as computed with the third and the fourth iteration were negligible, for both filters.

Since both UH8K@CFHT and the WFI@2.2m uses an *I*-band filter with a very similar characteristic (both resembling $I_{\rm Kron-Cousin}$), to calibrate our UH8K *I*-band photometry we proceeded in the following way. We compared star magnitudes for each individual UH8K chip with their counterparts in the Stetson secondary-standard catalog, and derived a zero-point correction per each UH8K chip. We verified that the linear color-term for the *I* filter was negligible: we plotted the magnitude differences ($I_{\rm Stetson}-I_{\rm instr.}$) vs. ($V^{\rm LBC}_{\rm calib.}-I_{\rm Stetson}$) and we derived a least-squared straight-line fit. The color-term obtained in this way was of the order of few parts per 10 000 for $V-I$ magnitude.

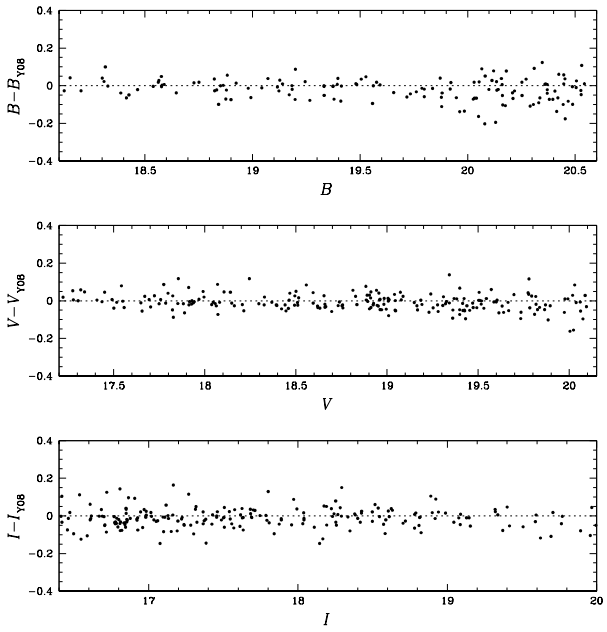

FIGURE 4.14— Magnitude differences between our photometry and the one presented in Yadav et al. (2008) catalog (indicated here with the subscript Y08) for the sources in common. From top to bottom, $B - B_{Y08}$ vs. B, $V - V_{Y08}$ vs. V, $I - I_{Y08}$ vs. I, respectively.

As a final test, in Fig. 4.14 we show, for common sources, the differences in magnitude between our *B*, *V*, *I* unsaturated photometry and the one published in Paper II.

4.5 Proper-motion measurements

Proper motions were obtained as described in Paper I. From the initial target list obtained from the peak map, we selected only those sources with a measure in all the LBC *V* and *B* and the UH8K *I* filters. This list is then used to calculate displacements between the two epochs, as follows.

We measured a chip-based flux and GD-corrected position using PSF-fitting for each object in the list in each chip of each exposure where it could be found. Then we organized the images in pairs of images from each epoch. For each object, in each pair, we computed the displacement (in the reference frame) between where the first-epoch predicts the object to be located, after having transformed its coordinates on the reference-frame system, and its actual-observed position in the second epoch image. Multiple measurements of displacements for the same object are then used to compute average displacements and rms.

It is clear that, in order to make these displacement predictions, we need a set of objects to be used as a reference to compute positional transformations between the two epochs for each source. The cluster members of M 67 are a natural choice, as their internal motion is within our measurement errors (~0.2 mas yr^{-1} Girard et al. 1989), providing an almost rigid reference system with the common systemic motion of the cluster.

We initially identified cluster members according to their location in the LBC *V* vs. $B - V$ color-magnitude diagram. By predominantly using cluster members, we ensure proper motions to be measured relative to the bulk motion of the cluster. We iteratively removed from the member list those objects with a field-type motion even though their colors may have placed them near the cluster sequences. During our iterations, we considered as cluster members all sources whose displacement is within 0.15 LBC pixels in 10.13 yr from the cluster mean

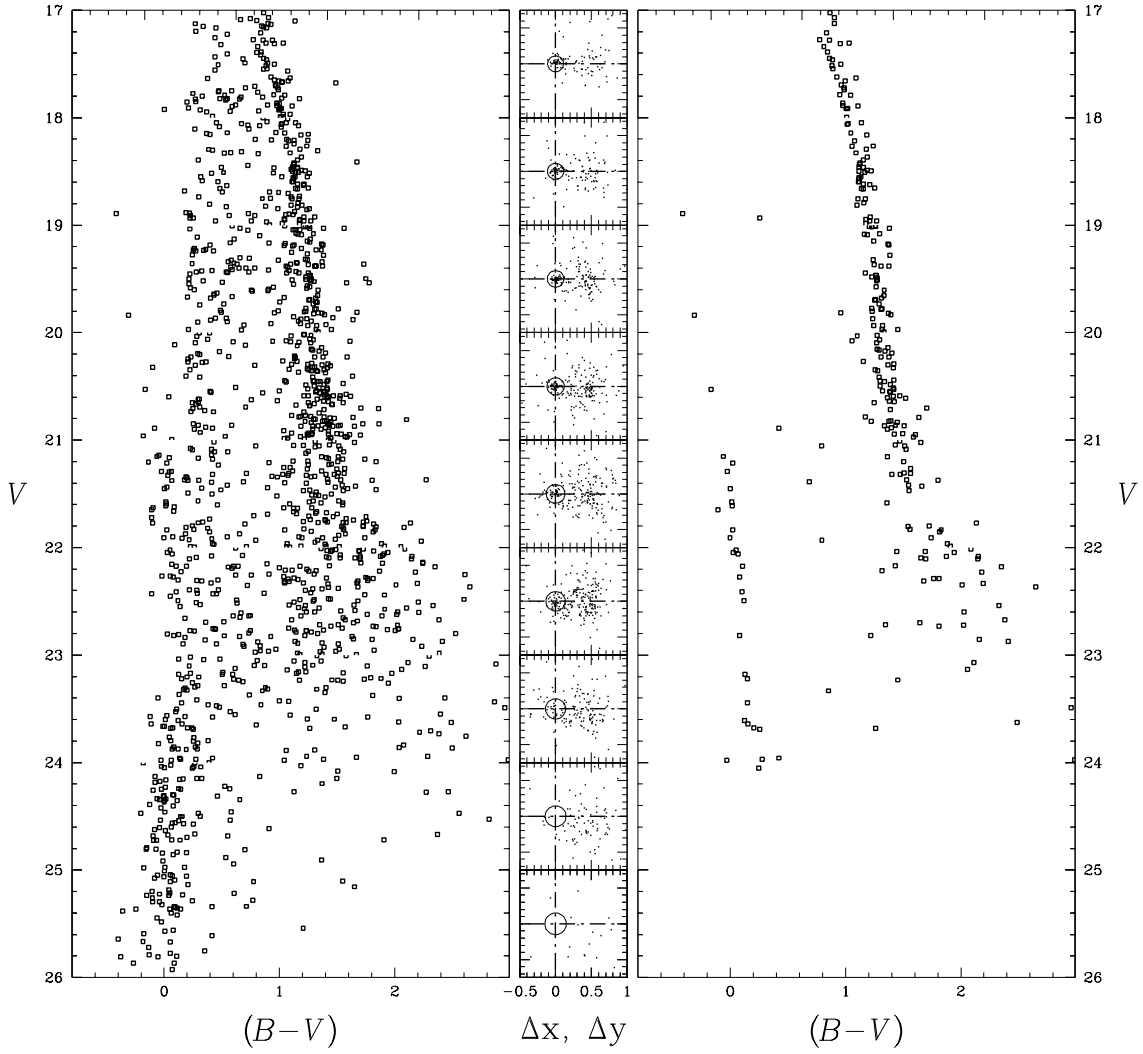

FIGURE 4.15— Left panel shows the CMD V vs. $B - V$ of all selected sources as plotted in Fig. 4.8 for which we have at least two individual displacement measurements. Middle panels show, for each magnitude bin, the VPD of the displacements in units of pixels per 10.13 year. The cluster mean motion is at the axes origin. In each bin, we considered as cluster members all stars within the circle of increasing radius, from top to bottom, from 0.11 to 0.15 pixels. The corresponding CMD for M 67 cluster members is plotted on the right.

motion[9]. We found this value to be the best compromise between losing (poorly measured) M 67 members and including field objects.

In order to minimize the influence of any uncorrected GD residual, proper motions for each object were computed using a local sample of members; specifically the 25 (at least) closest ($r<3'$), well-measured cluster stars (see Paper I for more details). Note that, in order to maximize the cluster-field separation, we used all the available images, in each filter, in both epochs. Our list of reference cluster members converged after three iterations. We iterated one more time and found negligible improvements in the measure of proper motions.

Finally, we corrected our displacements for atmospheric differential chromatic refractions (DCR) effects, as done in Papers I, III. The DCR effect causes a shift in the photocenter of sources, which is proportional to their wavelength, and a function of the zenithal distance: blue photons will occupy a position that differs from that of red photons. Unfortunately, within each epoch, the available data sets are not optimized to perform the DCR correction directly. We can, however, check if possible differences in the DCR effects between the two epochs could generate an apparent proper motion for blue stars relative to red stars.

We selected two samples of cluster member stars, one made by WDs in the magnitude interval $20<V<23$, and the other on the MS, within the same magnitude interval. For each sample, we derived the median $B-V$ color and the median proper motion along the X and Y axes, with dispersion obtained as the 68.27^{th} percentile around the median. We used a linear fit to derive the DCR corrections along both axes, as done in Papers I and III. We found that DCR corrections were always below 0.7 mas yr^{-1} $(B-V)^{-1}$.

Left panel of Fig. 4.15 shows the CMD V vs. $B-V$ of all selected sources as plotted in Fig. 4.8 for which we have at least two individual displacement measurements. Middle panels show, for each magnitude bin, the vector-point diagram (VPD) of the displacements in units of pixels per 10.13 year. The cluster mean motion is at the axes origin. In each bin, we considered as cluster members all stars within the circle of increasing radius, from top to bottom, from 0.11 to 0.15 pixels. The corresponding CMD for M 67 cluster members is plotted on the right. The MS and the WD CS are now well defined. Note that there are no cluster members fainter than $V\sim 24$.

4.6 Applications

Our proper motion catalog can be very useful to provide bona-fide cluster members for spectroscopic follow-ups. We are presently collaborating with Kurtis Williams and Michael Bolte in a project related to the spectroscopic analysis and characterization of M 67 WDs. Thanks to this collaboration, I went observing with them at Keck 1 for two nights with LRIS, the Low-Resolution Imaging Spectrometer. By chance, the second night observers at Keck 2 asked us to obtain a spectrum for a new GeV source discovered by the Fermi Large Area Telescope. Thanks to this fortuitous event, I'm a co-author of an ApJ Letter recently accepted for publication (Vanderbroucke et al. 2010).

Providing finding charts and membership probability for spectroscopic follow-ups are obviously not the only usefulness of our M 67 proper-motion faint-stars catalog. Indeed, for the first time, it is now possible to perform a direct, detailed analysis the WD CS of this cluster (which is actually the main purpose of our LBT SDT proposal), and derive its absolute proper motion. In the next two Chapters, we will address these two topics.

Bibliography

Anderson, J., & King, I. R. 2000, PASP, 112, 1360
Anderson, J., Bedin, L. R., Piotto, G., Yadav, R. S., & Bellini, A. 2006, A&A, 454, 1029, (Paper I)
Anderson, J. et al. 2008, AJ, 135, 2055
Bellini, A., & Bedin, L. R. 2009, PASP, 121, 1419
Bellini, A., et al. 2009, A&A, 493, 959, (Paper III)

[9]Since we used M 67 star members as reference to compute displacements between the two epochs, the origin of the coordinate coincides with the M 67 mean motion.

Bellini, A. & Bedin, L. R. 2010, A&A accepted, arXiv:1005.0848 (Paper IV)
Bellini et al. 2010, A&A 513, A50 (2010a)
Bellini, A., Bedin, L. R., Pichardo, B., Moreno, E., Allen, C., Piotto, G., & Anderson, J. 2010, A&A, 513, A51 (2010b)
Giallongo, E., et al. 2008, A&A, 482, 349
Girard, T., Grundy, W., Lopez, C., & van Altena, W. 1989, AJ, 98, 227
Vandenbroucke, J., et al. 2010, ApJ Letters accepted, arXiv:1004.1413
Yadav, R. K. S., Bedin, L. R., Piotto, G., Anderson, J., Villanova, S., Platais, I., Pasquini, L., Momany, Y., & Sagar, R. 2008, A&A, 484, 609, (Paper II)

chapterThe end of the white dwarf cooling sequence in M 67

In this Chapter we analyze the white dwarf (WD) cooling sequence (CS) of the old Galactic open cluster M 67. This direct study of the faintest WDs of this cluster is now possible, for the first time, thanks to our wide-field proper motion measurements (see Chapter 4). This Chapter contains results published in *Astronomy & Astrophysics* (Bellini et al. 2010a).

4.7 Introduction

The WD CS lies in one of the most unexplored parts of the color-magnitude diagram (CMD) of star clusters. In a recent deep photometric investigation of the metal rich open cluster NGC 6791, Bedin et al. (2005; 2008a,b) discovered an unexpectedly bright peak in its WD luminosity function (LF). This result raises questions about our understanding of the physical processes that rule the formation of WDs and their cooling phases. It is clear that, in order to improve our current understanding of WDs, in particular at high metallicities, we need to fill the age-metallicity parameter space of stellar clusters with new data.

Unfortunately, most of the metal-rich old open clusters for which the end of the WD CS is potentially reachable are relatively sparse. Because of this, the limited field of view of Hubble Space Telescope (*HST*) cameras allows us to cover only a small fraction of a single cluster, which implies that a very limited number of WDs can be observed.

The dispersion of the cluster stars over a large field has the additional inconvenience of a strong contamination of all of the evolutionary sequences in the CMD by foreground/background objects. The two wide-field imagers (WFIs) at the two prime foci of LBT provide us with a unique opportunity to overcome the field size problem. Moreover, the availability of multi-epoch imaging allows us to measure proper motions, thus alleviating the issue of field contamination.

Note that, although (in principle) it would be possible to entirely map an open cluster as large as M 67 with *HST*, during its 19 years of activity these kind of projects have never been approved. For reference, in the case of M 67 it would be necessary a minimum of ∼40 orbits – per epoch – to map the inner ∼20×20 arcmin^2, taking into account for: dump-buffer overheads, intra-orbit pointing limitations, and the necessity to have multiple exposures with large dithers. For practical reasons, for nearby clusters, ground-based telescopes with wide field of view (FoV) are more appropriate to achieve this purpose, and at much cheaper costs.

In this Chapter, we present a pioneering work on this subject. For the first time, we used wide-field astrometry and deep photometry to obtain a pure sample of WDs in the open cluster M 67 [$(\alpha,\delta)_{J2000.0}$=($8^h51^m23\overset{s}{.}3$,+11°49′02″), Yadav et al. (2008)]. First epoch photometry from a WFIs is available only from a 4m class telescope, and our LBC@LBT images were not acquired in optimal conditions. Yet we have been able to reach the end of the WD CS, remove field objects by using proper motions, and demonstrate the potentiality of a WFI (particularly if mounted on a 8m class telescope) for the WD study.

A WD study of M 67 was already published by Richer et al. (1998, hereafter R98) using the same data set that we use here as first epoch images. R98 could not directly see the end of the WD CS, because of the strong contamination by background field galaxies, but they could infer its location by a statistical analysis of star counts around the region in the CMD where the WDs are expected to be. The great news presented in this investigation is that we can now remove most of the field objects and present a clean WD CS down to its bottom.

4.8 Observations

We used as first-epoch data a set of images collected on January 10–13, 1997 at the CFHT 3.6m telescope. This data set (a sub-set of those used also by R98) consists of 15×1200 s *V*-band, and 11×1200 s *I*-band images, obtained with the UH8K camera (8 CCDs, 2K×4K pixels each, in a 4×2 array). Two chips (# 2 and 4) of this camera are seriously affected by charge transfer inefficiency. As a consequence, the FoV suitable for high precision

TABLE 4.2— Log of M 67 data used in this work.

Filter	#Images×Exp. time (s)	Airmass (sec z)	Seeing (arcsec)
UH8k@CFHT (First Epoch: 10–13 Jan 1997)			
$V_{\rm Johnson}$	15×1200	1.02–1.50	0.74–1.37
$I_{\rm Johnson}$	11×1200	1.02–1.70	0.75–1.26
LBC@LBT (Second epoch: 18 Feb–16 Mar 2007)			
$B_{\rm Bessel}$	56×180	1.07–1.14	0.79–1.88
$V_{\rm Bessel}$	1×15, 25×100	1.07–1.10	0.68–1.26
	17×110, 1×330	1.07–1.12	0.62–1.31

measurements is reduced to only six chips (for a total sky coverage of ∼400 arcmin^2). [We will see that none of our WDs fall within those detectors.] The median seeing is 1.″0.

The second epoch data, collected between February 16 and March 18, 2007, consists of 56×180 s *B*-band, and 1×15 s, 25×100 s, 17×110 s, 1×330 s *V*-band images, obtained with the LBC-blue camera (4 CCDs, 2K×4.5K pixels each, 3 aligned longside, one rotated 90° on top of them, FoV of ∼24′×25′, see Giallongo et al. 2008). This data set is not optimal: the original project consists in a set of 25×180s *B* and 25×110s *V* images for science purposes, plus 25×100s *V* images to solve for the geometric distortion (hereafter GD). All 100 s *V* images have anomalously high background (∼20 000 digital numbers (DNs) instead of an expected ∼3000). The median seeing is 1.″0 for the *V* filter, and 1.″3 for the *B* one. See Table 1 for the complete log of observations.

4.9 Measurements and Selections

We successfully exported our data reduction software developed for *HST* images (Anderson et al. 2008), adapting it to the case of ground-based WFIs. Below, we briefly describe our 3-step procedure, used on both LBC and UH8K data sets.

4.9.1 First step

We used the software described in Anderson et al. (2006) to obtain spatially varying empirical PSFs (in an array of 3×7 each chip for LBC, and in an array of 3×5 for each UH8K chip), with which we measured star positions and fluxes in each single chip of each individual exposure. We then corrected LBC raw positions for GD according to Bellini & Bedin (submitted). In a nutshell, we modeled the GD with a third-order polynomial, for each LBC chip independently. For each *i*-star in each *k*-chip, the distortion corrected position $(x^{\rm corr}_{i,k}, y^{\rm corr}_{i,k})$ is obtained as the observed position $(x_{i,k}, y_{i,k})$ plus the distortion correction $(\delta x_{i,k}, \delta y_{i,k})$:

$$\left\{ \begin{array}{rcl} x^{\rm corr}_{i,k} & = & x_{i,k} + \delta x_{i,k}(\tilde{x}_{i,k}, \tilde{y}_{i,k}) \\ y^{\rm corr}_{i,k} & = & y_{i,k} + \delta y_{i,k}(\tilde{x}_{i,k}, \tilde{y}_{i,k}), \end{array} \right.$$

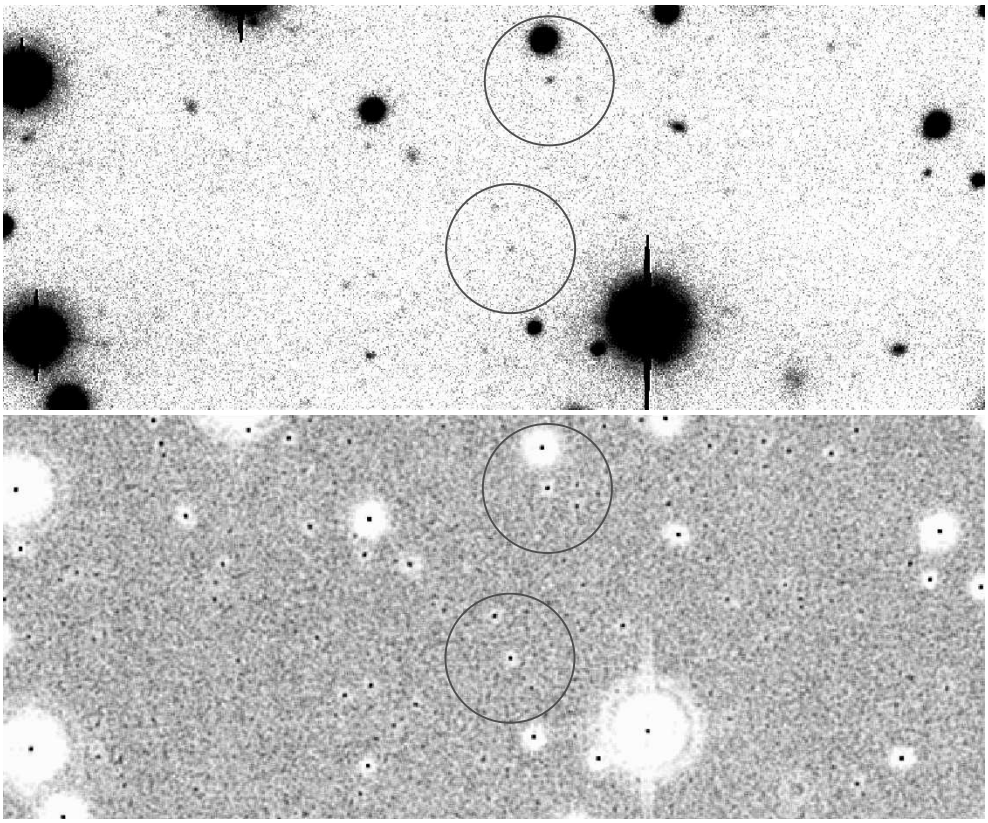

FIGURE 4.16— *(Top:)* A region of a LBT *V* image (110 s exposure, seeing ∼1″, North is up, East is to the left) in which two WDs are present, highlighted by open circles (the southern-most one is also the faintest WD in our sample). *(Bottom):* the same region as seen on our 3×3 overbinned peak map (cfr. also Fig. 4.6). The FoV is ∼170″×70″. See the text for details.

where $\tilde{x}_{i,k}$ and $\tilde{y}_{i,k}$ are normalized positions with respect to the center $(x_\circ, y_\circ)_k$ of the k-chip [assumed to be the pixel (1025,2305) for chips # 1 to 3, and (2305,1025) for chip # 4], and $(\delta x_{i,k}, \delta y_{i,k})$ are given as:

$$\begin{cases} \delta x &= a_1\tilde{x}+a_2\tilde{y}+a_3\tilde{x}^2+a_4\tilde{x}\tilde{y}+a_5\tilde{y}^2+a_6\tilde{x}^3+a_7\tilde{x}^2\tilde{y}+a_8\tilde{x}\tilde{y}^2+a_9\tilde{y}^3 \\ \delta y &= b_1\tilde{x}+b_2\tilde{y}+b_3\tilde{x}^2+b_4\tilde{x}\tilde{y}+b_5\tilde{y}^2+b_6\tilde{x}^3+b_7\tilde{x}^2\tilde{y}+b_8\tilde{x}\tilde{y}^2+b_9\tilde{y}^3 \end{cases}$$

(where we omitted here the subscript "i,k" for simplicity).

The GD solution is therefore fully characterized by 18 coefficients: $a_1, \ldots, a_9$, $b_1, \ldots, b_9$. We constrained the solution so that, at the center of the chip, it will have its x_k-scale equal to the one at the location $(x_\circ, y_\circ)_k$, and the corrected axis $y_k^{\rm corr}$ has to be aligned with its y_k-axis at the location $(x_\circ, y_\circ)_k$. This is obtained by imposing $a_{1,k} = 0$ and $a_{2,k} = 0$, so we are left with only 16 coefficients. Our average correction enables a relative astrometric accuracy of ∼10 mas per coordinate (see Bellini & Bedin for a detailed description of the GD solution derivation, and tables with the polynomial coefficients).

We then used these GD-corrected positions to register all of the LBC single chips into a common distortion-free frame (the master frame), using linear transformations. The transformations were computed using the best sources in the field (bright, isolated, and with a stellar profile). With this GD-corrected master frame we derived the GD correction also for the UH8K camera, by means of the same technique (used also in Bellini & Bedin 2009), and we corrected and registered all first- and second-epoch positions to the LBC master frame.

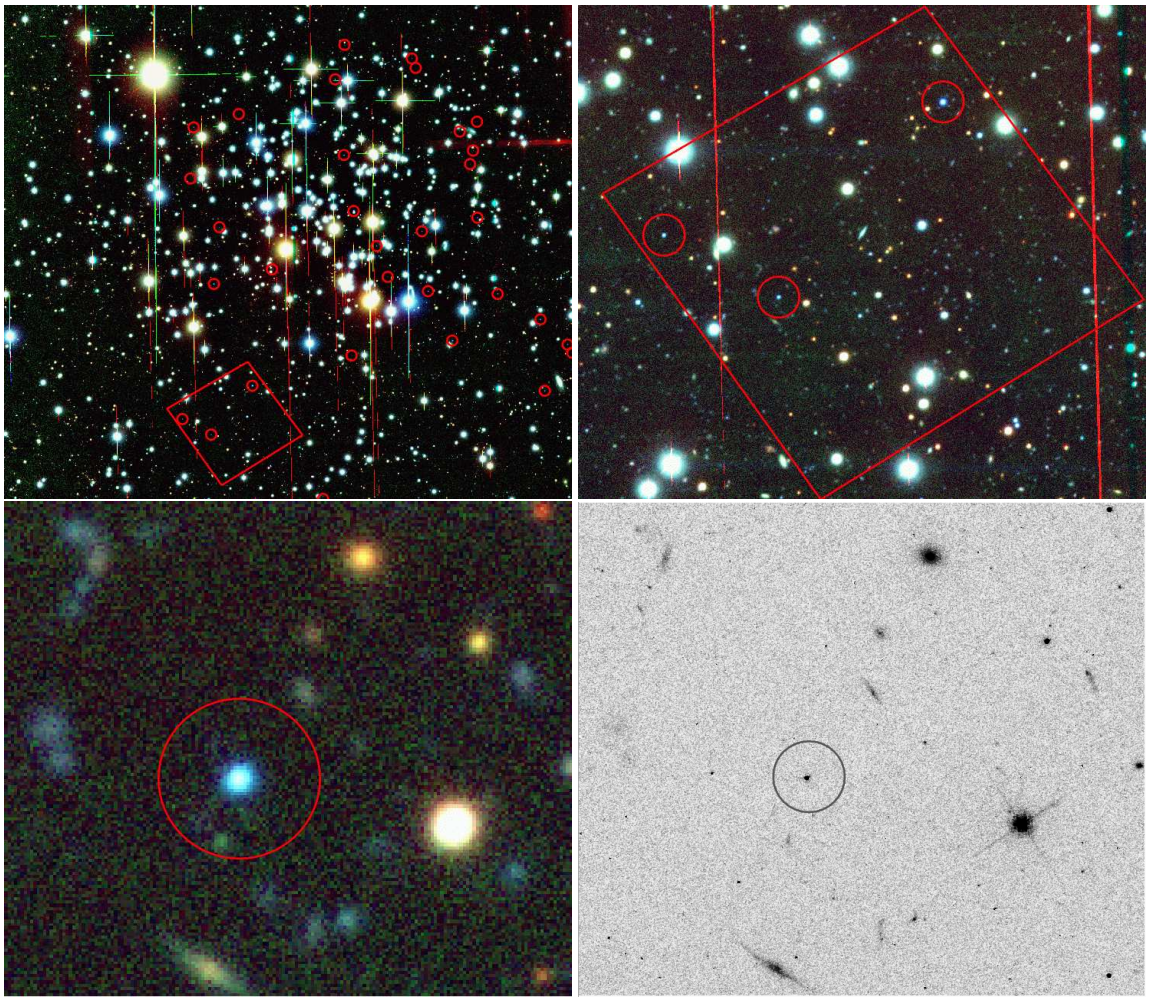

FIGURE 4.17— *(Top left):* The central ∼20×17 arcmin^2 region of our stacked trichromatic image from *BV*-LBT and *I*-CFHT frames. North is up, East is to the left. Red circles highlight the proper-motion selected WDs within the region. The red trapezoid indicates an *HST* ACS/WFC field from the archive (combining 1×400 s and 1×568 s images in filter F775W; GO-9984). *(Top right):* An enlargement of the area in common with the ACS/WFC field. *(Bottom left):* Zoom-in around the southern-most WD within the ACS/WFC field. The area is ∼40″ wide. The circle has a radius of 25 pixels. *(Bottom right):* The same portion of the field, but as seen in the ACS/WFC stacked image.

4.9.2 Second step

In the second step, we used every single local maximum detected within each single chip of each LBC *B*-image to build a peak-map image, i.e. a map of how often a local maximum occurred at a particular place in the field. A local maximum (peak) is any pixel of an image whose flux is strictly higher than any of its eight surrounding neighbors. We used *B* images for the construction of the peak map because they allowed us to detect the faintest sources. This peak map consists of an image with the same average pixel scale of the master frame, where we added 1 to a pixel count each time a local maximum, measured in a given image, fell within that pixel (once transformed with the aforementioned linear transformations).

A 3×3 box-car filter is applied to the peak map (as done in Anderson et al. 2008), in order to optimally highlight the signal from the faintest objects. This overbinning was necessary because very faint sources do not necessarily fall within the same pixels (due to noise fluctuations, the brightest pixel of a faint source might not be at the location predicted by the PSF, but instead in one of its neighbor pixels), and we want to consider all of the peaks that each source generates in order to maximize the signal.

In the top panel of Fig. 4.16 we show a region of the FoV (∼750×300 pixel^2, ∼170×70 arcsec^2) as imaged by a LBT *V* image of 110 s (seeing ∼1″). North is up, East to the left. The two sources marked with open circles are WDs, and the southern-most of the two, magnitude V=24.1, is the faintest M 67 WD detected in our sample (see Section 4.9.4). These two stars are barely visible in the single exposure, but they are easily detectable in the 3×3 overbinned peak map (bottom panel of Fig. 4.16). The faintest WD is able to generate a peak in 49/56 *B* exposures.

The peak map is then used to generate our faint-source list (the target list). We adopted a two-parameter algorithm: In order to be included in our initial list, a source has to (1) generate a peak which value is at least 60% of the number of exposures mapping its location, and (2) be at least 5 pixels away from any more significant source. These criteria correspond, on average, including 3.2σ detections above the local surrounding (where σ is the rms of the peak-map background; see Anderson et al. 2008 for more details). Lowering the threshold below this limit would dramatically increase the noise contribution to our sample. Our target list, does not contain sources located in patches of sky that were covered by less than 10 *B* images.

It is useful to construct stacked images so that we can examine the images of stars and galaxies that are hard to see clearly in individual exposures. The stacks (one each filter) are invaluable in helping us discriminate between real objects the software should classify as stars or galaxies, and objects that should be rejected as PSF bumps or artifacts. We used the positional transformations between each chip and the master frame to determine where each pixel in each exposure mapped onto the stack frame. The value of these pixels (sky subtracted) was properly scaled to match the photometric zero point of the master frame. For a given pixel of the stack image, we can dispose of several such mapping pixels. We assigned to a stack pixel the 3σ-clipped median of its mapping pixels, where σ is rms of the residuals around the median. Unlike Anderson et al. (2008), we did not iterate this procedure, since both LBC and UH8K cameras are not undersampled.

Top-left panel of Figure 4.17 shows the trichromatic stacked image (RGB color-coded with *I*, *V*, *B*, respectively) of the central region of M 67. Red circles mark M 67 WD members (see Section 4.9.4). The trapezoid delineates the patch of sky in common with an archive Advanced Camera for Survey (ACS) Wide Field Channel (WFC) *HST* field, from GO-9984. North is up, East to the left. The top-right panel shows a zoom-in around the region in common with ACS/WFC; on the bottom-left a closer view of the southernmost WD in previous panel; finally, the same region as it appears in an ACS/WFC stack (F775W filter, total exposure time ∼1070 s). It is clear that our stacked image is able to reveal as many objects as the ACS/WFC one.

More importantly, in our stacked images even the faintest WDs stand out well above the surrounding background noise. In the top-left panel of Fig. 4.19 we show a 40″×40″ region of the *B*-stacked image, centered around the faintest M 67 WD measured in this work (highlighted with an open circle). This star is clearly visible in our stacked image. Its brightest pixel has ∼75 DNs (sky subtracted) above a local sky noise of ∼4 DNs, therefore its detection is unambiguous. This star (that has a magnitude of V=24.1), is surrounded by many other fainter sources, the majority of which are background galaxies (note their more asymmetric and blurred shape, if compared to the WD).

4.9.3 Third step

We collected all the information for a given source, in each filter individually, following the prescriptions given in Anderson et al. (2008), and described here below. We used the positional transformations and the distortion corrections to calculate the position where each source of our target list falls in each individual exposure, and extracted a 11×11 array of pixels (raster) around the predicted position. Since the chips have different zero points, and the image quality is different from one image to the other, we corrected each raster (sky subtracted) to the

proper photometric zero point of the master frame.

Our local PSF model tells us the fraction of star light that is expected to fall in a pixel centered at an offset $(\Delta x, \Delta y)$ from the star's center, for any given image. Therefore, the flux P in each pixel (i, j) in each raster n is described by:

$$P_{i,j,n} - s_{*,n} = f_* \cdot \psi_{i,j,n}, \tag{4.5}$$

where f_* is the star's flux, $s_{*,n}$ is the local background value, and $\psi_{i,j,n}$ is the fraction of light that should fall in that pixel, according to the local PSF model. This is the equation of a straight line with a slope of f_* and a null intercept (note that our rasters are already sky subtracted). We fit the flux f_* for each star by a least-squares fit to all the pixels within r<5 pixel from the star's center, taking into account the expected noise in each pixel.

Unlike Anderson et al. (2008), we did not calculate a further local sky value prior to solving for f_* in Equation 4.5, because star light is spread all over the raster. We performed an additional procedure instead. After we had a first f_* value, we went back into every single raster and we subtracted the quantity $f_* \cdot \psi_{i,j}$ from each pixel value $P_{i,j}$. We used the 3σ-clipped average of the 40 pixels between r=3.5 and r=5 to estimate the background residual res_*. Finally, we recalculated the star's flux f_* by solving the new equation

$$f_* = \frac{P_{i,j,n} - s_{*,n} - \mathrm{res}_{*,n}}{\psi_{i,j,n}}. \tag{4.6}$$

We iteratively rejected the points that were more than 3σ discordant with the best-fitting model.

We fit always more than 790 individual-pixel values (cfr. Sect. 4 in Anderson et al. 2008), and up to ~4400. This has been done independently for each filter at each epoch, using the same star list. The uncertainty of the slope is the formal error of the least-squares fit, and provides our internal estimate of the photometric error. We will explain in Sec. 4.11 how to obtain a more reliable external estimate of the true errors. The flux is then converted into instrumental magnitudes, and calibrated to the *BV* Johnson *I* Kron-Cousin standard systems, using as secondary standards the objects from the Yadav et al. (2008) catalog. In Fig. 4.18 we show, for common sources, the differences in magnitude between our *B*, *V*, *I* unsaturated photometry and the one published in Yadav et al. (2008).

In panel (a) of Fig. 4.19 we show the V vs. $B-I$ CMD of all the sources measured this way. Our photometric-reduction techniques allow us to measure the faintest sources in our data set (V≥28). The M 67 main sequence (MS) and WD CS are embedded in a large number of foreground and background objects which prevent us from seeing the end of both sequences. In particular, we will show that the vast majority of sources forming the dense clump at V>23.5 and $B-I$<3 in the CMD are faint blue compact galaxies. This clump is almost exactly where we expect to find the bottom of the WD CS. In the next section, we will use proper motions to remove field sources from the CMD and isolate M 67 stars.

4.9.4 Proper motions

Proper motions were obtained as described in Anderson et al. (2006). Of the initial target list obtained from the peak map, we selected only those sources with a measure in both LBC *V* and *B* filters. This list is then used to calculate displacements between the two epochs, as follows.

We measured a chip-based flux and GD-corrected position using PSF-fitting for each object in the list in each chip of each exposure where it could be found. Then we organized the images in pairs of images from each epoch. For each object, in each pair, we computed the displacement (in the reference frame) between where the first-epoch predicts the object to be located, after having transformed its coordinates on the reference-frame system, and its actual-observed position in the second epoch image. Multiple measurements of displacements for the same object are then used to compute average displacements and rms.

It is clear that, in order to make these displacement predictions, we need a set of objects to be used as a reference to compute positional transformations between the two epochs for each source. The cluster members of

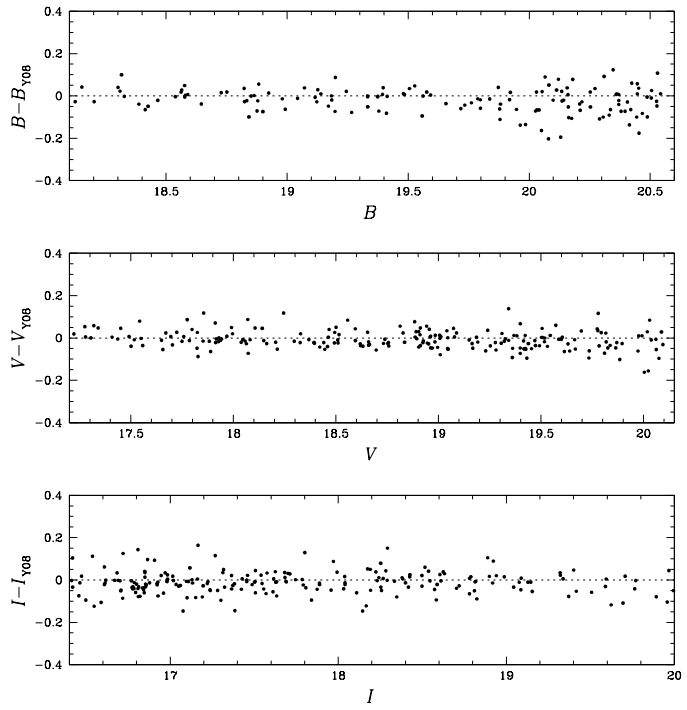

FIGURE 4.18— Magnitude differences between our photometry and the one presented in Yadav et al. (2008) catalog (indicated here with the subscript Y08) for the sources in common. From top to bottom, $B - B_{Y08}$ vs. B, $V - V_{Y08}$ vs. V, $I - I_{Y08}$ vs. I, respectively.

M 67 are a natural choice, as their internal motion is within our measurement errors (~0.2 mas yr^{-1} Girard et al. 1989), providing an almost rigid reference system with the common systemic motion of the cluster.

We initially identified cluster members according to their location in the LBC V vs. $B - V$ color-magnitude diagram. By predominantly using cluster members, we ensure proper motions to be measured relative to the bulk motion of the cluster. We iteratively removed from the member list those objects with a field-type motion even though their colors may have placed them near the cluster sequences. In our proper-motion selections (see panel (d) of Fig. 4.19), we considered as cluster members all sources whose displacement is within a circle of radius 0.15 LBC pixels in 10.13 yr [we found this to be the best compromise between losing (poorly measured) M 67 members and including field objects] in the vector-point diagram (VPD), slightly off-center with respect to the zero of the motion, in order to further reduce the number of field objects in our member list.

In order to minimize the influence of any uncorrected GD residual, proper motions for each object were computed using a local sample of members; specifically the 25 (at least) closest (r<3′), well-measured cluster stars (see Anderson et al. 2006 for more details). Note that, in order to maximize the cluster-field separation, we used all the available images, in every filter, in both epochs. Indeed, our aim here is to provide a pure sample of M 67 WDs, and we are not interested in removing systematic errors below the mas level at the expenses of the size of the WD sample. For a more careful proper-motion see Chapter 5 (see also Bellini et al. 2010b).

Finally, we corrected our displacements for atmospheric differential chromatic refractions (DCR) effects, as done in Anderson et al. (2006). The DCR effect causes a shift in the photocenter of sources, which is proportional to their wavelength, and a function of the zenithal distance: blue photons will occupy a position that differs from that of red photons. Unfortunately, within each epoch, the available data sets are not optimized to perform the

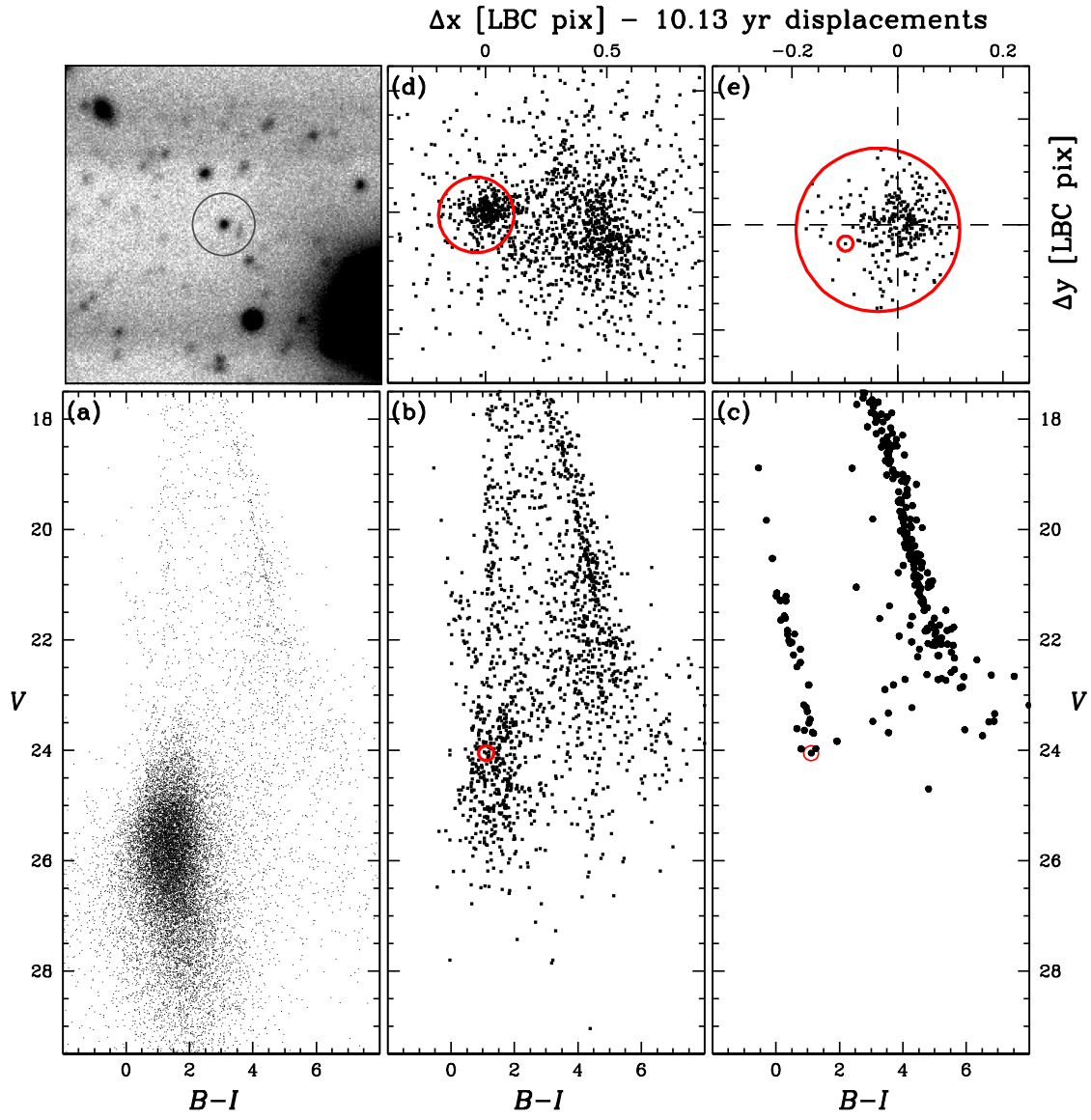

FIGURE 4.19— Panel (a) shows the V vs. $B-I$ CMD for all the objects in the target list. With our photometric-reduction technique we are able to measure sources as faint as $V\gtrsim 28$. It is clear from the figure that the bulk of faint blue compact galaxies occupy the same region as the WDs. Panel (b) shows the same CMD for objects for which we have a proper motion measurement. Our proper motions can reach a magnitude of $V\sim 26$. The relative VPD is shown in panel (d); a red circle includes the objects that we assumed to be cluster members (see the text for details). Panel (c) shows the CMD for the cluster members only, as selected in panel (d). Panel (e) shows the zoomed VPD for members. A small red circle in panels (b), (c), (e) identifies the faintest WD. In order to show the significance of the detection of this WD, top-left panel shows a $40''\times 40''$ region of the B-stacked image around this star, that stands clearly above the background. The brightest pixel of this star has ~75 DNs (sky subtracted) above a local sky noise of ~4 DNs, therefore its detection is unambiguous.

DCR correction directly. We can, however, check if possible differences in the DCR effects between the two

epochs could generate an apparent proper motion for blue stars relative to red stars.

We selected two samples of cluster member stars, one made by WDs in the magnitude interval $20<V<23$, and the other on the MS, within the same magnitude interval. For each sample, we derived the median $B-V$ color and the median proper motion along the X and Y axes, with dispersion obtained as the 68.27^{th} percentile around the median. We used a linear fit to derive the DCR corrections along both axes, as done in Anderson at al. (2006). We found that DCR corrections were always below 0.7 mas yr^{-1} $(B-V)^{-1}$.

In panel (b) of Fig. 4.19 we show the V vs. $B-I$ CMD of all the sources for which we have at least two individual displacement measurements. The red circle in the figure marks the location of the faintest M 67 WD measured in this work. It is clear from panel (b) that we can measure proper motions of sources more than two magnitudes fainter than this star. Panel (d) in the same figure shows the VPD of the sources in panel (b). Since we used M 67 star members as reference to compute displacements between the two epochs, the origin of the coordinate coincides with the M 67 mean motion. The red circle in panel (d) show our adopted membership criterion.

The cluster-field separation is ∼0.5 pixel in 10.13 yr (∼11 mas yr^{-1}). This separation is consistent with the one presented in Yadav et al. (2008). The V vs. $B-I$ CMD of the selected cluster members is shown in panel (c), and the corresponding VPD is shown (enlarged for a better reading) in panel (e). Again, we highlighted the position of the faintest measured M 67 WD with a small circle, in both panels. It is clear from panel (c) that the WD CS sharply drops at V∼24.1. This magnitude marks the bottom of the WD CS of M 67. The faintest WD has a proper motion consistent with the M 67 mean motion [see panel (e)]. A visual inspection of all the M 67 WDs on our stacked images confirmed that all of them are real stars.

4.9.5 Completeness

A complete investigation of the WD CS would require also the study of the WD LF. However, a proper study of the LF requires an appropriate estimate of the completeness of the star counts.

Computing completeness corrections taking into account both photometry and proper motions is a very complex and delicate matter, which is beyond the capability of our software, which was developed with the specific aim of deriving the most precise photometry and proper motions. A completeness correction that takes carefully into account proper motions opens a new series of problems, has never been properly treated in the literature. The aim of this work is to extract a clean sample of M 67 WD members to precisely locate them on the CMD, to study their main properties and to constrain theory. Our catalog will provide observers with a set of bona-fine WDs for spectroscopic follow-up investigations (at least for the bright WDs). We located the bottom of the WD CS just where the CS ends, not using statistical subtractions in the LF, as done, e.g. by R98 on the same cluster. However, it is important to emphasize here that our photometry and astrometry extends far below (about two magnitudes at the color of the faintest WD) the sharp WD CS cut off. Moreover, as shown by R98, at the $V<25$, the completeness, even in the shallower CFHT images, is >95%. We do not expect that our reduction software and the proper motion selection procedure can lower this completeness in any significant way. We defer the analysis of the completeness to when a new set of LBC images (project already approved by LBT TAC) will be available, providing a third epoch for a much more accurate proper motion measurement.

4.10 Comparison with previous studies

A thorough study of the WD CS in M 67 was already presented by R98. In R98, the authors removed background galaxies by mean of stellar-like shape parameter selections, and by statistically subtracting objects as measured in a blank field ∼1.°2 away from the center of M 67. As we can see in our stacked images, the majority of faint objects are indeed blue compact galaxies, stockpiled at the same location in the CMD as the end of the WD CS (see Fig. 4.19). We can also see that the faint galaxies are almost unresolved. This means that their profiles could mimic stellar profile, making the shape-like parameter selection criteria not very efficient. Moreover, a statistical subtraction of these galaxies using a blank field is subject to the problem of the cosmic variance (presence of

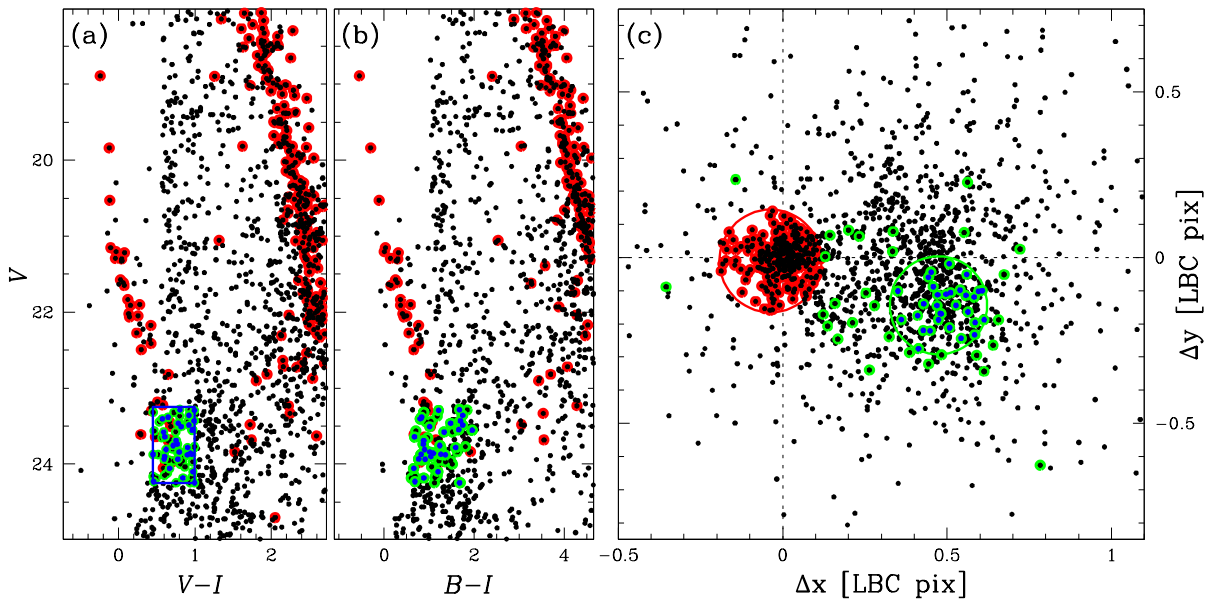

FIGURE 4.20— *(a)* V vs. $V-I$ CMD zoomed around the end of WD CS of M 67. *(b):* V vs. $B-I$ CMD of the same region. In both panels, black dots are objects with proper motion measurements. Red circles mark probable M 67 members, as defined in Section 4.9.4. In (a) we selected a sample of objects (highlighted with a blue rectangle), superimposed onto the end of the WD CS, which lie in the region of the CMD used by R98 to define the last two bins of his LF. *(c):* show the VPD of all the sources. In red are M 67 members (within the red circle), and in green color are the objects within the rectangle in panel (a). In blue (in all the three panels) are those selected objects which proper motion is within 1 σ [green circle in panel (c)] around their 3σ-clipped median motion.

cosmological structures that alter the statistics of extra-galactic background objects in different directions, within limited FoVs).

After the shape selection, R98 extracted the stars for the WD LF around a 0.7 $M_{\odot}$ CS derived using the interior models of Wood (1995) and the atmospheres of Bergeron, Wesemael, and Beauchamp (1995). In summary, in R98 WDs are never identified. Their LF has been derived only defining a strip on the CMD for object selection, and then applying a statistical subtraction of field objects. Despite all the aforementioned difficulties, the LF derived in R98 clearly shows a pile-up around $V\simeq24$ [and $(V-I)_0$=0.7], and it terminates at $V\simeq24.25$. These values are in very good agreement with the WD CS termination of V=24.1±0.1 that we find with our proper-motion selected sample of WDs.

The sharp peak of the LF identified with the bottom of the WD CS by R98 needs some more investigation. We can note, in our V vs. $B-I$ CMD [panel (b) of Fig. 4.19], a clump of objects very close to the end of the WD CS, but slightly redder. The same objects are almost superimposed onto the WD CS if we look at the V vs. $V-I$ CMD used by R98 in their investigation. The average $V-I$ color of these objects is ∼0.8, close to the $(V-I)_0\simeq0.7$, where R98 found a pile-up of objects that were treated by R98 as the bottom of the WD CS (note that R98 use 0.5 magnitude wide bins in color to select their WD candidates). We now further investigate the nature of these objects.

In Fig. 4.20 we plot our V vs. $V-I$ and V vs. $B-I$ CMDs in panels (a) and (b), respectively. Black dots are objects for which we have a proper motion measurement. Probable M 67 members, as defined in Section 4.9.4, are highlighted in red in both panels. In panel (a) we selected for investigation those objects within a (blue) rectangle, whose borders are defined as $V-I$=0.7±0.25, V=24.25, and V=23.25. This region of the V vs. $V-I$ CMD is

the same one used by R98 to define the last two bins of their WD LF. Panel (c) displays the VPD of the sources plotted in panels (a) and (b), on which we have marked in red our proposed M 67 members (stars within the red circle defined in Section 4.9.4), and in green the objects within the rectangle. Very few of these objects have a displacement that is close to the mean M 67 motion, and therefore could be M 67 stars, but the majority of them is concentrated around a location in the VPD that is close to the centroid of the relative motion of galaxies (Bellini et al. submitted). Therefore, by means of proper motion measurements, we conclude that the vast majority of the objects that form the clump close to the end of the WD CS are field-type objects, and not M 67 members.

As a further proof that these objects are mainly background galaxies, we performed the following test. We calculated the 3σ-clipped median displacement (where σ is the rms of the residuals around the median) of these objects on the VPD, and selected the ones within 1 σ from this position [big green circle in panel (c)]. This subsample, constituted by 31 objects, is highlighted in blue in all the three panels. We used the LBC V image of 330 s exposure (the deepest we have, and one with the best seeing $\sim$0.″7) to check whether or not these objects are actually galaxies or stars. Only 21 of them are present in this image. We measured the full width at half maximum (FWHM) along both LBC X and Y axes. PSF shapes and orientation vary with location on the chip, and from chip to chip; moreover, also galaxy shapes and orientations do vary. Nevertheless, we expect that, on average, the measured FWHMs of galaxies to be larger than the ones of stars.

In order to measure FWHMs of stars for this comparison, we selected 10 M 67 WDs in the same V magnitude interval as the investigated objects. Five of them are present in the 330 s image. We measured the FWHM for these 5 stars, again along both LBC X and Y axes. We then measured average values and errors for the FWHMs of stars and suspected galaxies. The results are as follows:

$$\text{stars}: \begin{cases} \overline{\text{FWHM}}^{*}_{X} = 3.2 \pm 0.1 \\ \overline{\text{FWHM}}^{*}_{Y} = 2.9 \pm 0.2 \end{cases}$$

$$\text{objects}: \begin{cases} \overline{\text{FWHM}}^{\text{obj.}}_{X} = 4.0 \pm 0.1 \\ \overline{\text{FWHM}}^{\text{obj.}}_{Y} = 3.7 \pm 0.1 \end{cases}$$

It is clear that objects within the green circle in panel (c), are sizably broader than WDs at the same luminosity, by $\sim$25% in both X and Y axes. On the basis of their average shape and of their proper motions, we conclude that the objects are indeed blue faint galaxies and not M 67 stars. This result does not invalidate what was done in R98, since we already showed that our estimated WD CS end, based on a pure sample of M 67 members, is in very good agreement with the R98 determination. However, we caution the readers to use the WD LF to infer information on the M 67 WD properties before an accurate LF, corrected for completeness, and based on a field-object cleaned WD CS can be produced.

4.11 Comparison with theory

In the same vein as our previous papers on the WD populations in Galactic star clusters (see, e.g. Bedin et al. 2009 and references therein), we compare the M 67 WD CS with theoretical WD models, and also assess the consistency with the results from modeling of the cluster's MS and turn off (TO) regions.

As a first step of our analysis, we compare the BaSTI [Fe/H]=+0.06 scaled solar isochrones (Pietrinferni et al. 2004 for an age of 3.75 and 4.00 Gyr to the (single stars only) V vs. $V-I$ CMD by Sandquist (2004) that covers MS, TO, red-giant branch (RGB) and the central He-burning phases. As shown in Fig. 4.21, the best fit to the MS and post-MS phases implies $(m-M)_0$=9.64 and E($B-V$)=0.023 [obtained from the E($V-I$) by using the Cardelli et al. (1989) extinction law, with R_V=3.1]. These values are consistent – within the uncertainties – with the recent [Fe/H]=+0.05±0.02 and E($B-V$)=0.04±0.03 derived by Pancino et al. (2009), and with the $(m-M)_0$=9.60±0.09 obtained by Percival & Salaris (2003). We will also adopt these values in the following, for comparisons of the observed WD sequence with theory.

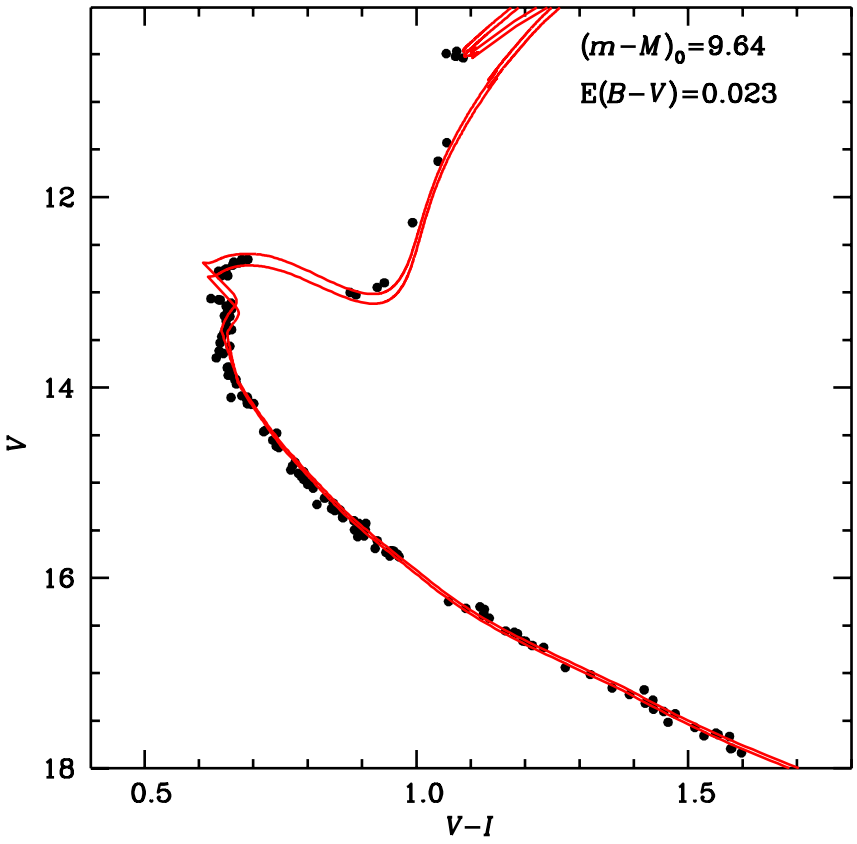

FIGURE 4.21— Fit of V vs. $(V-I)$ CMD by Sandquist (2004) with the BaSTI 3.75 and 4 Gyr isochrones with [Fe/H]=+0.06 and convective core overshooting.

Had we used a lower [Fe/H] in the fit to the Sandquist data set, the match to the RGB and red clump would have improved, but at the expense of the fit to the MS (the slope would not be matched as well as before). Had we lowered the [Fe/H] value in our isochrones by 0.1 dex (more than three times the quoted error bars from the spectroscopic determinations in Pancino et al. 2009) the resulting distance modulus from the overall fit would have increased by only a few (2–3) hundredths of a magnitude, the reddening by $\lesssim$0.01 mag, and the age would have hardly changed. All in all, the overall picture regarding distance, reddening and age would not be changed appreciably. This works in our favor, because these quantities are what matters most for the comparison with the WD CS. Moreover, the termination of the theoretical WD isochrones would not be really affected, because the luminosity of the faintest WDs is essentially driven by their cooling timescales, rather than the progenitor lifetimes (higher mass progenitors with small life times compared to the age of the cluster).

Fig. 4.21 shows that the best TO age estimate is 3.8–4.0 Gyr for BaSTI isochrones with convective core overshooting, in agreement with previous results (Carraro et al. 1996 and R98). A problem (Carraro et al. 1996) persists with the cluster RGB, which is significantly bluer for the same set of parameters, independently from the adopted models. We note that, at the age of M 67, the mass extension of convective cores in TO stars is small, and the overshooting extension in the BaSTI models (and in general in all models including convective core

overshooting) is in the regime of shrinking to zero with decreasing convective core masses (see Pietrinferni et al. 2004 for details).

The observed WD sequence is compared to a reference set of H-atmosphere (DA) CO-core WD isochrones computed using the Salaris et al. (2000) WD tracks, bolometric corrections from Bergeron, Wesemael, & Beauchamp (1995), progenitor lifetimes from the BaSTI (Pietrinferni et al. 2004) scaled solar models with [Fe/H]=+0.06 (the same used in the fit to the MS and TO regions), and the initial-final mass relationship (IFMR) from Salaris et al. (2009) extrapolated at its lower end to the TO mass of M 67. We have also employed, as a test, the relationship proposed by Kalirai et al. (2009) and found negligible differences in the resulting isochrones.

Figure 4.22 displays our WD isochrones for 3.75 and 4 Gyr, again using with $(m - M)_0$=9.64 and E($B - V$)=0.023 as in Fig. 4.21, compared to the observed WD cooling sequence in the V vs. $B - I$ CMD. The choice of this wide-color baseline enhances differences in the location of WDs due to variation in their mass or atmosphere composition, compared to either $B - V$ or $V - I$ – the other colors available from our photometry –, and provides more stringent tests for the theoretical modeling of the observed sequence. [In addition, V and $B - I$ photometric errors are independent.] Red error bars in Fig. 4.22 are the formal photometric errors directly derived from the uncertainty in the fit slope in Equation 4.6 (i.e., the internal errors).

Formal errors are generally a lower bound for the true errors. To obtain a more reliable – external – estimate of the errors, we randomly divided our photometric data set (for each filter) into four subsamples. Specifically, each of the four LBC B subsamples is constituted by 14 images, each LBC V subsample by 11 images, while UH8K I images are split into 3 groups of 3 images each, and a last group made with 2 images only (for a total of 11 images).

We selected only the WDs in our sample (see Fig. 4.22), and for each subsample separately, we repeated the last reduction step of our three-step procedures (see Section 4.9.3) to compute their BVI fluxes. For each WD, we obtained four independent measurements of the flux (in each filter), with formal errors. We weighted the four estimates of these fluxes according the their formal errors, and took a weighted mean of the four fluxes. We found that this mean flux was equal, within the round-off errors, to the value that we had found using the whole data set. [It was within few percent in nearly every case.] Finally, we derived an external estimate of the true photometric error, from the residuals of the individual values of the flux from their mean, using the same weights as we had used for the mean. These external photometric errors are indicated by the black error bars in Figure 4.22.

We note, instead, that error estimates based on artificial stars are also (as our formal internal errors) generally underestimated, and so less reliable. This is because artificial stars are always based on an input PSF model, which could significantly differ from the true local PSF, concealing our ignorance about the true sources' flux. Moreover, thanks to the large dither pattern of LBC observations, WDs fall each time in different locations on the LBC chips, in different chips as well, and under different observing conditions, contributing to further strengthening the reliability of the external estimates of the errors.

There is good agreement between the location of the WD isochrones and the observed sequence. The expected blue hook at the bottom of the WD sequence is also visible in the data. It is due to the presence of increasingly massive (lower radius) objects originating from more massive MS progenitors that had more time to cool down along the WD sequence. The location and color extension of the blue hook is well matched by the isochrones with ages consistent with the TO age. We recall that the observed V magnitude of the bottom end of the WD sequence ($V\sim$ 24.1±0.1 mag) is in very good agreement with the observed WD LF by R98, and with the predictions by Brocato, Castellani & Romaniello (1999, their Fig. 8), where an age of 4 Gyr, solar metallicity and a distance modulus $(m - M)_0$=9.6 were assumed.

A complementary method to estimate the age of M 67 uses a new age indicator, that has the advantage of being free from distance and extinction effects, and it is also independent from the age obtained from the TO. Similarly to the ΔV parameter employed in globular cluster studies (V-magnitude difference between the Horizontal Branch and Turn Off, see e.g., the review by Stetson, Vandenberg & Bolte 1996) it is possible to define the parameter ΔV(WDT − HB) as the difference between the V magnitude of the WD CS end [V(WDT)], and the mean level of the horizontal branch [V(HB) – see Brocato, Castellani & Romaniello 1999]. Once the metallicity of the cluster

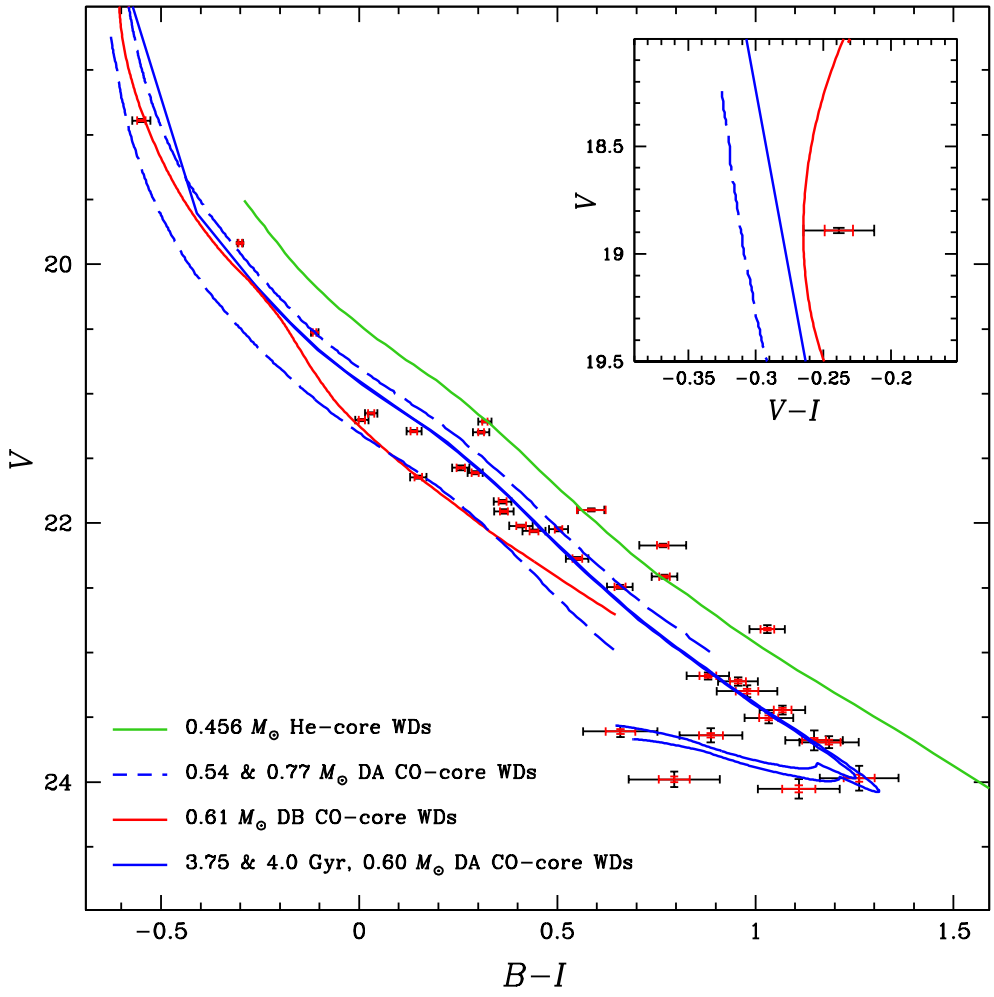

FIGURE 4.22— V vs. $(B-I)$ CMD of the WD sequence compared to our reference CO-core DA WD isochrones with age of 3.75 and 4 Gyr (blue solid lines), CO-core DA cooling tracks with masses equal to 0.54 $M_{\odot}$ and 0.77 $M_{\odot}$ (dashed blue lines), a 0.465 $M_{\odot}$ He-core WD (green solid line) and CO-core 0.61 $M_{\odot}$ DB track (red solid line). All isochrones and tracks have been shifted by the reference distance modulus and reddening values used in Fig. 4.21. The inset shows the position in the V vs. $V-I$ CMD of the brightest WD in our data compared to the reference isochrones, the 0.77 $M_{\odot}$ DA track and the DB track. Red error bars are our formal errors, black error bars are extern al estimates of the errors. See the text for details.

is known, this parameter is a function of the cluster age, increasing for older clusters (see Fig. 4.23). Here, we present the calibration of ΔV(WDT – HB) as a function of age for M 67 metallicity, while the general calibration for a wider range of chemical compositions will be presented in a forthcoming paper (Brocato et al. in prep.). Here it suffices to say that our data provide ΔV(WDT – HB)=13.6±0.1, that leads to an age of 3.9±0.1 Gyr. This estimate (which is formally independent of the CMD fitting procedure used in Fig. 4.21 to estimate the cluster age) is in agreement with the other estimates above discussed.

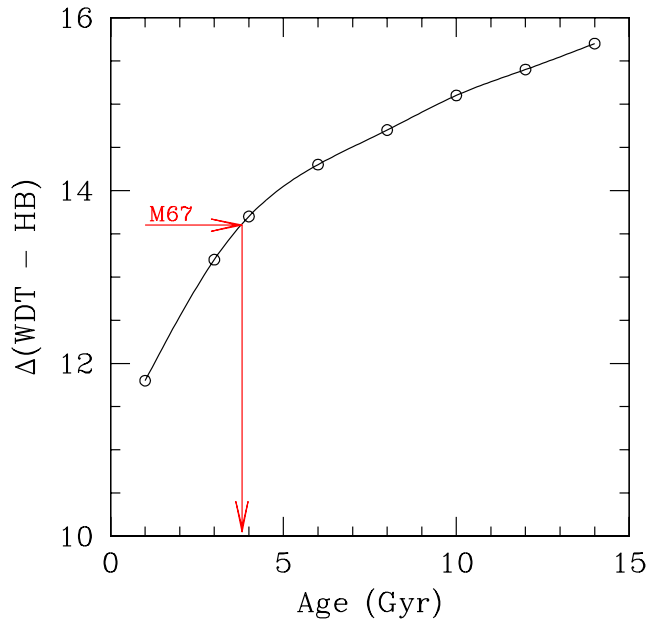

FIGURE 4.23— The theoretical value ΔV(WDT – HB) is plotted against the age of the simulated cluster. The value observed for M 67 in this work is also shown.

4.12 Discussion

Despite the good agreement between the location of the WD isochrone and the observed CS, and the consistency between TO and WD ages, in the V magnitude interval between ~19 and ~23 there are several objects that appear more than 3σ away from the theoretical sequence, and deserve a further analysis. We cannot exclude, a-priori, that these objects are WD+WD binaries, but this possibility is very unlikely, therefore in the following we will not treat this case. We have first considered the possible presence of a large spread in the cluster IFMR (see, e.g., Salaris et al. 2009 and Dobbie et al. 2009) for progenitor masses in the range ~1.5–2.5 $M_{\odot}$. Figure4.22 shows the cooling tracks of 0.54 $M_{\odot}$ and 0.77 $M_{\odot}$ DA CO-core WDs (dashed blue lines). In the appropriate magnitude range these two models are located on the red and blue side of the reference isochrone, respectively, that is populated by WDs with mass ~0.6 $M_{\odot}$. A spread of the IFMR towards higher values of WD masses can be explained by the spread of objects on the blue side of the isochrone, whereas the redder WDs are not so easy to explain. The 0.54 $M_{\odot}$ track is still about 0.1 mag bluer than 6 objects with V between ~19 and ~23. Taking into account that the core mass at the first thermal pulse is ~0.52–0.53 $M_{\odot}$ for the relevant progenitor mass range, it is difficult to match the position of these red objects with "standard" WD sequences. A possible way out of this problem is to invoke the presence of CO-core WDs with masses lower than the core masses at the beginning of the thermal pulse phase. As studied by Prada Moroni & Straniero (2009), anomalous and somewhat finely tuned mass loss processes during the RGB phase can produce CO-core WDs with masses as small as ~0.35 $M_{\odot}$ at the metallicity of M 67, for progenitors around 2–2.3 $M_{\odot}$. In this mass range there is a transition between electron degenerate and non degenerate He-cores along the RGB. These low mass WDs are potentially able to match the handful of objects redder than our reference isochrone. Their cooling timescales (e.g. Fig. 12 in Prada Moroni & Straniero 2009) are roughly consistent with their observed luminosities, assuming that they are produced by progenitors with masses around 2–2.3 $M_{\odot}$.

There is another possible interpretation. In order to reproduce the position of these WDs in the CMD, we

have considered the cooling track (green line in Fig. 4.22) of the 0.465 $M_{\odot}$ He-core WD discussed in Bedin et al. (2008a). At the cluster's metallicity, BaSTI models predict that the He-core mass of stars climbing the RGB (mass ~1.4 $M_{\odot}$) can be at most equal to ~0.47 $M_{\odot}$. This WD track represents therefore an approximate bluer boundary for the location of M 67 He-core WDs. All of the 6 red objects (that are more than 3σ away from the CO-core WD isochrone) lie close to this sequence. They can be massive He-core WDs produced by very efficient mass loss along the RGB phase. These same 6 objects are located around the He-core sequence also in $V-I$ colors although the separation between the sequences is smaller in that case (and even smaller in $B-V$). As for the objects at the blue side of the isochrones, Fig. 4.22 displays the cooling track of a 0.61 $M_{\odot}$ CO-core model with pure He-atmospheres (DB, red solid line). This is approximately the expected value of the DB mass evolving down to V~23 (where the track is truncated) for the chosen progenitor lifetimes and IFMR. At fainter magnitudes, DA and DB tracks of the same mass have approximately the same colors.

There is clearly one object at V~19, and two objects with V between ~21 and 22, that are well matched by the DB model and are therefore candidates to be He-atmosphere WDs. It is clear that without spectroscopic estimates of atmospheric composition and/or WD masses it is impossible to find a unique interpretation for these WDs that are not matched by the reference isochrone. But both $B-I$ and $V-I$ colors suggest that the brightest object at V~19 is a DB WD. The inset of Fig. 4.22 displays the position of this star in the V vs. $V-I$ CMD. In this CMD the bright part of the DB sequence is located on the red side of the reference DA isochrone, whereas at magnitudes fainter than V~20 the relative position of the two sequences is the same as in the $B-I$. The star is located at the red side of the DA isochrone in $V-I$, and at the blue side of the isochrone in the $B-I$, exactly as expected for DB objects, and in complete disagreement with its interpretation as a massive DA object.

Bibliography

Anderson, J., Bedin, L. R., Piotto, G., Yadav, R. S., & Bellini, A. 2006, A&A, 454, 1029
Anderson, J. et al. 2008, AJ, 135, 2055
Bedin, L. R., Salaris, M., Piotto, G., King, I. R., Anderson, J., Cassisi, S., & Momany, Y. 2005, ApJL, 624, L45
Bedin, L. R., King, I. R., Anderson, J., Piotto, G., Salaris, M., Cassisi, S., & Serenelli, A. 2008, ApJ, 678, 1279 (2008a)
Bedin, L. R., Salaris, M., Piotto, G., Cassisi, S., Milone, A. P., Anderson, J., & King, I. R. 2008, ApJL, 679, L29 (2008b)
Bedin, L. R., Salaris, M., Piotto, G., Anderson, J., King, I. R., & Cassisi, S. 2009, ApJ, 697, 965
Bellini, A., et al. 2009, A&A, 493, 959
Bellini, A., & Bedin, L. R. 2009, PASP, 121, 1419
Bellini, A., & Bedin, L. R. 2010, A&A accepted, arXiv:1005.0848
Bellini, A., et al. 2010, A&A, 513, A50 (2010a)
Bellini, A., Bedin, L. R., Pichardo, B., Moreno, E., Allen, C., Piotto, G., & Anderson, J. 2010, A&A, 513, A51 (2010b)
Bergeron, P., Wesemael, F., & Beauchamp, A. 1995, PASP, 107, 1047
Brocato, E., Castellani, V., & Romaniello, M. 1999, A&A, 345, 499
Cardelli, J. A., Clayton, G. C., & Mathis, J. S. 1989, ApJ, 345, 245
Carraro, G., Girardi, L., Bressan, A., & Chiosi, C. 1996, A&A, 305, 849
Dobbie, P. D., Napiwotzki, R., Burleigh, M. R., Williams, K. A., Sharp, R., Barstow, M. A., Casewell, S. L., & Hubeny, I. 2009, MNRAS, 395, 2248
Fellhauer, M., Lin, D. N. C., Bolte, M., Aarseth, S. J., & Williams, K. A. 2003, ApJL, 595, L53
Giallongo, E., et al. 2008, A&A, 482, 349
Girard, T., Grundy, W., Lopez, C., & van Altena, W. 1989, AJ, 98, 227
Kalirai, J. S., Saul Davis, D., Richer, H. B., Bergeron, P., Catelan, M., Hansen, B. M. S., & Rich, R. M. 2009, ApJ, 705, 408

Pancino, E., Carrera, R., Rossetti, E., & Gallart, C. 2009, arXiv:0910.0723
Percival, S. M., & Salaris, M. 2003, MNRAS, 343, 539
Pietrinferni, A., Cassisi, S., Salaris, M., & Castelli, F. 2004, ApJ, 612, 168
Prada Moroni, P. G., & Straniero, O. 2009, A&A in press, arXiv:0909.2742
Richer, H. B., Fahlman, G. G., Rosvick, J., & Ibata, R. 1998, ApJL, 504, L91 (R98)
Salaris, M., García-Berro, E., Hernanz, M., Isern, J., & Saumon, D. 2000, ApJ, 544, 1036
Salaris, M., Serenelli, A., Weiss, A., & Miller Bertolami, M. 2009, ApJ, 692, 1013
Sandquist, E. L. 2004, MNRAS, 347, 101
Stetson, P. B., Vandenberg, D. A., & Bolte, M. 1996, PASP, 108, 560
Wood, M. A. 1995, White Dwarfs, 443, 41
Yadav, R. K. S., Bedin, L. R., Piotto, G., Anderson, J., Villanova, S., Platais, I., Pasquini, L., Momany, Y., & Sagar, R. 2008, A&A, 484, 609

5

Absolute proper motion of the open cluster M 67

We derived the absolute proper motion (PM) of the old, solar-metallicity Galactic open cluster M 67 using observations collected with CFHT (1997) and with LBT (2007). About 50 galaxies with relatively sharp nuclei allow us to determine the absolute PM of the cluster. We find $(\mu_\alpha \cos\delta, \mu_\delta)_{J2000.0} = (-9.6 \pm 1.1, -3.7 \pm 0.8)$ mas yr^{-1}. By adopting a line-of-sight velocity of 33.78 ± 0.18 km s^{-1} , and assuming a distance of 815±50 pc, we explore the influence of the Galactic potential, with and without the bar and/or spiral arms, on the galactic orbit of the cluster. The proper-motion derivation employs a different sub-set of the data set presented in Chapters 2, 4 and 4.6, in order to minimize systematics. This Chapter contains results published in *Astronomy & Astrophysics* (Bellini et al. 2010b).

5.1 Introduction

The solar-metallicity Galactic open cluster M 67 (NGC 2682) is among the most-studied Galactic open clusters. Still, its absolute proper motion (PM) remains poorly constrained.

We applied for the first time on ground-based multi-epoch CCD wide-field images the PM techniques developed in Anderson et al. (2006, Paper I), Yadav et al. (2008, Paper II), Bellini et al. (2009, Paper III) to define an absolute reference frame using background faint galaxies. In the next section we describe the data set and the measurements, and a final section is dedicated to the study of the orbit of M 67 within the Galaxy under different assumptions for the Galactic potential.

5.2 Observations, data reduction, proper motions

Two data sets – collected with two different telescopes and at two different epochs – were used to measure the PM of objects in the field of M 67.

As the first epoch (hereafter, epoch 1) we employed images taken on Jan. 10–13, 1997, at the CFHT 3.6m telescope. These images were first presented by Richer et al. (1998). We took only a subsample of this data set, specifically 15 exposures of 1200 s in the *V* filter, with a median value for seeing and airmass of 1″ and 1.2 respectively. Each image was collected with the UH8K camera (8 CCDs, 2K×4K pixels each, with an average scale of 210 mas pixel^{-1}) covering a field-of-view (FoV) of ∼29′×29′.

The second-epoch (epoch 2) data were collected between Feb. 16 and Mar. 18 2007 and consist of 56 images of 180 s exposures in the *B*-band filter and 42 exposures of 100–110 s in the *V*-band, obtained with the LBC-

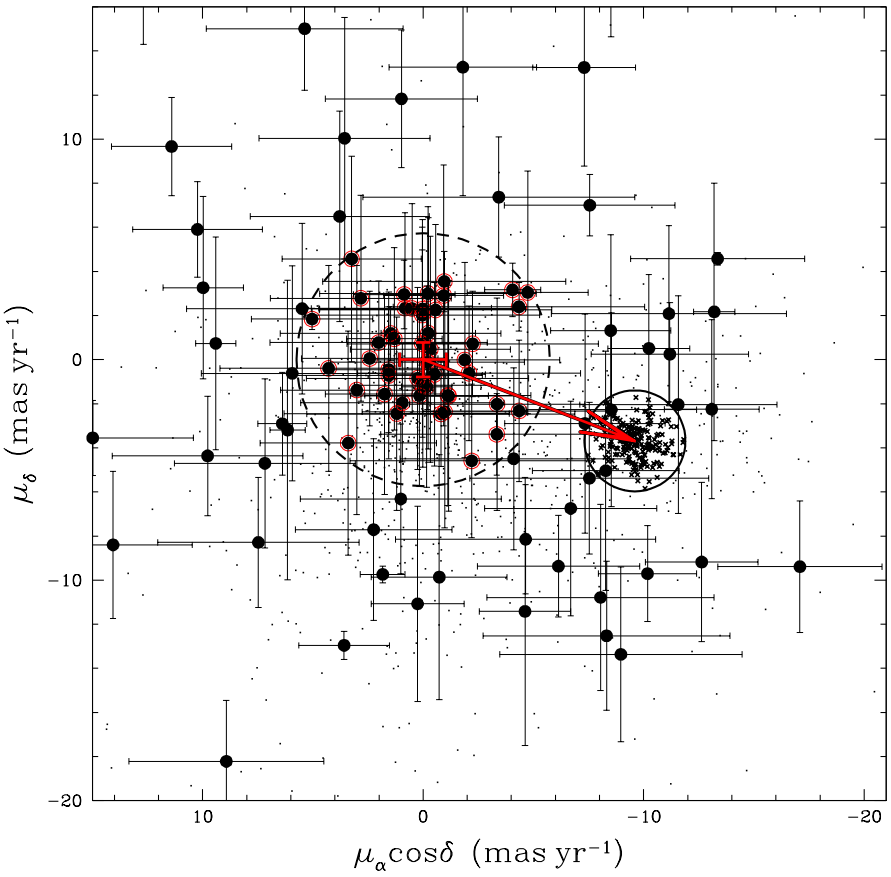

FIGURE 5.1— Vector-point diagram of the absolute PMs, in equatorial coordinates (J2000.0). Small crosses are M 67 members (within the solid circle), filled circles are the reference galaxies, 47 of which (marked with red open circles) were taken to compute the centroid of the galaxy distribution.

blue camera (4 CCDs, 2K×4.5K pixels each, FoV of ∼24′×26′). A large dither pattern (∼30% of the FoV) was employed for both filters. Median seeing and airmass were 1″ and 1.1 for the *V*, and 1.″3 and 1.1 for the *B* images. We selected only *B* images for finding objects, while those in *V* were taken to provide all the astrometric information. A more extensive description of the LBT data set is given in Chapters 2, 4, and 5 (see also Bellini & Bedin 2010, Bellini et al. 2010). Procedures and algorithms used to derive the list of objects, star positions and fluxes, and PMs are those explained in great detail in Paper I and in Anderson et al. (2008, A08). Below we briefly describe these reduction procedures, which were organized in three steps.

In the first step, we employed the software described in Paper I to obtain PSFs, star positions and fluxes in each chip of each exposure and for the best sources (bright, isolated, with a stellar profile). We corrected LBC raw positions for geometric distortion (GD), as described in Bellini & Bedin (2010), and we used these corrected positions to register all of the LBC single-chip images into a common distortion-free reference frame (the master frame) by means of linear transformations. With this master frame we derived the GD correction also for the UH8K positions, using the same technique (used also in Bellini & Bedin 2009).

The second step consisted of producing the list of objects (the target list). We took every single local maximum

detected within each individual chip of each LBC *B* image to build a peak-map image (A08). The peak map consists of an image with the same pixel scale of the master frame, where we added 1 to a pixel count each time a local maximum, measured in a given image, fell within that pixel (once transformed with the aforementioned linear transformations). A 3×3 box-car filter is applied to the peak map, and in our final list we considered as significant any object 3.2σ (where σ is the rms of the peak-map background) above the local surrounding. Our list contains objects generating a local maximum in at least 40% of the images covering the patch of sky where the maximum is found. We additionally required a minimum coverage of 10 *B* images.

With the *B* images we generated the target list because they are more numerous and have a lower background compared to *V* images. In addition, large dithers helped us to produce a list of solid detections even for the faintest sources. We further purged our list from excessively faint sources, keeping only objects with at least 100 DN above the local background and which showed up in at least one observation for each of the two *V*-filter epochs. We also excluded objects within chip # 2 and 4 of the UH8K camera, because these chips are highly affected by charge transfer inefficiency. As a consequence, the useful FoV is reduced by 25%.

In the last step we derived PMs (see Sect. 7 of Paper I for more details): We measured each object in the target list in each chip of each *V* exposure where it could be found, using PSF-fitting to get a chip-based flux and a GD-corrected position. Then we organized the images in pairs of one image from the first and one from the second epoch. For each object in each pair we computed the displacement (in the reference frame) between where epoch 1 predicts the object position in epoch 2, and the actually-observed position in epoch 2. Multiple measurements of displacements for the same object were then used to compute average displacements and rms.

It is clear that to make these predictions, we needed a set of objects as a reference to compute positional transformations between the two epochs for each source. The cluster members of M 67 were a natural choice, as their internal motion is within our measurement errors (∼0.2 mas yr^{-1} Girard et al. 1989), providing an almost rigid reference system with the common systemic motion of the cluster.

We initially identified cluster members according to their location in the *V* vs. $B-V$ color-magnitude diagram. We took only main sequence (MS) stars to transform each exposure into the master frame, because it spans a narrow range in color[1]. By predominantly using cluster members, we ensured the PMs to be measured relative to the bulk motion of the cluster. We iteratively removed from the member list those objects with a field-type motion (i.e., with a PM larger than 2.3 mas yr^{-1} from the mean M 67 motion), even though their colors may have placed them near the cluster MS. This particular cut value in the PMs represents a compromise between loosing (poorly measured) M 67 members and including field-type objects. Our final member list contains 209 color- and PM-selected objects. In order to minimize the influence of any uncorrected GD residual, PMs for each object were computed with a local sample of members; specifically the 25 (at least) closest ($r<3'$), well-measured cluster stars (see Paper I for more details).

Then we matched our master frame with the sources in the Digital Sky Survey (DSS) to compute scale and orientation for our master frame. We needed to know scale and orientation with an error of ∼ 1%. Even if only saturated stars could be matched with the DSS catalog, the used sample was good enough for this purpose. We divided our displacements for the time baseline between the two epochs (10.13 years) to obtain PMs in units of mas yr^{-1}. We kept in our final PM list only objects with at least two measurements of the displacement, and with PM rms <7 mas yr^{-1} in each coordinate. Finally, we corrected our PMs for differential chromatic refraction (DCR) effects, as done in Papers I & III, using M 67 white dwarfs and MS stars. We note that DCR corrections were always below 0.2 mas yr^{-1} $(B-V)^{-1}$.

On the basis of the PM dispersion of members (∼0.9 mas yr^{-1}) with respect to their mean (which reflects our measurement errors) we estimated the uncertainty on the adopted member reference system to be ±(0.1,0.1)

[1]Note that it was not possible to use the high-probability members derived in Paper II as starting reference members, because there are not enough stars in common between the two catalogs. Indeed, the PM catalog of Paper II includes stars in the range magnitude $9<V<21$ (with reliable PM measurements down to $V\sim19$), while our new PM determinations are in the magnitude range $18<V<26$.

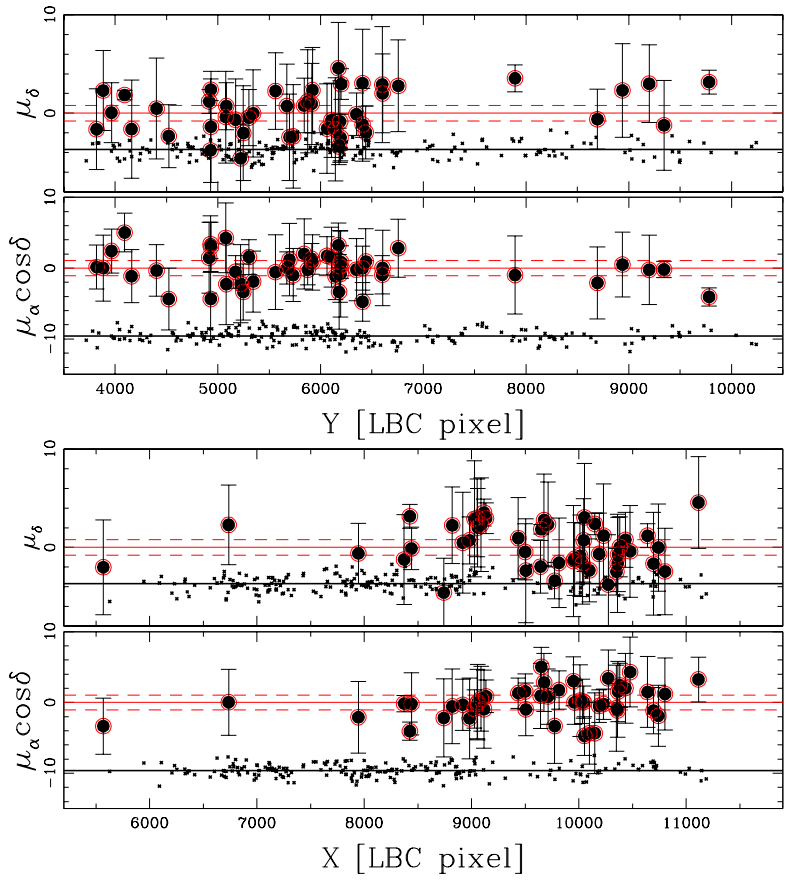

FIGURE 5.2— From top to bottom, μ_δ and $\mu_\alpha \cos\delta$ as a function of X and Y. When PMs are plotted as a function of their position in the master frame (X,Y), no clear systematic errors appear. Note that two chips of UH8K are not used (Y>7000, for X<5500 & X>9500), and that the cluster center is at location (X,Y)≃(7500,7000). These two effects both create gaps in the galaxy spatial distribution.

mas yr^{-1}. (Note that our estimate of the member dispersion is somehow biased because of the 2.3 mas yr^{-1} membership selection criterion we adopted in our proper-motion determination. Hence, the dispersion could be underestimated. Nevertheless, it still provides a good indication of the involved errors.) We were still left with the problem of finding the zero point of our PMs – which for now were only relative to the cluster's mean motion and not to an absolute reference system. Unfortunately, it was not possible to directly link our proper motions to the UCAC3[2] catalog (Zacharias et al. 2009), which includes stars mainly in the 8 to 16 magnitude range in a single bandpass between *V* and *R*, with no overlap with our catalog.

Background Galaxies can be considered as fixed points in the sky, and provide an excellent, and *directly-observable* absolute reference system. A visual inspection of the images revealed many such galaxies. About 100 of them show point-like nuclei, which could be fitted with our PSFs to measure positions and PMs (as done in Bedin et al. 2003, 2006).

[2]http://www.usno.navy.mil/USNO/astrometry/optical-IR-prod/ucac/.

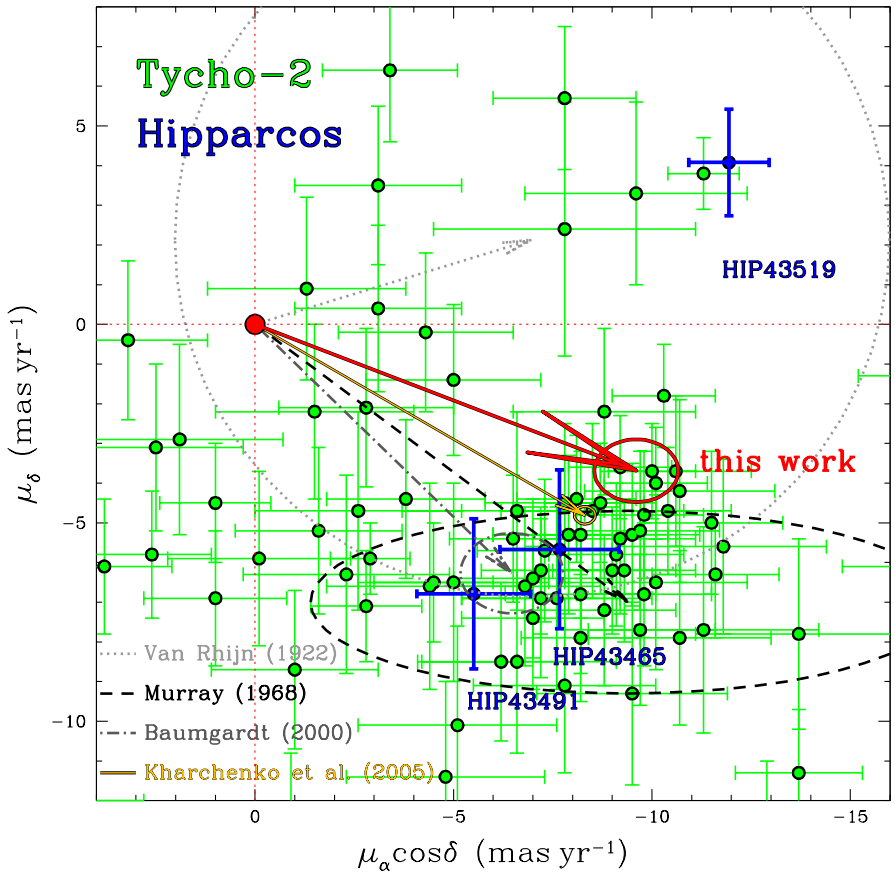

FIGURE 5.3— Comparison of our derived absolute PMs with values from the literature. The three blue points are Hipparcos PM determinations, while green points are from the Tycho-2 catalog. Our M 67 absolute PM is indicated with a red arrow, and the ellipse in its point shows our uncertainty. The other four arrows in different colors and types refer to previous values.

As expected, the errors of galaxy positions are several times larger than the typical error of star positions, and depend strongly on galaxy morphology. The comparison of the galaxy PMs (which should all be the same), suggests that we are underestimating their errors (which is not the case, for the point sources), as a result of a complex combination of seeing and galaxy shape. For this reason, we did not use their weighted mean to estimate the centroid of the galaxy PMs, but adopted an iterative σ_μ-clipped average instead.

We started with all the $N^{\rm G}\simeq$100 galaxies in the sample, for which the motion is within 20 mas yr^{-1} from the first-guess mean PM of galaxies, and we iteratively estimated their PM dispersion $\sigma_\mu^{\rm G}$ as the 1-D 68.27$^{\rm th}$-percentile of their distribution around the median motion. We then excluded from the sample those galaxies with PM>2.5$\sigma_\mu^{\rm G}$ from the median galaxies' PM, and we re-derived new values of $\sigma_\mu^{\rm G}$, median motion and $N^{\rm G}$. We iterated this procedure 10 times, noting that the values of median, $\sigma_\mu^{\rm G}$, and $N^{\rm G}$ converged after eight iterations. Final values for $\sigma_\mu^{\rm G}$ and $N^{\rm G}$ are 2.3 mas yr^{-1} and 47, respectively.

By adopting as the origin of the absolute PM system the final median value of the PM of galaxies, we found

TABLE 5.1— Non-axisymmetric Galactic model (Pichardo et al. 2003, 2004).

Parameter	Value	References
Bar half-length	3.1–3.5 kpc	Gerhard (2002)
Bar axial ratios	10:3.8:2.6	Freudenreich (1998)
Bar scale lengths	1.7, 0.64, 0.44 kpc	Freudenreich (1998)
Bar angle (respect to the Sun)	20^{o}	Gerhard (2002)
Bar mass	10^{10} $M_{\odot}$	Debattista et al. (2002)
Bar pattern speed (Ω_B)	30–60 km s^{-1} kpc^{-1}	(*)
Spiral Arms locus	Bisymmetric (Logthm)	Churchwell et al. (2009)
Spiral Arms pitch angle	15.5^{o}	Drimmel (2000)
Spiral Arms external limit	12 kpc	Drimmel (2000)
Spiral Arms: exp. with scale-length	2.5 kpc	Disk based
Spiral Arms force contrast	$\sim$ 10%	Patsis et al. (1991)
Spiral Arms pattern speed (Ω_S)	20 km s^{-1} kpc^{-1}	Martos et al. (2004)

Note: (*) Weiner & Sellwood (1999), Fux (1999), Ibata & Gilmore (1995), Englmaier & Gerhard (1999).

for M 67 an absolute PM (J2000.0) of:

$$(\mu_\alpha \cos\delta, \mu_\delta) = (-9.6, -3.7) \pm (1.1, 0.8) \text{ mas yr}^{-1},$$

where the uncertainties come from adding in quadrature the uncertainties of the centroid of M 67 members to the error of the location of the centroid of the galaxies (for each coordinate independently).

The entire sample of $\sim$100 galaxies was used to estimate the uncertainty associated with the displacement of a single, typical galaxy. This was calculated as the 1-D 68.27$^{\text{th}}$-percentile of the distribution of the galaxies around their median displacement (as computed above). Specifically: $(\sigma^{\rm G})_{\mu_\alpha \cos\delta}$=7.1 mas yr^{-1} and $(\sigma^{\rm G})_{\mu_\delta}$=5.3 mas yr^{-1}. Because we only used the most consistent subset of 47 galaxies to derive their relative median motion, we associated to the median of their displacements an uncertainty that statistically takes into account only those $N^{\rm G}$=47 galaxies. This is done by reducing the error on the single average galaxy by the factor $1/\sqrt{N^{\rm G}-1}$. This more-conservative approach might result in a overestimate of our internal errors. However, considering all the uncertainties involved in the assignment of an error to a galaxy displacement and their limited number, this is a preferable approach.

Figure 5.1 shows our absolute vector-point diagram (VPD) for all the objects in the final list (small dots). M 67 members are marked with small crosses. These are the stars within 2.3 mas yr^{-1} from the MS stars' mean PM (solid circle). Filled circles are visually-confirmed galaxies, and are shown with our estimated error bars. The best galaxies (selected with the aforementioned iterative procedure) are highlighted with red open circles. The Figure also shows the $2.5\sigma^{\rm G}$=5.7 mas yr^{-1} selection radius (dashed circle). The red arrow indicates our estimate of the absolute PM of M 67. The error bars at the base of the arrow indicate the total uncertainty (dominated largely by the estimates in the centroid of the relative PM distribution of the background galaxies). In Fig. 5.2, we used the same symbols as in Fig. 5.1 to show that there are no clear systematic errors in the galaxy PMs as a function of the coordinates of the master frame (X, and Y, parallel to α and δ, respectively).

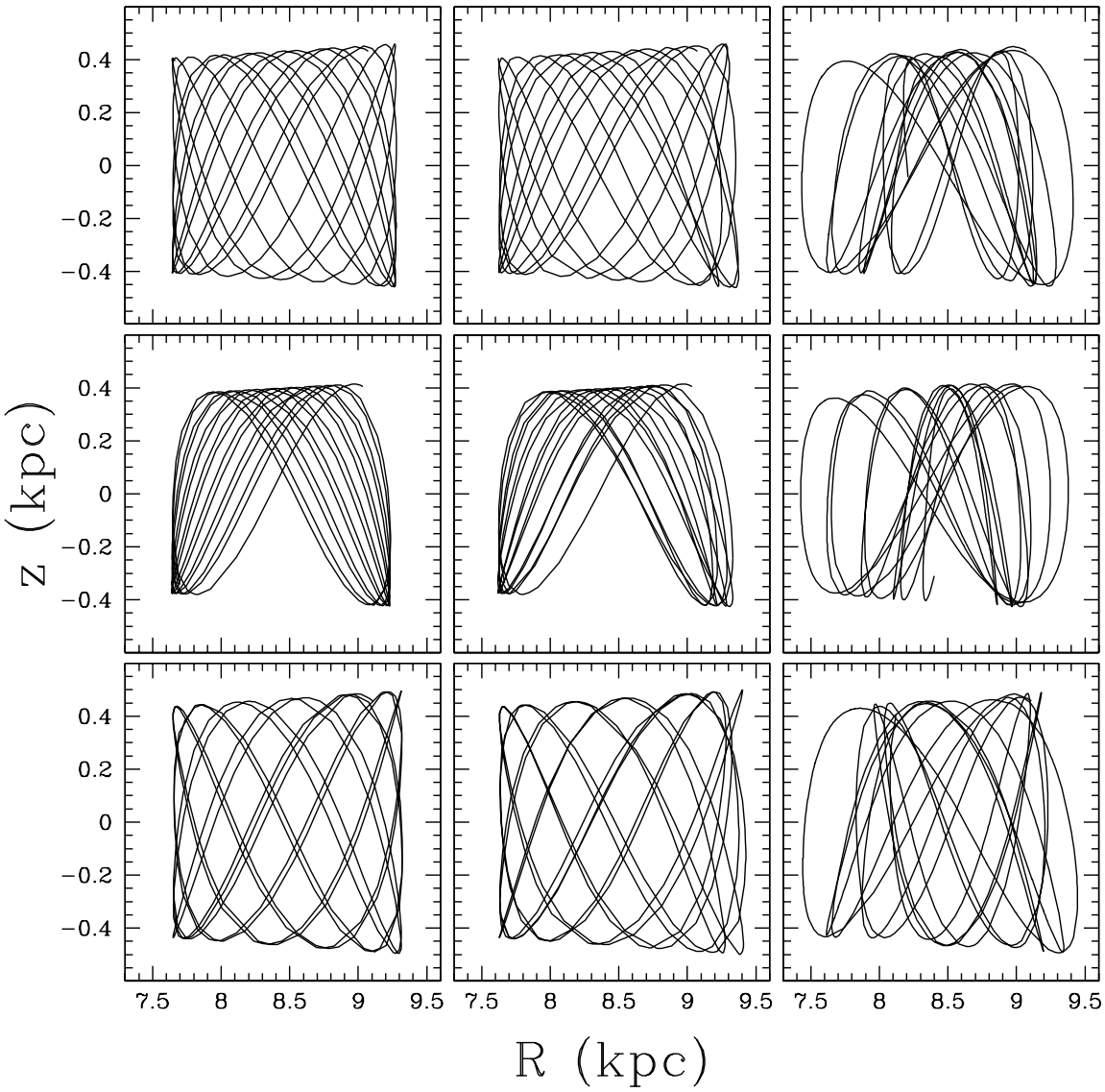

FIGURE 5.4— Meridional orbits using the three heliocentric distances; d=0.815 kpc (upper panels), 0.765 kpc (*middle panels*), and 0.865 kpc (*lower panels*), computed in the axisymmetric (*left panels*), barred (*central panels*), and with bar + spiral arms (*right panels*) scaled Galactic potential.

The absolute PM of M 67 has been measured by several authors. The first of these determinations comes from van Rhijn (1922), with $(\mu_\alpha \cos\delta, \mu_\delta) = (-7, +2) \pm (9, 9)$ mas yr^{-1}. Many years later, Murray (1968) computed $(\mu_\alpha \cos\delta, \mu_\delta) = (-9.4, -7.0) \pm (8.0, 2.3)$ mas yr^{-1}. The more contemporary work of Baumgardt et al. (2000), which made use of the two faint Hipparcos stars HIP-43491, HIP-43465 (V∼10), reports: $(\mu_\alpha \cos\delta, \mu_\delta) = (-6.47, -6.27) \pm$

TABLE 5.2— Local standard of rest initial velocity (U, V, W) and Galactic (Π, Θ) (km s^{-1}) for the three heliocentric distances d (kpc).

d	U	V	W	Π	Θ
0.815	31.92 ± 3.4	−21.66 ± 3.7	−8.71 ± 4.3	21.55 ± 3.2	233.53 ± 3.8
0.765	30.77 ± 3.0	−21.03 ± 3.4	−6.64 ± 3.6	20.98 ± 3.0	234.05 ± 3.5
0.865	33.06 ± 3.4	−22.28 ± 3.9	−10.78 ± 4.1	22.12 ± 3.4	233.02 ± 4.0

$(1.29, 1.01)$ mas yr^{-1}. Finally, Kharchenko et al. (2005) selected 27 M 67 members on the basis of their absolute PMs, as derived from the ASCC-2.5 catalog (Kharchenko 2001) —which is based on Hipparcos-Tycho family catalogs— and on their location on the V vs. $B-V$ color-magnitude diagram. The obtained mean-absolute motion of these 27 members is $(\mu_\alpha \cos\delta, \mu_\delta) = (-8.31, -4.81) \pm (0.26, 0.22)$ mas yr^{-1}.

Figure 5.3 shows (in blue) three stars in the field with Hipparcos PMs (HIP-43491, HIP-43465 and HIP-43519, with error bars), and the stars from the Tycho-2 catalog (in green). In the same plot, we mark with a red arrow our derived M 67 absolute PM, where the estimated PM error is indicated with an ellipse. Note that both the Hipparcos and the Tycho-2 stars are far too bright to be measured in our survey. Our M 67 absolute PM determination is marginally consistent with the bulk of Tycho-2 measurements for the objects in the same field. This is in line with the expected accuracies for Tycho-2. The same figure also shows (dashed arrows) previous determinations of the M 67 absolute motion.

We emphasize that the absolute PM presented here is based on *direct* observations of background galaxies, used to define the absolute reference frame. It is a purely differential measurement, which does not rely, as do previous measurements, on a complex registration to the International Celestial Reference System through a global network of objects. We end this section noticing the good agreement between the absolute PM value of M 67 as derived with the bright sources of the Hipparcos catalog (Kharchenko et al. 2005) and that based on the faint, "fix" galaxies (this Chapter).

5.3 The Galactic orbit of M 67

With the absolute PM of M 67 given in the previous section, its line-of-sight velocity of 33.78±0.18 km s^{-1} and its heliocentric distance of 815±50 pc (both from Paper II), we have computed the Galactic orbit of M 67. We employed a Galactic potential that includes the axisymmetric model of Allen & Santillán (1991) and the bar and spiral arms models of Pichardo et al. (2003, 2004). The axisymmetric background potential of Allen & Santillán (1991) has been scaled to give a rotation velocity of 254 km s^{-1} at the solar position, based on the most-recent radio astrometry observations by Reid et al. (2009). We keep the original value R_0=8.5 kpc of the solar galactocentric distance (Reid et al. (2009) give R_0=8.4±0.6 kpc). The adopted parameters for the bar and spiral arms and the corresponding references are provided in Table 5.1. The values of the parameters are based on recent observations of the Milky Way. The bar model is an inhomogeneous ellipsoidal potential that closely approximates model S of Freudenreich (1998) from the COBE/DIRBE data of the Galactic bar. For the spiral perturbation, Pichardo et al. (2003) refined their model until self-consistent orbital solutions were found. The orbital self-consistency of the spiral arms was tested through the reinforcement of the spiral potential by the stellar orbits (Patsis et al. 1991). For an extensive description of the models, see Pichardo et al. (2003, 2004).

Table 5.2 gives the local standard of rest (LSR) initial velocity (U, V, W) and the corresponding cylindrical

TABLE 5.3— Orbit parameters in the scaled axisymmetric potential for the three heliocentric distances.

d (kpc)	$r_{\rm min}$ (kpc)	$r_{\rm max}$ (kpc)	$z_{\rm max}$ (kpc)	e	P_ϕ (Myr)	P_r (Myr)	P_z (Myr)	h (kpc km s^{-1})	E (10^2 km^2 s^{-2})
0.815	7.65	9.28	0.46	0.096	207	146	76	2118.3	−1589.38
0.765	7.65	9.24	0.42	0.094	206	145	74	2114.7	−1591.50
0.865	7.66	9.33	0.50	0.098	208	147	78	2122.0	−1587.21

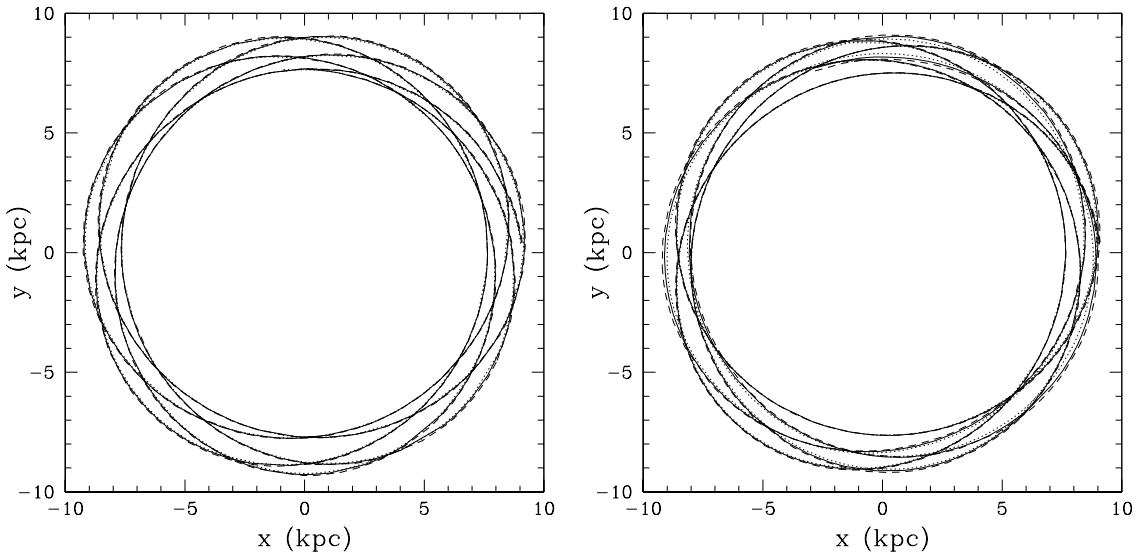

FIGURE 5.5— Projection of the orbit on the Galactic plane computed in the scaled axisymmetric potential (*left*), and in the bar + spiral arms scaled Galactic potential (*right*). We adopted an heliocentric distance d=0.815 kpc (full line), 0.765 kpc (dotted line), and 0.865 kpc (dashed line).

components (Π, Θ) for three different heliocentric distances of M 67 (central, minimum, and maximum). We used the solar motion (U, V, W)=(−10, 5.2, 7.2) km s^{-1} (Dehnen & Binney 1998). U is negative toward the Galactic center. In Table 5.3 we give some parameters of the Galactic orbits, corresponding to the three heliocentric distances, computed backwards in time during 1 Gyr in the scaled axisymmetric potential. Columns 2 and 3 show the minimum and maximum galactocentric distances and Col. 4 the maximum z-distance from the Galactic plane; the orbital eccentricity is given in Col. 5; Cols. 6 to 8 give the azimuthal, radial, and vertical periods respectively, and the last two columns the z-component of the angular momentum and energy per unit mass.

Previous computations of the Galactic orbit of M 67 were made by Keenan et al. (1973) and Allen & Martos (1988) in other axisymmetric potentials. Keenan et al. (1973) used the Galactic models of Schmidt (1956) (with an R_0 value of 8.2 kpc and a circular velocity at the Sun's position V_0=216 km s^{-1}) and of Innanen (1966) (with an R_0=10 kpc and a V_0=250 km s^{-1}). They obtained $R_{\rm max}$=8.8 kpc and 10.7 kpc respectively $z_{\rm max}$= 0.4 kpc and

an eccentricity of 0.1 for both models. Allen & Martos (1988) used their galactic model (Allen & Martos 1986) with R_0=8 kpc and V_0=225 km s^{-1}. They obtained $R_{\rm max}$=8.7 kpc, $z_{\rm max}$=0.48 kpc and an eccentricity of 0.11. In all cases, the orbit of M 67 has a small eccentricity, and the differences found are mostly attributable to the different Galactic parameters and values for the solar motion employed. Indeed, the different values obtained for $R_{\rm max}$ result mostly from the scaling of the Sun-center distance, as shown by the ratios $R_0/R_{\rm max}$, which are all between 1.07 and 1.09. The more contemporary, much-improved Galactic models and the precise value now available for the absolute proper motion of M 67 should result in a more reliable orbit for this cluster.

We also computed the Galactic orbit of M 67 in the non-axisymmetric potential, first including only the bar, then with the bar + spiral arms. The scaled background axisymmetric potential was considered. The angular velocity of the bar was taken as Ω_B=60 km s^{-1} kpc^{-1}; the other parameters of the non-axisymmetric components are given in Table 5.1. In the case with spiral arms, the mass of these arms was taken as 2.2% the mass of the scaled disk component, which is 3% of the mass of the original disk. This mass gives a force contrast as listed in Table 5.1.

Figure 5.4 shows the meridional orbits computed in the axisymmetric potential (left panels), axisymmetric + bar potential (central panels) and axisymmetric + bar + spiral arms potential (right panels), using the three heliocentric distances. As shown, the potential that includes only the Galactic bar gives an orbit similar to that obtained with the axisymmetric potential. This is because the orbit of M 67 lies far outside the region of the bar. However, the potential that includes both the bar and spiral arms shows a different behavior. The orbit is perturbed by the spiral arms, mainly in the radial direction. The radial dispersion is not very strong in M 67, but distorts what would be a box orbit. Thus, a moderate spiral potential has important effects in the kinematics of orbits near the Galactic plane, as is the case in M 67, and in general, as is the case for the solar neighborhood stars (Antoja et al. 2009). This result holds for the allowed variations in proper motion, radial velocity and distance, because the most important parameter that affects the orbit is the mass of the spiral arms.

In left panel of Fig. 5.5 we show the projection of the orbit on the Galactic plane, computed in the axisymmetric potential. At the scale shown in this figure there is no appreciable difference between the orbits using the three heliocentric distances. The right panel shows the corresponding orbits in the axisymmetric + bar + spiral arms potential. There is a slight difference in the azimuthal behavior in both figures.

We have also computed the tidal radius of M 67 in the axisymmetric + bar + spiral arms scaled potential. With a total mass in M 67 of 279 $M_\odot$, listed by Piskunov et al. (2008), using King's equation (King 1962) we obtained a mean tidal radius of 7.1 pc. With the alternative equation (1) in Allen et al. (2006) the tidal radius is 8 pc. Both results are near the 9.6 pc value listed by Piskunov et al. (2008).

Bibliography

Allen, C. & Martos, M. A. 1986, Rev. Mexicana Astron. Astrofis., 13, 137
Allen, C., & Martos, M. A. 1988, Rev. Mexicana Astron. Astrofis., 16, 25
Allen, C., & Santillán, A . 1991, Rev. Mexicana Astron. Astrofis., 22, 255
Allen, C., Moreno, E., & Pichardo, B. 2006, ApJ, 652, 1150
Antoja, T., Valenzuela, O., Pichardo, B., Moreno, E., Figueras, F., & Fernández, D. 2009, ApJ, 700, 78
Anderson, J., , Bedin, L. R., Piotto, G., Yadav, R. S., & Bellini, A. 2006, A&A, 454, 1029 (Paper I)
Anderson, J. et al. 2008, AJ, 135, 2055 (A08)
Baumgardt, H., Dettbarn, C., & Wielen, R. 2000, A&AS, 146, 251
Bedin, L. R., Piotto, G., King, I. R., & Anderson, J. 2003, AJ, 126, 247
Bedin, L. R., Piotto, G., Carraro, G., King, I. R., & Anderson, J. 2006, A&A, 460, L27
Bellini, A., & Bedin, L. R. 2009, PASP, 121, 1419
Bellini, A., et al. 2009, A&A, 493, 959 (Paper III)
Bellini, A., & Bedin, L. R. 2010, A&A accepted, arXiv:1005.0848
Bellini, A., et al. 2010, A&A 513, A50 (2010a)

Bellini, A., Bedin, L. R., Pichardo, B., Moreno, E., Allen, C., Piotto, G., & Anderson, J. 2010, A&A, 513, A51 (2010b)
Churchwell, E., et al. 2009, PASP, 121, 213
Debattista, V. P., Gerhard, O., & Sevenster, M. N. 2002, MNRAS, 334, 355
Dehnen, W., & Binney, J. 1998, MNRAS, 298, 387
Drimmel, R. 2000, A&A, 358, 13
Englmaier, P., & Gerhard, O. 1999, MNRAS, 304, 512
Freudenreich, H. T. 1998, ApJ, 492, 495
Fux, R. 1999, A&A, 345, 787
Gerhard, O. 2002, ASPC, 273, 73
Girard, T. M., Grundy, W. M., Lopez, C. E., & van Altena, W. F. 1989, AJ, 98, 227
Ibata, R. A., & Gilmore, G. F. 1995, MNRAS, 275, 605
Innanen, K. A. 1966, ApJ, 143, 153
Keenan, D. W., Innanen, K. A., & House, F. C. 1973, AJ, 78, 173
King, I. R. 1962, AJ, 67, 471
Kharchenko, N. V. 2001, Kinematika i Fizika Nebesnykh Tel, 17, 409
Kharchenko, N. V., Piskunov, A. E., Röser, S., Schilbach, E., & Scholz, R.-D. 2005, A&A, 438, 1163
Martos, M., Hernández, X., Yáñez, M., Moreno, E., & Pichardo, B. 2004, MNRAS, 350, 47
Murray, C. A. 1968, Royal Greenwich Observatory Bulletin, 141, 339
Patsis, P. A., Contopoulos, G., & Grosbol, P. 1991, A&A, 243, 373
Pichardo, B., Martos, M., Moreno, E., & Espresate, J. 2003, ApJ, 582, 230
Pichardo, B., Martos, M., & Moreno, E. 2004, ApJ, 609, 144
Piskunov, A. E., Schilbach, E., Kharchenko, N. V., Röser, S., & Scholz R. -D. 2008, A&A, 477, 165
Reid, M. J., et al. 2009, ApJ, 700, 137
Richer, H. B., Fahlman, G. G., Rosvick, J., & Ibata, R. 1998, ApJL, 504, L91
Schmidt, M. 1956, BAN, 13, 15
van Rhijn, P. J. 1922, Pub. of the Kapteyn Astronomical Lab. Groningen, 33, 1
Weiner, B. J., & Sellwood, J. A. 1999, ApJ, 524, 112
Yadav, R. K. S., et al. 2008, A&A, 484, 609 (Paper II)
Zacharias, N., et al. 2009, VizieR Online Data Catalog, 1315, 0

6

WFI@2.2m proper-motions of the globular cluster ω Centauri.

This and the following two Chapters are dedicated to most well-studied globular cluster of our Galaxy: ω Centauri. This puzzling object is distinguished by its numerous features: significant dispersion in metallicity, multiple populations, triple main-sequence, horizontal branch morphology, He-rich population(s), and extended star-formation history. Intensive spectroscopic follow-up observing campaigns targeting stars at different positions in the color-magnitude diagram promises to clarify some of these peculiarities. To be able to target cluster members reliably during spectroscopic surveys and both spatial and radial distributions in the cluster outskirts without including field stars, a high quality proper-motion catalog of ω Cen and membership probability determination are required.

The only available wide field proper-motion catalog of ω Cen is derived from photographic plates, and only for stars brighter than $B \sim 16$. Using ESO archive data, we create a new, CCD-based, proper-motion catalog for this cluster, extending to $B \sim 20$. We used high precision astrometric software developed specifically for data acquired by WFI@2.2m telescope and presented in Anderson et al. (2006) We demonstrated previously that a 7 mas astrometric precision level can be achieved with this telescope and camera for well exposed stars in a single exposure, assuming an empirical PSF and a local transformation approach in measuring star displacements. We achieved a good cluster-field separation with a temporal base-line of only four years. We corrected our photometry for sky-concentration effects. We provide calibrated photometry for $UBVR_CI_C$ wide-band data plus narrow-band filter data centered on Hα for almost 360 000 stars.

We confirm that the ω Cen metal-poor and metal-rich components have the same proper motion, and demonstrate that the metal-intermediate component in addition exhibits the same mean motion as the other RGB stars. We provide membership probability determinations for published ω Cen variable star catalogs. Our catalog extends the proper-motion measurements to fainter than the cluster turn-off luminosity, and covers a wide area ($\sim 33' \times 33'$) around the center of ω Cen. Our catalog is electronically available to the astronomical community.

This Chapter contains results published in *Astronomy & Astrophysics* (Bellini et al. 2009a).

6.1 Introduction

The globular cluster ω Centauri (ω Cen) is the most luminous and massive cluster in the Galaxy. Observational evidence collected over the years has indicated that ω Cen is also the most puzzling stellar system in terms of

stellar content, structure, and kinematics. Probably the most well studied of its peculiarities is one related to its stellar metallicity distribution (Norris & Bessell 1975; 1977; Freeman & Rodgers 1975; Bessell & Norris 1976; Butler et al. 1978; Norris & Da Costa 1995; Suntzeff & Kraft 1996; Norris et al. 1996). There is a significant dispersion in the iron abundance distribution of ω Cen, with a primary peak about [Fe/H] ~ -1.7––1.8 and a long tail, extending to [Fe/H] ~ -0.6, which contains another 3-4 secondary peaks. It is possible to identify these metallicity peaks with distinct stellar populations (Pancino et al. 2000; Rey et al. 2004; Sollima et al. 2005; Villanova et al. 2007). Ground-based (Lee et al. 1999; Pancino et al. 2000) and *Hubble Space Telescope* (*HST*) (Anderson 1997; Bedin et al. 2004; Ferraro et al. 2004) photometry show clearly that ω Cen hosts different stellar populations. In particular, Pancino et al. (2000) demonstrated that the ω Cen red giant branch (RGB) consists of at least four distinct branches, spanning a wide range of metallicity. On the other hand, the ω Cen sub giant branch (SGB) has an intricate web of 5 distinct sequences, indicating an extended range of metallicity and age (see Bedin et al. 2004; Hilker et al. 2004; Sollima et al. 2005; Stanford et al. 2006; Villanova et al. 2007).

Anderson (1997), Bedin et al. (2004), and Villanova et al. (2007), by studying fainter stars with deep and high resolution *HST* photometry, demonstrated that the main sequence (MS) is divided into 3 distinct sequences. The spectroscopic study of the MS stars of ω Cen by Piotto et al. (2005) showed that the bluest of the main sequences is more metal rich than any of the redder sequences, which increased the ambiguity surrounding the cluster. An overabundance of He in the blue MS could reproduce the ω Cen MS photometric and spectroscopic properties (Bedin et al. 2004; Norris 2004; Piotto et al. 2005), although the origin of the puzzling MS morphology is still far from being understood.

A deeper insight into the enigmatic stellar populations of ω Cen should combine a deep, high resolution analysis of the inner and most crowded regions, with a wide field observations of the outskirts. While the first type of data has been provided adequately by *HST*, wide field coverage of ω Cen requires ground-based data which are more difficult to obtain. Acquisition of data for a wider field-of-view will inevitably result in higher contamination by Galactic foreground/background populations. The only reasonable and efficient way to decontaminate the ω Cen outer stellar populations is by means of proper-motion analysis that help to isolate the Galactic contribution. The only available wide field ω Cen proper-motion catalog (van Leeuwen et al. 2000, hereafter vL00) is based on photographic observations and only provides measurements for stars brighter than $B \sim 16$. In this Chapter, we attempt to provide the first CCD-based proper motion catalog of ω Cen, extending the cleaned stellar populations down to $B \sim 20$, i.e. 4 mag. deeper than vL00.

In Anderson et al. (2006), hereafter Paper I, demonstrated that WFI@2.2m observations, with a time baseline of only a few years, allow a successful separation of cluster members from Galactic field stars in the two GCs closest to the Sun: NGC6121 and NGC6397. Here we apply the high precision astrometric and photometric techniques developed by Paper I to all available WFI@2.2m archive data of ω Cen.

In Sect. 2, we describe the available WFI observations of ω Cen, and the data sets that we used to derive proper motions. In Sect. 3, we discuss our photometric data reduction technique, the sky-concentration effect minimization, and the photometric calibration. In Sect. 4, we describe in detail how we treated the differential chromatic refraction (DCR) effects between the two epochs. Membership probability is discussed in Sect. 5, while in Sect. 6 we outline possible applications of our catalog. Finally, in Sect. 7, we summarize our results and describe the electronic catalog.

6.2 Observations

We used a collection of 279 archive images acquired between January 20, 1999 and April 14, 2003 at the ESO/MPI2.2m telescope at La Silla (Chile) equipped with the wide-field imager camera (WFI). A detailed log of observations is reported in Table 6.1. This camera, which consists of an array mosaic of 4×2 chips, 2141×4128 pixels each, has a total field of view of $34' \times 33'$, and a pixel scale of $0.238''$/pixel. More details of the instrumental setup were given in Paper I. Images were obtained using U, B, V, R_C, I_C wide-band and 658 nm (Hα) narrow-band filters, whose characteristics are summarized in Table 6.2.

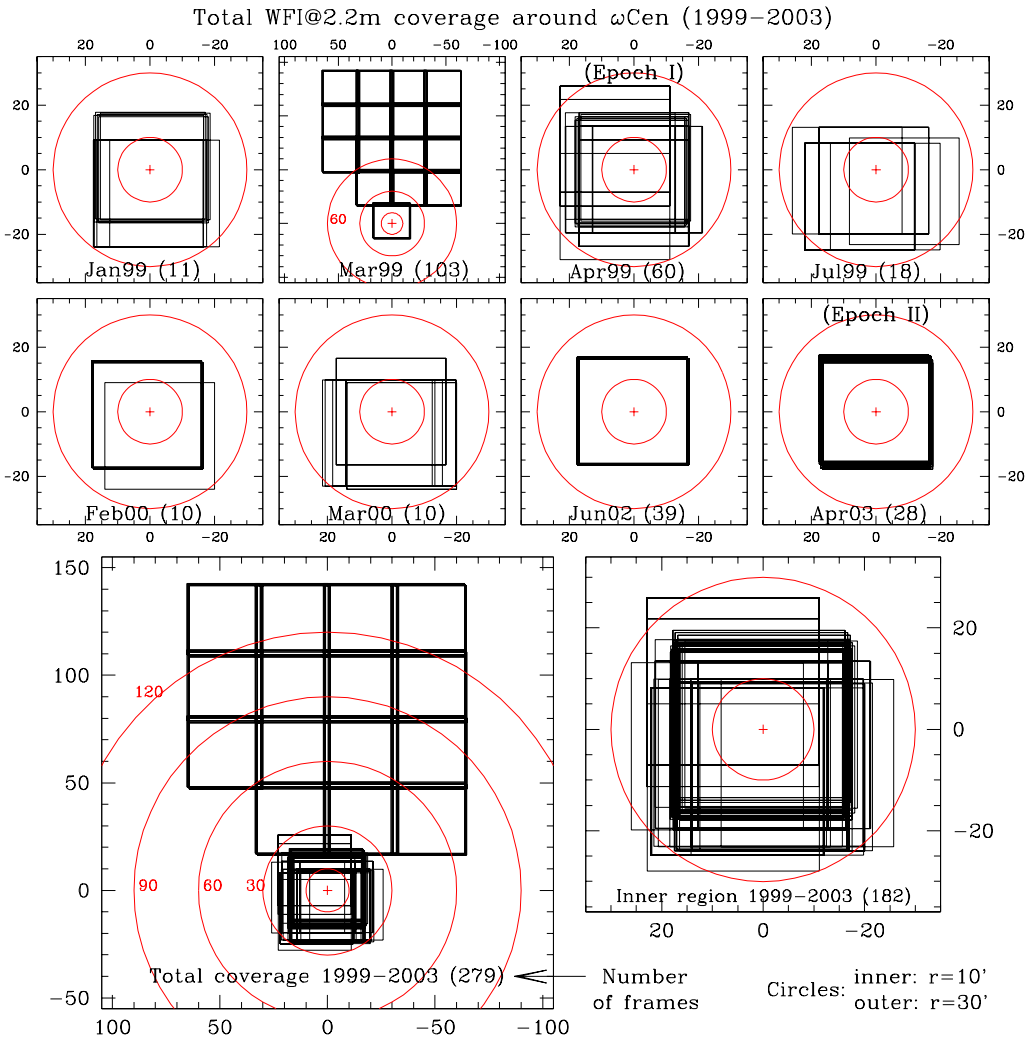

FIGURE 6.1— Position footprint of the entire sample of WFI images around the ω Cen center (marked with a "+"). The first two rows show the covered areas sorted by month and year. In the lower panels of the figure, the total coverage of all of the 279 images (on the left), and a zoom-in of the central part of the cluster (on the right) are shown. The numbers in parenthesis after the dates represent the total number of images for that observing run. North is up, East to the left.

For the derivation of proper motions, we used only *B* and *V* images acquired in April 1999 and April 2003 (see Sect. 6.4 for further details of this choice). The total field-of-view covered by the entire sample is indicated in Fig. 6.1, where axis coordinates are ($\Delta\alpha \cos\delta$, $\Delta\delta$), expressed in units of arcmin from the ω Cen center (North is up, East is to the left). Concentric circles have diameters, if not specified, of 10′ (inner circle) and 30′ (outer circle), and are centered on the cluster center: $\alpha = 201°.69065$, $\delta = -47°.47855$ (Van de Ven et al. 2006).

The first eight plots show the covered areas sorted by month and year, while in the bottom part of Fig. 6.1 the total coverage of all of the 279 images (on the left), and a zoom of the central part of the cluster (on the right) are shown. In the catalog presented here, the proper motion measurements are available only within the field-of-view

TABLE 6.1— Description of the data set used for the WFI@2.2m catalog.

filter	t_{exp}	seeing	airmass
	January, 1999		
B_{842}	3×30s,1×300s;	1.″0–1.″3	~ 1.20
658 nm	1×120s,5×180s,1×900s;	1.″0–1.″3	1.15–1.18
	March, 1999		
V_{843}	52×200s;	0.″8–1.″2	1.1–1.2
I_{845}	51×150s;	0.″7–1.″5	1.1–1.45
	April, 1999		
R_{844}	1×5s,1×10s,1×15,1×30,5×60s;	1.″0–1.″3	1.3–1.6
I_{845}	1×5s,1×10s,1×20s,1×45s,4×90s;	0.″74–1.″7	1.4–1.9
658 nm	2×30,4×120,5×180s;	0.″8–1.″15	1.1–1.2
	(epoch I)		
B_{842}	1×15s,1×30s,1×60s,5×120s;	0.″75–1.″3	1.2–1.5
V_{843}	3×5s,3×10s,1×15s,2×20s;	0.″7–1.″0	1.2–1.6
	1×30s,4×45s,10×90s;	0.″76–1.″36	1.1–1.5
	July, 1999		
U_{877}	2×1800s;	1.″4–1.″6	~ 1.14
B_{842}	1×10s,1×30s,1×40s,1×300s;	1.″4–1.″8	1.14–1.25
V_{843}	1×10s,1×20s,1×150s,1×240s;	1.″3–1.″6	1.15–1.25
I_{845}	1×10s,2×20s,1×240s;	1.″13–1.″6	1.17–1.25
658 nm	3×120s,1×1200s;	1.″13–1.″5	1.18–1.23
	February, 2000		
B_{842}	2×30s,2×240s;	1.″45–1.″7	~ 1.13
V_{843}	1×30s,2×240s;	1.″1–1.″2	~ 1.13
I_{845}	1×30s,2×240s;	~ 1.″0	~ 1.13
	March, 2000		
U_{841}	4×300s,1×2400s;	1.″1–1.″2	1.17–1.38
V_{843}	5×30s;	0.″9–1.″4	~ 1.45
	June, 2002		
U_{877}	4×30s,7×300s;	0.″8–2.″0	1.14–1.18
B_{878}	1×5s,3×8s,9×60s;	0.″8–1.″5	1.13–1.16
V_{843}	3×5s,3×40s,3×60s;	0.″75–2.″0	~ 1.13
I_{845}	3×20s,3×40s;	0.″7–1.″4	~ 1.13
	April, 2003 **(epoch II)**		
B_{878}	7×40s;7 × 120s;	0.″7–0.″9	1.14–1.16
V_{843}	7×40s;7 × 120s;	0.″8–1.″0	1.13

in common between the two epochs used (see Fig. 6.1).

6.3 Photometry, astrometry and calibration

6.3.1 Photometric reduction

For the reduction of the WFI@2.2m photometric data, we used the software img2xym_WFI, a modified version of img2xym_WFC.09x10 (Anderson & King 2003), which was written originally for *HST* images, adapted success-

TABLE 6.2— Characteristics of the used filters (from WFI manual) λ_c=central wavelength, FWHM=Full Width at Half Maximum, λ_p=transmission peak wavelength, T_p=transmission percentage at peak level. (*) LWP means Long Wave Pass: in this case the cutoff limit is determined by the CCD quantum efficiency.

Wide-band filters

Name	λ_c [nm]	FWHM [nm]	λ_p [nm]	T_p [%]
U_{877} (U/50)	340.4	73.2	350.3	82.35
U_{841} (U/38)	363.7	38.3	362.5	51.6
B_{878} (B/123)	451.1	133.5	502.5	88.5
B_{842} (B99)	456.3	99.0	475.0	91.2
V_{843} (V/89)	539.6	89.4	523.0	87.0
R_{844} (R_C)	651.7	162.2	668.5	93.9
I_{845} (I_C/lwp)	783.8	LWP*	1001.0	97.6

Narrow-band filters

Name	λ_c [nm]	FWHM [nm]	λ_p [nm]	T_p [%]
658 nm (Hα)	658.8	10.3	504.0	90.7

fully to ground-based data, and described in detail in Paper I. We closely followed the prescription given in Paper I for the data reduction of WFI images. This includes standard operations with the pixel data, such as de-biasing, flat-fielding, and correction for cosmic rays hits.

At the basis of the star position and flux measurements, there is the fitting of the *empirical* Point Spread Function (PSF). In our approach, the PSF is represented by a look-up table on a very fine grid. It is well known that the shape of the PSF changes with position in WFI@2.2m chips. This variability can be modeled by an array of PSFs across the chip. The img2xym_WFI software works in a fully-automated way to find appropriate stars to represent the PSF adequately. For practical purposes, the number of PSF stars per chip can vary between 1 and 15, depending on the richness of the star-field. An iterative process is designed to work from the brightest to the faintest stars and find their precise position and instrumental flux. A reasonably bright star can be measured with a precision of ~ 0.03 pixel (~ 7 mas) on a single exposure.

Another problem of the WFI@2.2m imager is a large geometric distortion in the focal plane that effectively changes the pixel scale across the field-of-view. There are different ways to map this geometric distortion. We adopted a 9×17 element look-up table of corrections for each chip, derived from multiple, optimally-dithered observations of the Galactic bulge in Baade's Window (Paper I). This look-up table provides the most accurate characterization of geometrical distortions available for the WFI@2.2m. At any given location on the detector, a bilinear interpolation between the four closest grid points on the look-up table provides the corrections for the target point. The derived look-up table may have a lower accuracy at the edges of a field, because of the way in which the self-calibration frames were dithered (see Paper I). An additional source of uncertainty is related to a possible instability distortions in the WFI@2.2m reported earlier. This prompted us to use the local transformation method to derive proper motions (see Sect. 6.4).

6.3.2 Sky-concentration correction

Once we obtained star positions and instrumental fluxes for all images, we had to minimize the so-called "sky-concentration" effect. The WFI@2.2m camera is affected significantly by this kind of light contamination (Manfroid & Selman 2001), which is caused by spurious reflections of light at discontinuities in the optics and the subsequent redistribution of light in the focal plane. The insidiousness of the effect is due to the fact that this

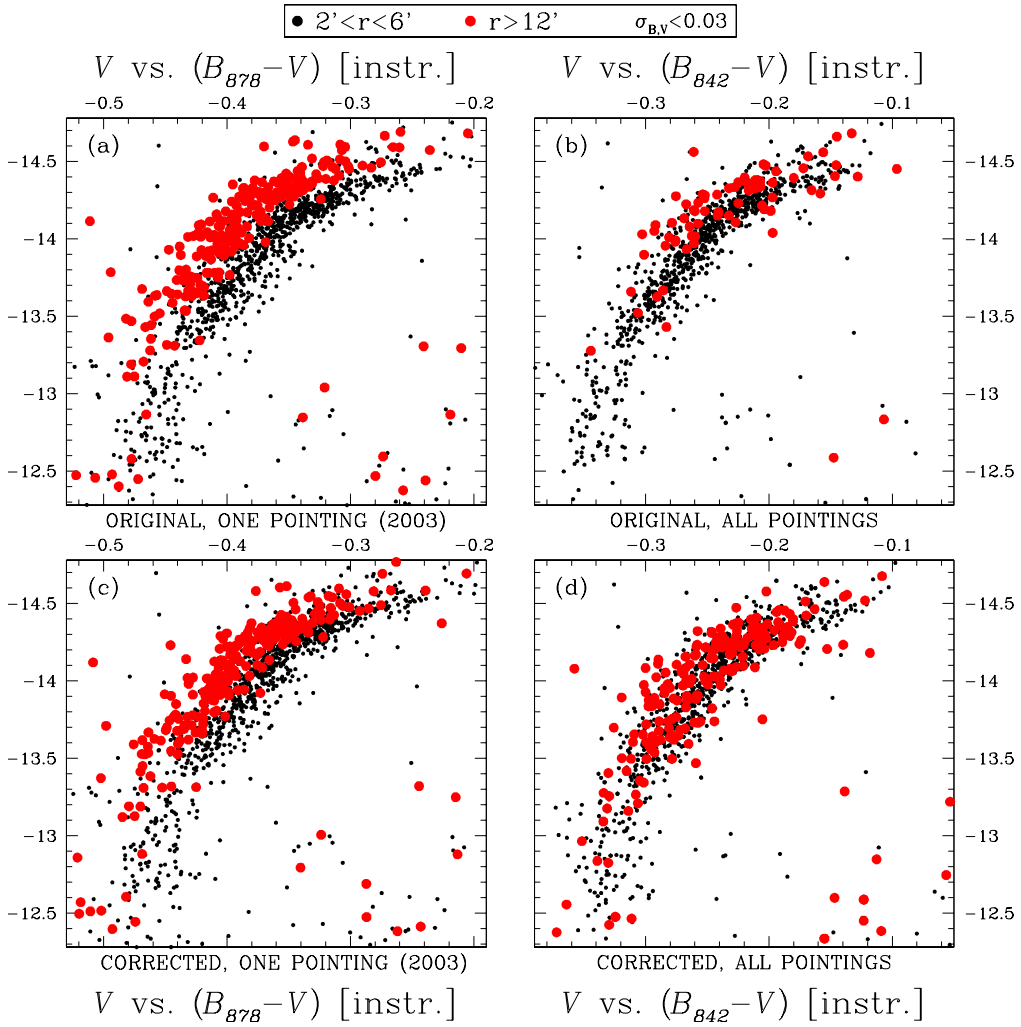

FIGURE 6.2— CMDs zoomed into the HB region of ω Cen. All plotted stars have $\sigma_{B,V} < 0.03$ mag. On the left, we used only images taken in April 2003 (i.e. only one pointing). On the right, we show photometry from all V and all B_{842} images that have independent pointings. Upper diagrams are for the original photometric catalogs. The lower ones are derived from sky-concentration-corrected catalogs. Black dots are stars located close to the mosaic center, while red dots are stars close to the mosaic edges.

redistribution of light affects both the science and the flat-field exposures.

Star fluxes are calculated by considering a local sky value, and therefore may be a negligible effect. However, since sky contamination also affects flat images, if it is not corrected properly during pre-reduction procedures, the quantum efficiency of the central pixel will be artificially lower with respect to that of the corner pixel. Consequently, the luminosity of a star measured in the middle of the mosaic camera will be underestimated by ~ 0.1–0.2 magnitudes (in V band) with respect to the luminosity of the same star detected close to the mosaic edges.

In Fig. 6.2a, we plot an instrumental[1] color-magnitude diagram (CMD), which has been zoomed into the

[1]Instrumental magnitudes are calculated to be $-2.5\times\log(\Sigma_i DN_i)$, where DN are the pixel's Digital Numbers above the local

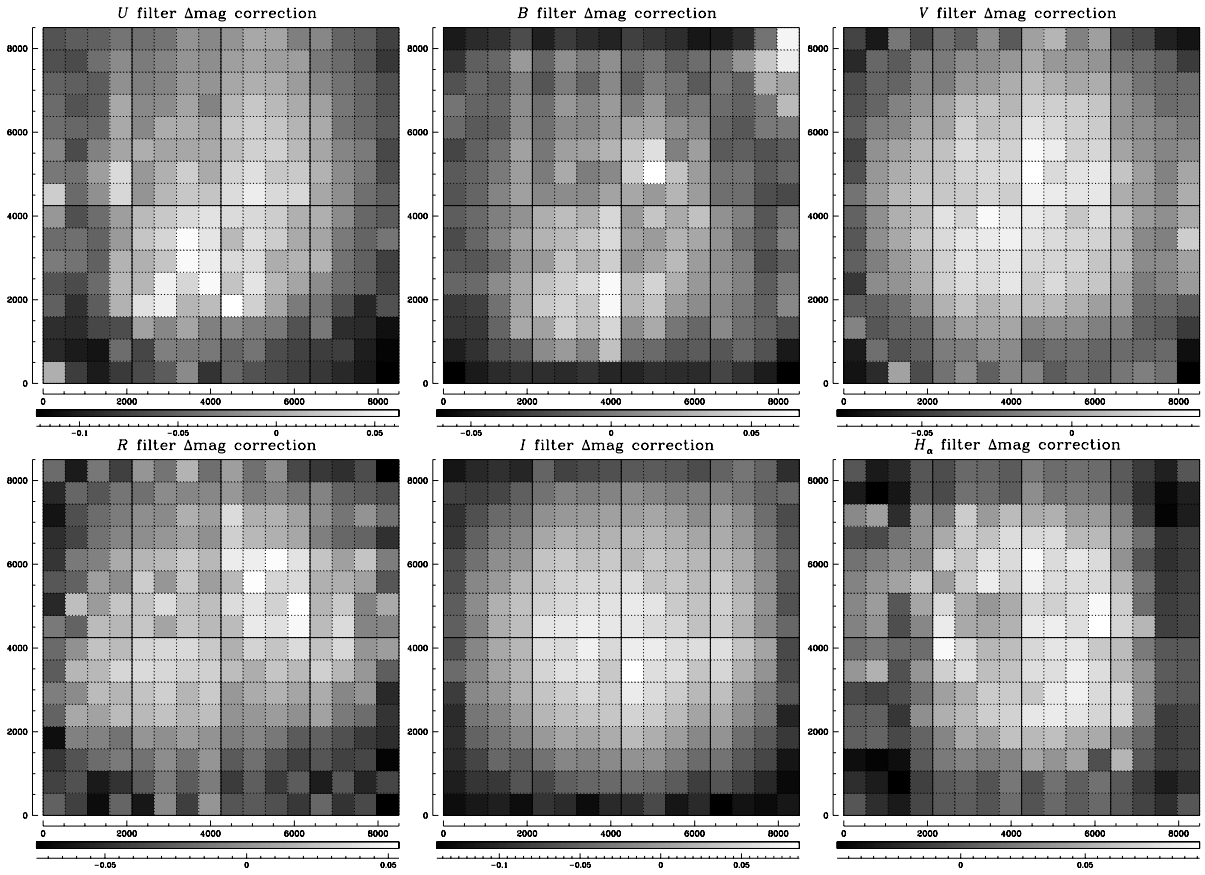

FIGURE 6.3— Final Δmag correction grids for the different filters (B means the B_{842} filter only). Coordinates are in units of WFI pixels. Each WFI chip is highlighted by continuous black lines. Each element of the correction grids is colored according to the corresponding Δmag correction applied. The grey scales are relative to the minimum/maximum correction for each filter.

horizontal-branch (HB) region of ω Cen, obtained by combining all V and B_{878} images of April 2003. We chose this particular data set to highlight the effect of sky concentration on undithered images. In fact, this data set has only one pointing, as shown in Fig. 6.1. The positions of stars on the CCD mosaic is almost identical from one image to another, implying a small contribution to the rms of the single star magnitude measurement due to sky-concentration effects. In Fig. 6.2a, we plotted 1252 stars with $\sigma_V < 0.03$ mag and $\sigma_B < 0.03$ mag, where σ_V and σ_B are the standard errors of a single measurement (rms).

However, with only one pointing, sky concentration maximizes its effect on the relative photometry of stars located at different positions on the image. In Fig. 6.2a, we highlight the CMD of stars located at different positions on the CCD mosaic: with black dots (994 objects precisely), we show all stars between 2′ to 6′ from ω Cen center, which is close to the mosaic center ($x = 4150.69, y = 4049.97$ on our master meta-chip). Red points are stars (258 objects) outside 12′. The displacement of the two HBs clearly shows that sky-concentration effects affect WFI photometry significantly if only one pointing is analyzed, and therefore needs to be corrected.

In our case, the analyzed data sets for different filters come from several pointings (except the case of B_{878} images). In the process of matching all catalogs (for a given filter) to create a single master-frame, the true sky-

sky summed within a 10-pixel circular aperture. For a mean seeing of 0.8″, saturation initiates at about ~ -14.5.

concentration effect is reduced. For a given star, we considered the mean of the star fluxes originating in different positions and for different pointings, so that the sky-concentration effect in the master frame was reduced. This process does, however, create systematic errors that affect the global photometry (see Selman 2001).

In Fig. 6.2b, we show the same zoomed HB region of ω Cen derived, in this case, by matching all the available V and B_{842} images obtained from the ESO archive. This data set contains several different pointings for both filters, so we were able to obtain photometry for the same stars located in some cases close to the mosaic center and in other pointings close to the mosaic edges. All plotted stars have again $\sigma_{B,V} < 0.03$ mag. In this case, only 972 stars (with the same previous convention, 896 black and 76 red) passed the selection criteria on the basis of photometric error. As explained before, matching catalogs for different pointing tends to minimize sky-concentration effects, but without an appropriate correction, rms of measurements for the stars are enhanced.

Andersen et al. (1995) studied the sky-concentration effect, typical of focal reducers, both by using simulations and analyzing data from the Danish telescope at La Silla. Their method for deriving the sky-concentration correction was based on the complex analysis of many star-field images taken at different orientations and positions during the night. Manfroid et al. (2001) applied a similar method to derive the sky-concentration effect for WFI@2.2m data, while Selman (2001) developed a method to estimate the sky-concentration effect by the analysis of the zero-point variation in 3 dithered stellar frames, by evaluating this variations using a Chebyshev polynomial fit. They were able to reduce the internal error from 0.034 to 0.009 magnitudes in the V filter, and used the same polynomial fit to correct in addition the photometry in the other filters (see also Selman & Melnick 2005). Koch et al. (2004) provided an analogous prescription to correct for the sky-concentration effect by comparing photometry derived with WFI and Sloan Digital Sky Survey (SDSS) data. Finally, Calamida et al. (2008) used some of the ω Cen images that we present in this Chapter to correct for the positional effects of the WFI camera by means of photometric comparisons with the local standard stars of ω Cen.

The correction given by the ESO team, based on the V filter, consists of a 9$^{\rm th}$ order bidimensional Chebyshev polynomial that should in principle be used also for the U and B filters. Selman (2001) found that his solution for the V band was able to reduce the internal photometric error from 0.029 to 0.010 mag in B, and from 0.040 to 0.014 in U, while for the other filters the V correction failed to reduce the internal photometric error. Selman (2001) argued that this is probably due to problems associated with atmospheric variations affecting data for different filters. Unfortunately, by using the same polynomial coefficients to correct both V and B magnitudes, it is impossible to remove the color degeneracy due to the different response of the CCD to the sky concentration in the two different photometric bands. This degeneracy is of the order of $\sim$ 0.04–0.05 mag in color in our V versus $B-V$ CMD between inner stars (r $\sim 4'$) and outer stars (r $> 12'$).

Our adopted solution consists of a self-consistent autocalibration of the sky-concentration map, and takes advantage of the high number of images analyzed, taken with different pointings. Below, we provide a description of the autocalibration procedure. We measured the raw magnitude $\mathrm{mag}_{i,j}$ of each i-star, in each j-image. We selected an image to be a reference frame (at the center of the dither pattern), and by using common stars with frame j we were able to compute the *average* magnitude shifts to bring each image-catalog onto the magnitude reference frame (Δ_j).

If there were no systematic errors, the same stars measured at different positions in two different frames, should have the same magnitude value, within the random measurement errors:

$$\mathrm{mag}_{i,0} - \Delta_0 = \ldots = \mathrm{mag}_{i,j} - \Delta_j = \ldots = \mathrm{mag}_{i,m} - \Delta_m,$$

where m is the total number of images in that filter, used to perform the autocalibration procedure.

However, the same star closer to the center of the camera is systematically fainter than when it is measured closer to the camera edges. For each star, measured in several different frames, and at different positions on the camera, we can compute an average of the values of the magnitudes in the reference system:

$$\overline{\mathrm{mag}_i} = \left(\frac{1}{m}\right) \sum_{j=1}^{m} \left(\mathrm{mag}_{i,j} - \Delta_j\right).$$

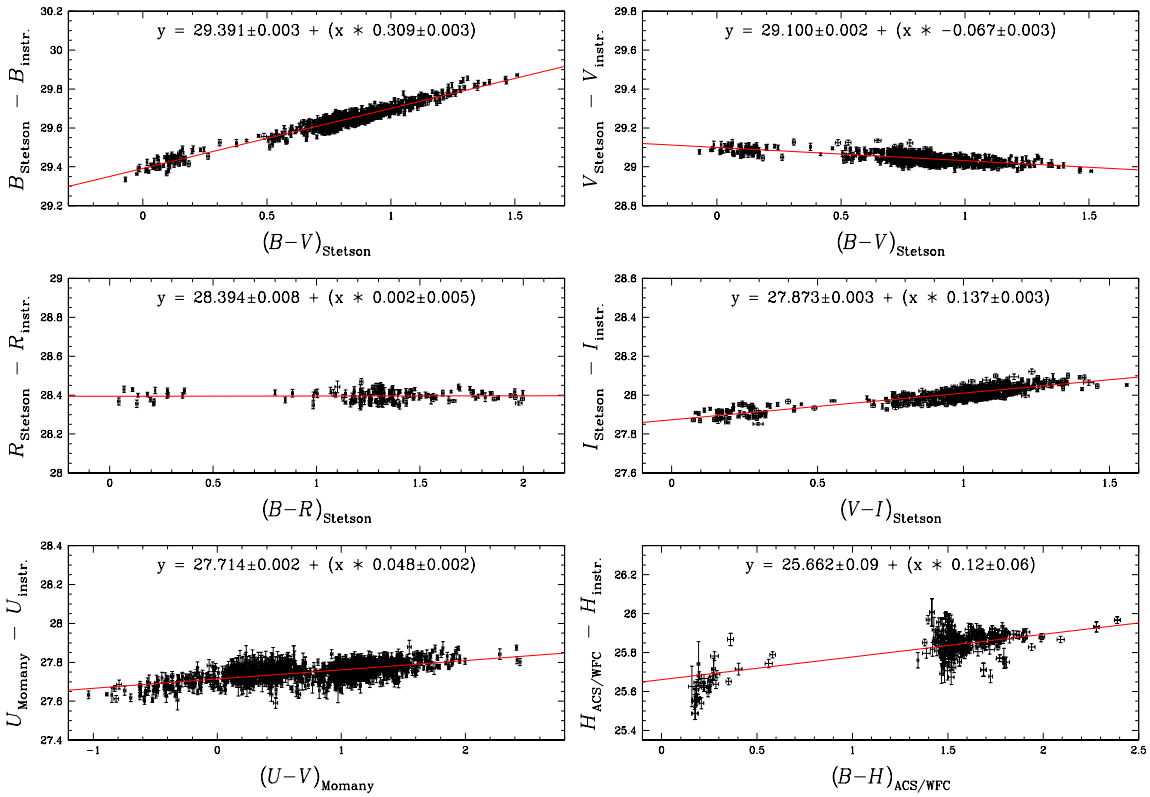

FIGURE 6.4— These figures show our calibration fits with the adopted color equations. For the B, V, R_C, I_C filters we used the on-line set of standard stars provided by Stetson, while for U and Hα bands we used as reference stars the Momany et al. (2003) catalog and the ACS/WFC catalog of Villanova et al. (2007), respectively. See the text for more details.

In the same way, we can compute a residual for the i-star in the j-image:

$$\delta_{i,j} = (\mathrm{mag}_{i,j} - \Delta_j) - \overline{\mathrm{mag}_i}.$$

All the residuals of stars close to the center will be systematically positive, and those close to the edges systematically negative. It appears clear that –at any given location on the camera– the average of the residuals from all the stars measured close to that location will provide a first spatial correction to our photometry. It also appears clear that the determination of the sky-concentration photometric correction will be an iterative process.

To guarantee convergence, we applied half of the recommended correction at the given location, to all our image catalogs. We then recomputed the Δ_j, and repeated the procedure until all the residual averages, at any given location, became smaller than 0.001 magnitudes. The null hypothesis of this procedure is that the same star is imaged several times at different locations on the detector. To avoid systematic error, we also select, for each filter, the same number of exposures per different pointing (as much as possible with the existing database).

We use only those stars of the image catalogs with high S/N ratio (i.e. instrumental magnitude from -11 to -14) with a quality PSF-fit smaller than 0.1 (as defined by Anderson et al. 2008), and not too close to the cluster center (which does not necessarily coincide with the center of the camera) to avoid crowding, which compromises the photometric precision. The exact closeness to the center of the cluster depends on the image exposure time; we excluded stars within a radius of 1000–2000 pixels from the ω Cen center.

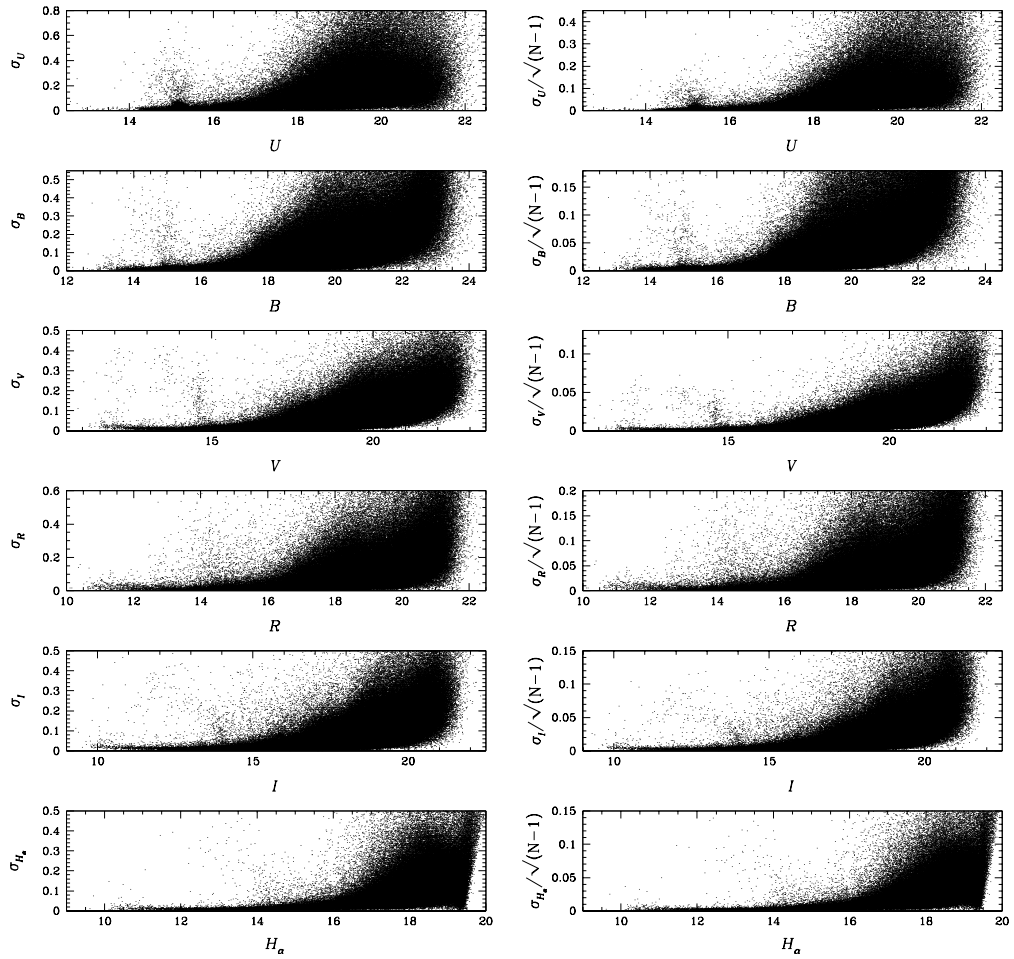

FIGURE 6.5— (*Left panels*): plot of magnitude rms (σ) as a function of magnitude. (*Right panels*): plot of the standard error of the mean ($\sigma/\sqrt{N-1}$, where N is the number of measurements) as a function of magnitude.

At this point, we define the expression of "given location". After several tests, we found a spatial grid of 16×16 boxes to be the most suitable compromise between a large number of residuals ($\delta_{i,j}$) and a spatial resolution of correction sufficiently high to be useful. In Fig. 6.3, we show our final correction grids, respectively for U, B_{842}, V, R_C, I_C, and Hα filters. For each filter, we present the final 16×16 element correction grid. Each element is colored according to the grey scale values (black for the minimum, white for the maximum). The grey scales vary linearly from the minimum to the maximum grid value for each filter. It is clear that sky concentration affects different filters in different ways, and each filter must therefore be corrected independently. To evaluate the correction at any point of the camera, we completed a bilinear interpolation of the closest 4 grid points. The adopted correction was less accurate close to the mosaic edges, where the peripheral grid-points have been stretched toward the boundaries. The available pointings for the other filters are also lower than for B_{842} and V, implying a less effective correction

of the sky concentration.

We emphasize that our correction is not completed by a star-to-star comparison. After the spatial correction, a single star cannot have a lower random error (higher precision) than $\overline{\mathrm{mag}_i}$. However, the systematic errors (accuracy) of single stars relies on the quality of individual grid-point solutions, which were always calculated to be the average of residuals for several stars within each of the 16×16 cells. Even if our random errors for individual stars are $\sim$ 0.1 mag, with just 10 stars [in the worst case we still have at least 10 such stars] we can reduce our systematic errors to $\sim$ 0.03 mag. The condition that each star has to be observed in each of the 16×16 cells is the ideal case. Deviations from this ideal case occur frequently, although overall, we are close to achieving the optimal solution.

The total amplitude of our correction for the V filter is 0.13 mag. For the same filter, Manfroid & Selman (2001) evaluated a 0.13 mag correction of similar spatial shape. Nevertheless, the two totally independent calibrations appear to be qualitatively the same. Based on the cell-to-cell scatter with the knowledge that sky-concentration is relatively flat, in V and I filters (for which we have more images) we estimate that the accuracy of our solution is as good as $\sim$ 0.03 mag. Although our corrections do not use any color information, we note that the post-corrected CMD is in excellent agreement with (to within a few hundreds of a magnitude) the HB location (Fig. 6.2).

To verify qualitatively the high quality of our sky-concentration correction procedure, we show in Fig. 6.2d the same CMD region (V vs. $B_{842} - V$), derived using all the available images, after applying our correction. Stars located at different positions on the meta-chip are not affected by the sky-concentration effect, and are located in the same CMD region. The total number of plotted stars (1227, all with $\sigma_{B,V} < 0.03$ mag) is comparable with that of Fig. 6.2a; this implies that we were able to remove the systematic contribution from our photometric rms values.

Our solution works well for the available ω Cen archive data sets (used to derive the corrections), but archive observations, in general, do not map every chip in a way that enables a sky-concentration correction that is universally applicable to be derived. We cannot guarantee that our solution can be applied to achieve the same positive results with other data sets. As proof of this issue, we applied our B_{842} solution, to B_{878} images with only one pointing.

Images collected using the B_{842} and B_{878} filters are not so different, in term of central wavelength (see Table 6.2): sky-concentration effects appear to be similar for almost identical filters (since they are related to atmospheric variations that affect the data for a range of different filters), so a photometric improvement is expected after correcting B_{878} images with our B_{842}-derived solution. If our solution fails to correct the B_{878} photometry, this is probably due to the different pointings of the two B filters instead of the filters themselves. As shown in Fig. 6.2c, we found that a photometric improvement is present, with respect to Fig. 6.2a, but that the correction is not satisfactory.

6.3.3 Instrumental $UBVR_CI_C$-Hα photometric catalog

We derived instrumental single-filter catalogs using all available images, by matching each chip individually to minimize the zero-point differences between WFI chips. Included stars were measured in at least three distinct images. Photometric single-filter catalogs were then linked to the astrometric one. Linked star positions agreed with those in the proper-motion catalog within 1 pixel for BVR_CI_CHα filters, while for the U filter we had to adopt a larger matching radius (3.5 pixels). This is mainly due to the poorer distortion solution in the U band.

Due to the aforementioned sky-concentration minimization problem with B_{878} images, our B photometry refers to the B_{842} filter.

As for the U photometry, we used only U_{877} images: in fact, U_{841} is a "medium" rather than a wide-band filter, of quite different central wavelength and a low transmission efficiency with respect to U_{877} (Table 6.2). If not specified otherwise, we refer to B_{842} and U_{877} simply using B and U, respectively.

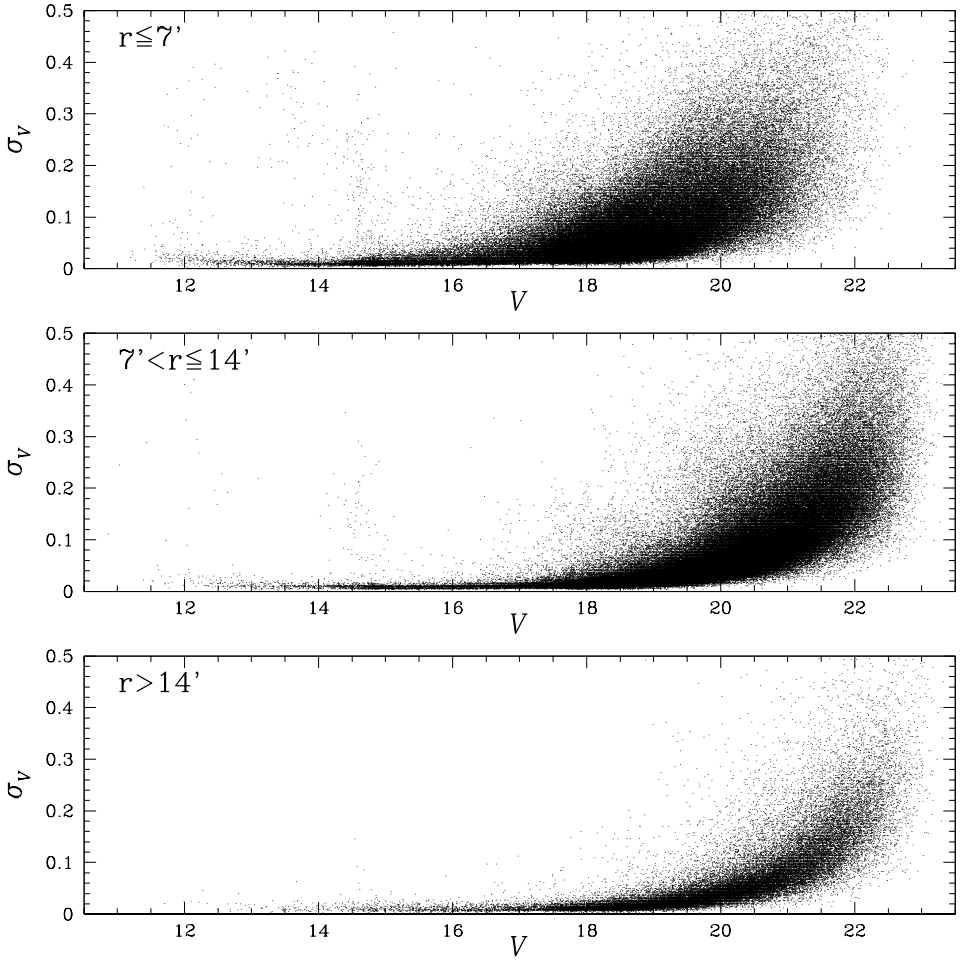

FIGURE 6.6— Photometric rms for stars within 7′ (*top panel*), from 7′ to 14′ (*middle panel*), and outside 14′ (*bottom panel*).

6.3.4 Photometric calibration

The photometric calibration of the WFI@2.2m data for BVR_CI_C bands was performed using a set of $\sim$ 3000 online wide field photometric ω Cen Secondary Standards stars (Stetson 2000, 2005). The Secondary Standards star catalog covers an area of about $30' \times 30'$ around the cluster center. We calibrated our U instrumental photometry by cross-correlating our photometry with Momany et al. (2003) U calibrated catalog (Stetson does not provide U photometry for the ω Cen Secondary Standards). For Hα calibration, we used as reference-standard stars the 3×3 central ACS/WFC mosaic photometric catalog in F658N band (GO 9442), which was presented by Villanova et al. (2007). This *HST* catalog was obtained using img2xym_WFC.09x10 software; instrumental magnitudes were transformed onto the ACS Vega-mag flight system following Bedin et al. (2005), and by using the zero points of Sirianni et al. (2005).

For BVR_CI_C bands, we matched our instrumental magnitudes and colors to the Stetson standard ones, and

derived calibration equations by means of an iterative least squares fitting of a straight line (see Fig. 6.4). For these filters, we found that only a first-order dependency of the color term affects our instrumental magnitudes. The linearity of our calibration equations, which cover a wide range of colors (being derived from both HB and RGB stars) is evident from the plots of Fig. 6.4.

As in the calibration of our U instrumental photometry, the Momany et al. (2003) catalog was not corrected for sky-concentration effects. We found a magnitude dependence related to the star positions. We adopted a straight line fit to derive the calibration equation, because we were unable to consider the different color/magnitude dependencies individually. Therefore, our calibrated U magnitudes were not more reliable than the 0.15 magnitude level (maximal error).

For the Hα filter, we again performed a straight line fit to derive the calibration equations, even though the data appear to suggest a second order color effect (see the corresponding panel of Fig. 6.4). ACS/WFC data cover only the inner $\sim 10' \times 10'$ region of our catalog, and are therefore taken in extremely crowded conditions. This effect might strongly influence our photometry mimicking the aforementioned second-order effect. In Fig. 6.5, we show in the left panels our photometric errors for each filter, as a function of the corresponding magnitude. The photometric errors (standard deviation) have been computed from multiple observations, all reduced to the common photometric reference frame in the chosen bandpass. In the right panels of Fig. 6.5, we plot the photometric standard error of the mean –to be defined as $\sigma/\sqrt{N-1}$, where N is the total number of observations– versus the magnitude, for each filter.

To illustrate more clearly the dependence of our photometric rms on crowding, we show (for the V filter only) in Fig.6.6 the photometric rms σ_V with respect to V for stars within $7'$ (top panel), from $7'$ to $14'$ (middle panel), and outside $14'$ (bottom panel). Stars located in the most crowded region of the field suffer higher uncertainty in their photometry.

Our final catalog consists of about 360 000 stars, in $UBVR_CI_C$ wide-band and 658 nm narrow-band filters, covering a wide area ($\sim 33' \times 33'$) centered on ω Cen. We reach 3 magnitudes in V band below the TO point with a photometric rms of 0.03 mag.

6.3.5 Zero-point residuals

Even if our sky-concentration correction works well, residuals are still present, especially close to the corners of our final catalog. Due to the wide field area analyzed in this Chapter, there is also the possibility of a contribution from differential reddening. Using *ubvy* Strömgren and $V\,I$ photometry, Calamida et al. (2005) developed an empirical method to estimate the differential reddening of ω Cen. The authors found that the reddening can vary in the range $0.03 \lesssim E(B-V) \lesssim 0.15$ from Strömgren filters, and $0.06 \lesssim E(B-V) \lesssim 0.13$ from $V\,I$ filters, within their analyzed field-of-view of $14' \times 14'$, which was centered on the center of ω Cen. However, the results by Calamida et al. (2005) were questioned by Villanova et al. (2007), and the quantitative value of the differential reddening still needs to be confirmed.

In the case of the $B-V$ color, the maximum zero-point residual in our final catalog is less than 0.1 mag. To minimize any zero-point variations, we used a method similar to that described by Sarajedini et al. (2007). Briefly, we defined the fiducial ridge-line of the most metal-poor component of the ω Cen RGB and tabulate, at a grid of points across the field, how the observed stars in the vicinity of each grid point may lie systematically to the red or the blue of the fiducial sequence; this systematic color offset is indicative of the local differential reddening.

Our on-line catalog magnitudes are not corrected for differential reddening to enable the user to adopt their preferred correction method in removing differential reddening and zero-point residuals.

6.4 Proper-motion measurements

To complete the proper-motion analysis, we used only the B and V images taken in April 1999 (epoch I) and April 2003 (epoch II). This choice was due to the fact that: (i) we have a fine-tuned geometric distortion correction map for V filter (Paper I), which has been proven to work well for the two B filters (Paper I); (ii) it offers the widest

possible time base-line of $\sim$ 4 yrs; and (iii) we have a relatively high number of images in both epochs, and with relatively deep exposures.

We first photometrically selected probable cluster members in the V versus $B-V$ color-magnitude diagram. These stars are located on the RGB (see the RGB selections in the top-panel of Fig. 6.13, within the magnitude interval $14.6 < V < 17.2$. We used these stars only as a local reference frame to transform the coordinates from one image to the system of the other images at different epochs and therefore derive relative proper motions. By using predominantly cluster stars, we ensure that proper motions will be measured relative to the bulk motion of cluster stars. The expected intrinsic velocity dispersion of ω Cen stars for which we can measure reliable proper motions, is between 10 and 15 km s^{-1} (Merritt, Meylan & Mayor 1997). If we assume a distance of 5.5 kpc for ω Cen, as reported by Del Principe et al. (2006), and isotropic distribution of stars (good to first order), then these translate into an internal dispersion of 0.4–0.6 mas yr^{-1}.

Over the four-year epoch, the difference would result in a displacement of only 1.5–2.3 mas, which is a factor of 3 smaller than the random measurement errors ($\sim$ 7 mas). Conversely, the tangential velocity dispersion of field stars is a factor of $\sim$ 10 larger than the intrinsic velocity dispersion of the cluster. For field stars, proper motions are clearly not negligible with respect to measurement errors, and this has an adverse effect on the coordinate transformations. We removed iteratively stars from the preliminary photometric member list that had proper motions clearly inconsistent with cluster membership, even though their colors placed them close to the fiducial cluster sequence.

To minimize the effects of geometric-distortion-solution residuals on proper motions, we used local transformations based on the closest 20 reference stars, typically extending over $\sim$ 30 arcsec. These were well-measured cluster stars of any magnitude selected to be on the same CCD chip, as long as their preliminary proper motion is consistent with cluster membership. No systematic errors larger than our random errors are visible close to the corners or edges of chips.

To avoid possible filter-dependent systematic errors, we measured proper motions in the V and B bandpasses only, for which the geometrical distortion corrections were derived originally (Paper I). Individual errors of proper motions for single stars were estimated as described in Sect. 7.3 of Paper I. For both epochs separately, we estimated the intra-epoch rms error from all same-epoch plates transformed locally to the same reference frame. The proper-motion errors were computed to be the rms of the proper motion, obtained by solving locally each first-epoch frame into each second-epoch frame. These errors, however, were not entirely independent because the same frames were used more than once. Therefore, to obtain our most reliable estimate of the proper-motion standard error, we added in quadrature the intra-epoch rms of each epoch.

In Fig. 6.7, we show our proper-motion rms, in units of mas yr^{-1}, versus V magnitudes, calculated as $\sigma_\mu = \sqrt{\sigma^2_{\mu_\alpha \cos\delta} + \sigma^2_{\mu_\delta}}$. The top panel presents stars within 7′ of the center of ω Cen, the middle panel is for stars between 7′ and 14′, while the lower panel shows the errors for stars outside 14′. The vertical dashed line indicates the saturation limit of the deepest exposures ($V = 14.6$), while the continuous line is at $V = 16.5$, the vL00 faintness limit. The precision of our proper-motion measurement is $\lesssim$ 0.03 WFI pixels in 4 yrs down to $V \sim 18$ mag (i.e. $\sigma \lesssim 1.9$ mas yr^{-1}). At fainter magnitudes, the errors gradually increase, reaching $\sim$ 5 mas yr^{-1}at $V = 20$. The stars brighter than $V \sim 13$ magnitude show a higher dispersion because of the image saturation even in the shortest exposures. Horizontal lines in Fig. 6.7 indicate the median proper-motion rms of unsaturated stars brighter than $V = 16.5$. We have 1.3 mas yr^{-1}, 1.1 mas yr^{-1}, and 1.3 mas yr^{-1}for the top, middle, and bottom panel, respectively. The higher value for the inner stars is due to crowding while, for the outer stars, there is a combination of three factors: (1) our geometrical distortion solution is less accurate close to the WFI mosaic edges; (2) there are fewer cluster members, per unit area, usable as a reference for deriving proper motions; (3) we have a lower number of images that overlap with the external areas of the field-of-view.

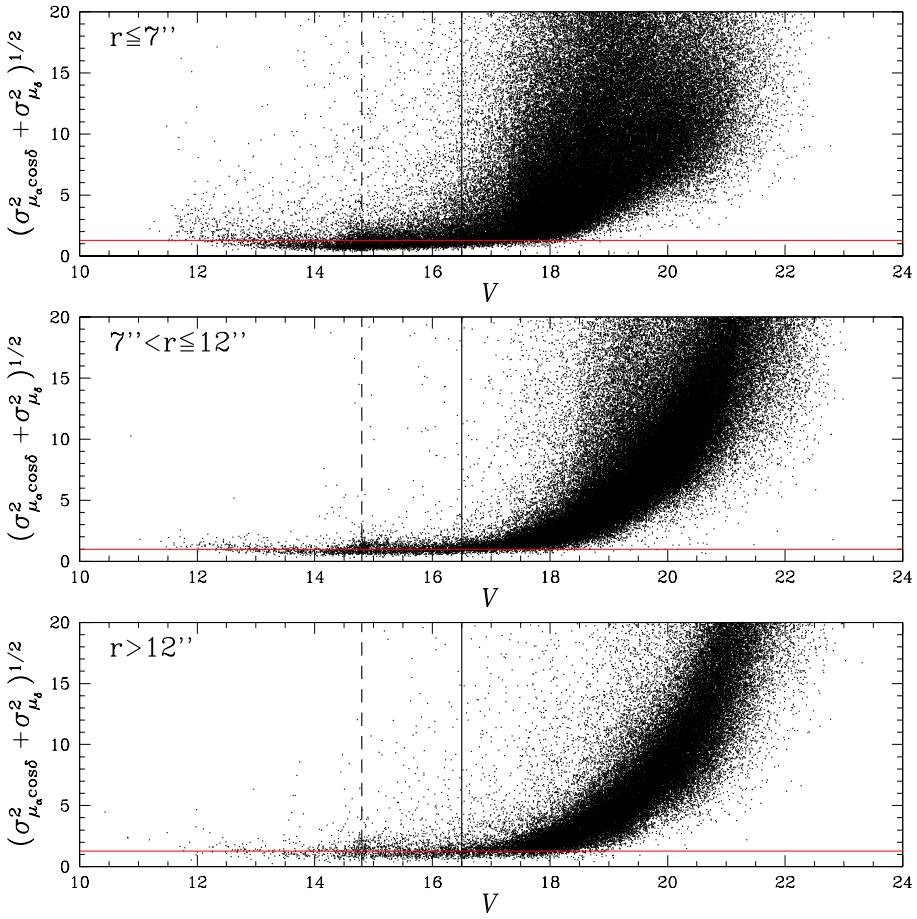

FIGURE 6.7— Proper-motion errors for stars within 7′ (*top panel*), from 7′ to 14′ (*middle panel*), and outside 14′ (*bottom panel*). The proper-motion errors are expressed in the units of mas yr^{-1}.

6.4.1 Cluster CMD decontamination

To probe the effectiveness of our proper motions in separating cluster stars from the field stars, we show in Fig. 6.8 the vector-point diagrams (VPDs, top panels), and the CMDs in the V vs. $B-V$ plane (bottom panels). In the left panels, we show the entire sample of stars; the middle panels display what we considered to be probable cluster members; the right panels show predominantly the field stars. Plotted stars have a V rms lower than 0.03 mag.

In the VPDs, we draw a circle around the cluster centroid of radius 3.9 mas yr^{-1}. Provisionally, we define as cluster members all points in the VPD within this circle. The chosen radius is the optimal compromise between missing cluster members with uncertain proper motions, and including field stars that have velocities equal to the cluster mean proper motion. Even this approximate separation between cluster and field stars demonstrates the power of proper motions derived in this study. A description of membership probability is given in Sect. 6.5.

6.4.2 Differential chromatic refraction (DCR)

The DCR effect causes a shift in the photon positions in the CCD, which is proportional to their wavelength, and a function of the zenithal distance: blue photons will occupy a position that differs from that of red photons. The

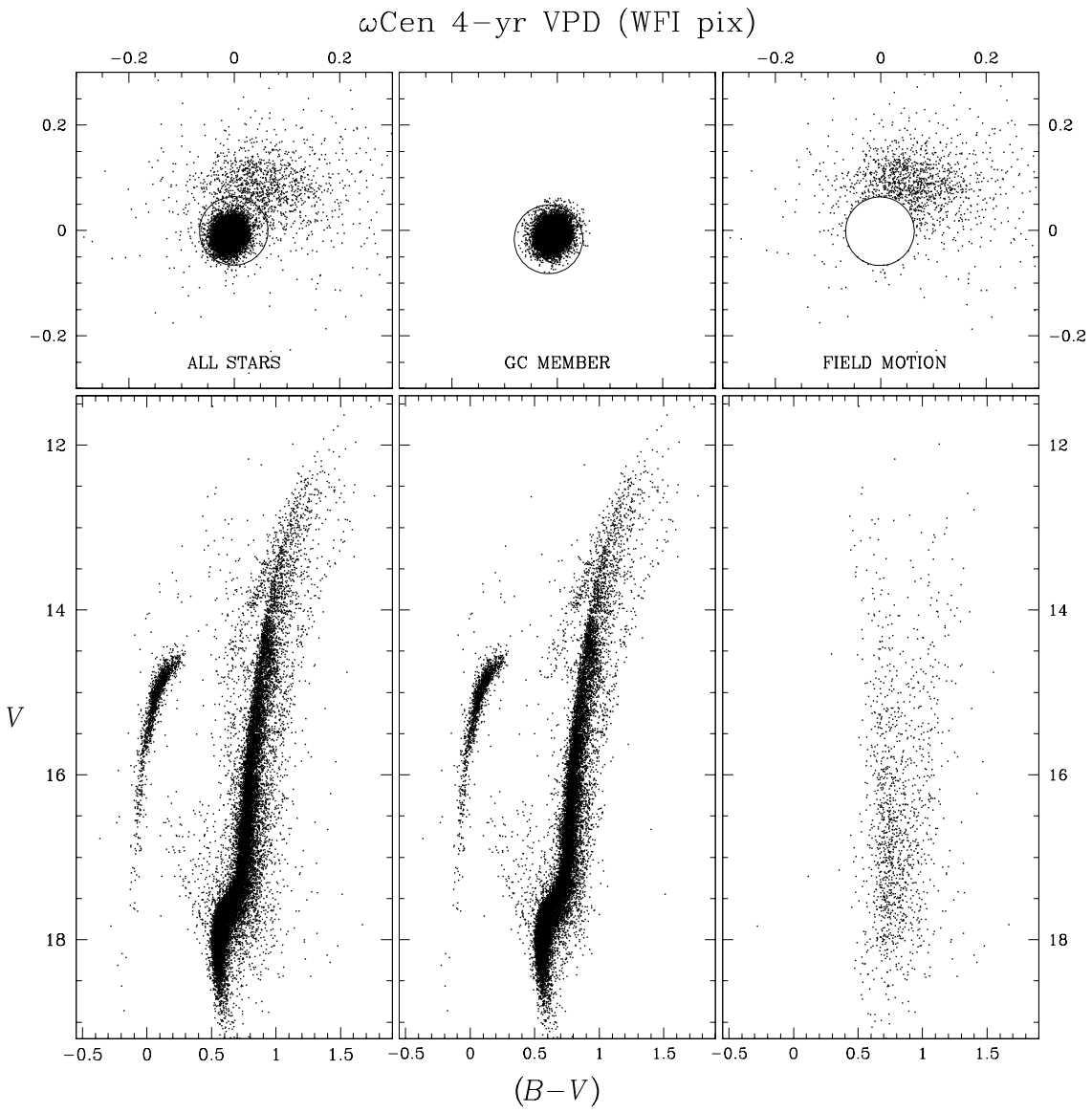

FIGURE 6.8— (*Top-panels*): proper-motion vector-point diagram. Zero point in VPD is the mean motion of cluster stars candidates. (*Bottom panels*): calibrated V, $(B-V)$, color-magnitude diagram. (*Left*): the entire sample. (*Center*): stars in VPD with proper motion within 0.065 pixels (i.e. $\sim 3.9\,\mathrm{mas\,yr^{-1}}$) around the cluster mean. (*Right*): probable background/foreground field stars in the area of ω Cen studied here. All plots show only stars with proper-motion σ smaller than 0.032 pixels (i.e. $\sim 1.9\,\mathrm{mas\,yr^{-1}}$) and V magnitude rms smaller than 0.02.

DCR effect is easier to detect and remove from CCDs, due to their linearity.

Unfortunately, within each epoch, the available data sets are not optimized to perform the DCR correction directly (Monet et al. 1992), because the images have not been taken at independent zenithal distances. We can,

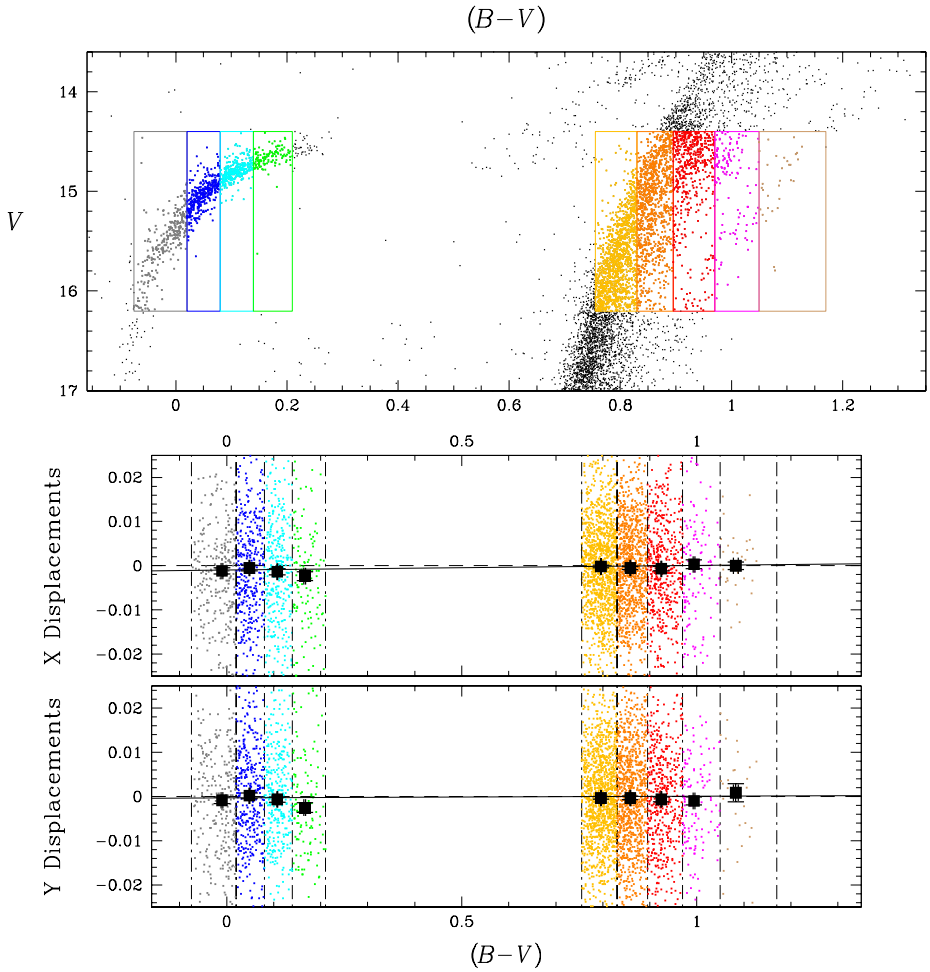

FIGURE 6.9— (*Top panel*): selected stars in the CMD of ω Cen for DCR effect correction. (*Middle and bottom panels*): star displacements along *X* and *Y* axes, as a function of stars ($B-V$) color. The median shift of the nine samples are also showed, with errors. The continuous lines show the adopted fits used to quantify the DCR effects.

however, check if possible differences in the DCR effect between the two epochs could generate an apparent proper motion for blue stars relative to red stars.

We selected four samples of stars located on the HB, and five on the RGB, as shown in Fig. 6.9 (top panel), with different colors to estimate the DCR effect, in a magnitude interval of 1.8 mag in V ($14.4 \leq V \leq 16.2$), with proper motions ≤ 3.8 mas yr^{-1}and rms ≤ 1.9 mas yr^{-1}. We chose this magnitude range to: (i) avoid luminosity-dependent displacements (if any); (ii) include stars with a low rms in positions and fluxes (see Fig. 6.5, 6.7), excluding saturated stars; and (iii) cover the widest possible color baseline according to the above points (i) and (ii). For each of the nine samples, we derived the median color and the median proper motion along $\mu_\alpha \cos\delta$ and μ_δ, and their respective errors. Proper motions were expressed in the terms of a displacement over 4 years, that is

in the units of WFI pixels along the X and Y axes of a detector (parallel to the RA and Dec directions).

In Fig. 6.9, we show, in the top panel, the selected stars on the CMD used to examine the DCR effect; the linear fits adopted for the X and Y displacements are shown in the lower part of the figure. We found a negligible DCR effect along both X and Y axes. For this reason, we have not corrected our measurements for this effect.

In Fig. 6.10, we show, on the left, our calibrated V, $B-V$ CMD, divided into eight magnitude bins. In each bin, we adopted different selection criteria to identify cluster members, which were more stringent for stars with more reliable measurements from data of high signal-to-noise ratio, and less restrictive for star with less precise measurements. Plotted stars have a proper-motion rms of < 1.8, mas yr^{-1} for the brightest bin, to 5 mas yr^{-1} for the faintest one. The Photometric rms for both the bands range between 0.02 mag for the brightest bin to 0.05 for the faintest one, which is sufficient to include main-sequence stars down to $V = 20$. For each magnitude bin, we considered as cluster members those stars with a proper motion within the circle shown in the middle column of Fig. 6.10.

On the right side of Fig. 6.10, we show the color-magnitude diagram for stars assumed to be cluster members. The available archive images are again not sufficiently deep to derive reliable proper motions below the TO. The proper motions presented here are not sufficiently accurate to study the internal motion of ω Cen. The main purpose of the proper motion presented in this Chapter is to provide a reliable membership probability for spectroscopic follow-up projects, star counts, and the study of the radial distribution of the different branches (Bellini et al. 2009b).

6.4.3 Astrometric calibration

To translate the pixel coordinates into the equatorial coordinate system, we adopted the UCAC2 catalog (Zacharias et al. 2004) as a reference frame. Due to the severe crowding in images of the inner parts of ω Cen, this catalog was however inadequate for calibration purposes close to the center of ω Cen (the central $10' \times 10'$ area corresponds almost entirely to a void in UCAC2). Another possible reference frame, especially for the cluster center, is the vL00 catalog. However, the precision of published coordinates is lower than $\sim$ 20 mas and no analysis was provided by vL00 for the presence of potential systematic errors in the positions. Examination of vL00 proper motions by Platais et al. (2003) indicated that *a priori* these systematic errors could not be discounted. These deficiencies in the vL00 positional catalog were eliminated by re-reducing the original Cartesian coordinates (of formal precision equal to 2 mas), kindly provided by F. van Leeuwen.

First, we selected only Class 0-1 stars from vL00 (i.e. their images were isolated or only slightly disturbed by an adjacent image). Second, a trial equatorial solution was obtained for vL00 stars using the UCAC2 catalog as a reference frame. Third, the new set of vL00 coordinates was tested against the UCAC2 positions as a function of coordinates, magnitude, and color of stars. There are $\sim$ 3000 stars in common between these two sets of coordinates. Assuming that the UCAC2 positions are free of magnitude- color-related systematic errors, we found that the original vL00 Cartesian coordinates were biased by up to 16 mas·mag^{-1}. There is also a detectable quadratic color-dependent bias along the declination. Both magnitude- and color-related biases were removed from the vL00 Cartesian coordinates before the final equatorial solution was obtained.

The new reference catalog, covering a region of $1\overset{\circ}{.}5 \times 1\overset{\circ}{.}5$ and magnitudes to $V \sim 16.5$, contains 10 291 stars and consists of approximately equal parts of the UCAC2 (trimmed down to stars with positional accuracies of higher quality than 75 mas) and the updated vL00 coordinates on the system of ICRS and epoch J2000.0.

This new reference catalog was used to obtain the equatorial coordinates of our ω Cen stars. The WFI pixel coordinates of these stars were translated into global Cartesian system coordinates and corrected for geometric distortions. A simple low-term-dominated plate model was sufficient to calculate equatorial coordinates. The standard error of this solution, employing $\sim$ 5500 reference stars, was 45–50 mas in each coordinate. These errors were higher than those listed in Yadav et al. 2008, Paper II), which is based on similar WFI@2.2m data for the open cluster M67. We understand that image crowding remains a dominant source of increased scatter in our solution for ω Cen. Although we removed all stars with obviously poor astrometry, even a close but not overlapping image

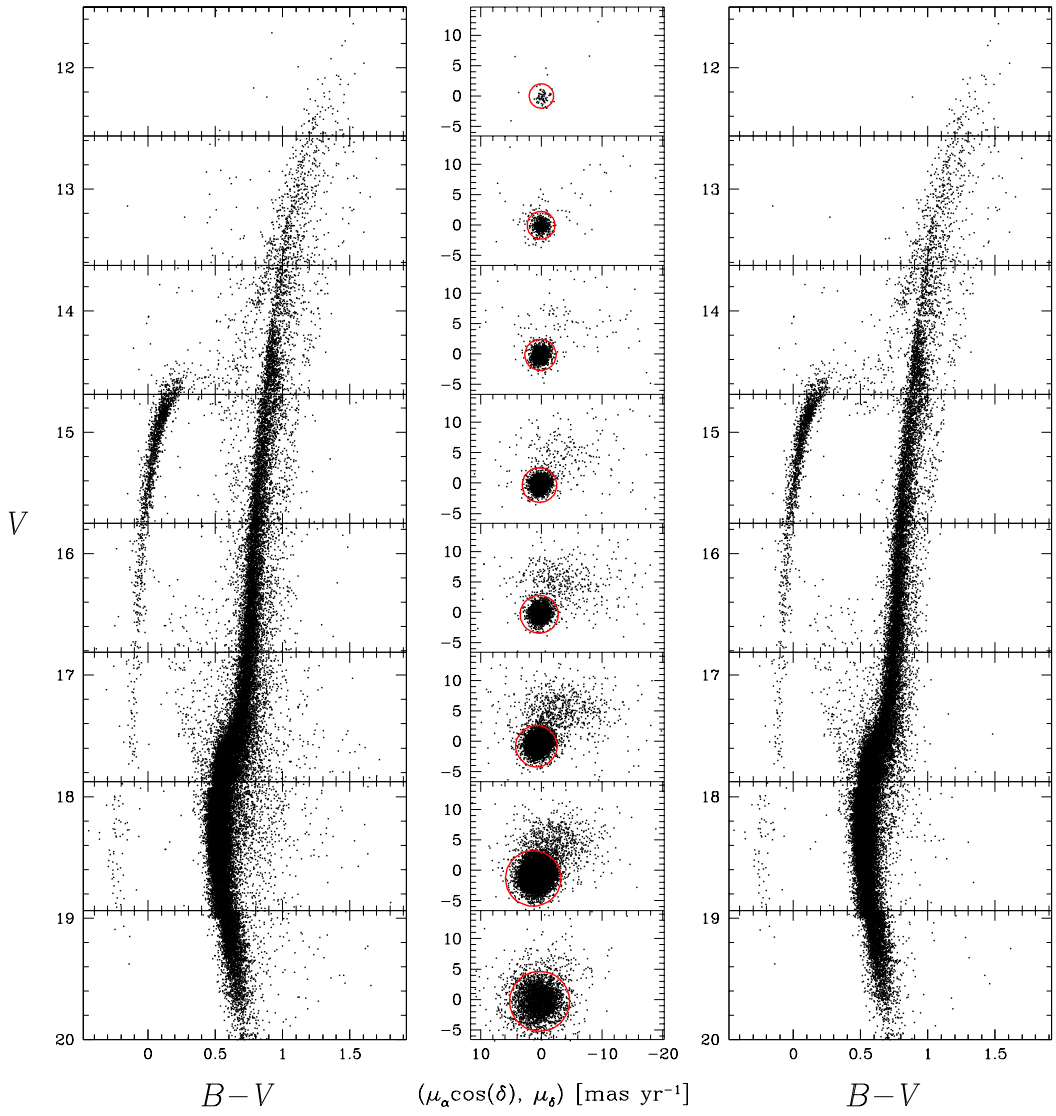

FIGURE 6.10— (*Left*): color-magnitude diagram, split into eight magnitude bins, for all the stars having a proper-motion rms increasing from 1.8 mas yr^{-1} for the brightest bin to 5 mas yr^{-1} for the faintest one, and photometric rms from 0.02 mag to 0.05 mag, generous enough to include main sequence stars down to $V = 20$. (*Middle*): proper motions for the stars in the corresponding magnitude intervals. A circle in each diagram shows the adopted membership criterion. (*Right*): color-magnitude diagram for assumed cluster members.

might slightly distort the position of a star, especially in photographic plates. The J2000 positions of all stars for the epoch 2003.29 are given in Table 6.

The proper motions shown here have not been translated into the absolute values, because there are too few

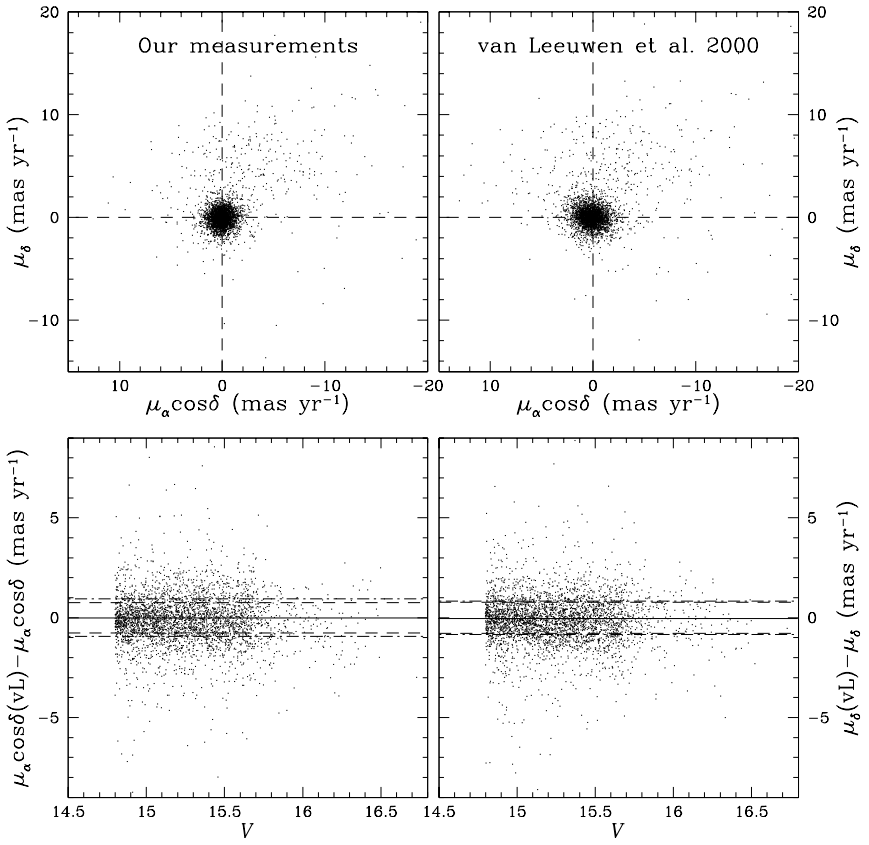

FIGURE 6.11— (*Top panels*): vector-point diagrams of common stars in our catalog (left) and those of vL00 (right), with respect to the mean cluster motion. (*Bottom panels*): right ascension (*left*) and declination (*right*) proper-motion residuals as a function of the V magnitudes. Horizontal dashed and point-dashed lines show the 3σ-clipped median of the proper-motion dispersion for the selected cluster members, for our measurements and for vL00, respectively.

background galaxies suitable for defining an absolute reference frame.

6.4.4 Comparison with other ω Cen proper-motion catalogs

We compare our results with the proper-motion catalog by vL00. First, we considered the common, unsaturated stars in our catalog ($V > 14.6$) to the vL00 faint limit ($V \sim 16.5$). The selected samples contained $\sim$ 3400 stars. Since vL00 proper motions are given in an absolute reference system, we subtracted from the individual vL00 proper motions the absolute mean motion of the cluster provided by the same authors [$(\mu_\alpha \cos\delta, \mu_\delta)$=(−3.97, −4.38) mas yr^{-1}].

In the top panels of Fig. 6.11, we show on the left the vector-point diagram from our measurements, while on the right we show the vL00 values. In both diagrams, a concentration of stars at (0,0) mas yr^{-1} corresponds to the cluster members, while a diffuse distribution of stars around (−3, 5) mas yr^{-1}, consists of the field objects in the foreground and possibly the background of ω Cen.

The size of the proper-motion dispersions of the cluster members reflect both internal motions in the cluster

and random errors. However, the internal motions are expected to be negligible. Assuming a distance of 5.5 kpc, and the Meylan et al. (1995) measurement of the dispersion in the transverse velocity of $\sim$10 km s^{-1} (in the outskirts of the cluster that we are probing) the expected dispersion in the proper motions would be $\sim$ 0.4 mas yr^{-1}. Our estimated errors for the selected sample was 0.74 mas yr^{-1} for $\mu_\alpha \cos\delta$, and 0.77 mas yr^{-1} for μ_δ. Therefore, the internal proper motions should not affect more than 10–15% of the observed dispersions.

To estimate the observed proper-motion dispersion in the two samples (this work and vL00), we adopted the 68.27-th percentile of the distribution (σ) about the median (estimated iteratively with a 3σ-clipping), and for each coordinate independently. Due to the significance differences between cluster and field object motion, this procedure allowed us to isolate a sub sample of members.

Our results were:

$$\text{ours}: \begin{cases} \sigma(\mu_\alpha \cos\delta) = 0.76 \text{ mas yr}^{-1} \\ \sigma(\mu_\delta) = 0.78 \text{ mas yr}^{-1} \end{cases}$$

$$\text{vL00}: \begin{cases} \sigma(\mu_\alpha \cos\delta) = 0.94 \text{ mas yr}^{-1} \\ \sigma(\mu_\delta) = 0.83 \text{ mas yr}^{-1} \end{cases}$$

For the selected sample, it is clear that our distribution is tighter, rounder, and in good agreement with our estimate of the errors. Even if our proper motions originate in images representing half the total number of plates used by vL00, we note that we study more than 3 mag fainter in V, and use a time baseline that equals only $\sim 1/12$ of that used by vL00.

The above performed test could be a bit unfair versus the vL00 catalog, because we used our non-saturated stars only, which are the faintest in the vL00 catalog. vL00 demonstrated emphatically that not all stars are suitable for astrometric measurements. We therefore performed a second test in which we chose the stars in vL00 with the most reliable measurements (belonging to class 0 and 1 only) that were brighter than $V = 16$, and had a good probability of being a cluster member (P_μ(vL00) $> 75\%$); we compared the measurements for these stars with those in catalog.

The results were as follows:

$$\text{ours}: \begin{cases} \sigma(\mu_\alpha \cos\delta) = 0.68 \text{ mas yr}^{-1} \\ \sigma(\mu_\delta) = 0.69 \text{ mas yr}^{-1} \end{cases}$$

$$\text{vL00}: \begin{cases} \sigma(\mu_\alpha \cos\delta) = 0.71 \text{ mas yr}^{-1} \\ \sigma(\mu_\delta) = 0.62 \text{ mas yr}^{-1} \end{cases}$$

These results illustrate the slightly higher precision of the vL00 catalog, but the dispersions n the measurements are, in any cases, comparable. The dispersion obtained with our catalog, which now also includes saturated star measurements, is more reliable than found with the first test. The explanation of this apparent paradox is that, by selecting the best proper-motion measured stars in the vL00 catalog (class 0 and 1, among the most isolated stars), we also selected the most isolated stars in our catalog, making the PSF-wings fitting more effective. Once again, it appears clear the huge potential that wide field CCD imager will have in astrometry in the future.

6.5 Membership probability

In the vector-point diagrams of Figs. 6.8 and 6.10, two distinct groups of stars are clearly detectable: the bulk of stars belong to ω Cen, with no mean motion ($\mu_\alpha \cos(\delta) = \mu_\delta = 0.0$ mas yr^{-1}), and there is a secondary broad group, which corresponds to field stars.

Vasilevskis et al. (1958) were the first to formulate the proper-motion membership probability. This method was later developed by many authors (Sanders 1971, Zhao & He 1990, Tian et al. 1998, Balaguer-Núnez et al. 1998, and references therein) for several open and globular clusters. To derive our membership probability, we followed a method based on proper motions described by Balaguer-Núnez et al. (1998).

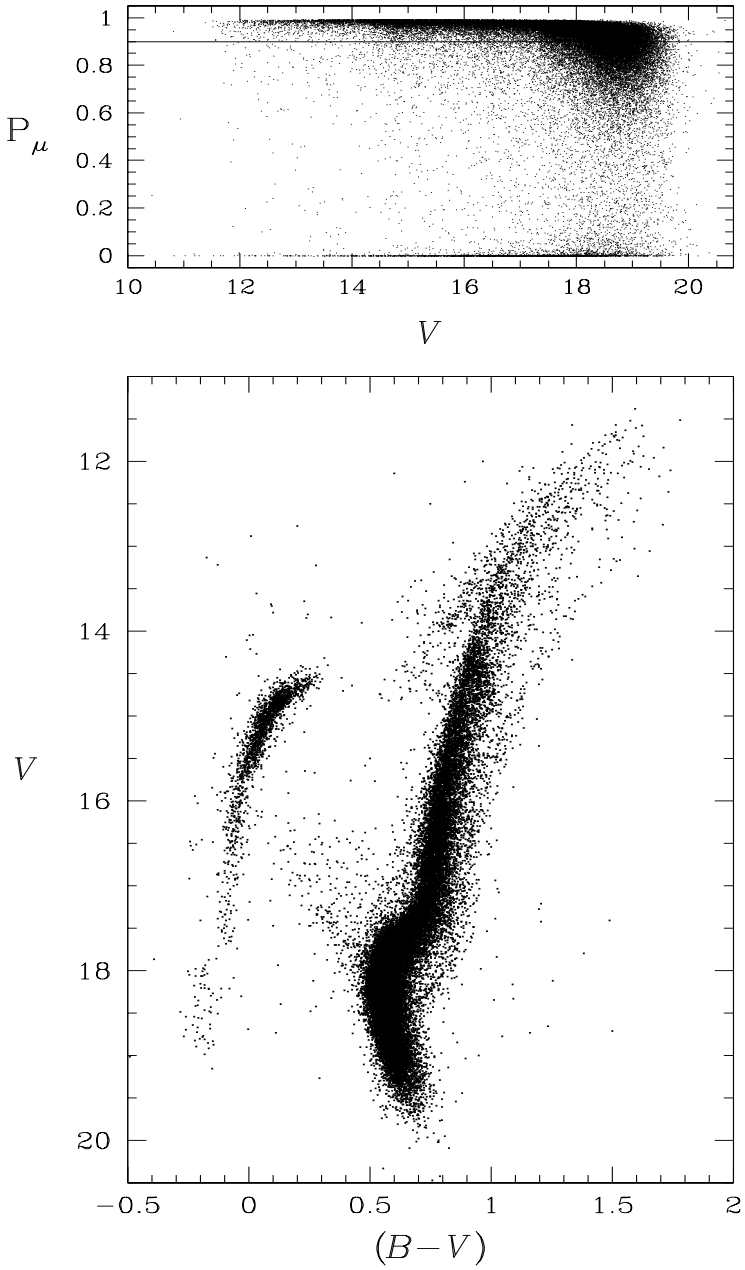

FIGURE 6.12— Membership probability P_μ versus V magnitude for stars with $\sigma_{V,B} < 0.05$ mag and proper-motion rms < 5 mas yr^{-1}. Horizontal line show the $P_\mu = 90\%$ level. The resulting CMD for stars with $P_\mu > 90\%$ is shown on the bottom panel.

First of all, we constructed frequency functions for both cluster and field stars, Φ_c^ν and Φ_f^ν respectively, derived from the cluster and field star distribution in the VPD. For the $i^{\rm th}$ star, these functions were as follows:

$$\Phi_c^\nu = \frac{\exp\left\{-\frac{1}{2}\left[\frac{(\mu_{x_i}-\mu_{x_c})^2}{\sigma_{x_c}^2+\epsilon_{x_i}^2}+\frac{(\mu_{y_i}-\mu_{y_c})^2}{\sigma_{y_c}^2+\epsilon_{y_i}^2}\right]\right\}}{2\pi(\sigma_{x_c}^2+\epsilon_{x_i}^2)^{1/2}(\sigma_{y_c}^2+\epsilon_{y_i}^2)^{1/2}},$$

and

$$\Phi_f^\nu = \frac{\exp\left\{-\frac{1}{2(1-\gamma^2)}\cdot\left[\frac{(\mu_{x_i}-\mu_{x_f})^2}{\sigma_{x_f}^2+\epsilon_{x_i}^2}-\frac{2\gamma(\mu_{x_i}-\mu_{x_f})(\mu_{y_i}-\mu_{y_f})}{(\sigma_{x_f}^2+\epsilon_{x_i}^2)^{1/2}(\sigma_{y_f}^2+\epsilon_{y_i}^2)^{1/2}}+\frac{(\mu_{y_i}-\mu_{y_f})^2}{\sigma_{y_f}^2+\epsilon_{y_i}^2}\right]\right\}}{2\pi(1-\gamma^2)^{1/2}(\sigma_{x_f}^2+\epsilon_{x_i}^2)^{1/2}(\sigma_{y_f}^2+\epsilon_{y_i}^2)^{1/2}};$$

where (μ_{x_i},μ_{y_i}) are the $i^{\rm th}$ star proper motions along the X and Y axes, $(\epsilon_{x_i},\epsilon_{y_i})$ represent the respective displacement rms, (μ_{x_f},μ_{y_f}) and (μ_{x_c},μ_{y_c}) are the central points of the field and cluster star proper motion, $(\sigma_{x_f},\sigma_{y_f})$ and $(\sigma_{x_c},\sigma_{y_c})$ are the field and cluster star proper-motion intrinsic dispersion, and γ is the correlation coefficient, calculated to be

$$\gamma = \frac{(\mu_{x_i}-\mu_{x_f})(\mu_{y_i}-\mu_{y_f})}{\sigma_{x_f}\sigma_{y_f}}.$$

The spatial distribution was ignored due to the relatively small size of our field ($\sim 33'\times 33'$) with respect to the ω Cen radial extent of $r_t \simeq 57'$ (Harris 1996). For our calculations, we considered only stars with an rms in proper motion < 1.9 mas yr^{-1}to define Φ_c^ν and Φ_f^ν. The center of the proper-motion distribution in the VPD for cluster stars was found to be at $x_c = 0.00$ mas yr^{-1}, and $y_c = 0.00$ mas yr^{-1}, with rms values of $\sigma_{x_c} = 0.83$ mas yr^{-1}, and $\sigma_{y_c} = 0.83$ mas yr^{-1}. For field stars, we have: $x_f = -3.57$ mas yr^{-1}, $y_f = 5.12$ mas yr^{-1}, $\sigma_{x_f} = 5.06$ mas yr^{-1}, and $\sigma_{y_f} = 2.86$ mas yr^{-1}, respectively.

The distribution function for all the stars can be computed as follows:

$$\Phi = (n_c\cdot\Phi_c^\nu)+(n_f\cdot\Phi_f^\nu) = \Phi_c+\Phi_f;$$

where n_c and n_f are the normalized number of stars for cluster and field ($n_c+n_f=1$). Therefore, for the $i^{\rm th}$ star the resulting membership probability is

$$P_\mu(i) = \frac{\Phi_c(i)}{\Phi(i)}.$$

In Fig. 6.12, we show in the upper panel the P_μ distribution versus V magnitude. To include also faint stars and reach $V = 20$, plotted stars have proper-motion rms < 5 mas yr^{-1} and $\sigma_{V,B} < 0.05$ mag. The horizontal line marks the 90% probability level. The lower panel contains the CMD for stars with $P_\mu > 90\%$.

When calculating formal membership probabilities for ω Cen, we have a paradoxical situation in which the main concern is to assign a reasonable probability to field stars. This is because in our sample the number of cluster stars is significantly higher than the small number of field stars. In addition, proper-motion errors have a strong dependence on magnitude (Figs. 6.7, 6.10), which is not accounted for in our membership probability P_μ calculation. We therefore, also used the so-called local sample method (e. g., Paper II) for membership probability calculation. In this method, for each target star a sub-sample of stars was selected to reflect closely the properties of a target. This assures a smooth transition in the calculated P_μ as a function of the chosen parameter. For ω Cen, the obvious choice of parameter was the mean error σ_μ of the proper motions. Given the wide range of σ_μ, we chose to consider only stars with σ_μ<7 mas yr^{-1}. Less accurate proper motions are marginally useful for membership studies. We note that σ_μ is calculated in the same way as in Sect. 4 and Fig. 6.9.

For each target star, we then selected a star a subsample of 3000 stars almost with identical proper-motion errors to that of a target star. The trial calculations indicated that we cannot model the distribution of field stars with a Gaussian because the number of potential field stars in the vector-point diagram is extremely low in the

vicinity of the cluster-star centroid (Fig. 6.11). A reasonable alternative to a Gaussian is a flat distribution of field stars.

In essence, the membership probability P_μ is driven by the distribution of cluster stars. If the modulus of the proper-motion vector of a star exceeds 2.5–3σ_μ, the corresponding P_μ is less than 1%. We provide these alternative estimates of P_μ (called $P_\mu(2)$, to distinguish this from the first mentioned method $P_\mu(1)$) for 120 259 stars. For the majority of stars, both values of P_μ are similar. However, there are a number of cases in which the P_μ estimates for the two methods differ radically. In the case of high proper-motion errors for cluster stars, the local sample method clearly provides a more realistic membership probability. A closer inspection of these cases indicates indirectly a potential problem in calculating the proper motion. If the error of proper motion along one axis is several times larger than the error along the other axis, or if this error is too high for a particular magnitude, the chances are that our proper-motion value is corrupted and, hence, its formal membership probability is meaningless.

Unless specified otherwise, we mean $P_\mu(1)$ determination when referring to P_μ.

6.6 Applications

Our ω Cen proper-motion catalog can be used for different purposes. The first application was the selection of the most probable ω Cen members for spectroscopic follow-up studies. In Villanova et al. (2007), we used a preliminary proper-motion catalog for the same data set presented here, to pre-select sub-giant branch stars. This helped us to avoid the Galactic field stars close to the TO level. All resultant radial velocities were close to the ω Cen mean value, which confirmed their membership. On the other hand, the high photometric quality and the availability of several filters covering a wide area around the cluster, imply that this catalog is an excellent photometric reference frame on which to register photometry from different telescopes and cameras (Bellini et al. 2009b).

Besides these obvious applications, our ω Cen proper-motion catalog also provides an observational constraint of the origin of the composite stellar populations in ω Cen. Our catalog provides the necessary wide-field coverage and photometric accuracy to investigate the radial distribution of the different ω Cen sub-population from the center of the cluster to $\sim 22'$ (in the corners). We will report on this analysis in Chapter 8 (see also Bellini et al. 2009b).

6.6.1 The proper motion of the RGB sub-populations

Ferraro et al. (2002) cross-correlated the WFI photometric catalog of Pancino et al. (2000) with the vL00 photographic proper-motion catalog. Their goal was to investigate the nature of the anomalous metal-rich RGB of ω Cen, the so-called RGB-a. In particular, they investigated the presence of proper-motion mean differences between the ω Cen bulk population (metal-poor RGB, so-called RGB-MP) and the minor, but yet important, metal-rich RGB-a population (Pancino et al. 2000). Their Fig. 2 showed significant variation in the relative proper motion of RGB-a stars with respect to ω Cen RGB-MP motion. In particular, they found that the RGB-a stars had a mean proper motion of $|\delta\mu_{\rm tot}| = 0.8$ mas yr^{-1} that is offset from that of the RGB-MP population. Therefore, they concluded that the RGB-a subpopulation must have had an independent origin with respect to the RGB-MP one.

Unsurprisingly, the Ferraro et al. (2002) study triggered new interest in the ω Cen proper motion, and Platais et al. (2003) presented a detailed reanalysis of the vL00 catalog. Platais et al. (2003) concluded that the reported proper-motion offset between the ω Cen sub-populations could be attributed to instrumental bias. However, Hughes et al. (2004) commented that there was no residual color term in the omega Cen proper motions, and that these authors misinterpreted the observed offsets. Specifically, Hughes et al. (2004) asserted that the summary effect of color terms (before the corrections) amounted to no more than 1 mas yr$^{-1}\cdot$mag^{-1} in $B-V$, while the offset in the proper motions for the anomalous omega Cen stars reached 2 mas yr^{-1} and did not have the same direction as the color term. Regardless of the reason for the reported offset in the vL00 catalog, the presence of this offset was not confirmed by the new *HST*-based preliminary proper motions (Anderson 2003a).

Two spectroscopic studies completed by Pancino et al. (2007) and Johnson et al. (2008) indicated that there was no evidence for any of the RGB stellar populations to have an offset in the mean radial velocity, or a different

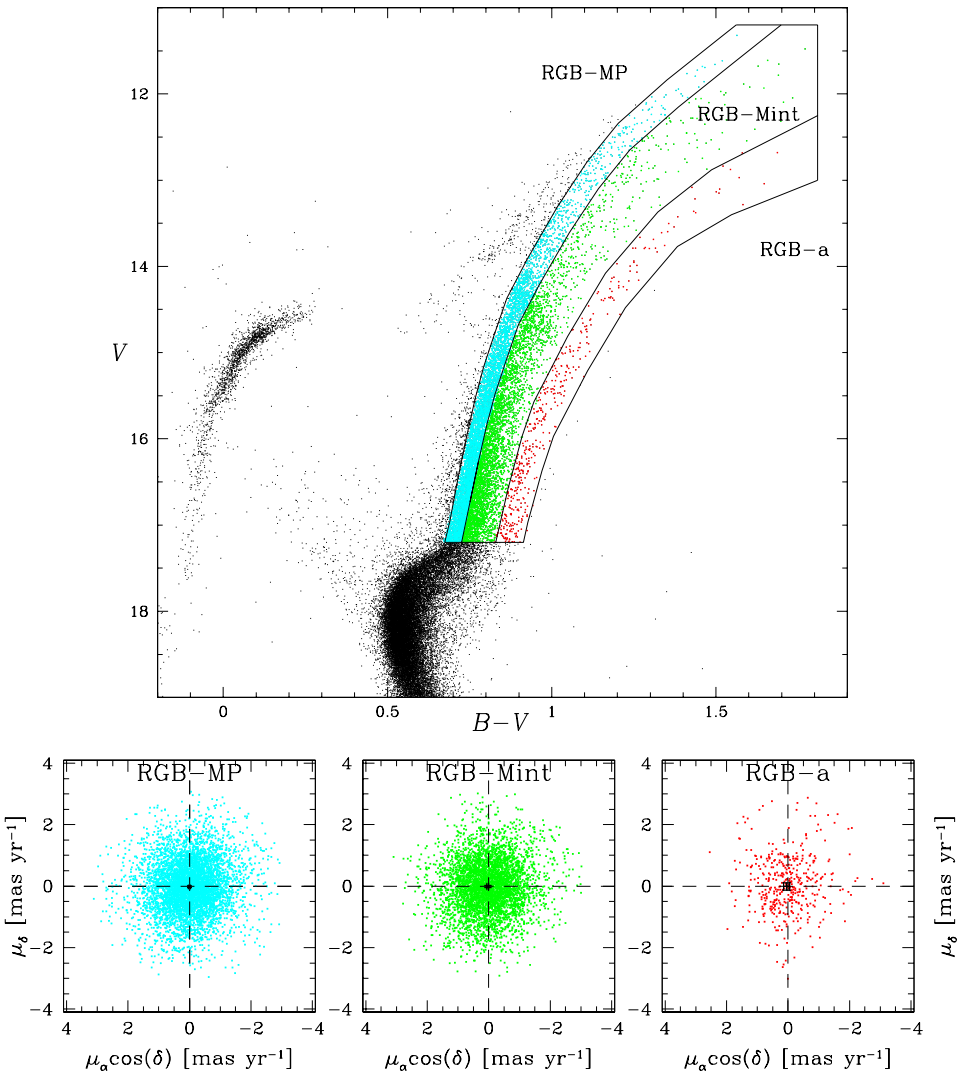

FIGURE 6.13— (*Top panel*): V vs. $B-V$ CMD of proper-motion-selected member stars on which we defined three RGB subsamples: RGB-MP (cyan), RGB-Mint (green), and RGB-a (red). See the text for the definition of the subpopulations. (*Bottom panels*): Proper motions of RGB-MP (*left*), RGB-Mint (*middle*), and RGB-a (*right*) subpopulations.

radial velocity dispersion. This result applied also to the RGB-a sub-population.

Our astrometric catalog provided an independent data set with which we could test the Ferraro et al. (2002) conclusions. We repeated the same analysis performed in Ferraro et al. (2002). First, we divided the ω Cen RGB population into three subpopulations (see top panel of Fig. 6.13): RGB-MP (cyan), RGB-a (red), and RGB-Mint (RGB stars between RGB-MP and RGB-a, green). All plotted stars had high membership probability ($P_\mu > 90\%$), and photometric errors ranging from 0.02 mag for bright stars to 0.05 mag for faintest ones, in both filters.

The RGB samples include all stars with $V \leq 17.2$ mag. MP and Mint RGB stars merge with each other at fainter magnitudes. Sollima et al. (2005) and Villanova et al. (2007) clearly showed that the SGB region of

ω Cen includes five subpopulations (see again Fig. 6.15). Three of these merge into each other and form the RGB-MP and RGB-Mint samples. We emphasize that our population sub-division extends to fainter magnitudes than in Ferraro et al. (2002), and therefore provides a higher RGB sampling and more robust statistics. Our samples contain 5182 RGB-MP stars, 3127 RGB-Mint stars, and 313 RGB-a stars.

A closer look at the three RGB sub-population proper motions is presented in the bottom panels of Fig. 6.13: RGB-MP on the left, RGB-Mint in the middle, and RGB-a on the right. The red crosses report the median value (estimated iteratively) of the proper motion of the three sub-samples. For the RGB-MP sample, we have:

$$\begin{cases} < \mu_\alpha \cos\delta >= (0.00 \pm 0.01)\ \mathrm{mas\,yr^{-1}} \\ < \mu_\delta >= (-0.02 \pm 0.01)\ \mathrm{mas\,yr^{-1}}, \end{cases}$$

for RGB-Mint stars:

$$\begin{cases} < \mu_\alpha \cos\delta >= (0.03 \pm 0.01)\ \mathrm{mas\,yr^{-1}} \\ < \mu_\delta >= (-0.01 \pm 0.01)\ \mathrm{mas\,yr^{-1}}, \end{cases}$$

and for the RGB-a sample:

$$\begin{cases} < \mu_\alpha \cos\delta >= (0.05 \pm 0.03)\ \mathrm{mas\,yr^{-1}} \\ < \mu_\delta >= (-0.01 \pm 0.04)\ \mathrm{mas\,yr^{-1}}. \end{cases}$$

We found no evidence for the presence of differences among the relative proper motions of the three RGB sub-populations at the level of 0.05 mas yr^{-1} in $\mu_\alpha \cos\delta$ and of 0.04 mas yr^{-1} in μ_δ (i.e. relative tangential velocities of $\lesssim 1.3$, and $\lesssim 1.1$ km s^{-1}, assuming a distance of 5.5 kpc for ω Cen). All three RGB sub-samples exhibit the same mean proper motion, within the errors.

We therefore, agree with the results of both Platais et al. (2003) and Johnson et al. (2008) for RGB-a, and show that the RGB-Mint proper motion is also consistent with the other ω Cen sub-populations.

A final word on this issue requires an internal stellar proper-motion analysis, but suitable catalogs are not yet available.

6.6.2 Membership probability of published ω Cen variable stars

The study of variable stars in ω Cen can certainly benefit from our proper-motion catalog and cluster membership derivation.

Using the 1.0m Swope Telescope, Kaluzny et al. (2004) measured light curves of $\sim$ 400 variable stars in ω Cen, 117 of which were new identifications. We cross-checked our proper-motion catalog with their own, and found a total of 338 variable stars in common, which had both V and B measurements in our catalog. In particular, there were 90 variable stars for which Kaluzny et al. (2004) did not provide B and/or V magnitudes. Our proper-motion catalog was also useful to locate these stars in the color-magnitude diagram. The position of the Kaluzny et al. (2004) variables in our CMD, as well as their membership probability, is shown in the left panel of Fig. 6.14. Depending on our measured membership probability, we divide the Kaluzny et al. (2004) sample into three categories: (1) $P_\mu < 30\%$ (red squares); (2) $30\% \leq P_\mu < 80\%$ (green triangles); and (3) $P_\mu \geq 80\%$ (blue circles). Of the 117 new variable identifications, 112 are in common with our catalog. Of these 112 stars, 15 have $P_\mu < 30\%$, and therefore these are probably not cluster members. On the other hand, 19 of these new variables have $30\% \leq P_\mu < 80\%$ and their membership remains uncertain. The remaining 78 stars ($P_\mu \geq 80\%$) are almost certainly ω Cen members. In Table 6.3, we report the membership probability values for all Kaluzny et al. (2004) variable stars identified in our catalog. New Kaluzny et al. (2004) identifications have their IDs starting with "N".

The Kaluzny et al. (2004) variable star catalog was cross-checked with the X-ray sources detected by the XMM-Newton analysis presented by Gendre et al. (2003). For the 9 stars in common (see also Table 2 of Kaluzny et al. 2004), we can now provide (see Table 6.4) a membership probability based on our proper-motion analysis. A quick glance at Table 4 allows us to infer that only NV383 and NV369 are very likely cluster members, whereas the remaining 7 stars are most probably field population.

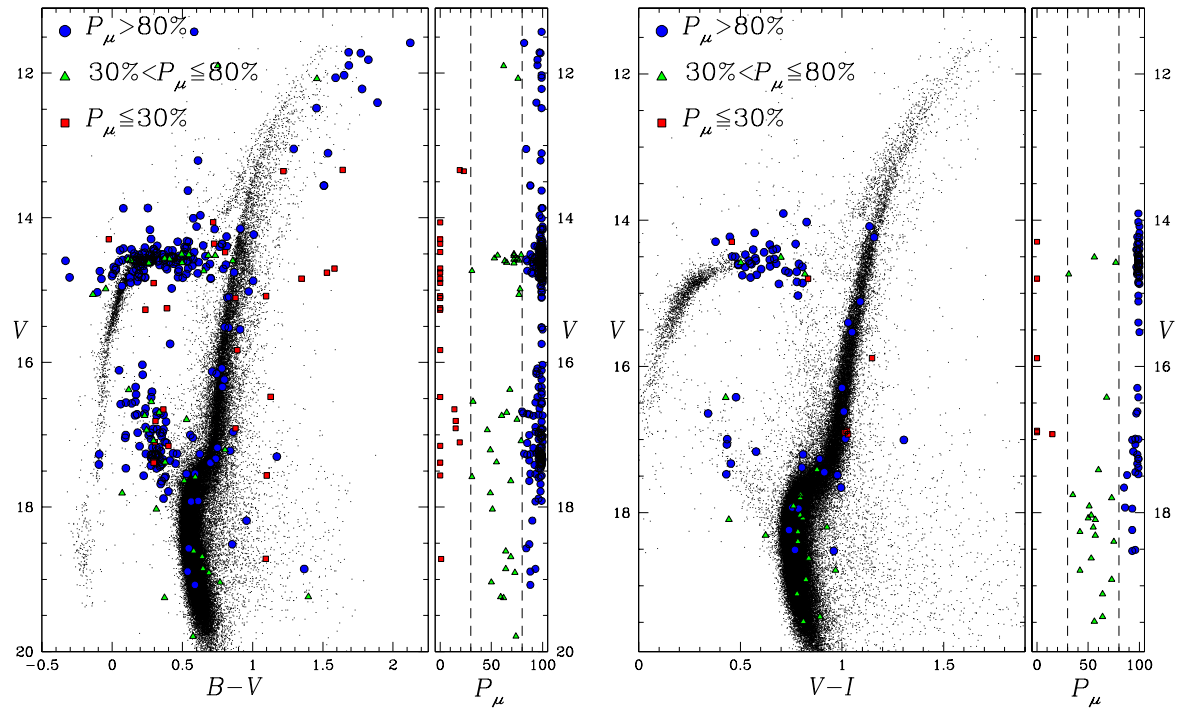

FIGURE 6.14— (*Left*): ω Cen CMD with the cross-checked variable stars from the Kaluzny et al. (2004) catalog; red squares mark stars with a membership probability $P_\mu < 30$; green triangles are stars with $30 \leq P_\mu < 80$, while blue circles are those with a probability to be cluster members $P_\mu \geq 80$. The membership probability P_μ versus the V magnitude is also shown. (*Right*): comparison with Weldrake et al. (2007) catalog.

Using the 1.0m Telescope of the Australian National University, Weldrake et al. (2007) detected a total of 187 variable stars covering a wide area around ω Cen. These stars were matched with the Kaluzny et al. (2004) catalog, and 81 variable stars were found to be new discoveries. A cross-check of our catalog with that of Weldrake et al. (2007) provided 102 variable stars in common. Their location in the V versus $V - I$ CMD is shown in the right panel of Fig. 6.14. As completed for the Kaluzny et al. (2004) sample, different symbols mark different membership probability ranges, and Table 6.5 reports our membership probability for the Weldrake et al. (2007) variable catalog. Of the 81 Weldrake et al. (2007) new variable stars, 16 have counterparts in our proper-motion catalog. Four of these new variables are clearly not cluster members. These field objects include a detached eclipsing binary (V59), and three long-period variables (V31, V125, and V126).

6.7 Summary

We have applied the photometric and astrometric technique developed by Anderson et al. (2006, Paper I) to the most puzzling globular cluster of the Milky Way: ω Centauri.

Based on CCD observations taken with only four years of temporal base-line, our measurements provide accurate proper motions to $B \sim 20$, four magnitudes deeper than the photographic catalog of vL00. We have minimized the sky-concentration effects in our photometry. We provide a membership probability for all stars. Our catalog contains almost 360 000 stars with measured proper motion, and covers a wide area ($\sim 33 \times 33$ arcmin^2) around the cluster center. In Fig. 6.15, we show a summary of our photometric catalog: we plot several

TABLE 6.3— Membership probability for the Kaluzny et al. (2004) variable star catalog. ID_K are the Kaluzny identification labels, while ID_{tw} refer to our IDs.

ID_K	P_μ	ID_{tw}	ID_K	P_μ	ID_{tw}	ID_K	P_μ	ID_{tw}	ID_K	P_μ	ID_{tw}	ID_K	P_μ	ID_{tw}	ID_K	P_μ	ID_{tw}
V1	99	290466	V66	99	311494	V132	96	184072	V214	97	42989	NV296	99	356415	NV354	97	263543
V2	74	271987	V67	99	352882	V135	97	181199	V216	99	155556	NV297	32	250290	NV355	93	196052
V3	99	248511	V68	100	345639	V136	99	213549	V217	98	218342	NV298	100	87382	NV356	49	206069
V4	97	279540	V70	98	93459	V137	99	225149	V218	96	358729	NV299	98	310461	NV357	92	158687
V5	100	298983	V71	99	209884	V139	90	215311	V219	88	347441	NV300	98	284928	NV358	99	129801
V8	99	200194	V74	100	360819	V141	100	177819	V220	100	321724	NV301	96	170554	NV359	46	222238
V9	100	238167	V75	99	352935	V142	65	193092	V221	96	320315	NV302	19	252220	NV360	100	118132
V10	98	273997	V76	100	340408	V143	90	217472	V223	0	355759	NV303	98	145690	NV361	64	234998
V11	99	302079	V77	99	316247	V144	95	201059	V224	99	349215	NV304	98	341374	NV363	93	321474
V12	99	283465	V78	0	243506	V145	91	143665	V225	96	274338	NV305	0	343091	NV364	93	243121
V13	99	259326	V81	99	270509	V146	72	177889	V226	99	167657	NV306	96	198996	NV365	0	71679
V14	97	26311	V82	99	236315	V147	97	143269	V227	98	287148	NV307	82	211960	NV366	97	132355
V15	100	273754	V83	99	323500	V148	95	209005	V228	96	92375	NV308	98	327308	NV367	0	350053
V16	100	40312	V85	98	292312	V150	100	58317	V229	97	285982	NV309	85	193994	NV368	0	349013
V17	99	261135	V86	99	242948	V152	82	177559	V231	99	59688	NV310	15	127228	NV369	94	124330
V18	98	267824	V87	97	255154	V153	100	238719	V233	99	336053	NV311	91	170132	NV370	0	358442
V19	100	205260	V88	94	261450	V154	96	155744	V234	0	157490	NV312	95	183516	NV372	93	290428
V20	99	204861	V90	89	239287	V155	98	272492	V235	87	309505	NV313	98	134090	NV373	59	300775
V21	99	246994	V91	92	241579	V156	99	128871	V236	85	282601	NV314	85	163946	NV374	99	312254
V22	99	86072	V92	99	327526	V157	98	221081	V237	99	286453	NV315	60	267539	NV375	0	349760
V23	100	273446	V94	98	305927	V158	31	153087	V238	99	179489	NV316	99	142842	NV376	0	189233
V24	99	84169	V95	94	188847	V161	76	149737	V239	99	179912	NV317	100	361100	NV377	0	324933
V25	99	199162	V96	63	225607	V162	97	108440	V240	99	239985	NV318	98	246801	NV378	31	341736
V26	98	226616	V97	99	256623	V163	100	337663	V241	1	289203	NV319	94	145544	NV379	99	328605
V27	96	201410	V98	99	227653	V164	99	334394	V242	98	171250	NV320	99	80363	NV380	96	148727
V29	62	191401	V99	99	210796	V165	85	227981	V249	99	236550	NV321	87	209026	NV381	0	311380
V30	99	168094	V100	77	215927	V166	72	241584	V250	92	62410	NV322	93	214126	NV382	96	343538
V32	100	322448	V101	99	169863	V167	23	87332	V251	97	231812	NV323	65	265232	NV383	99	336713
V33	98	184952	V102	100	162564	V168	0	124934	V252	98	187128	NV324	68	154689	NV384	93	46225
V34	99	103189	V103	98	195140	V169	99	285765	V253	99	209800	NV325	80	163821	NV385	99	35533
V35	99	309218	V104	99	92705	V184	100	134524	V254	99	214031	NV326	98	268304	NV386	98	218806
V38	98	52122	V105	98	111797	V185	99	320506	V258	99	253920	NV327	14	235193	NV387	96	190420
V39	99	76656	V106	99	202932	V186	94	200024	V259	99	177256	NV328	69	129813	NV388	0	205940
V40	99	150793	V107	100	147114	V187	91	107554	V261	98	324469	NV329	51	235596	NV389	49	169916
V41	72	145915	V108	99	178628	V188	95	160942	V263	100	243242	NV330	64	271511	NV390	100	262766
V42	88	177086	V109	99	174888	V189	99	175684	V264	98	157202	NV331	69	244602	NV391	99	46483
V43	99	227377	V110	100	164532	V190	99	243006	V265	98	192064	NV332	84	137605	NV393	99	36249
V44	100	78476	V111	95	193829	V191	99	301765	V266	85	206486	NV333	62	192856	NV394	95	81813
V45	98	219445	V112	78	158996	V192	100	319396	V267	99	234518	NV334	88	183248	NV395	88	177086
V46	99	249013	V113	99	130486	V193	99	318939	V268	99	243048	NV335	99	362118	NV397	94	244021
V47	99	281501	V114	97	159704	V194	99	128211	V270	98	164847	NV336	96	106751	NV398	96	267455
V48	98	158259	V115	99	83123	V195	81	274973	V271	98	165504	NV337	97	118163	NV399	98	165850
V49	99	36832	V116	56	204728	V197	79	126226	V272	99	248016	NV338	98	136414	NV400	99	129220
V50	99	214772	V117	75	179957	V198	55	145299	V273	99	223751	NV339	99	169580	NV401	98	130105
V51	99	278945	V118	96	160390	V199	87	194465	V274	77	305738	NV340	97	216161	NV402	87	52179
V52	53	205670	V119	91	140617	V200	75	243370	V275	94	214740	NV341	94	191217	NV403	0	229293
V53	99	56123	V120	99	110236	V201	99	369578	V276	99	101192	NV342	99	199357	NV404	99	244779
V54	98	352756	V121	97	129294	V203	100	372023	V277	99	217316	NV343	99	174660	NV405	88	252122
V56	98	38620	V122	99	105971	V204	99	45537	V280	99	300999	NV344	99	271739	NV406	100	292866
V57	100	48194	V123	100	44090	V205	96	302520	V285	99	74726	NV345	87	174082	NV407	88	309849
V58	96	284348	V124	99	26731	V206	97	57769	V288	99	289087	NV346	90	202477	NV408	50	234623
V59	96	171211	V125	99	14416	V207	98	297708	V289	99	324714	NV347	79	211972	NV409	73	322122
V60	99	110456	V126	99	15927	V208	97	244408	V291	98	97939	NV349	88	212595	NV410	0	180157
V61	100	216835	V127	99	193936	V209	99	297731	V292	98	129991	NV350	84	149574			
V62	99	208493	V128	100	162142	V210	15	58394	V293	99	85152	NV351	84	215235			
V64	99	54131	V129	19	185687	V211	90	298164	NV294	97	265591	NV352	99	183506			
V65	0	50869	V131	100	173358	V212	99	293439	NV295	99	340398	NV353	72	208251			

ω Cen CMDs, derived with all the available filters and different color-baselines (top and middle rows). Plotted stars have a membership probability of $P_\mu > 90\%$. Photometric errors range from 0.02 mag for brighter stars to 0.05 mag for the fainter ones. In the bottom panels of Fig. 6.15, we show the SGB region of ω Cen in the B versus $B-R$ CMD on the left, and two color-color diagrams with different colors on the right.

The high precision of our astrometry and multi-band photometry once again emphasizes the importance of accurate representation of the PSF across the entire field-of view, especially for wide-field imagers, exemplified by the concept of empirical PSF (Paper I).

TABLE 6.4— Membership probability of XMM-Newton X-Ray counterparts candidates. The IDs refer to Kaluzny et al. work.

ID_K	P_μ	ID_K	P_μ
NV367	0	NV376	0
NV375	0	NV377	0
V167	23	NV369	94
V223	0	NV383	99
NV378	31		

TABLE 6.5— Membership probability for the Weldrake et al. (2007 variable star catalog. ID_W are Weldrake et al. identification labels, ID_{tw} come from our IDs. The symbol (*) marks new Weldrake et al. identifications.

ID_W	P_μ	ID_{tw}	ID_W	P_μ	ID_{tw}	ID_W	P_μ	ID_{tw}	ID_W	P_μ	ID_{tw}	ID_W	P_μ	ID_{tw}	ID_W	P_μ	ID_{tw}
V31*	0	234574	V48	100	360819	V102	15	58394	V119	51	126839	V142	42	208115	V160*	73	292364
V32	99	236315	V59*	0	23863	V103	99	54131	V120	68	154689	V143	98	201164	V161	73	322122
V33	100	205260	V60	48	40133	V104	93	46225	V121	53	159019	V144*	100	247143	V162	99	311494
V34	99	239985	V61	100	48194	V105	99	83123	V122	100	162685	V145*	99	270697	V163	93	321474
V35	56	214167	V62	97	42989	V106	100	78476	V123	99	155556	V146	100	243242	V164	99	327526
V36	98	267824	V63	99	86072	V107	99	103189	V124	75	137352	V147	99	246994	V165	99	320506
V37	0	243506	V64	99	84169	V108	48	92977	V125*	0	127167	V148	77	305738	V166	31	341736
V38	99	270509	V65	99	128211	V109	99	110456	V126*	0	85789	V150	50	302398	V167	100	345639
V39	100	292866	V66	98	111797	V110	99	105971	V133	94	201061	V151	2	283256	V168	64	347475
V40	99	289620	V67	98	93459	V111	99	110236	V134	53	234700	V152	100	298983	V169	100	337663
V41	99	293439	V68*	99	120134	V112	86	153744	V135	85	205826	V153	65	297730	V170	99	352882
V42	99	285765	V69*	98	108406	V113	98	136502	V136	50	228136	V154	98	287148	V171	98	352756
V43	99	324714	V70	100	162564	V114	55	160877	V137	42	225221	V155	64	283990	V172	96	358729
V44*	93	328996	V71*	88	132518	V115	57	158023	V138	99	215061	V156	97	279540	V173	98	219445
V45	99	316247	V72*	73	133191	V116	60	141176	V139	56	204728	V157*	96	273996	V174	99	249013
V46*	96	320258	V81*	96	6069	V117	97	129294	V140	57	224813	V158	98	273997	V176	98	292312
V47	99	352935	V101	99	36832	V118	35	151268	V141	51	218172	V159*	93	287079	V178	36	309751

The primary aim of this Chapter is, of course, to provide wide-field membership probability measurements for spectroscopic follow-up studies, down to the turn-off region of the cluster. However, the high quality of our photometric and astrometric measurements also provide a crucial observational constraint of the multiple ω Cen sub-populations. Due to our proper-motion-selected RGB sub-populations, we can confirm that the metal-poor, metal-intermediate, and metal-rich components have the same proper motions which is that of ω Cen, within our measurements uncertainties.

We finally provide membership probability determinations for the Kaluzny et al. (2004) and Weldrake et al. (2007) ω Cen variable star catalogs.

6.7.1 Electronic catalog

The catalog is available at the SIMBAD on-line database[2]. Description of the catalog: column (1) contains the ID; columns (2) and (3) give the J2003.29 equatorial coordinates in decimal degrees; columns (4) and (5) provide the pixel coordinates x and y of the distortion-corrected reference meta-chip. Columns (6) and (7) contain the proper-motion values along $\mu_\alpha \cos\delta$ in units of mas yr^{-1}, with the corresponding rms; columns (8) and (9) provide the proper-motion values along μ_δ, with the corresponding rms, in the same units. Columns from (10) to (21) give the photometric data, i.e. U, B, V, R_C, I_C, Hα magnitudes and their errors. The last two columns give the proper-motion membership probability $P_\mu(1)$ for all the stars (22), and for a sub-sample of 120,259 stars with the alternative

[2] `http://simbad.u-strasbg.fr/simbad/`

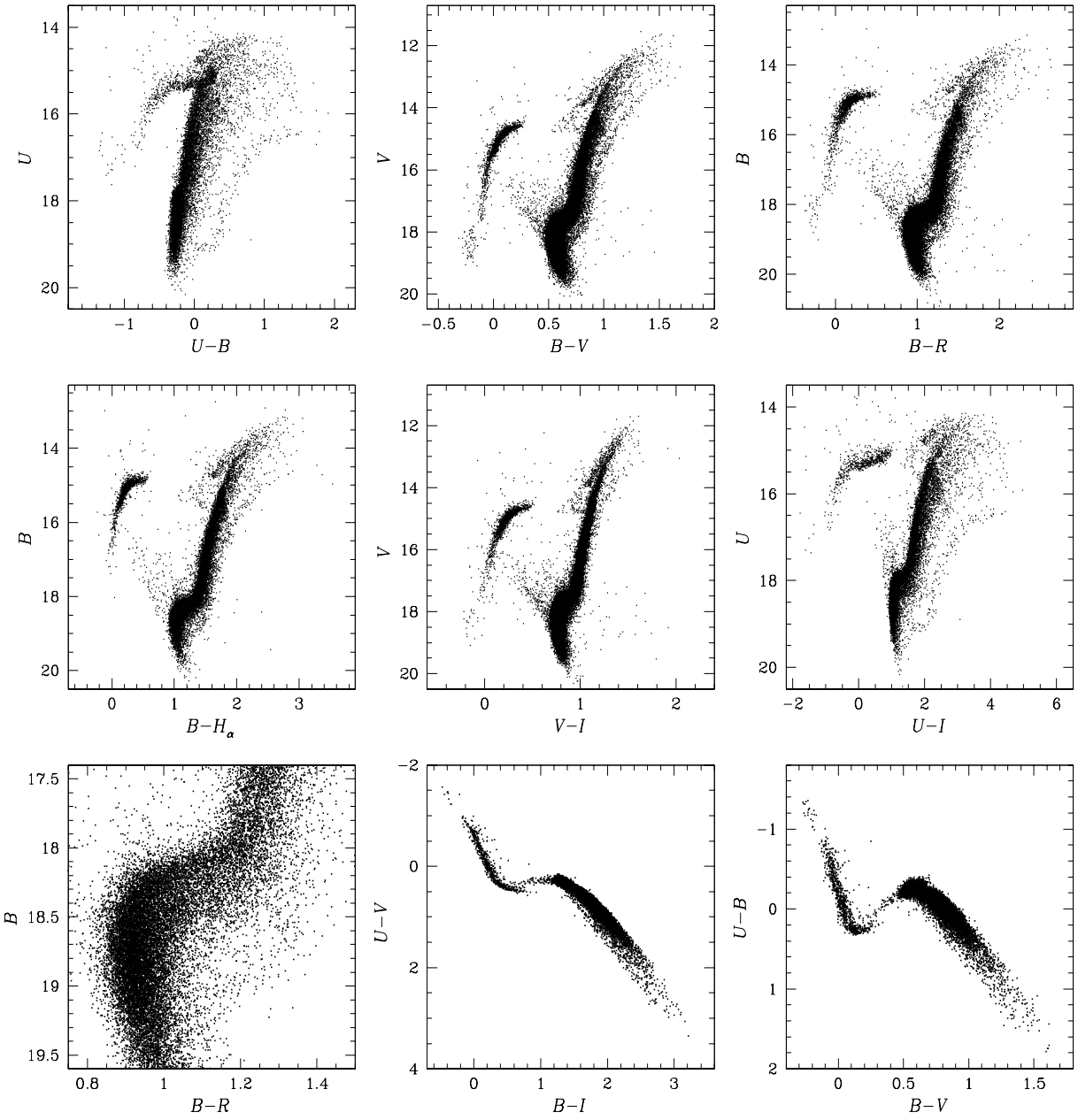

FIGURE 6.15— (*Top)*: membership probability selected ($P_\mu > 90\%$) ω Cen CMDs. From left to right U vs. $(U-B)$, V vs. $(B-V)$, and B vs. $(B-R)$. Plotted stars have photometric errors going from 0.02 mag for the brighter to 0.05 for the faintest ones. (*Middle*): same star selection criteria. From left to right: B vs. $(B-\mathrm{H}\alpha)$, V vs. $(V-I)$, and U vs. $(U-I)$. (*Bottom*): the B vs. $(B-R)$ CMD, zoomed in the SGB region, is shown on the left. The two plots on the right show two color-color diagrams obtained from different filters.

membership determination $P_\mu(2)$ (23). In this case, if the second membership determination is not provided, we flag it with the value -1.

If photometry in a specific band is not available, a flag equal to 99.999 is set for magnitude and error.

Table 6 contains the first lines of the on-line catalog.

Bibliography

Andersen, M. I., Freyhammer, L., & Storm, J. 1995, Calibrating and Understanding HST and ESO Instruments, 87
Anderson, J., 1997, ph.D. thesis, Univ. California, berkeley
Anderson, J., 2003, in ASP. Conf. Ser. 296, New Horizons in Globular Cluster Astronomy, ed. G. Piotto, G. Meylan, D. Djorgovski, & M. Riello (San Francisco: ASP), 125
Anderson, J., & King, I. R. 2003, PASP, 115, 113
Anderson, J., Bedin, L. R., Piotto, G., Yadav, R. S., & Bellini, A. 2006, A&A, 454, 1029, (Paper I)
Anderson, J. et al. 2008, AJ, 135, 2055
Balaguer-Núnez, L., Tian, K. P., & Zhao, J. L. 1998, A&AS, 133, 387
Bedin, L. R., Piotto, G., Anderson, J., Cassisi, S., King, I. R., Momany, Y., & Carraro, G. 2004, ApJL, 605, L125
Bedin, L. R., Cassisi, S., Castelli, F., Piotto, G., Anderson, J., Salaris, M., Momany, Y., & Pietrinferni, A. 2005, MNRAS, 357, 1038
Bellini, A., et al. 2009, A&A, 493, 959 (2009a)
Bellini, A., Piotto, G., Bedin, L. R., King, I. R., Anderson, J., Milone, A. P., & Momany, Y. 2009, A&A, 507, 1393 (2009b)
Bessell, M. S., & Norris, J. 1976, ApJ, 208, 369
Butler, D., Dickens, R. J., & Epps, E. 1978, ApJ, 225, 148
Calamida, A., et al. 2005, ApJL, 634, L69
Calamida, A., Corsi, C. E., Bono, G., Stetson, P. B., Freyhammer, L. M., & Buonanno, R. 2008, ArXiv e-prints, 801, arXiv:0801.0693
Cassisi, S., Schlattl, H., Salaris, M., & Weiss, A. 2003, ApJL, 582, L43
Del Principe, M., et al. 2006, ApJ, 652, 362
Ferraro, F. R., Bellazzini, M., & Pancino, E. 2002, ApJL, 573, L95
Ferraro, F. R., Beccari, G., Rood, R. T., Bellazzini, M., Sills, A., & Sabbi, E. 2004, ApJ, 603, 127
Freeman, K. C., & Rodgers, A. W. 1975, ApJL, 201, L71
Gendre, B., Barret, D., & Webb, N. A. 2003, A&A, 400, 521
Harris, W. E. 1996, AJ, 112, 1487
Hilker, M., Kayser, A., Richtler, T., & Willemsen, P. 2004, A&A, 422, L9
Hughes, J., Wallerstein, G., van Leeuwen, F., Hilker, M. 2004, AJ, 127, 980
Johnson, C. I., Pilachowski, C. A., Simmerer, J., & Schwenk, D. 2008, ArXiv e-prints, 804, arXiv:0804.2607, ApJaccepted
Kaluzny, J., Olech, A., Thompson, I. B., Pych, W., Krzemiński, W., & Schwarzenberg-Czerny, A. 2004, A&A, 424, 1101
Koch, A., Odenkirchen, M., Grebel, E. K., & Caldwell, J. A. R. 2004, Astronomische Nachrichten, 325, 299
Lee, Y.-W., Joo, J.-M., Sohn, Y.-J., Rey, S.-C., Lee, H.-C., & Walker, A. R. 1999, Nature, 402, 55
Manfroid, J., & Selman, F. 2001, The Messenger, 104, 16
Merritt, D., Meylan, G., & Mayor, M. 1997, AJ, 114, 1074
Meylan, G., Mayor, M., Duquennoy, A., & Dubath, P. 1995, A&A, 303, 761
Momany, Y., Cassisi, S., Piotto, G., Bedin, L. R., Ortolani, S., Castelli, F., & Recio-Blanco, A. 2003, A&A, 407, 303
Monet, D. G., Dahn, C. C., Vrba, F. J., Harris, H. C., Pier, J. R., Luginbuhl, C. B., & Ables, H. D. 1992, AJ, 103, 638

Norris, J., & Bessell, M. S. 1975, ApJL, 201, L75
Norris, J., & Bessell, M. S. 1977, ApJL, 211, L91
Norris, J. E., & Da Costa, G. S. 1995, ApJL, 441, L81
Norris, J. E., Freeman, K. C., & Mighell, K. J. 1996, ApJ, 462, 241
Norris, J. E., 2004, ApJ, 612, 25
Pancino, E., Ferraro, F. R., Bellazzini, M., Piotto, G., & Zoccali, M. 2000, ApJL, 534, L83
Pancino, E., Galfo, A., Ferraro, F. R., & Bellazzini, M. 2007, ApJL, 661, L155
Piotto, G., et al. 2005, ApJ, 621, 777
Platais, I., Wyse, R. F. G., Hebb, L., Lee, Y.-W., & Rey, S.-C. 2003, ApJL, 591, L127
Rey, S.-C., Lee, Y.-W., Ree, C. H., Joo, J.-M., Sohn, Y.-J., & Walker, A. R. 2004, AJ, 127, 958
Sanders, W. L. 1971, A&A, 14, 226
Sarajedini, A., et al. 2007, AJ, 133, 290
Selman, F. J., 2001, "Determining a zero–point variation map for the WFI" (http://www.ls.eso.org/lasilla/Telescopes/-2p2T/E2p2M/WFI/zeropoints)
Selman, F. J., & Melnick, J. 2005, A&A, 443, 851
Sirianni, M., et al. 2005, PASP, 117, 1049
Sollima, A., Pancino, E., Ferraro, F. R., Bellazzini, M., Straniero, O., & Pasquini, L. 2005, ApJ, 634, 332
Stanford, L. M., Da Costa, G. S., Norris, J. E., and Cannon R. D., 2006, ApJ, 647, 1075
Stetson, P. B. 2000, PASP, 112, 925
Stetson, P. B. 2005, PASP, 117, 563
Suntzeff, N. B., & Kraft, R. P. 1996, AJ, 111, 1913
Tian, K.-P., Zhao, J.-L., Shao, Z.-Y., & Stetson, P. B. 1998, A&AS, 131, 89
van de Ven, G., van den Bosch, R. C. E., Verolme, E. K., & de Zeeuw, P. T. 2006, A&A, 445, 513
van Leeuwen, F., Le Poole, R. S., Reijns, R. A., Freeman, K. C., & de Zeeuw, P. T. 2000, (vL00) A&A, 360, 472
Vasilevskis, S., Klemola, A., & Preston, G. 1958, AJ, 63, 387
Villanova, S., et al. 2007, ApJ, 663, 296
Weldrake, D. T. F., Sackett P.D., & Bridges T. J., 2007, AJ, 133, 1447
Yadav, R. K. S., Bedin, L. R., Piotto, G., Anderson, J., Villanova, S., Platais, I., Pasquini, L., Momany, Y., & Sagar, R. 2008, A&A, 484, 609, (Paper II)
Zacharias, N., Urban, S. E., Zacharias, M. I., Wycoff, G. L., Hall, D. M., Monet, D. G., & Rafferty, T. J. 2004, AJ, 127, 3043
Zhao, J. L., & He, Y. P. 1990, A&A, 237, 54

ID	α	δ	x	y	$\mu_\alpha \cos\delta$	$\sigma_{\mu_\alpha \cos\delta}$	μ_δ	σ_{μ_δ}	U	σ_U	B	σ_B	V	σ_V	R	σ_R	I	σ_I	Hα	$\sigma_{\mathrm{H}\alpha}$	$P_\mu(1)$	$P_\mu(2)$
(1)	(2)	(3)	(4)	(5)	(6)	(7)	(8)	(9)	(10)	(11)	(12)	(13)	(14)	(15)	(16)	(17)	(18)	(19)	(20)	(21)	(22)	(23)
[#]	[°]	[°]	[pixel]	[pixel]	[mas/yr]	[mas/yr]	[mas/yr]	[mas/yr]	[mag]	[mag]	[mag]	[mag]	[mag]	[mag]	[mag]	[mag]	[mag]	[mag]	[mag]	[mag]	[%]	[%]
1	201.802078	-47.750278	3016.264	-93.270	-3.25	0.52	11.78	6.12	99.999	99.999	20.535	0.056	19.842	0.155	19.332	0.219	18.729	0.071	99.999	99.999	0	28
2	201.763730	-47.750272	3407.004	-93.189	7.26	8.23	1.98	3.16	99.999	99.999	19.254	0.064	18.681	0.044	18.214	0.063	17.909	0.033	99.999	99.999	69	-1
3	201.799369	-47.750242	3043.872	-92.734	-0.41	14.48	7.24	6.54	99.999	99.999	21.173	0.080	20.441	0.046	19.854	0.044	19.437	0.058	99.999	99.999	39	-1
4	201.641896	-47.750155	4648.364	-92.553	11.20	8.53	9.50	6.65	99.999	99.999	20.938	0.060	20.242	0.083	19.708	0.051	19.308	0.081	99.999	99.999	43	-1
5	201.611638	-47.750119	4956.656	-92.562	0.43	0.63	11.93	3.89	99.999	99.999	17.145	0.015	16.632	0.016	16.238	0.007	15.953	0.035	99.999	99.999	19	0
6	201.609219	-47.750121	4981.298	-92.651	-1.55	6.82	1.60	7.53	99.999	99.999	20.856	0.036	20.202	0.064	19.660	0.040	19.263	0.047	99.999	99.999	57	-1
7	201.506294	-47.749911	6029.910	-92.178	6.71	5.49	21.84	4.47	99.999	99.999	19.905	0.033	19.095	0.031	18.552	0.039	18.136	0.060	99.999	99.999	0	-1
8	201.721527	-47.750125	3837.015	-91.161	1.23	3.45	7.76	9.23	99.999	99.999	20.844	0.057	20.116	0.017	19.692	0.068	19.347	0.069	99.999	99.999	62	-1
9	201.714951	-47.750153	3904.018	-91.634	5.27	3.52	2.33	6.89	99.999	99.999	20.354	0.050	19.696	0.028	19.261	0.051	18.909	0.032	99.999	99.999	70	-1
10	201.629034	-47.750053	4779.417	-91.229	4.24	3.80	7.46	1.69	99.999	99.999	19.275	0.024	18.694	0.024	18.310	0.030	17.953	0.057	99.999	99.999	0	55
[...]	[...]	[...]	[...]	[...]	[...]	[...]	[...]	[...]	[...]	[...]	[...]	[...]	[...]	[...]	[...]	[...]	[...]	[...]	[...]	[...]	[...]	[...]

TABLE 6.6— First lines of the electronically available catalog.

7

Radial distribution of the multiple stellar populations in ω Centauri

In this Chapter we present a detailed study of the radial distribution of the multiple populations identified in the Galactic globular cluster ω Cen. We used both space-based images (ACS/WFC and WFPC2) and ground-based images (FORS1@VLT and WFI@2.2*m* ESO telescopes) to map the cluster from the inner core to the outskirts (∼20 arcmin). These data sets have been used to extract high-accuracy photometry for the construction of color-magnitude diagrams and astrometric positions of ∼ 900 000 stars.

We find that in the inner ∼2 core radii the blue main sequence (bMS) stars slightly dominate the red main sequence (rMS) in number. At greater distances from the cluster center, the relative numbers of bMS stars with respect to rMS drop steeply, out to ∼8 arcmin, and then remain constant out to the limit of our observations. We also find that the dispersion of the Gaussian that best fits the color distribution within the bMS is significantly greater than the dispersion of the Gaussian that best fits the color distribution within the rMS. In addition, the relative number of intermediate-metallicity red-giant-branch stars which includes the progeny of the bMS) with respect to the metal-poor component (the progeny of the rMS) follows a trend similar to that of the main-sequence star-count ratio $N_{\rm bMS}/N_{\rm rMS}$. The most metal-rich component of the red-giant branch follows the same distribution as the intermediate-metallicity component. We briefly discuss the possible implications of the observed radial distribution of the different stellar components in ω Cen.

This Chapter contains results published in *Astronomy & Astrophysics* (Bellini et al. 2009b).

7.1 Introduction

The globular cluster (GC) ω Centauri is the most-studied stellar system of our Galaxy, but nevertheless one of the most puzzling. Its stars cover a wide range in metallicity (Cannon & Stobie 1973; Norris & Bessell 1975, 1977; Freeman & Rodgers 1975; Bessell & Norris 1976; Butler et al. 1978; Norris & Da Costa 1995; Suntzeff & Kraft 1996; Norris et al. 1996), with a primary component at [Fe/H] ~ -1.7 to -1.8, and a long tail extending up to [Fe/H] ~ -0.6, containing three or four secondary peaks (see Johnson et al. 2009 for a recent update). It has been shown, both with ground-based photometry (Lee et al. 1999; Pancino et al. 2000; Rey et al. 2004; Sollima et al. 2005a; Villanova et al. 2007) and *Hubble Space Telescope* (*HST*) photometry (Anderson 1997; Bedin et al. 2004; Ferraro et al. 2004), that ω Cen hosts different stellar populations, most of them clearly visible in most of their evolutionary phases.

These populations have been linked to the aforementioned metallicity peaks, in photometric studies of the red-giant branch (RGB) (Pancino et al. 2000; Hilker & Richtler 2000; Sollima et al. 2005a), the subgiant branch (SGB) (Hilker et al. 2004; Sollima et al. 2005b; Stanford et al. 2006; Villanova et al. 2007), and the main sequence (MS) (Piotto et al. 2005). The most puzzling feature in ω Cen was discovered by Piotto et al. (2005), who showed that, contrary to any expectation from stellar-structure theory, the bluer of the two principal main sequences (bMS) is more metal-rich than the redder one (rMS). The only possible way of reconciling the spectroscopic observations with the photometric ones is to assume a high overabundance of He for the bluer MS (Bedin et al. 2004; Norris 2004; Piotto et al. 2005). How such a high He content could have been formed is still a subject of debate (see Renzini 2008 for a review).

One of the scenarios proposed to account for all the observed features of ω Cen is a tidal stripping of an object that was originally much more massive (Zinnecker et al. 1988; Freeman 1993; Dinescu et al. 1999; Ideta & Makino 2004; Tsuchiya et al. 2004; Bekki & Norris 2006; Villanova et al. 2007). In this scenario, the cluster was born as a dwarf elliptical galaxy, which was subsequently tidally disrupted by the Milky Way. Since all the populations of such a galaxy pass through the center, the nucleus would have been left with a mixture of all of them.

It has also been suggested (Searle 1977; Makino et al. 1991; Ferraro et al. 2002) that ω Cen could have been formed by mergers of smaller stellar systems. In apparent support of this scenario, Ferraro et al. (2002) claimed that the most metal-rich RGB component of ω Cen (RGB-a, following the nomenclature of Pancino et al. 2000) has a significantly different mean proper motion from that of the other RGB stars, and they concluded that RGB-a stars must have had an independent origin. However, Platais et al. (2003) showed that the proper-motion displacement seen could instead be an uncalibratable artifact of the plate solution. More recently Bellini et al. (2009), with a new CCD-based proper-motion analysis, were able to demonstrate that all ω Cen RGB stars share the same mean motion to within a few km/sec. Anderson & van der Marel (2010) also find that the lower-turnoff population (the analog of the RGB-a) shows the same bulk motion as the rest of the cluster. Thus there is no longer a reason to think this population is kinematically distinct and an indication of a recent merger. Another indication that the cluster likely did not form by mergers can be found in the observation in Pancino et al. (2007) that all three RGB components share the cluster rotation, which would not be the case if different populations had different dynamical origins, or at least would require an unlikely degree of fine tuning.

While ω Cen was long thought to be the only cluster to exhibit a spread in abundances, we now know that it is not alone. M54 also clearly exhibits multiple RGBs (Sarajedini & Layden 1995; Siegel et al. 2007), SGBs (Piotto 2009), and has hints of multiple MSs. The complexity of M54 makes good sense, because it coincides with the nucleus of the tidally disrupting Sagittarius dwarf-spheroidal galaxy. M54 might be the actual nucleus or, more likely, it may represent a cluster that migrated to the nucleus as a result of dynamical friction (Bellazzini et al. 2008). ω Cen and M54 are the two most massive GCs in our Galaxy, and it is quite possible that they are the result of similar—and peculiar—evolutionary paths (Piotto 2009). In any case, even ω Cen and M54 are not the only clusters to exhibit non-singular populations. Exciting new discoveries, made in the last few years, clearly show that the GC multi-population zoo is quite populated, inhomogeneous, and complex.

Piotto et al. (2007) published a color-magnitude diagram (CMD) of the globular cluster NGC 2808, in which they identified a well-defined triple MS (D'Antona et al. 2005 had already suspected an anomalous broadening of the MS and had associated it with the three populations proposed by D'Antona & Caloi 2004 to explain the complex horizontal branch (HB) of this cluster). Another globular cluster, NGC 1851, must have at least two distinct stellar populations. In this case, the observational evidence comes from the split of the SGB (Milone et al. 2008). There are other GCs which undoubtedly show a split in the SGB, like NGC 6388 (Moretti et al. 2009; Piotto 2009), M22 (Marino et al. 2009), 47 Tuc (Anderson et al. 2009), which also shows a MS broadening, or in the RGB, like M4 (Marino et al. 2008). Recent investigations (Rich et al. 2004; Faria et al. 2007) suggest that also other galaxies might host GCs with more than one population of stars.

Multiple-population GCs offer observational evidence that challenges the traditional view. For half a century, a GC has been considered to be an assembly of stars that (quoting Renzini & Fusi Pecci 1988): "*represent the purest and simplest stellar populations we can find in nature, as opposed to* field *populations, which result from an*

admixture of ages and compositions". If we allow for the fact that all the GCs for which Na and O abundances have been measured show a well defined Na/O anti-correlation (Carretta et al. 2006, 2008), suggesting an extended star-formation process, and that 11 of the 16 intermediate-age Large Magellanic Cloud GCs have been found to host multiple populations (Milone et al. 2009), multi-populations in GCs could be more the rule than the exception. *De facto*, a new era in globular-cluster research has started, and understanding how a multiple stellar system like ω Cen was born and has evolved is no longer the curious study of an anomaly, but rather may be a key to understanding basic star-formation processes.

One way to understand how the multiple populations may have originated is to study the spatial distributions of the different populations, which might retain information about where they formed. In particular, theoreticians have been finding that if the second generation of stars is formed from an interstellar medium polluted and shocked by the winds of the first generation, then we would expect that the second generation would be more concentrated towards the center of the cluster than the first one (see D'Ercole et al. 2008; Bekki & Mackey 2009; Decressin et al. 2008). In the last of these references it is shown that in such a scenario the two generations of stars would interact dynamically and would homogenize their radial distributions over time. As such, spatial gradients represent a fading fossil record of the cluster's dynamical history.

Since ω Cen has such a long relaxation time (1.1 Gyr in the core and 10 Gyr at the half-mass radius, Harris 1996), it is one of the few clusters where we might hope to infer the star-formation history by studying the internal kinematics and spatial distributions of the constituent populations. These measurements will provide precious hints and constraints to allow theoreticians to develop more reliable GC dynamical models.

In a recent paper, Sollima et al. (2007) showed that the star-count ratio $N_{\rm bMS}/N_{\rm rMS}$ is flat beyond $\sim 12'$, but that inward to $\sim 8'$ it increases to twice the envelope value. Thus the bMS stars (i.e., the supposed "He-enriched" population) are more concentrated towards the center than the rMS, which is presumed to be the first generation. Unfortunately, Sollima et al. (2007) could not provide information about the trend of $N_{\rm bMS}/N_{\rm rMS}$ within $\sim 8'$, which corresponds roughly to 2 half-mass radii (r_h).

On the other hand, the radial distribution of RGB subpopulations has been analyzed by many authors (Norris et al. 1997; Hilker & Richtler 2000; Pancino et al. 2000, 2003; Rey et al. 2004; Sollima et al. 2005a; Castellani et al. 2007; Johnson et al. 2009). All these works agree that the intermediate-metallicity population (RGB-MInt) is more centrally concentrated than the more metal-poor one (RGB-MP). However, there is a disagreement about the most metal-rich population (RGB-a): Pancino et al. (2000), Norris et al. (1997), and Johnson et al. (2009) found that the most metal-rich stars (RGB-a) are as concentrated as the intermediate-metallicity ones, and consequently more concentrated than the most metal-poor stars, whereas Hilker & Richtler (2000) and Castellani et al. (2007) considered the RGB-a component to be the least-concentrated population. (Since our work in progress was already favoring the former view over the latter, we were concerned to reach the definitive truth of this matter).

In this Chapter, we trace the radial distribution of the stars of ω Cen , both on the MS and in the RGB region. Our radial density analysis covers both the center and the outskirts of the cluster, taking advantage of the combination of four instruments on three different telescopes, and of our proper-motion measurements on ground-based multi-epoch wide-field images (Bellini et al. 2009). In Section 2 we describe in detail the photometric data and the reduction procedures. Section 3 presents our analysis of the radial distribution of the stars on the two MSs. In Section 4 we perform an analogous study for the RGB stars. A brief discussion follows in Section 5.

7.2 Observations and data reductions

To trace the radial distribution of the different stellar populations in ω Cen, we analyzed several data sets, from four different cameras. To probe the dense inner regions of the cluster we took advantage of the space-based high resolving power of *HST*, using both the Wide Field Channel (WFC) of the Advanced Camera for Surveys (ACS), and the Wide Field and Planetary Camera 2 (WFPC2). For the relatively sparse outskirts of the cluster, we instead made use of deep archival ground-based observations collected with the FORS1 camera of the ESO Very Large Telescope (VLT). In addition, to link all the different data sets into a common astrometric and photometric reference

system, we used the Wide Field Imager (WFI) at the focus of the ESO 2.2*m* telescope (hereafter WFI@2.2*m*). This shallower data set was also used to study the red-giant branch in the outskirts of the cluster.

Figure 7.1 shows the footprints of the data sets, centered on the recently determined accurate center of ω Cen: RA = 13:26:47.24, Dec = −47:28:46.45 (J2000.0, Anderson & van der Marel 2010). The red footprints are those of *HST* observations. The larger ones are the ACS/WFC data sets, a 3×3 mosaic centered on the cluster center and a single field ∼17′ SW of the center. The smaller red field, ∼7′ S of the center, was observed with WFPC2. Blue rectangles show the partially overlapping FORS1@VLT fields, extending from ∼6′ to ∼25′. The large field in magenta is the $\sim 33' \times 33'$ field-of-view of our WFI@2.2*m* proper-motion catalog (Bellini et al. 2009). The figure also shows the major and minor axes (solid lines), taken from van de Ven et al. (2006). We divided the field into four quadrants, centered on the major and minor axes. The quadrants are labeled with Roman numerals and separated by dashed lines. We will use them to derive internal estimates of the errors of the star-count distribution. Concentric ellipses, aligned with the major/minor axes, have ellipticity of 0.17, coincident with the average ellipticity of ω Cen Geyer et al. 1983). These ellipses will be used to define radial annuli, in Section 2.8. Thick black circles mark the core radius ($r_c = 1.'4$) and the half-mass radius ($r_h = 4.'18$) (from Harris 1996). If we assuming a cluster distance of 4.7 kpc (van de Ven et al. 2006; van der Marel & Anderson 2010), the two radii correspond to 1.9 pc and 5.7 pc, respectively.

The details of the data sets are summarized in Table 7.1. In the following subsections we give brief descriptions of the reduction procedures, which have been presented in more detail in various other papers. The FORS1 data, however, were taken by Sollima et al. (2007), for a purpose similar to ours; we will give a full description of our reduction in subsection 7.2.4.

7.2.1 *HST*: ACS/WFC inner 3×3 mosaic

This data set (inner nine red rectangles in Fig. 7.1, GO-9442, PI A. Cool) consists of a mosaic of 3×3 fields obtained with the ACS/WFC through the F435W and F625W filters. This camera has a pixel size of ∼50 mas and a field of view of $3.'3 \times 3.'3$. Each of these nine fields has one short and three long exposures in both F435W and F625W. The mosaic covers the inner ∼10′×10′, the most crowded region of ω Cen. These images, which were used by Ferraro et al. (2004) and by Freyhammer et al. (2005), and which we used in both Bedin et al. (2004), and Villanova et al. (2007), were reduced using img2xym_WFC.09x10, which is a publicly available FORTRAN program, described in Anderson & King (2006b). The program finds and measures each star in each exposure by fitting a spatially-variable effective point-spread function. The independent measurements of the stars were collated into a master star list that covers the entire 3×3 mosaic field. For each star we constructed an average magnitude in each band, and computed the rms deviation of the multiple measurements about this average. Instrumental magnitudes were transformed into the ACS Vega-mag flight system following the procedure given in Bedin et al. (2005), using the zero points of Sirianni et al. (2005). Since the zero points are valid only for fluxes in the `_drz` exposures, we computed calibrated photometry for a few isolated stars in the `_drz` exposures and used this to set the zero points for the photometry that was based on the individual `_flt` images. Saturated stars in short exposures were treated as described in Section 8.1 in Anderson et al. (2008). Collecting photoelectrons along the bleeding columns allowed us to measure magnitudes of saturated stars up to 3.5 magnitudes above saturation (i.e., up to $m_{\rm F435W} \simeq 12$ mag), with errors of only a few percent (Gilliland 2004). We used the final catalog, which contains more than 760 000 stars, to trace the radial distribution of RGB and MS stars in this most crowded region of the cluster.

7.2.2 *HST*: ACS/WFC outer field

The outer ACS field (∼17′ SW of the cluster center, see Fig. 7.1) comes from proposals GO-9444 and GO-10101 (both with PI I. R. King), using the F606W and F814W filters. The photometry from the first-epoch observations was published in Bedin et al. (2004). The photometry presented here comes from the full two-epoch data set for this field; the two epochs also allow us to derive proper motions and perform a critical cluster/field separation.

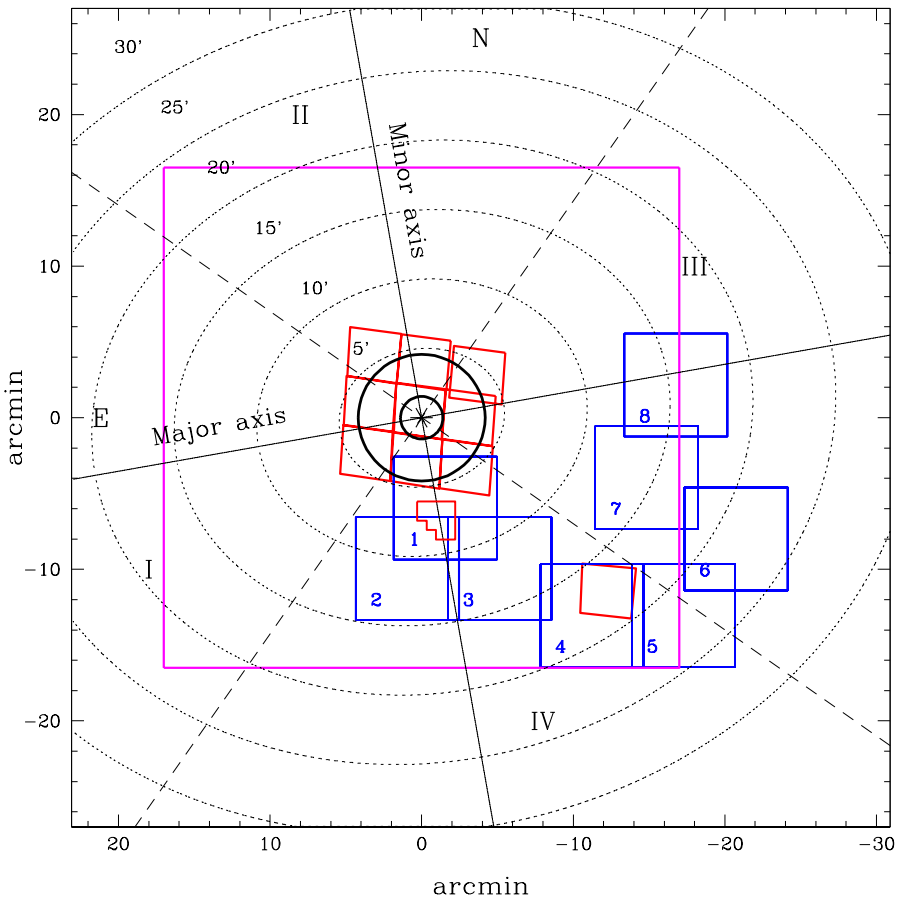

FIGURE 7.1— The footprints of the ω Cen data sets used in this work. North is up, east to the left. The "$*$" marks the cluster center. The 3×3 ACS/WFC mosaic (in red) is that of GO-9442, while the 8 FORS1 fields are marked in blue. The largest field (in magenta) comes from the WFI proper-motion catalog (Bellini et al. 2009). This wide-field catalog has been used to register the FORS1 and the ACS/WFC inner-mosaic data into a common astrometric and photometric reference system (see text). The smaller WFPC2 field at ~7′ south and the outer ACS/WFC field at ~17′ from the cluster center are also shown (in red). Concentric ellipses, centered on the center of ω Cen and aligned with the major and minor axes, show the radial bins that we created. Ellipses are split into quadrants (dashed lines), labeled with Roman numerals. Each quadrant is bisected by the major or minor axis. Thick black circles mark the core radius (r_c = 1.′4) and the half-mass radius (r_h = 4.′18) (from Harris 1996).

The reduction and calibration of these data sets use procedures similar to those used for the central mosaic, and provided photometry for ~3500 stars.

7.2.3 *HST*: WFPC2 field

We also make use of one WFPC2 field, ~7′ south of the cluster center (see Fig. 7.1). This data set consists of $2 \times 300 + 600$s exposures in F606W, and $2 \times 400 + 1000$s in F814W (GO-5370, PI R. Griffiths), and contains 9214 stars. These images have been reduced with the algorithms described in Anderson & King (2000). The field was calibrated to the photometric Vega-mag flight system of WFPC2 according to the prescriptions of Holtzman

TABLE 7.1— Data sets used in this work.

Data set	Filter	# images × Exp. time (s)
3 × 3 ACS/WFC inner mosaic	F435W	27 × 340, 9 × 12
	F625W	27 × 340, 9 × 8
ACS/WFC ∼17′	F606W	2 × 1285, 2 × 1300, 2 × 1331, 2 × 1375
	F814W	4 × 1331, 2 × 1340, 2 × 1375
WFPC2@*HST* ∼7′	F606W	2 × 300, 1 × 600
	F814W	2 × 400, 1 × 1000
FORS1@VLT	*B*	20 × 1100
	R	20 × 395
WFI@2.2*m*	*B*	1 × 10, 1 × 15, 11 × 30, 1 × 40, 1 × 60, 1 × 120,2 × 240, 2 × 300
	R_C	1 × 5, 1 × 10, 1 × 15, 1 × 30, 5 × 60
	V	6 × 5, 9 × 10, 1 × 15, 3 × 20, 2 × 30, 10 × 40, 4 × 45, 3 × 60, 10 × 90, 7 × 120, 1 × 150, 3 × 240

et al. (1995). This WFPC2 field is particularly important in tracing the distribution of stars in the MS of ω Cen, because it is at a radial distance from the center of the cluster where there are no suitable ACS/WFC observations and where ground-based observations are almost useless because of crowding.

7.2.4 VLT: eight FORS1 fields

The VLT data set consists of eight partially overlapping FORS1 fields, each with a pixel size of 200 mas and a field of view of 6.′8 × 6.′8. These fields (the blue rectangles in Fig. 7.1) probe the regions between 6′ and 25′ from the center of ω Cen . The set of images consists of 20 × 1100s exposures in *B*, and 20 × 395s in *R*, and are the same images used by Sollima et al. (2007). There are four images in each field (two per filter), except that the third and fourth fields have four images per filter (see Fig. 7.1 for field numbers). This is the only data set that we reduced specifically for this work. For this reason we give a more detailed description of our reduction procedure.

We retrieved the data sets from the ESO archive; master-bias and flat-field frames were constructed using standard IRAF routines. Photometric reduction of the images was performed using P. Stetson's DAOPHOT-ALLSTAR-ALLFRAME packages (Stetson 1987, 1994). For each exposure we constructed a quadratic spatially variable point-spread function (PSF) by using a Penny function[1], and for each individual exposure we chose—by

[1]A Penny function is the sum of a Gaussian and a Lorentz function. In this case we used five free parameters: half-width at half-maximum of the Penny function, in the *x* and in the *y* coordinate; the fractional amplitude of the Gaussian function at the peak of the stellar profile; the position angle of the tilted elliptical Gaussian; and a tilt of the Lorentz function in a different

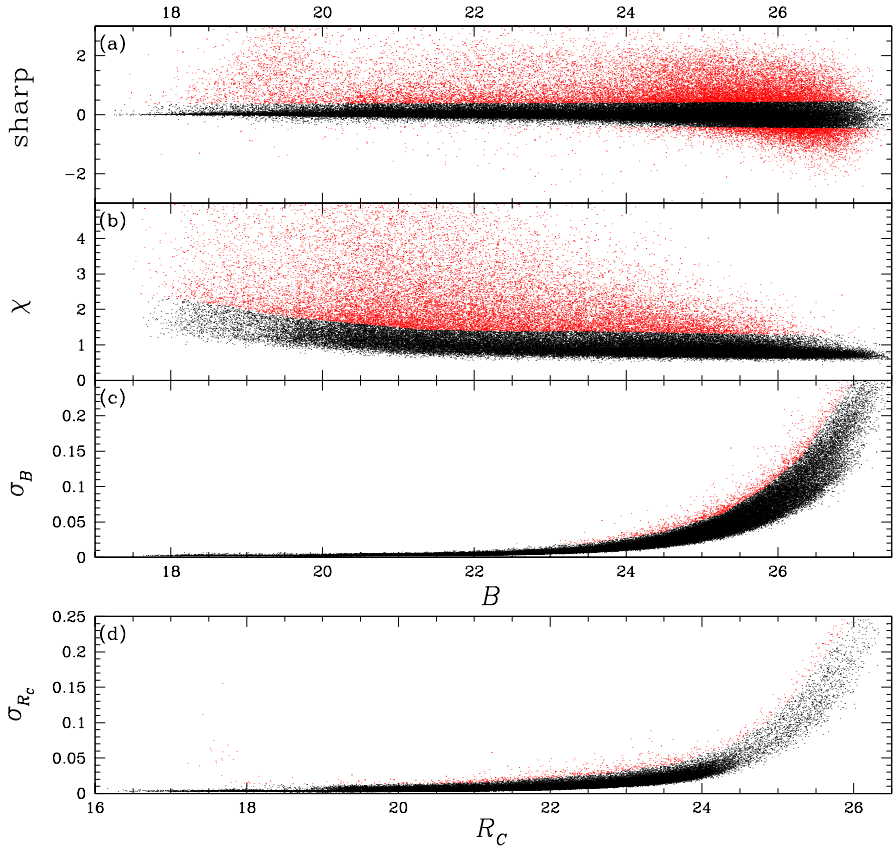

FIGURE 7.2— Selection criteria used to isolate FORS1@VLT stars for our MS subpopulation analysis. Panel (a) shows sharp values versus B magnitude, and panel (b) χ versus B. Panels (c) and (d) show the photometric errors as a function of the B and Cousins-R_C magnitudes respectively. Only stars that passed the sharp selection criterion (black in the first panel), are plotted in the subsequent panels; similarly, only stars that also survived the χ selection are shown in the remaining two panels.

visual inspection—the best 100 (at least) isolated, bright, unsaturated stars that were suitable for mapping the PSF variations all over the image. We used ALLFRAME on each individual field, keeping only stars measured in at least four images. The photometric zero points of each field were registered to the instrumental magnitudes of the fourth field (the less crowded of the two that have more exposures). Finally, photometric and astrometric calibration was performed using the WFI@2.2*m* astrometric-photometric catalog by Bellini et al. (2009) as a reference. As a result, we brought the FORS1 R magnitudes to the Cousins-R_C photometric system used by WFI@2.2*m*. Our final FORS1 catalog contains ~133 000 objects.

Since the innermost FORS1 field is seriously affected by crowding, we did not use it in this analysis. Fig. 7.2 plots the sharp, χ, and σ_B and σ_{R_C} calculated by ALLFRAME, as functions of stellar magnitude, for the stars in the FORS1 catalog. To choose the well-measured stars, we drew by eye the cut-off boundaries in the quality parameters that retained objects that were most likely to be well-measured stars. Panel (a) shows sharp values versus B magnitude. Stars that passed the selection criterion are shown in black. Panel (b), which includes only stars that passed the sharp cut, shows χ values versus B. Stars that also passed the χ criterion are in black. In

direction from the Gaussian. The Lorentz function may be elongated too, but its long axis is parallel to the x or y direction.

panel (c) we plot the σ_B values versus B, for the stars that survived these two selections. Again, the stars with good photometry are shown in black. Finally, in the last panel we plot σ_{R_C} values versus R_C, for all the survivors, and we highlight in black those that survived this selection too. At the end of these selection procedures, we are left with a catalog of ∼66 500 stars. We note that while these selection criteria affect stars at different magnitudes differently, they should not affect the ratio of stars on the bMS and rMS, since at a given magnitude the two populations should both have about the same photometric error, and the same probability of making it into our catalog.

7.2.5 WFI@2.2*m*

This data set was collected at the 2.2*m* ESO Telescope, with the WFI camera, between 1999 and 2003. The WFI@2.2*m* camera is made up of a mosaic of 4×2 chips, 2048×4096 pixels each, with a pixel scale of 238 mas/pixel). Thus, each WFI exposure covers $\sim 34' \times 33'$. The ω Cen astrometric, photometric, and proper-motion catalog based on this data set and presented in Bellini et al. (2009) is public, and contains several wide-band (U, B, V, R_C, I_C) filters plus a narrow-band filter (658 nm), and covers an area of $\sim 33' \times 33'$ centered on the cluster center. We refer the reader to Bellini et al. (2009) for a detailed discussion of the data-reduction and calibration procedures.

Briefly, photometry and astrometry were extracted with the procedures and codes described in Anderson et al. (2006a). Photometric measurements were corrected for "sky concentration" effects[2] and for differential reddening, as described in Manfroid & Selman (2001) and Bellini et al. (2009). Global star positions are measured to better than ∼45 mas in each coordinate. Photometric calibration in the B, V, R_C, I_C bands is based on a set of ∼3000 secondary standard stars in ω Cen , available on-line (Stetson 2000, 2005). Color equations were derived to transform our instrumental photometry into the photometrically calibrated system using an iterative least-squares linear fit. Thanks to the four-year time-baseline, we were able to successfully separate cluster members from field stars by means of the local-transformation approach (Anderson et al. 2006a), giving us proper motions more precise than ~ 4 mas yr^{-1}down to $B \sim 20$ mag, for ∼54 000 stars.

7.2.6 The astrometric and photometric reference frame

The large field of view of the WFI@2.2*m* camera makes our WFI catalog an ideal photometric and astrometric reference frame to which to refer all the other observations, from different telescope-camera-filter combinations. For each catalog we made the tie-in by means of stars that were in common with the reference catalog. For positions we derived a general six-parameter linear transformation to the astrometric system of the WFI catalog. For photometry we used as a reference standard the B and Cousins-R_C magnitudes of the WFI@2.2*m* catalog, and transformed the magnitudes of each other catalog to this standard. For the $m_{\rm F435W}$ and $m_{\rm F625W}$ magnitudes of the central mosaic of 3×3 ACS/WFC fields, we used ∼3300 stars that had been observed in common, located outside $4'$ from the cluster center to avoid the most crowded regions in the WFI data set (top-left panel of Fig. 7.3). We excluded from this sample saturated stars in the WFI data set, keeping only the brighter ($14.9 < B < 16.5$) and well measured ($\sigma_{B,R_C} < 0.02$ mag) ones (top-right panel in Fig. 7.3). The adopted calibration fits are shown in the bottom panels of Fig. 7.3. We did similarly for the FORS1 B and R magnitudes.

Calamida et al. (2005) measured a differential reddening of up to E($B - V$) ∼0.14 in a region of $\sim 14' \times 14'$ centered on ω Cen. This result has been questioned by Villanova et al. (2007); in their Figs. 1–6, the sharpness of the SGB sequences suggests that the existence of any serious differential reddening is very unlikely. But in any case, a proper radial-distribution analysis needs correction even for a differential reddening that is of the order of few hundredths of a magnitude. Our corrections for differential reddening followed the method outlined by Sarajedini et al. (2007), which uses the displacements of individual stars from a fiducial sequence to derive a reddening map.

[2]Light contamination caused by internal reflections of light in the optics, causing a redistribution of light in the focal plane.

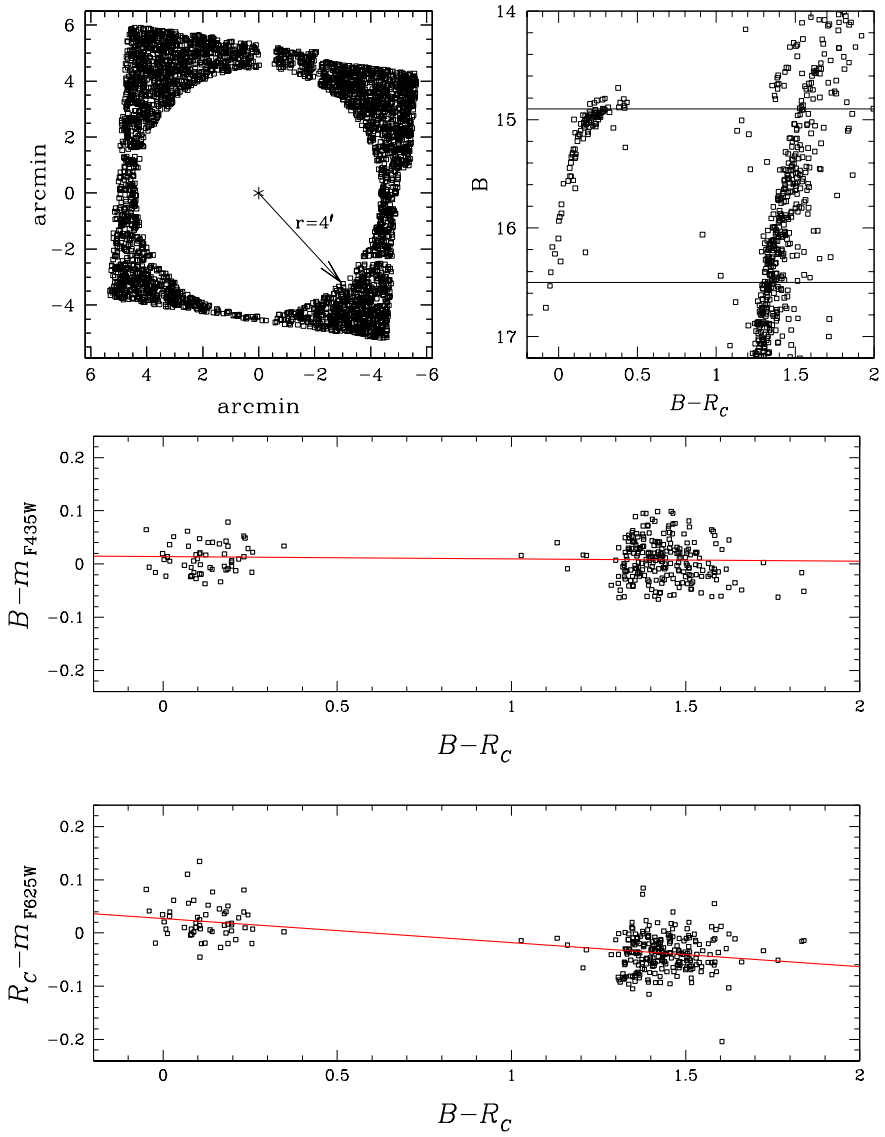

FIGURE 7.3— (*Top left:*) Selected stars in common between the ACS/WFC 3×3 mosaic and the WFI@2.2*m* data sets. (*Top right:*) Horizontal lines mark the magnitude interval used to derive calibration equations. (*Bottom panels:*) Calibration fits used to transform Vega-mag ACS/WFC $m_{\rm F435W}$ and $m_{\rm F625W}$ magnitudes into the WFI@2.2*m* photometric system. See the text for details.

The outer ACS/WFC field at ∼17′ from the cluster center and the WFPC2 field at ∼7′ provide stellar photometry in the F606W and F814W bands. For the ACS field we have overlap with the WFI catalog, which allows us to calibrate the photometry, but the stars available are all on the main sequence above $m_{\rm F606W} = 21$, so they have a very narrow range in color, and we cannot empirically determine the color term in the calibration. For the WFPC2 field, in addition to the problem of the limited color baseline, the WFI photometry in this inner field is of low quality on account of ground-based crowding. For these reasons, we decided to not transform the photometry

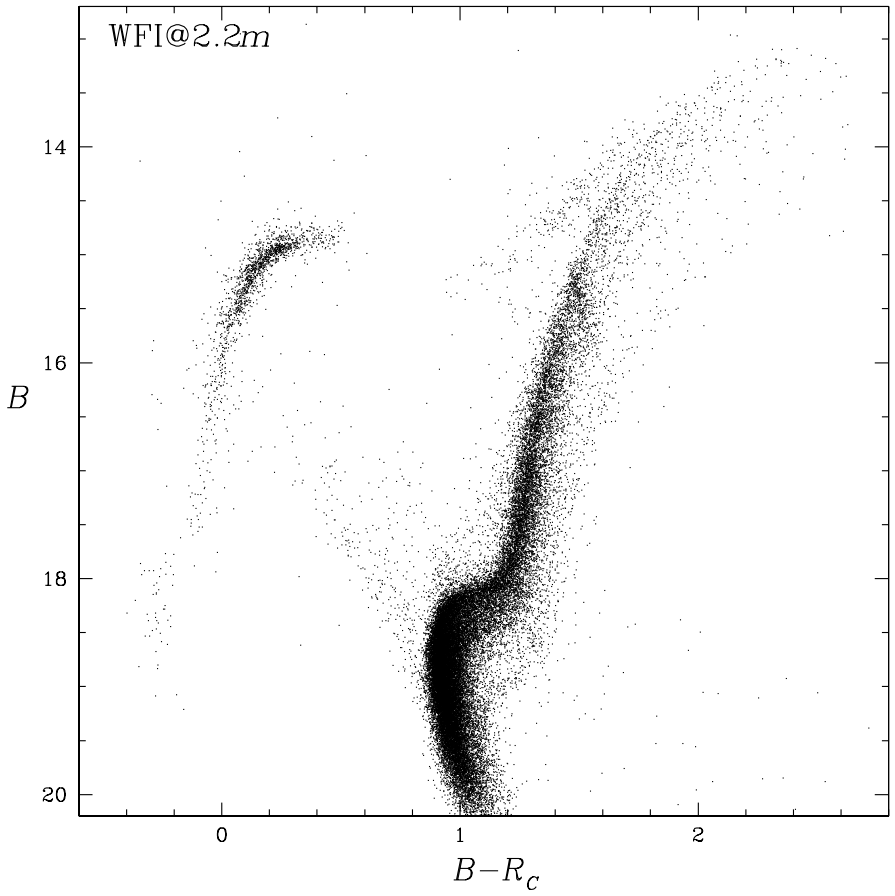

FIGURE 7.4— B vs. $B - R_C$ CMD of WFI@2.2*m* stars, after calibration and proper-motion selection (see Bellini et al. 2009).

of these two fields into the photometric reference system of WFI@2.2*m*, but dealt with them in the *HST* Vega-mag flight system.

7.2.7 The deep color-magnitude diagrams

Our proper-motion-selected WFI@2.2*m* B vs. $B - R_C$ CMD is shown in Fig. 7.4. All the main features of the cluster are clearly visible, except for the split MS, since the WFI data go down only a magnitude or so below the turnoff. The CMDs of the other data sets that we analyzed are presented in Fig. 7.5, where the top-left panel refers to the eight FORS1@VLT fields, the middle-left panel to the proper-motion-selected CMD of the external ACS/WFC, the bottom-left panel the CMD from the WFPC2 field, and the right panel of Fig. 7.5 the CMD of the inner 3×3 ACS/WFC mosaic. It is clear that the MS population can be studied in all but the WFI CMD, and the RGB population can be studied in the WFI and inner ACS data sets.

Now that we have a comprehensive sample of ω Cen stars, both for the bright stars and for the faint ones, covering the central region all the way out to $\sim 25'$, we can define robust selection criteria for the subpopulations to track how the population fractions vary with radius.

7.2.8 The *angular* radial distance: r^*

Since ω Cen is elongated in the plane of the sky, it does not make sense to analyze its radial profile via circular annuli. We therefore decided to extract radial bins in the following way. We adopted the position angle (P.A.) of 100° for the major-axis (van de Ven et al. 2006), and an average ellipticity of 0.17 Geyer et al. 1983). To define the bins of the radial distribution we adopted elliptical annuli, whose major axes are aligned with the ω Cen major axis, and stars were extracted accordingly (see Fig. 7.1). To indicate the angular radial distance from the cluster center, we used the equivalent radius r^*, defined as the radius of the circle with the same area as the corresponding ellipse (i.e., the geometrical mean of the semi-major and semi-minor axes). Each of the small fields (the outer ACS field and the WFPC2 field), we considered as a single radial bin.

7.3 MS subpopulations

Our goal in putting together these varied catalogs is to quantify the differences in the radial profiles of the various subpopulations of ω Cen. One way to do this would be to measure the surface density profile for each group and compare them directly, but this would require accurate completeness corrections and careful attention to magnitude bins. Since our interest, however, is simply to determine how the populations vary with respect to each other, we need only measure the *ratio* of the populations as a function of radius. This ratio should be independent of completeness corrections and the details of the magnitude bins used, since the bMS and rMS differ only slightly in color and are observed over the same magnitude range.

Our analysis of the $N_{\rm bMS}/N_{\rm rMS}$ ratio is based mostly on the data sets from the inner ACS/WFC 3×3 mosaic and FORS1@VLT, which allow us to map the ratio of bMS/rMS from the cluster center out to ∼25′, once the photometry and astrometry have been brought into the same reference system. The other two fields, each of which covers only a small region, provide only one point each in our analysis of $N_{\rm bMS}/N_{\rm rMS}$ versus radius. Moreover, since we were not able to bring $m_{\rm F606W}$ and $m_{\rm F814W}$ photometry of the outer ACS and the WFPC2 field into the WFI B and R_C photometric system, we kept the WFPC2 and the outer ACS/WFC data sets in their native photometric system, and used them only for a further (though important) confirmation of the radial gradient found with the FORS1 and inner ACS/WFC data sets.

7.3.1 Straightened main sequences

In order to analyze the color distribution of the stars along the MS in a more convenient coordinate system, we adopted a technique previously used with success in ω Cen (Anderson 1997, 2002), and in other works (Sollima et al. 2007; Villanova et al. 2007; Piotto et al. 2007; Milone et al. 2008, Anderson et al. 2009).

We defined fiducial lines in the CMDs (drawn by hand), such as to be equidistant from the ridge lines of the bMS and rMS stars. We avoided choosing the ridge line of either sequence as our fiducial line, because we wanted a system in which both the sequences are as parallel and as rectified as possible. We used different fiducial lines for the B, $B-R_C$ CMDs of the inner ACS/WFC and the FORS1 data sets and for the ($m_{\rm F606W}$, $m_{\rm F606W}-m_{\rm F814W}$) CMDs of the WFPC2 and outer ACS/WFC data sets. In this way, we were sure to straighten the MSs in the same consistent way for the two different sets of filters. Then we subtracted from the color of each star the color of the fiducial line at the same luminosity as the star.

In Fig. 7.6 we show the CMDs in the ω Cen MS region for the central mosaic of ACS/WFC data (left panel), the FORS1@VLT (middle panel), and the WFPC2 ∼7′ field and the ACS/WFC field at ∼17′ (right panels). In the case of the central ACS/WFC data, we plotted only a randomly chosen 8% of the stars, in order to show the two sequences clearly. In all the CMDs the MS splitting is clearly visible. For the inner ACS/WFC and FORS1 data sets we restricted our MS analysis to the magnitude range $20.9 \leq B \leq 22.1$ (dashed lines in Fig. 7.6), the interval in which the two MSs are most separated in color and are parallel. For the same reasons we analyzed stars in the magnitude range $20.6 \leq m_{\rm F606W} \leq 21.9$ for the WFPC2 and the outer ACS/WFC data sets. The bright limit also avoids the saturated stars in the deep WFC exposures. The adopted fiducial lines are again plotted in red.

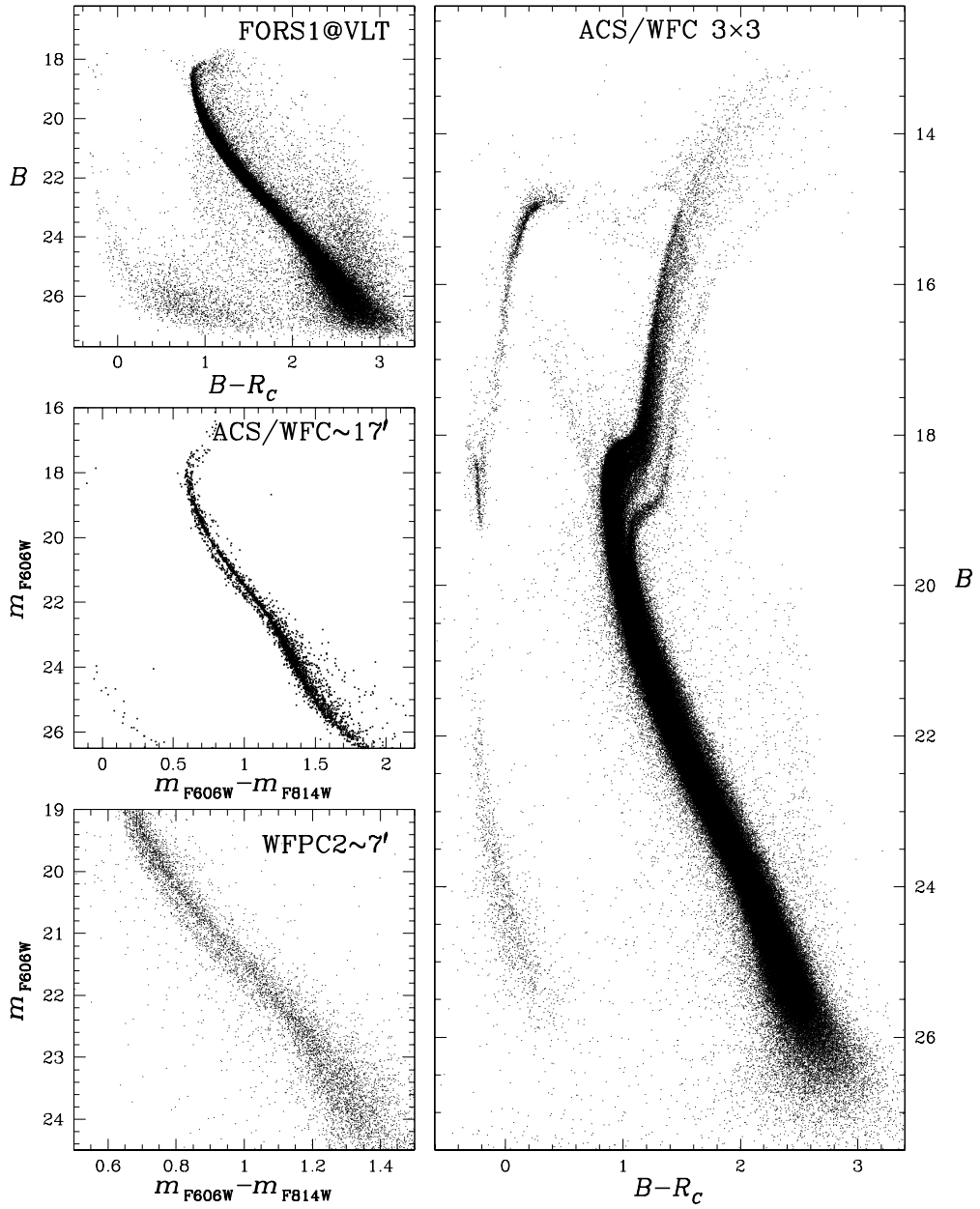

FIGURE 7.5— (*Top left*): CMD from the eight FORS1@VLT fields. We can measure stars from the bottom of the RGB down to B ~27.5 mag. (*Middle left*): proper-motion-selected CMD from the outer ACS/WFC field. (*Bottom left*): CMD from the WFPC2 images located ~7′ south of the cluster center. (*Right panel*): CMD of the inner 3×3 ACS/WFC fields. In the top left and the right-hand CMDs, the bMS and rMS fail to show separately only because the profusion of points blackens their whole region.

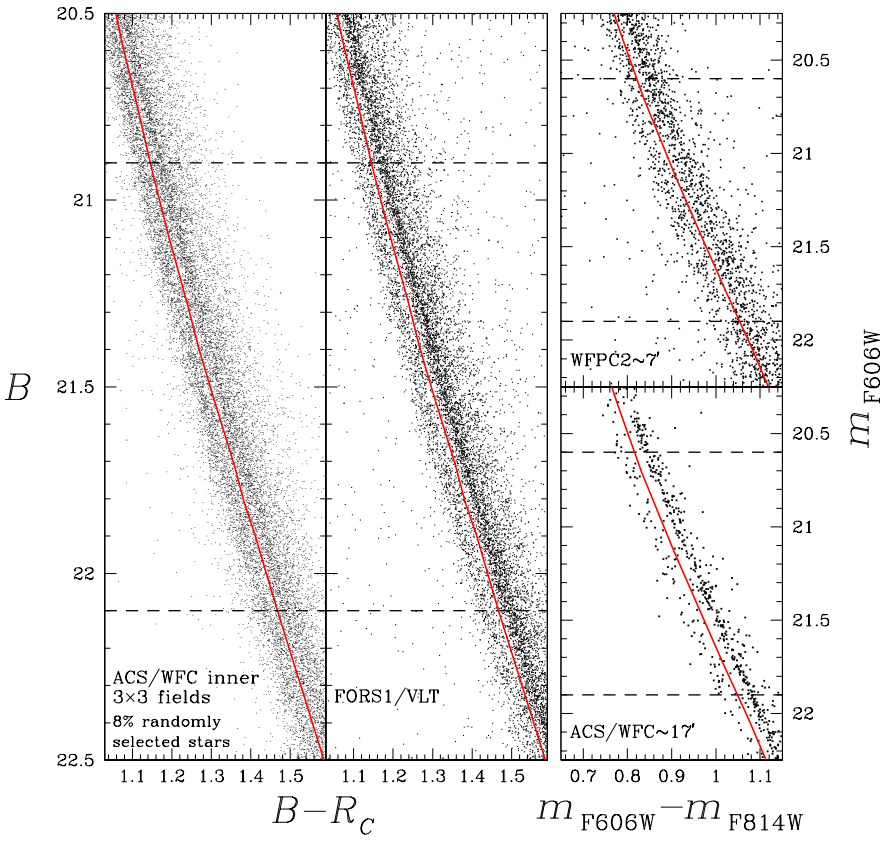

FIGURE 7.6— The left panel shows a randomly selected 8% of the stars in the CMD of the inner ∼10′ × 10′ ACS/WFC images, in the region of the MS where the two branches are most separated in color. The middle panel shows the CMD of the FORS1@VLT fields. The right panels show the outer ACS/WFC field (bottom) and WFPC2 field (top). The MS duality is clearly detected in all diagrams (see also Fig. 7.7). The dashed horizontal lines mark the selected magnitude range for the definition of the bMS and rMS samples used in the derivation of their radial profiles. The fiducial lines (drawn by hand) that were used to straighten and separate the sequences are also plotted (in red in the color version).

In Fig. 7.7 we show straightened CMDs for the same data sets shown in Fig. 7.6, with the only difference being that we now plot a 20% randomly generated sample of stars for the inner ACS/WFC data set, since the expanded color baseline allows more points to be seen. It is worth noting that even a simple inspection shows the $N_{\rm bMS}/N_{\rm rMS}$ ratio clearly decreasing as we go from the central cluster regions to the outer ones. It is also clear that the spread in the bMS is somewhat greater than that of the rMS.

Finally, note that we call the color deviation of a star from the fiducial line $\Delta(B-R_C)$. We shall use this notation frequently in what follows.

Our aim in selecting the best-measured stars in the previous sections was so that we would be able to assign the stars to the different populations as accurately as possible. Similarly, as much as possible we transformed our photometry into the same system, so that our population selections throughout the cluster would be as consistent as possible.

Even with these careful steps, however, it is still difficult to ensure that we are selecting stars of the same population in the inner parts of the cluster as in the outer parts. Even if we had observations with the same detector

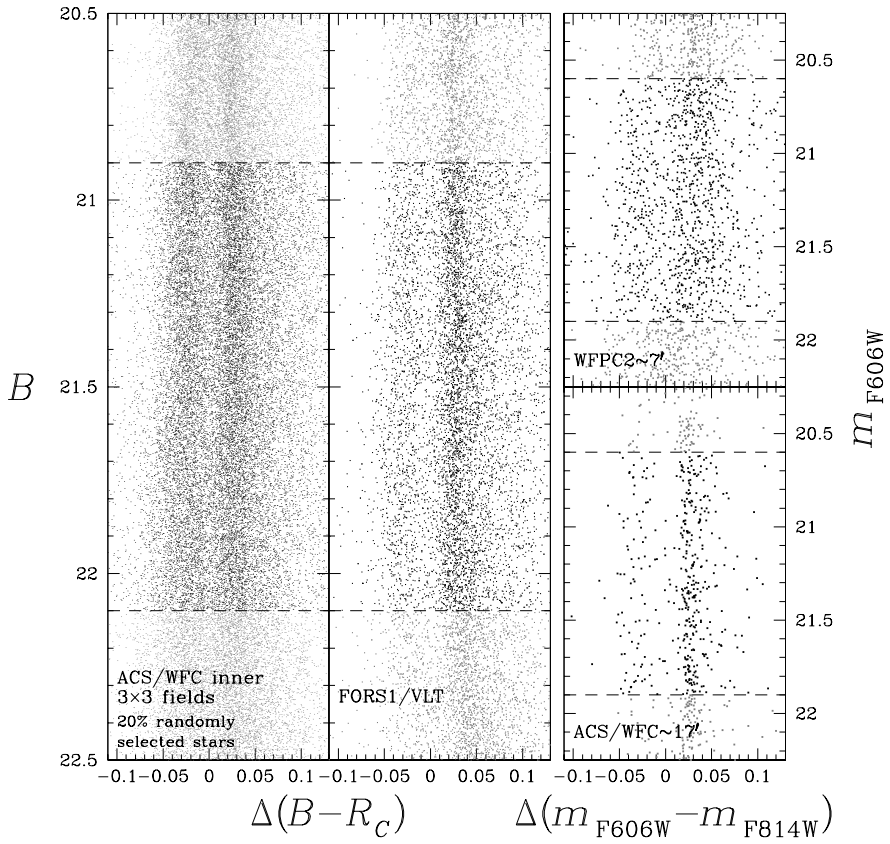

FIGURE 7.7— Same as Fig. 7.6, but after subtraction, from the color of each star, of the color of the fiducial line at the same luminosity. In the left panel we show a randomly selected 20% of the stars from the ACS/WFC central-mosaic data (rather than the previous 8%, since the color-scale is now less compressed).

at all radii, the greater crowding at the center would increase the errors there. On the other hand, our use of ground-based images for the outer fields actually makes those fields even *more* vulnerable to crowding effects.

Another complication comes from main-sequence binaries, which at the distance of a globular cluster are unresolved. Relaxation, causing mass segregation, will concentrate them to the cluster center and cause a redward distortion of the main sequence there.

Moreover, in the lower-density outer regions of the cluster we can get the same statistical significance only by using larger areas, with an increased vulnerability to inclusion of field stars. Finally, the red side of the main sequence is contaminated by the anomalous metal-rich population (hereafter MS-a), which is clearly connected with RGB-a. Even if these stars include only ∼5% of the total cluster members (Lee et al. 1999; Pancino et al. 2000; Sollima et al. 2005a; Villanova et al. 2007), they are an additional source of pollution for rMS stars—against which we now take specific precautions.

7.3.2 Dual-Gaussian fitting

There is no way of dealing with the above issues perfectly, but we did our best to make our measurements as insensitive to them as possible. To this end, we measured the bMS and rMS fractions by simultaneously fitting the

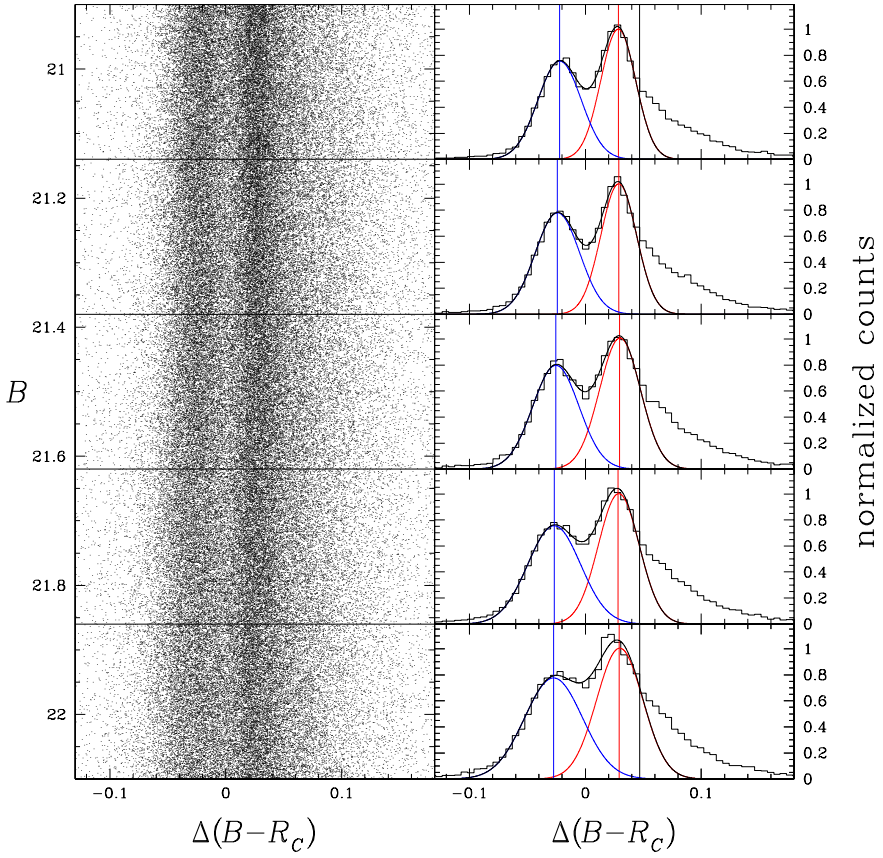

FIGURE 7.8— (*Left panel*): B versus $\Delta(B-R_C)$ diagram for selected stars in our data set from the ACS/WFC 3×3 mosaic, divided into five magnitude intervals. We now plot *all* the stars in this sample, not just a randomly selected subset. (*Right panels*): $\Delta(B-R_C)$ histograms with the Gaussian best fits. See the text for details.

straightened color distributions with two Gaussians, and taking the area under each Gaussian as our estimate of the number of stars in each population. By keeping the width of each Gaussian an adjustable parameter, we allowed in a natural way for the fact that the photometric scatter differs from one radius and data set to another.

While the dual Gaussians provide a natural way of measuring the two populations in data sets that have different color baselines and different photometric errors, there is one serious complication. As we have indicated, there is an unresolved, broad population of stars redward of the rMS that consists of blends, binaries, and members of the MS-a branch. Since it is unclear what relation this mixed population has with the two populations that we are studying, we wanted to exclude it from the analysis as much as possible. We did so by cutting off the reddest part of the color range, and confining our fitting to the color range that is least disturbed by the contaminated red tail.

In order to choose the red cutoff as well as possible, we gathered together all of the stars in each data set. Below we will describe for simplicity only the case of the central 3×3 mosaic of ACS images in B and R_C. The procedure followed is, however, the same for the other data sets.

Within this data set we chose the MS stars that were in the magnitude range $20.9 \leq B \leq 22.1$ (within which the

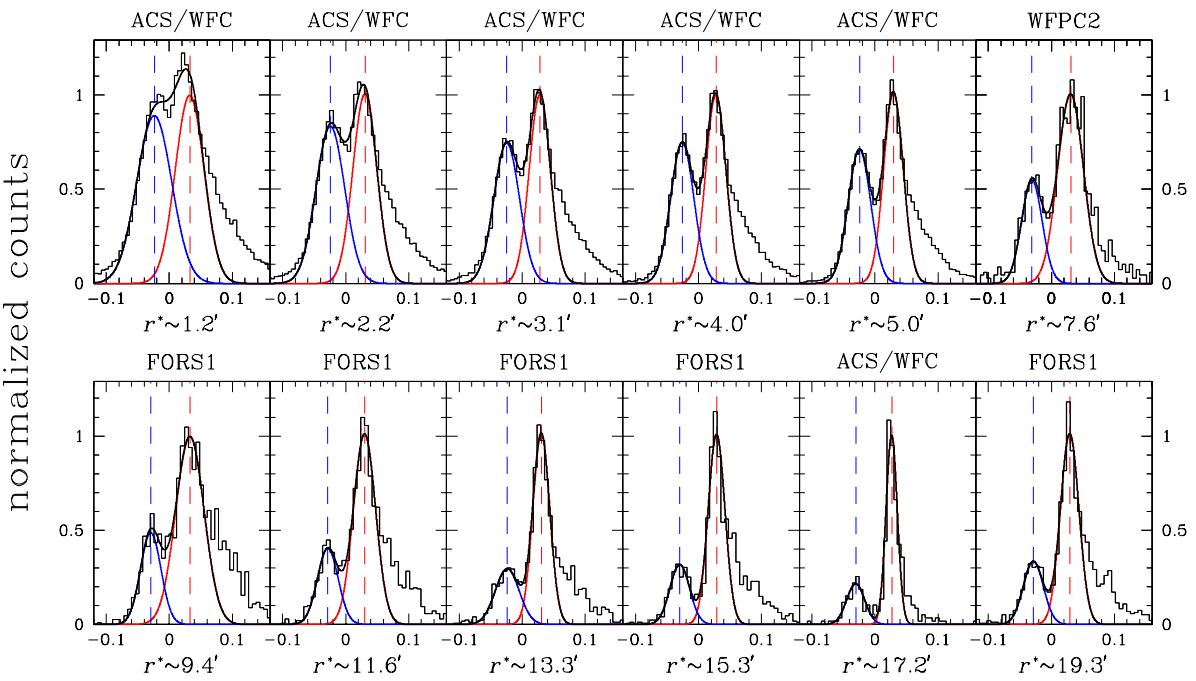

FIGURE 7.9— Dual-Gaussians fits. As in Fig. 7.8, the Gaussian fits to the bMS and rMS are in blue and red respectively, and their sum in black. The vertical dashed lines mark the centers of the individual Gaussians. The individual panels are arranged in order of effective radius. (Note that *all* our fields are shown here, in radial order, so that the WFPC2 field follows the inner ACS fields, and the outer ACS field falls between two of the FORS1 fields.)

two MSs are almost parallel and are maximally separated in color) and in the color range $-0.25 \leq \Delta(B-R_C) \leq 0.25$ mag. We emphasize that this ensemble of the data set, within which we will later see a considerable gradient in the relative numbers of bMS and rMS stars, will not be used to derive population results in the case of the inner ACS/WFC data set, but only to choose the red cutoff. We divided these stars into five magnitude intervals, because the observational errors, which increase the spread of the sequences, depend on magnitude. Next, we plotted histograms of the $\Delta(B-R_C)$ distribution within each magnitude interval, using a bin size of 0.006 mag. This size is ~1/4 of the typical photometric error in color; it makes a good compromise between a fine enough color resolution, on the one hand, and adequate statistics, on the other hand.

The actual choice of the red cutoff is a two-tiered procedure. We must first develop a procedure for the fitting of dual Gaussians to a set of bins that has a red cutoff; then we must decide on a value of $N_{\rm red}$, the number of bins that we include on the redder side of the red Gaussian.

Although from a mere inspection of the histograms it is clear where, approximately, the peak of the red Gaussian should lie, the narrowness of the bins leaves it uncertain in which particular bin the peak of the red Gaussian will actually fall. Since the red cutoff, $N_{\rm red}$, is defined as being counted from that bin, we had to resort to an iterative procedure to locate the cutoff for a given value of $N_{\rm red}$. We began by choosing a cutoff safely to the red of where we guessed that the cutoff would actually fall, and then using that cutoff in a first try at fitting the dual Gaussians. The iteration then consisted of placing the cutoff just beyond $N_{\rm red}$ bins on the red side of the peak of the red Gaussian and fitting again; this new fit might cause the red peak to move to a different bin. When the red peak stays in the same bin, the iteration has converged; this happened after very few iterations.

We assumed trial values of $N_{\rm red}$ from 2 to 5, and for each of those values we iteratively computed the Gaussian

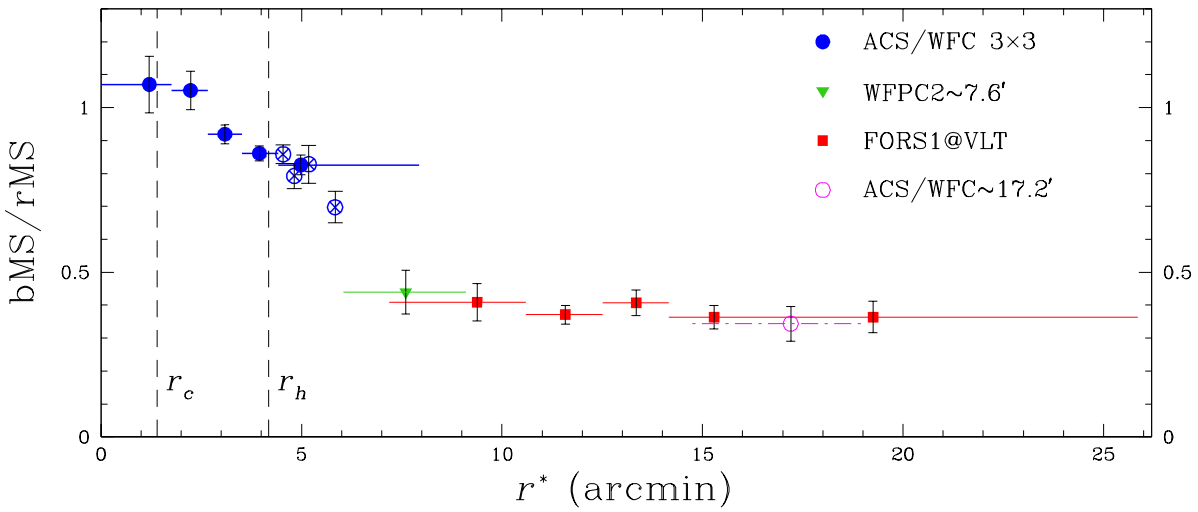

FIGURE 7.10— $N_{\rm bMS}/N_{\rm rMS}$ ratio versus equivalent radius r^*. Different colors and symbols refer to different data sets. Dashed vertical lines mark the core radius and the half-mass radius. Error bars were calculated from the residuals of values in individual subdivisions (quadrants for the inner ACS/WFC mosaic, magnitude intervals in each outer field). To improve the radial resolution for the outermost annulus of the inner ACS/WFC mosaic, we also divided it into four sub-annuli (crossed open circles). See text for a fuller explanation.

parameters for each of the five magnitude intervals. We chose as the best value for $N_{\rm red}$ the one for which the five values of $N_{\rm bMS}/N_{\rm rMS}$ were the most consistent. This value turned out to be $N_{\rm red} = 3$. With this choice made, we then moved on to fit dual Gaussians to each of our detailed data sets.

Fig. 7.8 shows the results of this procedure. In the left panel we show our selected stars in the B versus $\Delta(B-R_C)$ diagram—all of the stars this time, rather than a random selection of a fraction of them. The horizontal lines delineate our five magnitude intervals. On the right we show the final $\Delta(B-R_C)$ histogram for each magnitude interval, and the dual-Gaussian fit to it. The individual Gaussians are shown in blue and red, respectively, and the black curve is their sum. The vertical blue and red lines are the centers of the respective Gaussians, and the vertical black line shows the red cutoff. Note that we do not show the vertical boundaries between the bins of a histogram, because on this scale they would be too close to each other. Nor do we show the Poisson errors of the counts in the bins, because they are small and would obscure the bin values themselves; the size of the errors is amply clear from the smoothness of the values in neighboring bins. The counts in the histograms are normalized so as to make the height of the red Gaussian equal to unity.

7.3.3 The Radial Gradient of $N_{\rm bMS}/N_{\rm rMS}$

Having chosen the position of the red cutoff, we were able to perform dual-Gaussian fitting on each of our data sets. Figure 7.9 shows our fits. We divided the inner ACS/WFC mosaic and the outer FORS1@VLT data sets into five radial intervals for each. The intervals were chosen in such a way as to have the same number of selected stars in each of them, so that the statistical sampling errors will be uniform. (The reader should note that Fig. 7.9 shows *all* of our fields, in radial order, so that the WFPC2 field follows the inner ACS fields, and the outermost ACS field falls between two of the FORS1 fields.)

Figure 7.10 shows our results for the radial variation of the bMS to rMS ratio, for the five radial parts of the inner ACS mosaic, the five radial intervals of our FORS1 fields, the WFPC2 field, and the outer ACS field. Symbols of a different shape distinguish the various types of field. The outermost radial interval of the ACS/WFC

TABLE 7.2— Dual-Gaussian fitting results. For each data set (first column) we give in Cols. 2–4 the radial extent (minimum, median, and maximum r^*). In Cols. 5–8 are the sigmas of the Gaussians that best fit the bMS and rMS color distributions, with errors. In the next two columns are the $N_{\rm bMS}/N_{\rm rMS}$ ratio and its error. The next-to-last column gives the color difference between the two Gaussian peaks, and the final column identifies the color baseline of the data set.

data set	r^* min ($'$)	r^* median ($'$)	r^*max ($'$)	$\sigma_{\rm bMS}$ Δcolor	rms($\sigma_{\rm bMS}$) Δcolor	$\sigma_{\rm rMS}$ Δcolor	rms($\sigma_{\rm rMS}$) Δcolor	$N_{\rm bMS}/N_{\rm rMS}$	$\sigma(N_{\rm bMS}/N_{\rm rMS})$	(rMS$_{\rm cen}$ − bMS$_{\rm cen}$) Δcolor	color
ACS/WFC	0.00	1.21	1.76	0.027	0.0020	0.023	0.0014	1.07	0.09	0.056	$B-R_C$
(3×3)	1.76	2.24	2.66	0.023	0.0018	0.018	0.0011	1.05	0.06	0.055	$B-R_C$
	2.66	3.09	3.51	0.020	0.0012	0.017	0.0008	0.92	0.03	0.053	$B-R_C$
	3.51	3.95	4.42	0.018	0.0010	0.016	0.0007	0.86	0.02	0.054	$B-R_C$
	4.42	4.98	7.93	0.018	0.0011	0.015	0.0007	0.82	0.03	0.054	$B-R_C$
subdivision	4.42	4.54	4.67	0.019	0.0012	0.015	0.0011	0.86	0.03		
of last bin	4.67	4.82	4.98	0.018	0.0013	0.016	0.0011	0.79	0.04		
	4.98	5.18	5.44	0.018	0.0013	0.015	0.0010	0.83	0.06		
	5.44	5.84	7.93	0.018	0.0013	0.015	0.0010	0.70	0.05		
WFPC2	6.04	7.57	9.10	0.017	0.0010	0.020	0.0020	0.42	0.07	0.061	$m_{\rm F606W}-m_{\rm F814W}$
FORS1	7.18	9.38	10.60	0.017	0.0023	0.020	0.0021	0.41	0.06	0.062	$B-R_C$
	10.60	11.58	12.51	0.017	0.0019	0.017	0.0013	0.37	0.03	0.058	$B-R_C$
	12.51	13.34	14.16	0.019	0.0018	0.014	0.0009	0.41	0.04	0.054	$B-R_C$
	14.16	15.29	16.75	0.016	0.0022	0.014	0.0009	0.36	0.04	0.059	$B-R_C$
	16.75	19.25	26.19	0.016	0.0020	0.014	0.0010	0.36	0.05	0.058	$B-R_C$
ACS/WFC	14.68	17.21	19.69	0.014	0.0020	0.009	0.0020	0.34	0.05	0.057	$m_{\rm F606W}-m_{\rm F814W}$

mosaic is a special case, however, since it consists largely of the four corners of the mosaic, and it spans a larger radial extension. To better map the bMS/rMS distribution in this radial interval, we decided to further split it into four sub-annuli. In this way we increase the radial resolution, but pay the price of larger sampling errors. We have therefore plotted the outermost radial interval of the inner ACS/WFC mosaic twice, once as a whole annulus, and once as four sub-annuli (marked as crossed open circles in Fig. 7.10).

Our choice of using ellipses with fixed ellipticity and position angle to extract radial bins could have introduced some systematics in our derived $N_{\rm bMS}/N_{\rm rMS}$ ratios. To address this issue, we recalculated the $N_{\rm bMS}/N_{\rm rMS}$ ratios by extracting radial bins using simple circles, and we found no significant differences between the two radial binning methods.

Estimating the errors of our points required special attention. First we took the Poisson errors of the numbers of stars, and used them to generate Poisson errors for the values of $N_{\rm bMS}/N_{\rm rMS}$. These, however, are only a lower bound for the true error, which has additional contributions that are impossible to estimate directly; they come from blends, binaries, etc. To estimate the true errors empirically, for each value of $N_{\rm bMS}/N_{\rm rMS}$ we subdivided the sample of stars that had been used. In the inner ACS/WFC mosaic the subsamples were the quadrants shown in Fig. 7.1, while for each of the outer fields, where we do not have symmetric azimuthal coverage, we divided the sample into magnitude intervals, four for each FORS1@VLT field and three each for the WFPC2 field and the outer ACS/WFC field.

We treated each set of subsamples as follows: Within each subsample we performed a dual-Gaussian fit, and derived from it the value of $N_{\rm bMS}/N_{\rm rMS}$. We weighted each subsample according to the number of stars in it, and took a weighted mean of the four (or three) values of $N_{\rm bMS}/N_{\rm rMS}$, to verify that this mean was equal, within acceptable round-off errors, to the value that we had found for the whole sample. (It was, within a per cent or two in nearly every case.) Finally we derived an error for the sample, from the residuals of the individual $N_{\rm bMS}/N_{\rm rMS}$ values from their mean, using the same weights as we had used for the mean. These are the error bars that are shown in Figure 7.10. These errors are indeed larger than the Poisson errors, but only by about 10%. We must note, however, that in addition to the random error represented by the error bars, it is likely that there is still some systematic error in our values of $N_{\rm bMS}/N_{\rm rMS}$, due to the effects of blends and binaries. On the one hand, blends have the same photometric effect as true binaries; they tend to move bMS stars into the rMS region, while many of the rMS stars that are similarly affected are eliminated by our red cut-off. This effect tends to reduce our observed value of $N_{\rm bMS}/N_{\rm rMS}$. It is less easy to predict, however, how such effects increase toward the cluster center. Blends, on the one hand, increase because of the greater crowding. Binaries, on the other hand, increase because their greater mass gives them a greater central concentration. To repeat, the result has been that our values of $N_{\rm bMS}/N_{\rm rMS}$ are somewhat depressed toward the cluster center, so that the gradient of $N_{\rm bMS}/N_{\rm rMS}$ that we report is probably a little lower than the real one.

Fig. 7.10 clearly shows a strong radial trend in the ratio of bMS to rMS stars, with the bMS stars more centrally concentrated than the rMS stars. The most metal-rich population, MS-a, is too sparse, and also too hopelessly mixed with the red edge of the rMS, to allow any reliable measurement of its radial distribution, but in the next section we will examine the distribution of its progeny, RGB-a. Table 7.2 summarizes our results. The first column identifies the data set. Columns 2–4 give, for the inner ACS/WFC 3x3 mosaic, the minimum, median, and maximum radius of the central circle or the annulus, while for the other fields these columns give the inner, median, and maximum radius that the field covers. The sigmas of the Gaussians that best fit the bMS and rMS color distributions, with their uncertainties, are in Columns 5–8. Columns 9 and 10 give the $N_{\rm bMS}/N_{\rm rMS}$ ratio and its error. Column 11 gives the difference (in straightened color) between the peaks of the Gaussians that best fit the bMS and rMS. The last column gives the color baseline of each data set. By Δcolor we mean a color difference or width, in the straightened CMD [either (B, $B-R_C$) or ($m_{\rm F606W}$, $m_{\rm F606W}-m_{\rm F814W}$), whichever applies].

Our results are qualitatively consistent with those of Sollima et al. (2007), within the common region of radial coverage. We confirm the flat radial distribution of $N_{\rm bMS}/N_{\rm rMS}$ outside ~8–10 arcmin, and a clear increase of $N_{\rm bMS}/N_{\rm rMS}$ toward the cluster center. For the first time, and as a complement to the Sollima et al. (2007) investigation, our ACS/WFC 3×3 mosaic data set has enabled us to study the distribution of ω Cen MS stars in the

innermost region of the cluster. Inside of ∼1.5 r_c (i.e., inward of ∼2′), the $N_{\rm bMS}/N_{\rm rMS}$ ratio is almost flat and close to unity, with a slight overabundance of bMS stars. At larger distances from the cluster center, the $N_{\rm bMS}/N_{\rm rMS}$ ratio starts decreasing. Between ∼3′ and ∼8′ (the latter corresponding to ∼2 half-mass radii) the ratio rapidly decreases to ∼0.4, and remains constant in the cluster envelope. Better azimuthal and radial coverage of the region where the maximum gradient is observed would be of great value. In the radial interval between 1 and 2 half-mass radii, we can use only the corners of the ACS/WFC 3×3 mosaic, and the FORS1 photometry, which inside of 10′ is seriously affected by crowding and saturated stars. In any case, the star counts and even visual inspection of the histograms in Fig. 7.9 leave no doubt about the overall gradient.

Note that in the two innermost bins there are more bMS than rMS stars, even though the heights of the two peaks would suggest the opposite. The apparent contradiction disappears, however, when we note the much greater width of the bMS Gaussian, which more than makes up for the difference in heights. This seems to be consistent with a greater spread in chemical composition for metal-intermediate than for metal-poor stars, as first seen by Norris et al. (1997). Our approach, using a dual-Gaussian fit, has been optimized to estimate the value of the number ratio of bMS to rMS stars, avoiding as much as possible any contamination by blends, binaries, and MS-a stars.

We must also address the fact that the $N_{\rm bMS}/N_{\rm rMS}$ values found by Sollima et al. (2007) are consistently lower than our values. The difference is largely due to their use, on the red side, of a wide color range (see their Fig. 5) that includes nearly all of the contamination by blends, binaries, and MS-a stars that our method has so studiously avoided. This makes their numbers of rMS stars much too high—easily enough to account for their finding a value of ∼0.16 in the cluster envelope, rather than our ∼0.4, which is certainly much closer to the truth. Note also that we have concentrated exclusively on the *ratio* of numbers of bMS and rMS stars, making no attempt to derive absolute numbers for each component. We felt that absolute numbers would be subject to different incompleteness corrections in our different data sets, whereas the incompleteness in each data set should be the same for each component and should therefore not affect their ratio.

Finally, the robustness of our method is shown by the close agreement of our — proper-motion selected — outer ACS field (magenta open circle in Fig. 7.10), which has almost no crowding problems, with the outer ground-based FORS1 fields (last two red squares in Fig. 7.10), which are certainly affected somewhat by crowding.

7.3.4 Artificial star tests

Even with the technique that we have used to exclude the effects of photometric blends and binaries, which lie above and to the red of any MS, there is a concern that some bMS stars would be shifted into the rMS region (and some rMS stars lost on the red side of the MS), and that these shifts would distort the $N_{\rm bMS}/N_{\rm rMS}$ ratio. As a check against this possibility we have made two tests using artificial stars (AS). In each test we introduced the same AS into both the F435W and the F625W images, as follows.

For each test, we first created 45 000 artificial stars, with random F435W instrumental magnitudes between −11.1 and −9.9 (corresponding to $20.9 < B < 21.1$), and random positions. We then took each of these 45 000 AS, assigned it a color that placed it on the bMS, and inserted it in the F625W images, at the same position but with the F625W magnitude that corresponds to this color. We then repeated this procedure for 45 000 new AS, but this time we gave them colors that put them on the rMS. (What we mean by "on" [bMS or rMS] differs between the two tests; see below for an explanation of the difference.) Each artificial star in turn was added, measured, and then removed, so as not to interfere with the other AS that were to be added after it; this procedure is that of Anderson et al. (2008), where it is explained in detail.

In order to test the effects of crowding, each of the two tests used two fields from the central 3×3 mosaic: the central field where crowding effects are maximal, and one of the corner fields, about 5 arcmin ($3.6r_{\rm c}$) southeast of the center (see Fig. 7.1 for a map of the 3×3 mosaic of fields).

The first of the tests (TEST1) was aimed at checking the photometric errors in the colors. To do this, we chose the color of each AS so as to put it exactly on the ridge line of the bMS or rMS; the color spread of the recovered

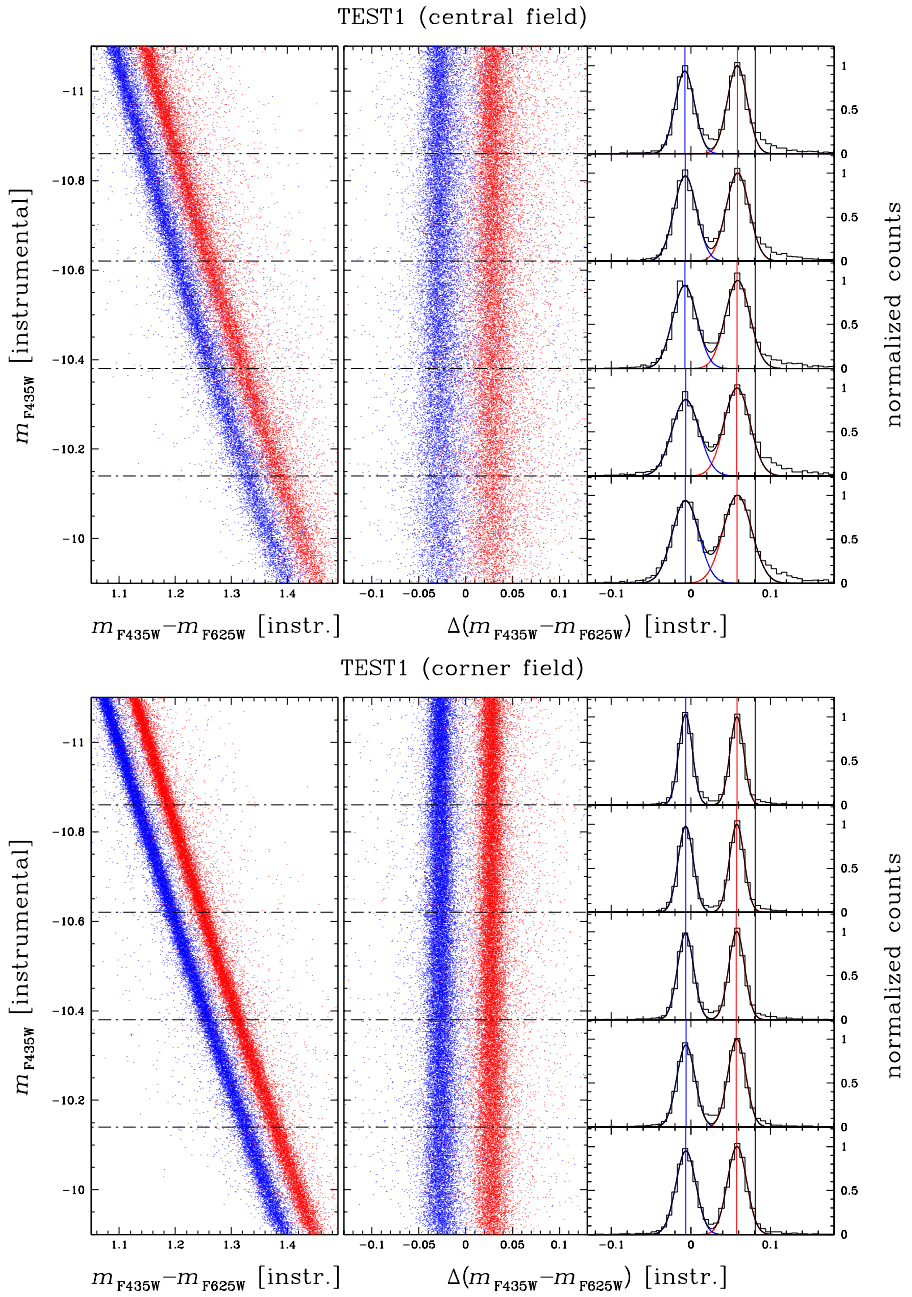

FIGURE 7.11— TEST1 artificial star analysis for the central ACS/WFC 3×3 mosaic field (top panels), and for the corner field (bottom panels). For each panel, we show the CMD with the recovered stars (in blue for the bMS stars and in red for the rMS stars), for five magnitude intervals. The straightened MSs are plotted in the middle, while on the right we show the color histograms, with the dual-Gaussian fits. The vertical lines in blue, red, and black mark, respectively, the centers of the two Gaussians and the red cut-off. See the text for details.

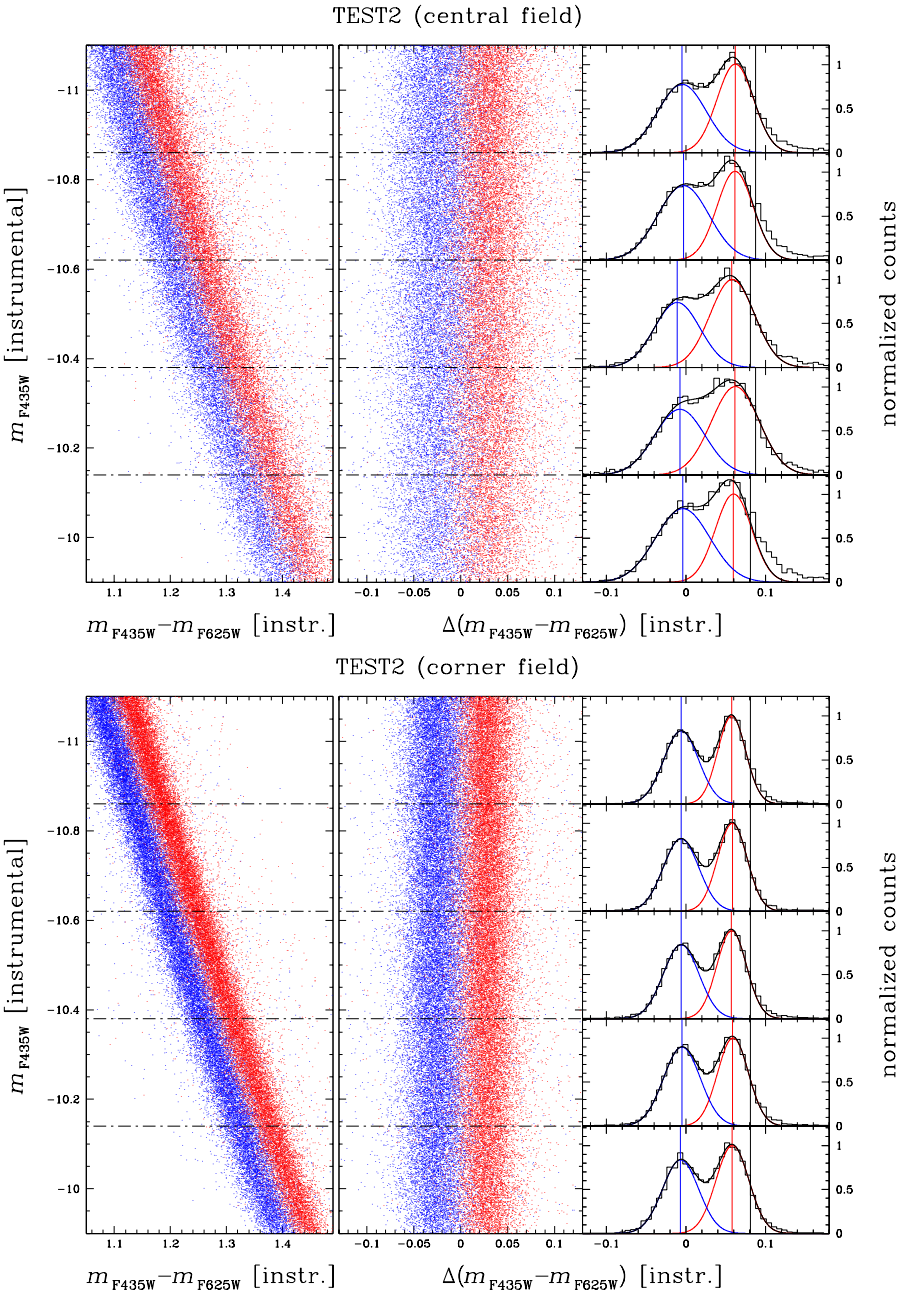

FIGURE 7.12— Same as Fig. 7.11, but now for TEST2. See text for details.

TABLE 7.3— Results of the two artificial-star tests. For each of the two fields (first column), we give in Cols. 2–4 the values of $N_{\rm bMS}/N_{\rm rMS}$ for the AS that were inserted, and the color dispersions that were given to the AS that were put on the bMS and rMS, respectively. In Cols. 5–8 are, respectively, the $N_{\rm bMS}/N_{\rm rMS}$ of the AS that were recovered, with error, followed by the sigmas of the two Gaussians that were fitted to them. See the text for details.

Field	$(N_{\rm bMS}/N_{\rm rMS})_{\rm ins.}$	$(\sigma_{\rm bMS})_{\rm ins.}$	$(\sigma_{\rm rMS})_{\rm ins.}$	$(N_{\rm bMS}/N_{\rm rMS})_{\rm rec.}$	$\sigma(N_{\rm bMS}/N_{\rm rMS})_{\rm rec.}$	$(\sigma_{\rm bMS})_{\rm rec.}$	$(\sigma_{\rm rMS})_{\rm rec.}$
			TEST1				
central	1.000	0.000	0.000	0.946	0.013	0.013	0.013
corner	1.000	0.000	0.000	0.992	0.013	0.009	0.009
			TEST2				
central	1.000	0.021	0.016	1.008	0.079	0.026	0.021
corner	1.000	0.016	0.013	0.996	0.027	0.019	0.016

AS would then serve as a lower-limit estimate of our photometric error.

The aim of TEST2 is to verify our ability to insert AS with $N_{\rm bMS}/N_{\rm rMS}$=1 and then recover that value, when the two MSs have intrinsic dispersions in color. To do this, we first derived the intrinsic spreads of the two sequences by taking from the fifth and seventh columns of Table 7.2 the simple unweighted mean of the entries in lines 1 and 2 for the central field, and in lines 4 and 5 for the corner one. (The more fastidious procedure, weighting the entry in each of the two lines according to the number of stars contributed by that annulus, would have been quite laborious and would have made no significant change in the results.) These are the observed total color spreads (intrinsic spread plus measuring error) of the bMS and rMS, respectively, in the two fields that we are using here. From these total spreads we quadratically subtracted the corresponding measuring-error spreads that we had found in TEST1, so as to get estimates of the intrinsic color spreads of the two sequences. We created AS in the same manner as in TEST1, but this time instead of placing the AS on the center lines of bMS and rMS, we adjusted the F625W magnitudes so as to give the AS a Gaussian spread in color around each sequence, using the intrinsic sigmas that we had just found. After the measuring process, these AS should duplicate the observed total spreads, and can be used to estimate the amount of contamination between the two main sequences. To repeat, each test was performed both on both the central and the corner field.

The results of these AS tests are summarized in brief numerical form in Table 7.3 and in graphical form in Figures 7.11 and 7.12. In each figure the left and right halves refer to the central and corner fields, respectively, while each half figure is divided into three panels that show, from left to right, the CMD, the straightened CMD, and the decomposition of the number densities of the latter into best-fitting Gaussians. Each panel showing the Gaussian fits is subdivided into five magnitude intervals, (very similarly to what is done in Fig. 8). Cols. 2–4 of Table 7.3 give, for each field and AS test, the $N_{\rm bMS}/N_{\rm rMS}$ ratio of the inserted AS and the dispersions of the MSs. The recovered values (weighted mean of the five magnitude bins and its error, as explained in detail for real stars in Sect. 3.3) are shown in Cols. 5–8.

From the results of TEST1 we conclude that in each field the color spread introduced by measuring error is the same for bMS stars as for the rMS, and that it is about 40% higher in the central field than in the less-crowded corner field. TEST1 has served two purposes: (1) It gave us a clear, effective measure of the effect of crowding on the color spread. (2) It evaluated the color spreads due to measuring error alone, which we used in setting up TEST2. (Its results for $N_{\rm bMS}/N_{\rm rMS}$ are given, pro forma, but they have no real significance, since the color

spreads used in TEST1 are so narrow that our color bin-width does not sample them adequately.) It is TEST2 which directly tests our previous conclusions about the size of $N_{\rm bMS}/N_{\rm rMS}$. We conclude from it that the AS tests recover our input values of $N_{\rm bMS}/N_{\rm rMS}$, within the uncertainties of the measurement.

In this section we have demonstrated, on two extreme fields of the ACS inner mosaic, that our dual-Gaussian fitting method is fully effective in overcoming the effects of crowding on the distribution of colors, and that it reliably estimates the relative star numbers in the two sequences. (Note that we use this same method for all of our other data sets too). As we noted at the end of Sect. 3.3, the excellent agreement between the results from our completely uncrowded outer ACS field and those from our outer FORS1 fields establishes the validity of the latter, without recourse to any additional AS texts for them.

7.4 Radial gradients in the RGB subpopulations

It has been known since the end of the 60s that the RGB of ω Cen is broader than would be expected from photometric errors (Woolley & Dickens 1967), but it was only in 1999 that Lee et al. (1999) clearly detected at least two distinct RGBs. Later on, Pancino et al. (2000) demonstrated that there is a correlation between the photometric peaks across the RGB and three peaks in the metallicity distribution. On this basis, they defined the three RGB groups: RGB-MP, RGB-MInt, and RGB-a, characterized by an increasing metallicity. In this section we will present a detailed study of the radial distributions of these components.

7.4.1 Defining the RGB-MP, RGB-MInt, and RGB-a subsamples

Unfortunately the WFPC2, FORS1, and outer ACS/WFC data sets we used to analyze the main-sequence population in the previous section are saturated even at the MS turn-off level, and are therefore unusable for the study of the RGB radial distributions.

Our WFI@2.2*m* photometric and proper-motion catalog (Bellini et al. 2009), however, is an excellent data base for this study, particularly in view of the fact that we can safely remove field objects in the foreground and background, thanks to our accurate proper motions. This proper-motion cleaning is of fundamental importance in the outer envelope of the cluster, where there can be more field stars than cluster giants. In the central regions of the cluster, the WFI@2.2*m* data are less accurate due to the poorer photometry caused by the crowded conditions, so there we take advantage of our high-resolution inner ACS/WFC 3×3 mosaic, which included short exposures to measure the bright stars. Below we describe how we extracted the ω Cen RGB subsamples from these two data sets.

Because of the complex distribution of the stars along the RGB we were forced to use bounding boxes to select the different RGBs. This selection procedure is less accurate than what we were able to do for the bMS and the rMS; nevertheless it is still accurate enough to study the general trend of the radial distribution of the relative numbers of RGB-MP, RGB-Mint, and RGB-a stars. The Poisson error from the smaller number of RGB stars makes the more precise procedure less critical.

For the ACS data, we defined bounding boxes for the RGB subpopulations of ω Cen in the CMD obtained from the data set of the ACS/WFC 3×3 mosaic, for which the large-number statistics make the separation among the different RGBs easier to see. We extracted three RGB subpopulations, in a way very similar to that used by Ferraro et al. (2002). [Note that other authors (e.g. Rey et al. 2004; Sollima et al. 2005a, Johnson et al. 2009) have defined four or even five RGB subpopulations]. The left panel of Fig. 7.13 shows the three RGB bounding-box regions drawn in the CMD from the ACS/WFC 3×3 mosaic, to identify the three subgroups RGB-MP, RGB-MInt, and RGB-a. Our RGB selections are limited to magnitudes brighter than $B = 17.9$, and contain 5184 RGB-MP stars, 4379 RGB-MInt stars, and 383 RGB-a stars.

In extracting the RGB subpopulations from our WFI@2.2*m* data set we chose to define the subpopulations in the $B, B-V$ CMD. Even though we cannot adopt exactly the same selection boxes in the $B, B-R_C$ CMD as for the ACS/WFC 3×3 mosaic. This choice might appear awkward, not only because the color baseline $B-V$ is shorter than the $B-R_C$ baseline, but also because the WFI R_C filter is very similar to the ACS/WFC $F625W$ filter. There

are other good reasons for adopting the $B-V$ color baseline, however. The most important one is that the WFI photometry obtained with the V filter has ten times as much integration time, and more dithered images than those available for the R_C filter. Therefore our V photometry is considerably more precise, and more accurate, than our R_C magnitudes. Moreover, our empirical sky-concentration correction (very important for such studies) is better defined in V than in R_C (see Bellini et al. 2009).

In this WFI@2.2*m* B vs. $B-V$ CMD, we tried to define the bounding boxes in a way that was as consistent as possible with what we did for the data set from ACS/WFC 3×3 mosaic. We cross-identified the stars that are in common between the sample that we had selected from the RGB CMD of the ACS/WFC 3×3 mosaic, on the one hand, and the WFI@2.2*m* $B-V$ data set on the other hand, and we carefully drew by hand, in the (B, $B-V$) CMD, bounding boxes that would include the same stars as in the sample from the ACS/WFC 3×3 mosaic.

In addition, we selected from the WFI@2.2*m* data set the stars that were measured best (both photometrically and astrometrically), and were most likely to be members of ω Cen. To make the selection we used the error quantities in columns 7, 9, 13, and 15 of Table 6 of Bellini et al. (2009). These are the errors of the two components of proper motion and of the B and V magnitudes. Our selection consisted of choosing, at the bright end of the RGB, stars whose proper-motion error has a magnitude less than 1.8 mas yr^{-1}, and whose photometric error is less than 0.02 mag in each band,; we also required that the proper motion of a star differs from the mean motion of cluster stars by no more than 2.1 mas yr^{-1}. At the faint end of the RGB we allowed these three tolerances to rise to: 2.1 mas yr^{-1}, 0.03 mag and 3.8 mas yr^{-1}, respectively. This high-quality data set comprised 4993 RGB-MP stars, 3057 RGB-MInt, and 292 RGB-a stars.

The right-hand panel of Fig. 7.13 shows the WFI@2.2*m* RGB subpopulations that were selected in this way. We note that whereas the RGB-a sample is well separated from the other two RGB components, the RGB-MP and RGB-MInt components are separated only by an arbitrary dividing line, so that small differences in defining the bounding boxes might result in some cross-contamination in those two samples.

7.4.2 Relative radial distributions of RGB stars

We divided our WFI@2.2*m* data set into ten radial bins, each containing approximately the same number of RGB-MInt stars, and the ACS/WFC 3×3 data set into five radial bins, again with the same equal-number criterion. For each of these bins we counted the number of RGB stars in each subpopulation.

In Fig. 7.14 we show the derived radial gradients. As it has not been possible to perform the same error analysis as was done for the MS stars (because of the much smaller number of stars), the error bars in Fig. 7.14 represent only Poisson errors, and should be considered a lower limit to the real errors. In panel (a) we show the radial distribution of the ratio RGB-a/RGB-MInt. Blue full circles refer to the ACS/WFC 3×3 data set, and red triangles to the WFI@2.2*m* data. Vertical dashed lines mark the core radius r_c and the half-mass radius r_h. We found that, within the errors, the RGB-a and the RGB-MInt stars share the same radial distribution, since their ratio is constant over the entire radial range covered by our two data sets. In panel (b), we plot the ratio RGB-MInt/RGB-MP for the two data sets. The RGB-MInt stars are more centrally concentrated than the RGB-MP stars, with a flatter trend within $\sim 1\ r_h$, a rapid decline out to $\sim 8'-10'$, and again a flat relative distribution outside. There is a hint, also, that the RGB-MInt/RGB-MP ratio could be nearly constant within the half-mass radius. We find that the general radial trend of the RGB-MInt/RGB-MP star-count ratio is consistent with that of $N_{\rm bMS}/N_{\rm rMS}$. This result provides additional evidence (in agreement with the metallicity measurements by Piotto et al. 2005) that the bMS and the RGB-MInt population must be part of the same group of stars, with the same metal content and the same radial distribution within the cluster. Panel (c) shows that the ratio RGB-a/RGB-MP resembles, within the errors, the RGB-MInt/RGB-MP trend. We were unable to examine this trend for the MS part of the RGB-a population, since the MS-a sequence cannot be followed below B $\sim$20.

Our analysis confirms the results by Norris et al. (1997), Hilker & Richtler (2000); Pancino et al. (2000), and Rey et al. (2004), and Johnson et al. (2009), who found that the most metal-poor RGB stars are less concentrated than the RGB-MInt ones. Moreover, we can also confirm that the RGB-a and the RGB-MInt share the same radial

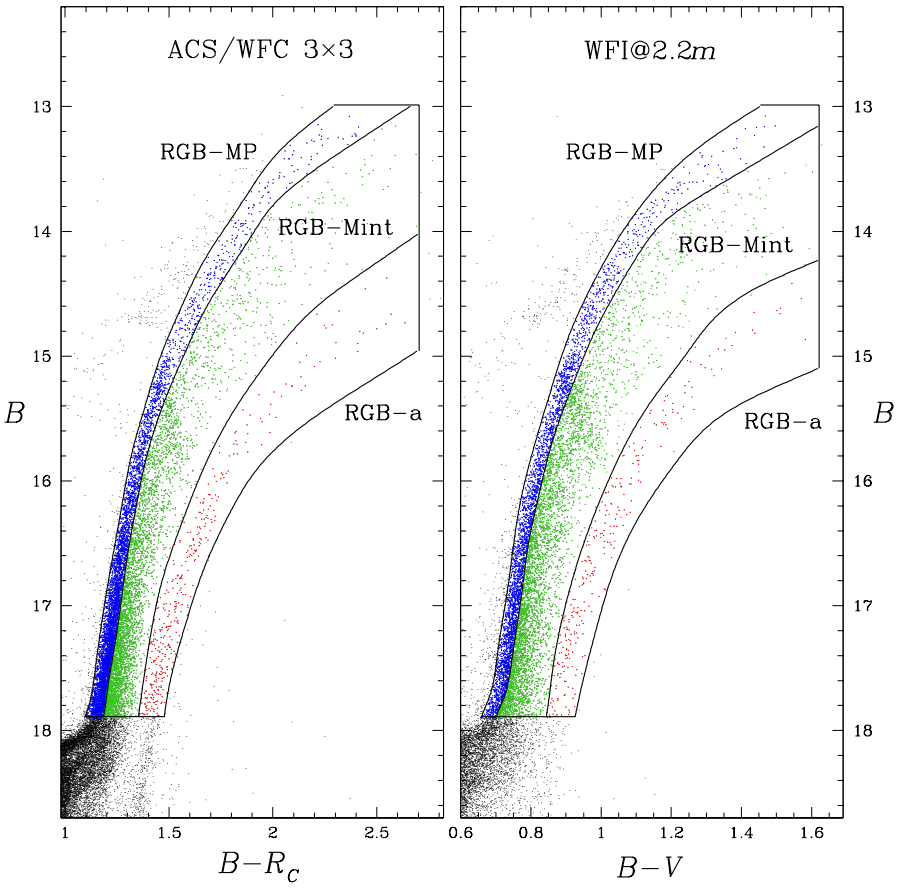

FIGURE 7.13— CMDs of the ω Cen RGB from ACS/WFC 3×3 mosaic (B vs. $B - R_C$, *left panel*) and from WFI@2.2*m* data (B vs. $B - V$, *right panel*). The RGB subpopulations selected are also plotted with different colors. See the text for details.

distribution within ω Cen, as found by Norris et al. (1997), Pancino et al. (2000), and Pancino et al. (2003) for RGB-a only.

It is important to note that because we were able to use proper motions to construct a pure cluster sample, our results are not affected by field-star contamination, which would tend to enhance the RGB-a star counts in the cluster outskirts with respect to the more populous RGB-MP sample (which also covers a smaller region in the CMD). Field-star contamination is likely the reason that Hilker & Richtler (2000) and Castellani et al. (2007) found the RGB-a/RGB-MP ratio to *increase* with distance from the cluster center — the opposite trend from what is seen here. Moreover, it is interesting to note that the different RGB-Mint subgroups (as highlighted, e.g., by Sollima et al. 2005a) might well have a different radial behavior, but necessarily—since we cannot distinguish them in the CMD—we have to treat them together and study only their average gradient.

7.5 Discussion

In this investigation we have analyzed the radial distribution of the different MS and RGB components in the globular cluster ω Centauri. We used high-resolution ACS/WFC images to study the inner regions of the cluster, and ACS/WFC, WFPC2 and FORS1@VLT images, as well as WFI@2.2*m* images, for the cluster envelope. We

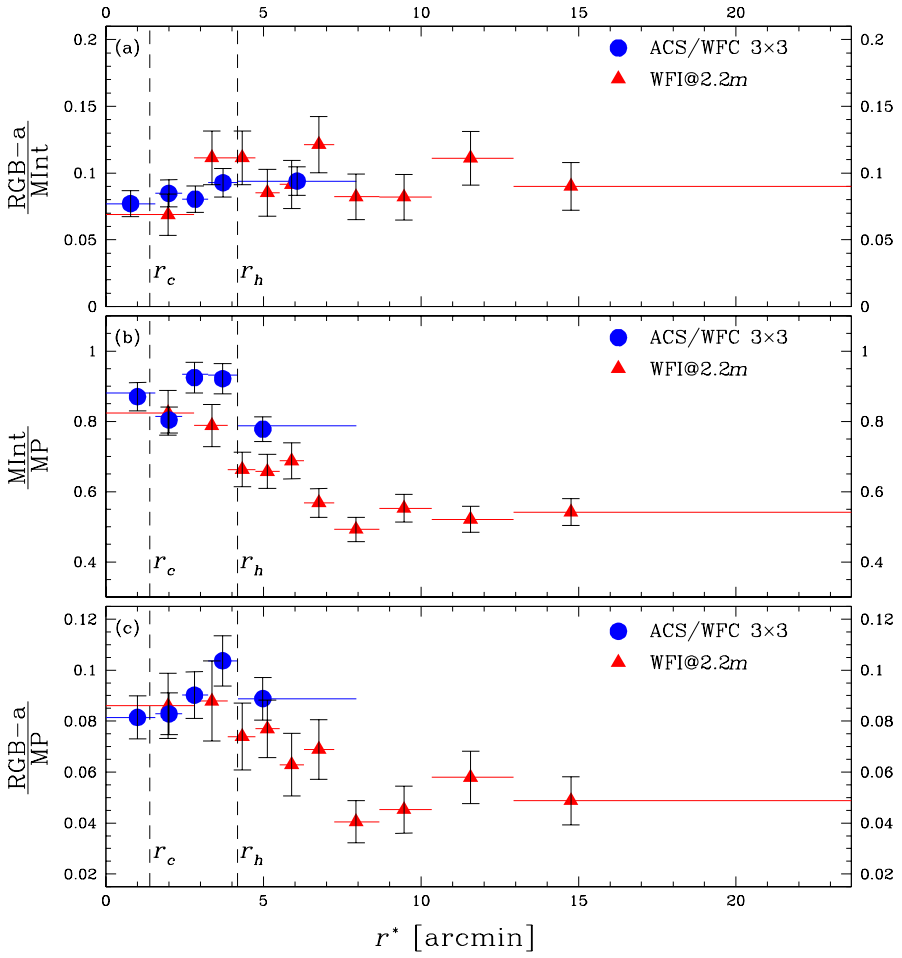

FIGURE 7.14— *(a)*: Radial distribution of the ratio RGB-a/RGB-MInt for the WFI@2.2*m* data set (red triangles) and for the ACS/WFC 3×3 data set (blue circles). Vertical dashed lines mark the core radius and the half-mass radius, respectively. *(b)*: Radial distribution of the ratio RGB-MInt/RGB-MP. *(c)*: Radial distribution of the ratio RGB-a/RGB-MP. See the text for details.

found that there are slightly more bMS stars than rMS stars in the inner 2 core radii. At larger distances from the cluster center, out to ~8 arcmin, the relative number of $N_{\rm bMS}/N_{\rm rMS}$ stars drops sharply, and then remains constant at $N_{\rm bMS}/N_{\rm rMS}$~0.4, out to half the tidal radius of the cluster.

Our most precise photometry comes from the outer ACS field at 17′ (12 r_c), where we find that the color dispersion (σ) of the bMS is about 50% larger than that of the rMS. The other observations are consistent with this, though they are unable to measure σ so precisely, on account of crowding (in the inner ACS field) and other errors (in the ground-based fields).

The RGB-MInt population (associated with the bMS by Piotto et al. 2005) and the RGB-MP sample (which includes the progeny of the rMS) follow a trend similar to that of $N_{\rm bMS}/N_{\rm rMS}$. The most metal-rich component of the RGB, RGB-a, also follows the same distribution as the RGB-MInt component.

On the hypothesis that the bMS, the presumably helium-rich population, is a second generation of stars formed

by the low-velocity material ejected by a primordial population (which we assume to be the more metal-poor rMS population), the bMS must have formed from matter that collected in the cluster center via some kind of cooling flow. This is in qualitative agreement with the recent models by Bekki & Norris (2006) and D'Ercole et al. (2008). The very long relaxation time (half-mass relaxation time longer than 10 Gyr, according to the Harris 1996 compilation) has preserved some information about the original kinematic and spatial distribution of the material from which the younger component took form. Interestingly enough, the third, most-metal-rich population is also more concentrated than the most metal-poor component, and has a radial distribution that is rather similar to that of the intermediate-metallicity sample. It is also noteworthy that the bMS component has a broader color distribution than the rMS one. This fact may reflect, at least in part, the large dispersion in iron abundance of the intermediate-metallicity component (e.g. Norris & Da Costa 1995). Alternatively, this bMS spread could be an indication of the dispersion of other chemical elements, including He. Only a detailed analysis of the metal content of the two MSs can solve this issue, but for this we might need to wait for the next generation of 30+ meter telescopes, on account of the faintness of these stars.

7.6 Bibliography

Anderson, J., Ph.D. thesis, Univ. of California, Berkeley, 1997
Anderson, J., & King, I. R. 2000, PASP, 112, 1360
Anderson, J. 2002, in Omega Centauri, A Unique Window into Astrophysics, ed. F. van Leeuwen, J. D. Hughes, & G. Piotto, ASP Conf. Ser., 265 (San Francisco: ASP), p. 87
Anderson, J., Bedin, L. R., Piotto, G., Yadav, R. S., & Bellini, A. 2006, A&A, 454, 1029
Anderson, J., & King, I. R. 2006, ACS/ISR 2006-01 (Baltimore: STSci)
Anderson, J., et al. 2008, AJ, 135, 2055
Anderson, J., Piotto, G., King, I. R., Bedin, L. R., & Guhathakurta, P. 2009, ApJL, 697, L58
Anderson, J., & van der Marel, R. P. 2010, ApJ, 710, 1032
Bedin, L. R., Piotto, G., Anderson, J., Cassisi, S., King, I. R., Momany, Y., & Carraro, G. 2004, ApJL, 605, L125
Bedin, L. R., Cassisi, S., Castelli, F., Piotto, G., Anderson, J., Salaris, M., Momany, Y., & Pietrinferni, A. 2005, MNRAS, 357, 1038
Bellazzini, M., et al. 2008, AJ, 136, 1147
Bellini, A., et al. 2009, A&A, 493, 959
Bellini, A., Piotto, G., Bedin, L. R., King, I. R., Anderson, J., Milone, A. P., & Momany, Y. 2009, A&A, 507, 1393 (2009b)
Bekki, K., & Norris, J. E. 2006, ApJL, 637, L109
Bekki, K., & Mackey, A. D. 2009, MNRAS, 394, 124
Bessell, M. S., & Norris, J. 1976, ApJ, 208, 369
Butler, D., Dickens, R. J., & Epps, E. 1978, ApJ, 225, 148
Calamida, A., et al. 2005, ApJL, 634, L69
Cannon, R. D., & Stobie, R. S. 1973, MNRAS, 162, 207
Carretta, E., Bragaglia, A., Gratton, R. G., Leone, F., Recio-Blanco, A., & Lucatello, S. 2006, A&A, 450, 523
Carretta, E., Bragaglia, A., Gratton, R. G., Lucatello, S. 2008, arXiv:0811.3591v1
Castellani, V., et al. 2007, ApJ, 663, 1021
D'Antona, F., & Caloi, V. 2004, ApJ, 611, 871
D'Antona, F., Bellazzini, M., Caloi, V., Fusi Pecci, F., Galleti, S., & Rood, R. T. 2005, ApJ, 631, 868
D'Ercole, A., Vesperini, E., D'Antona, F., McMillan, S. L. W., & Recchi, S. 2008, MNRAS, 391, 825
Decressin, T., Baumgardt, H., & Kroupa, P. 2008, A&A, 492, 101
Dinescu, D. I., Girard, T. M., & van Altena, W. F. 1999, AJ, 117, 1792
Faria, D., Johnson, R. A., Ferguson, A. M. N., Irwin, M. J., Ibata, R. A., Johnston, K. V., Lewis, G. F., & Tanvir, N. R. 2007, AJ, 133, 1275

Ferraro, F. R., Bellazzini, M., & Pancino, E. 2002, ApJL, 573, L95
Ferraro, F. R., Sollima, A., Pancino, E., Bellazzini, M., Straniero, O., Origlia, L., & Cool, A. M. 2004, ApJL, 603, L81
Freeman, K. C., & Rodgers, A. W. 1975, ApJL, 201, L71
Freeman, K. C. 1993, in The Globular Cluster–Galaxy Connection, ed. G. H. Smith & J. P. Brodie ASP Conf. Ser., 48 (San Francisco: ASP), p, 608
Freyhammer, L. M., et al. 2005, ApJ, 623, 860
Geyer, E. H., Nelles, B., & Hopp, U. 1983, A&A, 125, 359
Gilliland, R. 2004, ACS/ISR 2004-01 (Baltimore: STScI)
Harris, W. E. 1996, AJ, 112, 1487, as updated in February, 2003
Hilker, M., & Richtler, T. 2000, A&A, 362, 895
Hilker, M., Kayser, A., Richtler, T., & Willemsen, P. 2004, A&A, 422, L9
Holtzman, J. A., Burrows, C. J., Casertano, S., Hester, J. J., Trauger, J. T., Watson, A. M., & Worthey, G. 1995, PASP, 107, 1065
Ideta, M., & Makino, J. 2004, ApJL, 616, L107
Johnson, C. I., Pilachowski, C. A., Rich, R. M., & Fulbright, C. P. 2009, ApJ, 698, 2048
Lee, Y.-W., Joo, J.-M., Sohn, Y.-J., Rey, S.-C., Lee, H.-C., & Walker, A. R. 1999, Nature, 402, 55
Makino, J., Akiyama, K., & Sugimoto, D. 1991, Ap&SS, 185, 63
Manfroid, J., & Selman, F. 2001, The Messenger, 104, 16
Marino, A. F., Villanova, S., Piotto, G., Milone, A. P., Momany, Y., Bedin, L. R., & Medling, A. M. 2008, A&A, 490, 625
Marino, A. F., Milone, A. P., Piotto, G., Villanova, S., Bedin, L. R., Bellini, A., & Renzini, A. 2009, A&A, 505, 1099
Milone, A. P., et al. 2008, ApJ, 673, 241
Milone, A. P., Bedin, L. R., Piotto, G., & Anderson, J. 2009, A&A, 497, 755
Moretti, A., et al. 2009, A&A, 493, 539
Norris, J., & Bessell, M. S. 1975, ApJL, 201, L75
Norris, J., & Bessell, M. S. 1977, ApJL, 211, L91
Norris, J. E., & Da Costa, G. S. 1995, ApJL, 441, L81
Norris, J. E., Freeman, K. C., & Mighell, K. J. 1996, ApJ, 462, 241
Norris, J. E., Freeman, K. C., Mayor, M., & Seitzer, P. 1997, ApJL, 487, L187
Norris, J. E. 2004, ApJL, 612, L25
Pancino, E., Ferraro, F. R., Bellazzini, M., Piotto, G., & Zoccali, M. 2000, ApJL, 534, L83
Pancino, E., Seleznev, A., Ferraro, F. R., Bellazzini, M., & Piotto, G. 2003, MNRAS, 345, 683
Pancino, E., Galfo, A., Ferraro, F. R., & Bellazzini, M. 2007, ApJL, 661, L155
Piotto, G., et al. 2005, ApJ, 621, 777
Piotto, G., et al. 2007, ApJL, 661, L53
Piotto, G. 2009, in The Ages of Stars, ed. E. E. Mamajek, D. R. Soderblom, & R. F. G. Wyse, IAU Symposium No. 258 (Cambridge: Cambridge University Press), p. 233
Platais, I., Wyse, R. F. G., Hebb, L., Lee, Y.-W., & Rey, S.-C. 2003, ApJ, 591, L127
Renzini, A., & Fusi Pecci, F. 1988, ARA&A, 26, 199
Renzini, A. 2008, MNRAS, 391, 354
Rey, S.-C., Lee, Y.-W., Ree, C. H., Joo, J.-M., Sohn, Y.-J., & Walker, A. R. 2004, AJ, 127, 958
Rich, R. M., Reitzel, D. B., Guhathakurta, P., Gebhardt, K., & Ho, L. C. 2004, AJ, 127, 2139
Sarajedini, A., & Layden, A. C. 1995, AJ, 109, 1086
Sarajedini, A., et al. 2007, AJ, 133, 1658
Searle, L. 1977, in Evolution of Galaxies and Stellar Populations, ed. B. M. Tinsley, & R. B. Larson (New Haven: Yale Univ. Obs.), p. 219

Siegel, M. H., et al. 2007, ApJL, 667, L57
Sirianni, M., et al. 2005, PASP, 117, 1049
Stetson, P. B. 1987, PASP, 99, 191
Stetson, P. B. 1994, PASP, 106, 250
Stetson, P. B. 2000, PASP, 112, 925
Stetson, P. B. 2005, PASP, 117, 563
Sollima, A., Ferraro, F. R., Pancino, E., & Bellazzini, M. 2005, MNRAS, 357, 265 (2005a)
Sollima, A., Pancino, E., Ferraro, F. R., Bellazzini, M., Straniero, O., & Pasquini, L. 2005, ApJ, 634, 332 (2005b)
Sollima, A., Ferraro, F. R., Bellazzini, M., Origlia, L., Straniero, O., & Pancino, E. 2007, ApJ, 654, 915
Stanford, L. M., Da Costa, G. S., Norris, J. E., & Cannon, R. D. 2006, ApJL, 653, L117
Suntzeff, N. B., & Kraft, R. P. 1996, AJ, 111, 1913
Tsuchiya, T., Korchagin, V. I., & Dinescu, D. I. 2004, MNRAS, 350, 1141
van de Ven, G., van den Bosch, R. C. E., Verolme, E. K., & de Zeeuw, P. T. 2006, A&A, 445, 513
van der Marel, R. P., & Anderson, J. 2010, ApJ, 710, 1063
Villanova, S., et al. 2007, ApJ, 663, 296
Woolley, R. V. d. R., & Dickens, R. J. 1967, Roy. Obs. Bull., No. 128
Zinnecker, H., Keable, C. J., Dunlop, J. S., Cannon, R. D., & Griffiths, W. K. 1988, in The Harlow-Shapley Symposium on Globular Cluster Systems in Galaxies, ed. J. E. Grindlay & A. G. D. Philip, IAU Symposium No. 126 (Cambridge: Cambridge University Press), p. 603

8

New *HST* WFC3/UVIS observations of ω Centauri

We used archival multi-band *Hubble Space Telescope* observations obtained with the *Wide Field Camera 3* in the *UV-optical* channel to present important new observational findings on the color-magnitude diagram (CMD) of the Galactic globular cluster ω Centauri. The UV WFC3 data have been coupled with available WFC/ACS optical band data. The new CMDs, obtained from the combination of colors coming from eight different bands, disclose an even more complex stellar population than previously identified. This Chapter discuss the detailed morphology of the CMDs, and contains results accepted for publication in *The Astronomical Journal* (Bellini et al. 2010).

8.1 Introduction

No doubt, ω Centauri is the most studied and the most enigmatic among the Milky Way satellites. For a long time it has been considered a globular cluster (GC), but a number of peculiarities, such as its mass, its chemical composition, its stellar content and its kinematics, suggest that it might be the remnant of a larger stellar system (Bekki & Freeman 2003, Lee et al. 2009, and references therein).

Since the discovery that its stars span a wide range of metallicities, including iron-peak elements (Cannon & Stobie 1973; Freeman & Rodgers 1975; Johnson et al. 2009 and references therein), great interest and great efforts have been dedicated to this object.

With the advent of wide-field imagers and thanks to the increasingly high photometric precision in the densest cluster regions, new discoveries have revived interest in ω Cen, and surely complicated the already inexplicable enigma represented by its composite stellar population. Lee et al. (1999) and Pancino et al. (2000) announced that its red giant branch (RGB) resolves into several distinct stellar sequences. Anderson (1997) found that, over a range of about two magnitudes, the main sequence (MS) splits into a blue (bMS) and a red sequence (rMS). The result has been confirmed by Bedin et al. (2004), who discovered a third, less populated MS (MS-a) on the red side of the rMS (see also Villanova et al. 2007, hereafter V07). A totally unexpected discovery came from the spectroscopic analysis by Piotto et al. (2005), who revealed that the bMS is more metal-rich than the rMS. Only greatly enhanced helium can explain the color and metallicity difference between the two MSs. Bellini et al. (2009, see also Sollima et al. 2007), found that bMS stars are more centrally concentrated than rMS ones, with a bMS over rMS ratio ranging from $\sim$1.0 ($r \lesssim 2\farcm5$) to $\sim$0.40 ($r \gtrsim 8'$).

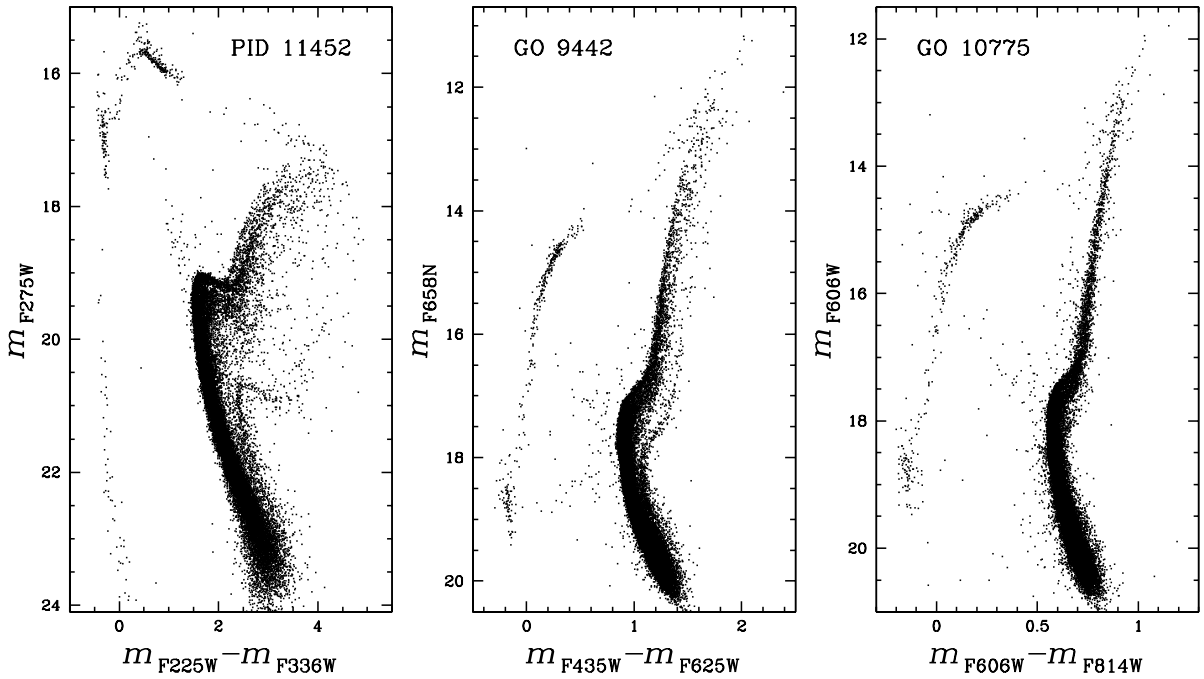

FIGURE 8.1— Collection of CMDs from our three data sets: the WFC3/UVIS CMD in the UV filters $m_{\rm F275W}$ vs. $m_{\rm F225W} - m_{\rm F336W}$, from PID-11452 (*left*); the ACS/WFC $m_{\rm F658N}$ vs. $m_{\rm F435W} - m_{\rm F625W}$ CMD, from GO-9442 (*center*); and the ACS/WFC $m_{\rm F606W}$ vs. $m_{\rm F606W} - m_{\rm F814W}$ CMD, from GO-10775 (*right*). We plotted only the best $\sim$ 32 000 stars in common among the three data sets (see the text for details).

Perhaps, the most complex region of the color-magnitude diagram (CMD) is the sub-giant branch (SGB). Photometric studies showed that the SGB of ω Cen is split into 4 or 5, possibly, distinct stellar populations (Lee et al. 2005, Sollima et al. 2005, V07).

In this work we present high-accuracy photometry obtained with both the *Wide Field Camera 3* (WFC3) in the *UV-optical* channel (UVIS), and the *Wide Field Channel* of the *Advanced Camera for Survey* (WFC/ACS) of the *Hubble Space Telescope* (*HST*). Not surprisingly, we obtained astonishingly complex CMDs unveiling a number of new details which make the ω Cen stellar population appear even more complex than previously shown, and create a real challenge for the the understanding the star formation history in this cluster.

The purpose of this work is just to present these new CMDs to the astronomical community, discuss their detailed morphology – with the hope of adding important information and deeper insight into ω Cen – and help to add up all the pieces of what still remains a broken puzzle. The multi-band astro-photometric catalog presented in this work will be publicly available to the astronomical community, for further analysis.

8.2 Observations, Measurements and Selections

For calibration purposes, ω Cen has been observed many times with *HST*, using a huge variety of filters. Recent observations were collected with the newly installed WFC3. On September 9$^{\rm th}$ 2009, a set of well-dithered exposures through the broad-band ultraviolet filters F225W, F275W, and F336W were released to the community. The data were collected in July 15, 2009, for general calibration purposes (PID-11452). The portion of the data that we used in this work consists of 9 exposures, each of 350 s, for each filter. The archive images were standard pipe-line

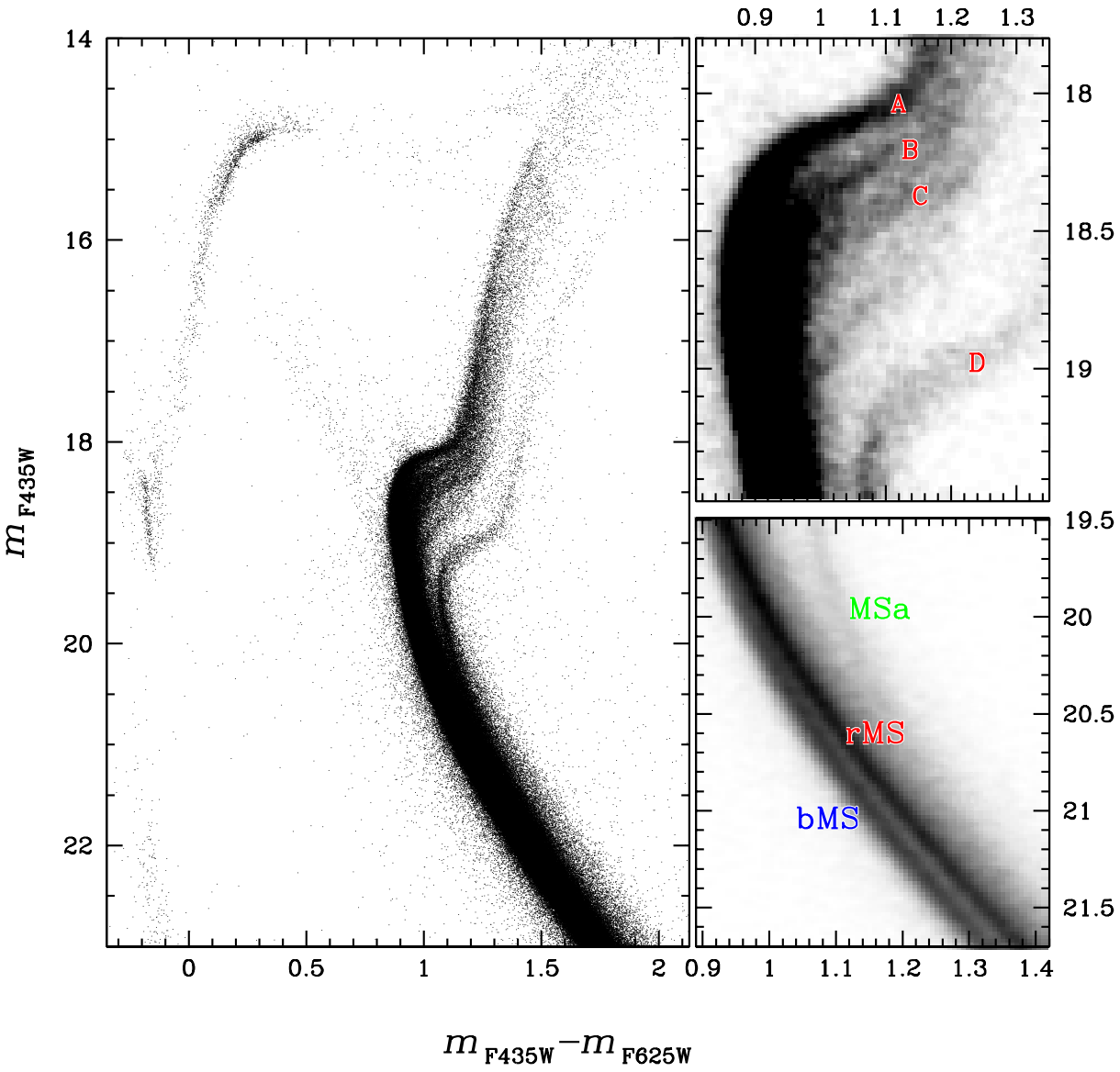

FIGURE 8.2— Definition of the main CMD branches used in this work.

pre-reduced FLT, and we measured star positions and fluxes with software mostly based on img2xym_WFI (Anderson et al. 2006). Star positions and fluxes have been corrected for geometric distortion and pixel area using the geometric distortion solution provided by Bellini & Bedin (2009), and calibrated as in Bedin et al. (2005).

We complement these UV data with the optical photometry obtained with the ACS/WFC in the filters F435W, F625W, F658N, F606W, and F814W. Details on these data sets and their photometry can be found in V07, and Anderson et al. (2008).

Since we are focused on high-accuracy photometry, this work only concerns relatively isolated stars with small photometric and astrometric errors, and high point-spread function (PSF)-fit quality. A detailed description

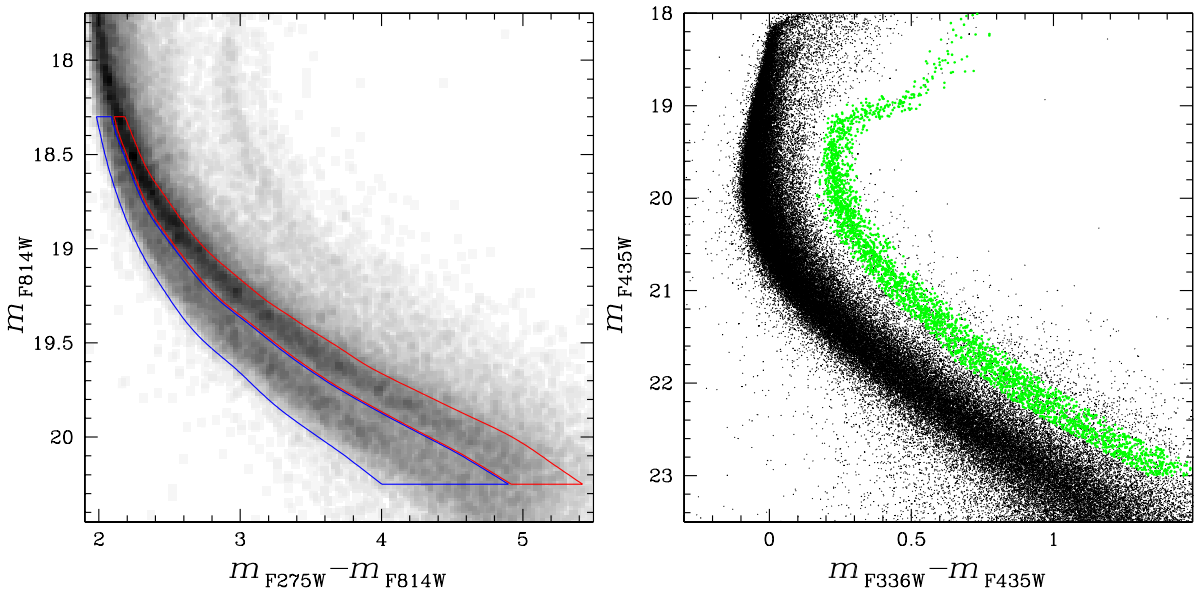

FIGURE 8.3— *(Left)*: Selection of bMS (blue boundary) and rMS (red boundary) stars. *(Right)*: Selection of MS-a (green points) stars.

of the selection procedures adopted here is given in Milone et al. (2009). Finally, we corrected our photometry for both reddening variations in the field of view (FoV) and spatial-dependent photometric errors, introduced by small variations of the PSF shape, which are not accounted for in our PSF models. To achieve this aim, we used a method similar to that used by Sarajedini et al. (2007) and Milone et al. (2008). Briefly, we determined the average MS ridge line (RL) for each CMD, and then analyzed the color residuals as a function of the position within the FoV. We corrected the effect of spatial photometric variations suffered by each star by computing the average color residuals from the MS RL of its 50 well-measured neighbors, and then correcting the star color by this amount.

8.3 Color-Magnitude Diagrams

Figure 8.1 shows a collection of CMDs from multi-band WFC3/UVIS and ACS/WFC photometry. All CMDs encompass all the evolutionary sequences, from faint MS stars, down to a well-developed white dwarf cooling sequence (see Fig. 8.1). A close examination of these CMDs leads to the realization that each of them is a mine of information on the stellar content of ω Cen. A model-based interpretation of these CMDs is severely complicated by the heterogeneity of the composition of each sequence and by possible age differences, and requires a very accurate analysis, which is beyond the purpose of this investigation.

Many of the features that we observe in these CMDs are well known, and widely studied. For completeness of information, and in order to make the following discussion clearer to the reader, we show in Fig. 8.2 (left panel) the CMD resulting from the 10×10 arcmin^2 mosaic of ACS images centered on the cluster center, that was already analyzed in several papers (Bedin et al. 2004, V07, Cassisi et al. 2009, Bellini et al. 2009, and D'Antona, Caloi, & Ventura 2010). The high accuracy of the ACS photometry has already revealed a large number of evolutionary sequences in the CMD. We used Hess diagrams on the right panels of Fig. 8.2 to highlight the four main SGBs and the triple MS, following the notation of V07.

In the following, we will focus our attention on a number of details in the CMD that can be revealed for the first time by the high-accuracy multi-band photometry presented here.

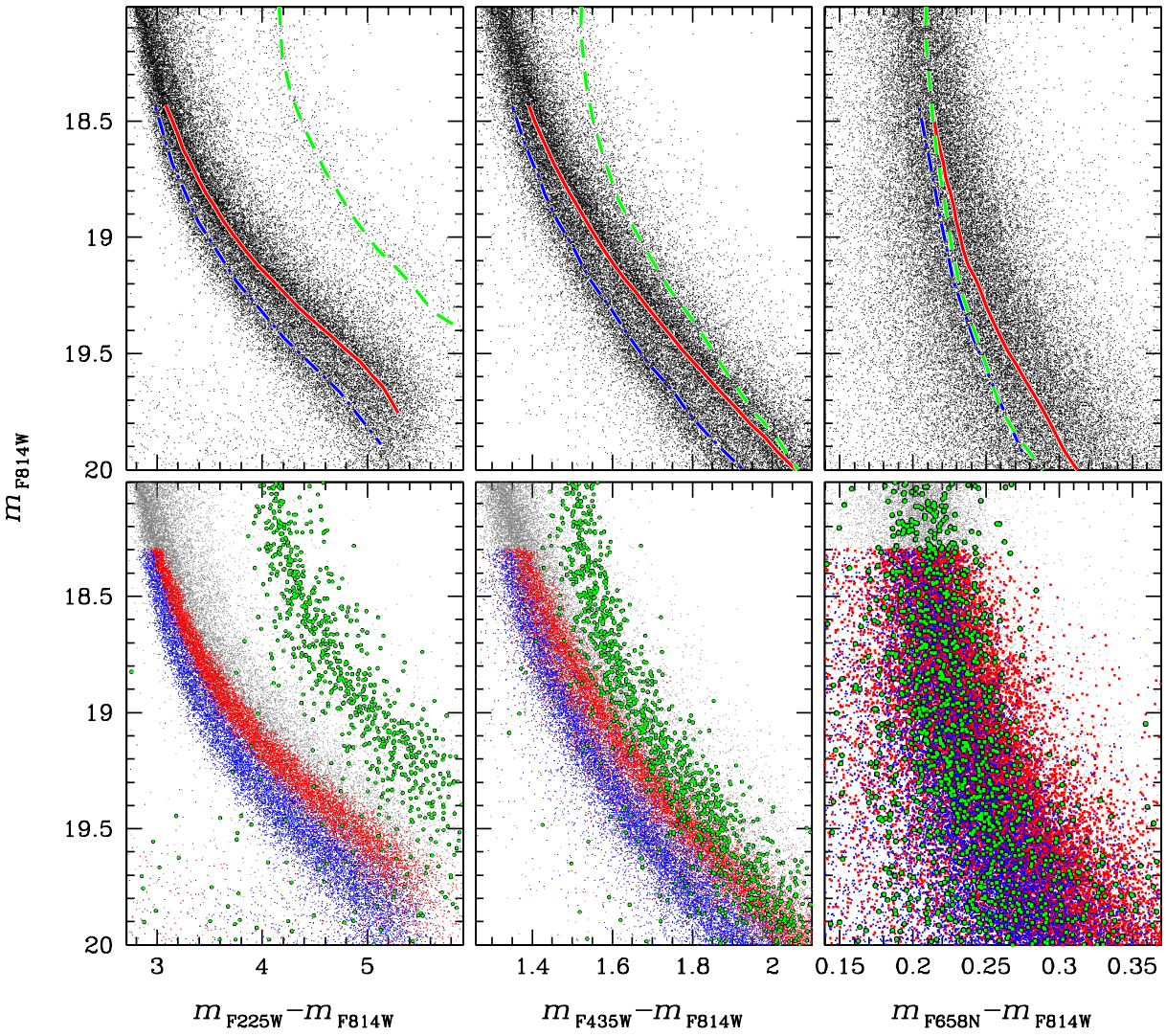

FIGURE 8.4— Example of the definition of the MS RLs.

8.3.1 The triple main sequence

The new, multi-band data set provided by WFC3, combined with the ACS data, opens a new observational window on the complex MS of ω Cen.

The wide color baseline of the m_{F814W} vs. $m_{F275W} - m_{F814W}$ CMD plotted in the left panel of Fig. 8.3 allows us to isolate the two groups of bMS and rMS stars indicated by blue and red color-coded regions. Similarly, we can select a sample of MS-a stars from the m_{F435W} vs. $m_{F336W} - m_{F435W}$ CMD where the MS-a is most clearly separated from the remaining MSs of ω Cen. Selected stars are highlighted in green in the right panel CMD of Fig. 8.3.

We have high-accuracy photometric measurements in eight bands, which allow us to plot seven distinct CMDs involving the F814W band. For each of them, we plotted m_{F814W} magnitudes as a function of the $m_X - m_{F814W}$ color, where $m_X = m_{F225W}$, m_{F275W}, m_{F336W}, m_{F435W}, m_{F606W}, m_{F625W} and m_{F658N}.

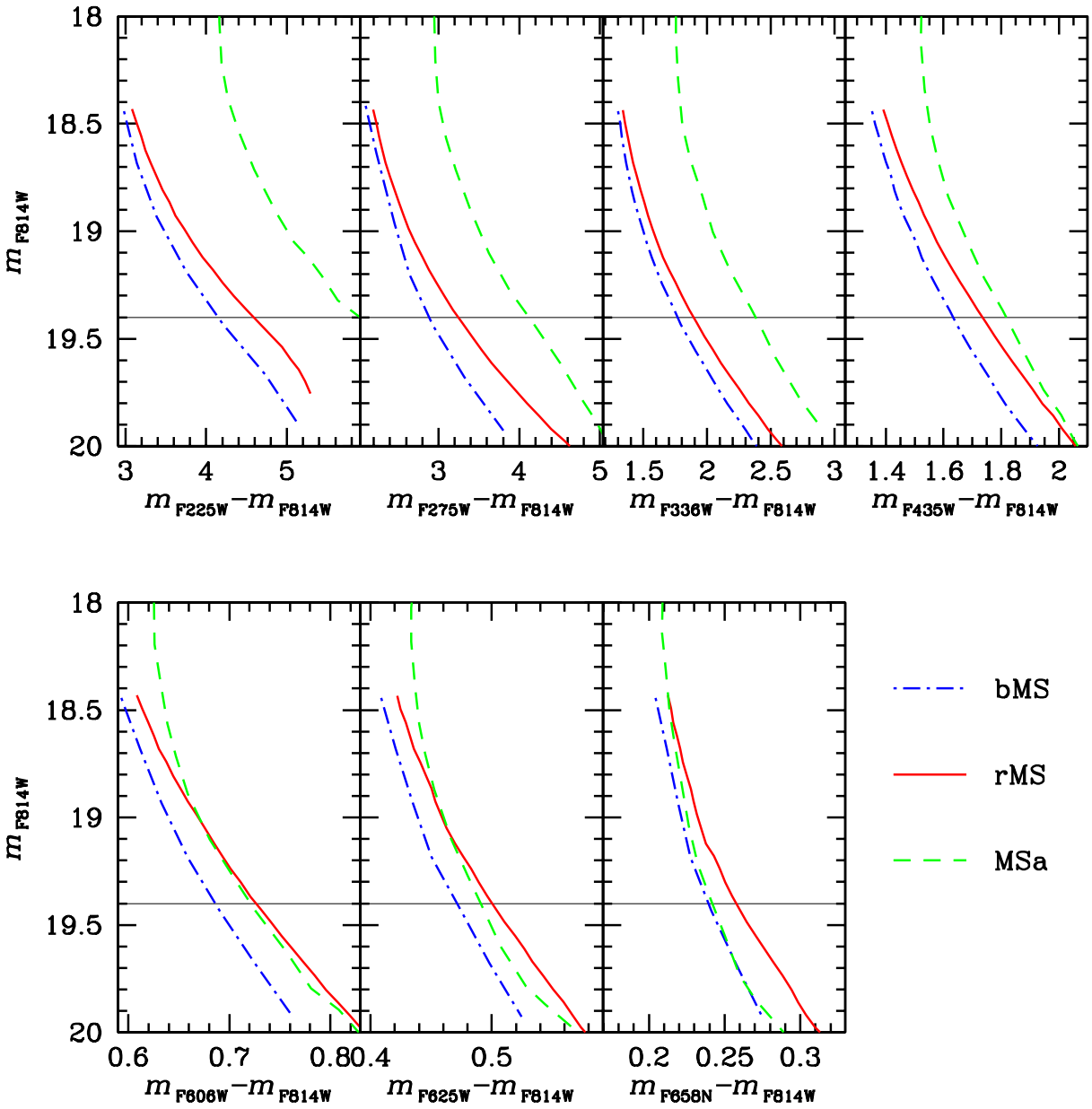

FIGURE 8.5— The bMS and the MS-a run almost parallel in all CMDs. In some CMDs the MS-a seems to cross the rMS.

The bottom panels of Fig. 8.4 show the three most representative of these CMDs (zoomed around the MS region). We assigned to each star a blue, red or green color code according to whether it belongs to the bMS, rMS, or MS-a sample, as defined in Fig. 8.3. In the upper panels of Fig. 8.4 we overimposed on the observed CMDs the MS RLs corresponding to the three MSs, extracted from the CMD using the method described in Milone et al. (2008). Briefly, we divided the CMD in intervals of 0.2 magnitudes in the F814W band and calculated for each of them the median color and magnitude for the bMS, rMS, and MS-a stars. We fitted these median points with

TABLE 8.1— Color distances from the rMS RL for bMS stars ($\Delta^{\rm bMS}_{\rm COLOR}$) and MS-a stars ($\Delta^{\rm MS-a}_{\rm COLOR}$) at $m_{\rm F814W} = 19.4$.

COLOR	$\Delta^{\rm bMS}_{\rm COLOR}$	$\Delta^{\rm MS-a}_{\rm COLOR}$
$m_{\rm F225W} - m_{\rm F814W}$	1.30 ± 0.01	$-0.46 \pm .010$
$m_{\rm F275W} - m_{\rm F814W}$	0.87 ± 0.01	$-0.37 \pm .010$
$m_{\rm F336W} - m_{\rm F814W}$	0.49 ± 0.01	$-0.13 \pm .010$
$m_{\rm F435W} - m_{\rm F814W}$	0.08 ± 0.01	$-0.10 \pm .010$
$m_{\rm F606W} - m_{\rm F814W}$	-0.01 ± 0.01	$-0.04 \pm .010$
$m_{\rm F625W} - m_{\rm F814W}$	-0.01 ± 0.01	$-0.03 \pm .010$
$m_{\rm F658N} - m_{\rm F814W}$	-0.02 ± 0.01	$-0.02 \pm .010$

a spline and obtained a first guess for the MS RL. Then, we calculated the difference between the color of each star and the color of the MS RL corresponding to magnitude of the star, and we took as σ the $68.27^{\rm th}$ percentile of the absolute value of the color difference. We rejected all stars with color differences larger than 4σ, and we recalculated the median points.

The RLs for the three MSs are shown in Fig. 8.5 for the seven CMDs analyzed in this section. We note a few interesting features: (i) the RLs of the bMS and the MS-a are nearly parallel in all the CMDs in the magnitude range $m_{\rm F814W} \sim 18.5 - 20.0$, while the RL of the rMS have a different slope; (ii) when using $m_{F606W} - m_{\rm F814W}$ and $m_{F625W} - m_{\rm F814W}$ colors the RL of the MS-a seems to intercept (or merge with) the rMS going from the brightest to the faintest stars. MS-a stars become even bluer than the rMS ones in the $m_{\rm F658N} - m_{\rm F814W}$ color.

This is the most intriguing CMD, in terms of the He content: He abundance affects the color of MS stars. The F658N filter maps essentially the Hα feature, with a very small influence by other elements. It measures the strength of the Hα which, for MS stars cooler than 8000 K, is a function of the $T_{\rm eff}$, but also of the hydrogen content, if it is allowed to vary. MS-a stars are more metal-rich than rMS stars, being the progenitors of SGB-D and of the RGB-a (Pancino et al. 2002, V07). For this reason, the fact that MS-a stars become even bluer than the rMS in the $m_{\rm F658N} - m_{\rm F814W}$ color, overlapping with the bMS, might imply that also MS-a is enriched in He (as suggested by Norris 2004). In fact, He enhancement tends to move the MS to bluer colors. The shape of the MS-a, parallel to the bMS, might also be an indication that its stars are He enriched. However, we also know that the MS-a has higher iron content than the bMS. Higher metallicity implies redder MS colors. It is a combination of different metal abundances, including CNO, and He content which results in the observed behavior of the MS-a color.

In order to quantify the color differences among the three MSs as a function of the color baseline, in Fig. 8.6 we plotted the central wavelength λ of the $m_{\rm X}$ filter versus the measured color difference Δ(color) of both bMS stars (blue points) and MS-a stars (green points), with respect to the rMS RL color, at $m_{\rm F814W} = 19.4$ (this magnitude level is also indicated with a horizontal line in Fig. 8.5).

The color distances plotted in Fig. 8.6 are listed in Table 8.1.

8.3.2 The intrinsic broadening of the rMS

A visual inspection of the $m_{\rm F275W}$ vs. $m_{\rm F275W} - m_{\rm F336W}$ CMD of Fig. 8.7 suggests that the rMS is broadened. In this section we will investigate the possible presence of this intrinsic color spread among rMS stars, by using the same approach followed in recent studies on the MS broadening of 47 Tuc (Anderson et al. 2009) and of NGC 6752 (Milone et al. 2010).

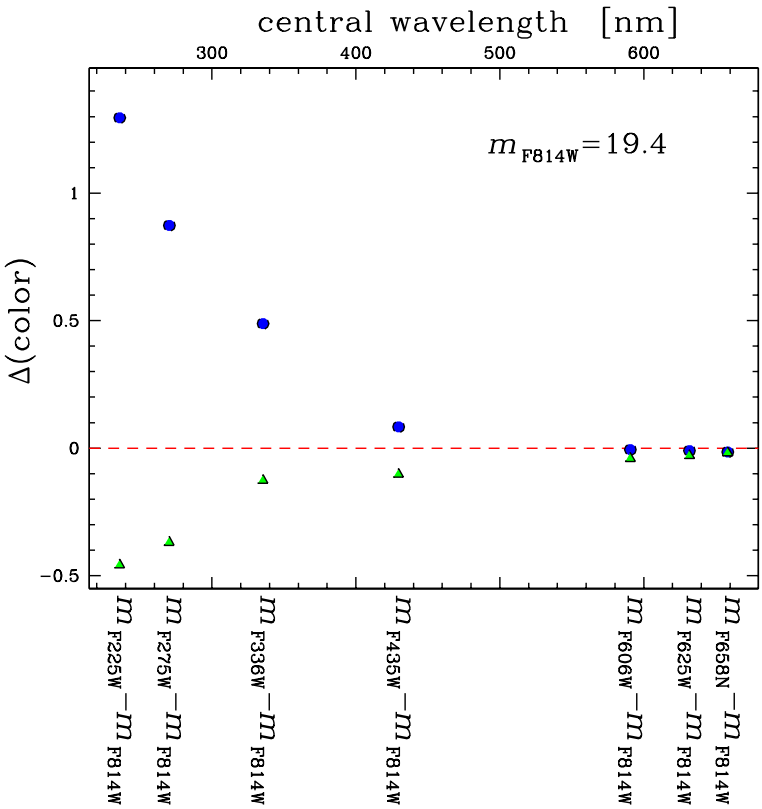

FIGURE 8.6— Color distance from the rMS RL for bMS stars (blue points) and MS-a stars (green triangles) at m_{F814W} = 19.4, plotted as a function of the central wavelength of the m_X filter.

We started by dividing F275W and F336W images in two halves (hereafter, samples 1 and 2), and considered only those stars measured in both sub-samples. From each of the two independent sub sets, we plotted a CMD. As an example we show the CMD from the first data set in panel (a) of Fig. 8.8. The selected bMS and MS-a stars are represented with blue and green colors, while rMS stars are plotted in red (in all the plots, star colors are given according to their classification, as defined in Fig. 5). The dashed line is the RL of the rMS, obtained as described in the previous section. Then we subtracted from the observed color (hereafter C) of each star the RL color at the same magnitude, obtaining the quantity ΔC. The straightened MSs for the first and second data sets are plotted in panels (b) and (c), respectively. In panel (d) we show the color distribution of the straightened MS from the whole data set [indicated as $(\Delta C_1 + \Delta C_2)/2$]. In this case, the errors are smaller by a factor of $\sqrt{2}$ with respect to those of the two data halves.

Panel (e) shows the distribution of the difference between the colors in each half of the images [i.e., $(\Delta C_1 - \Delta C_2)/2$] which is indicative of the color error. The histogram distribution of $(\Delta C_1 + \Delta C_2)/2$ and $(\Delta C_1 - \Delta C_2)/2$ are plotted in panels (f) and (g), respectively. In Table 8.2 we give the estimated values of the intrinsic and error dispersion of the rMS, for four equally spaced magnitude intervals, assuming a Gaussian distribution. As suggested by a visual inspection of panel (d), there is no doubt that the rMS is larger than that expected from the color-error distribution shown in panel (e)[1]. Even in the worst case of the last considered magnitude bin, we have an intrinsic

[1]Note that we are aware of the significantly different efficiencies of the two CCDs of WFC3/UVIS toward UV. For this reason, thanks to the large dither pattern of the observations, we were able to repeat the analysis creating two subsamples made

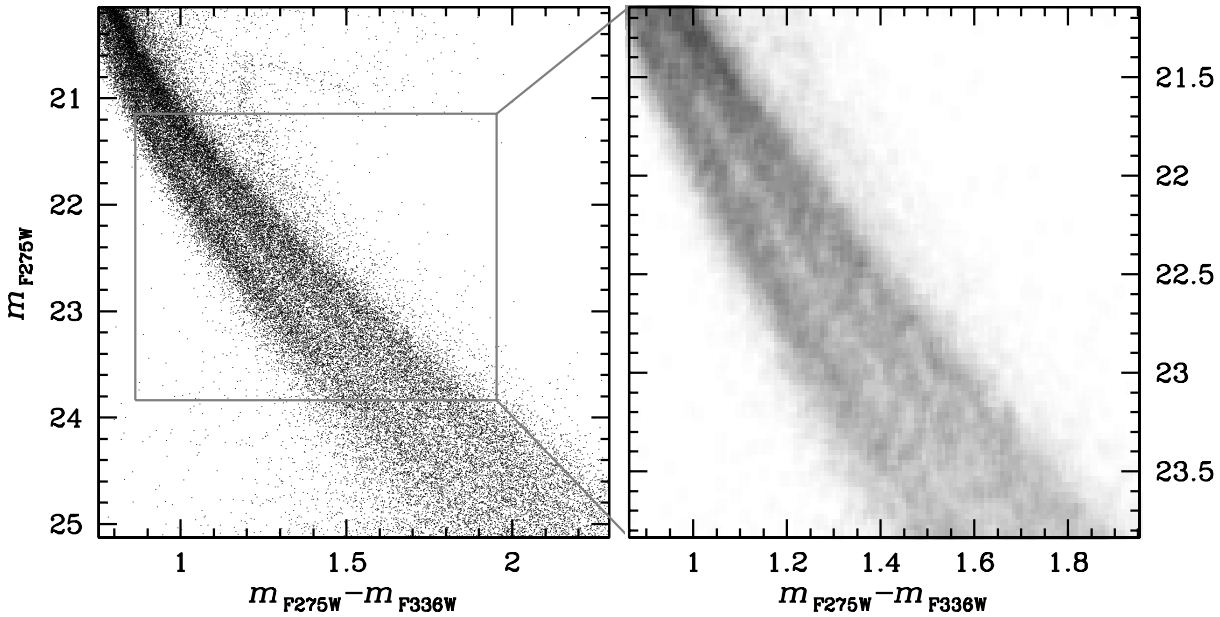

FIGURE 8.7— The rMS is broadened (see the text for details).

TABLE 8.2— The two quantities representing estimates of the intrinsic dispersion (second column), and of our measurements uncertainties (third column), in four different magnitude intervals (indicated in the first column).

m_{F275W}	$\sigma_{(\Delta C_1+\Delta C_2)/2}$	$\sigma_{(\Delta C_1-\Delta C_2)/2}$
21.13–21.81	0.048 ± 0.002	0.021 ± 0.001
21.81–22.48	0.067 ± 0.002	0.033 ± 0.001
22.48–23.16	0.082 ± 0.003	0.040 ± 0.002
23.16–23.83	0.100 ± 0.004	0.051 ± 0.002

dispersion of 0.100 ± 0.004, which is significantly larger (at the level of more than 10σ) than the error dispersion (0.051 ± 0.002).

Figure 8.7 and the bottom two panels of Col. (f) of Fig. 8.9 might suggest a possible split. We cannot assess the significance of this feature, but we think it is worth of further investigation. As shown by V07, the rMS evolves into the brightest SGB-A sequence. The fact that the rMS is broadened shall not come as a surprise. In Piotto et al. (2005), stars in this sequence were found to have a large spread in C, much larger than that of stars on the bMS. If light-element abundances are correlated, as happens in all the massive clusters, this also implies a spread in N and O. We do not know the magnitude of this spread, but it surely must be reflected in the photometry, especially in the blue-UV filters where CH and CN bands are located.

up with only one, or the other, CCD. We find (in the smaller region of the overlap) the same color distribution for the rMS.

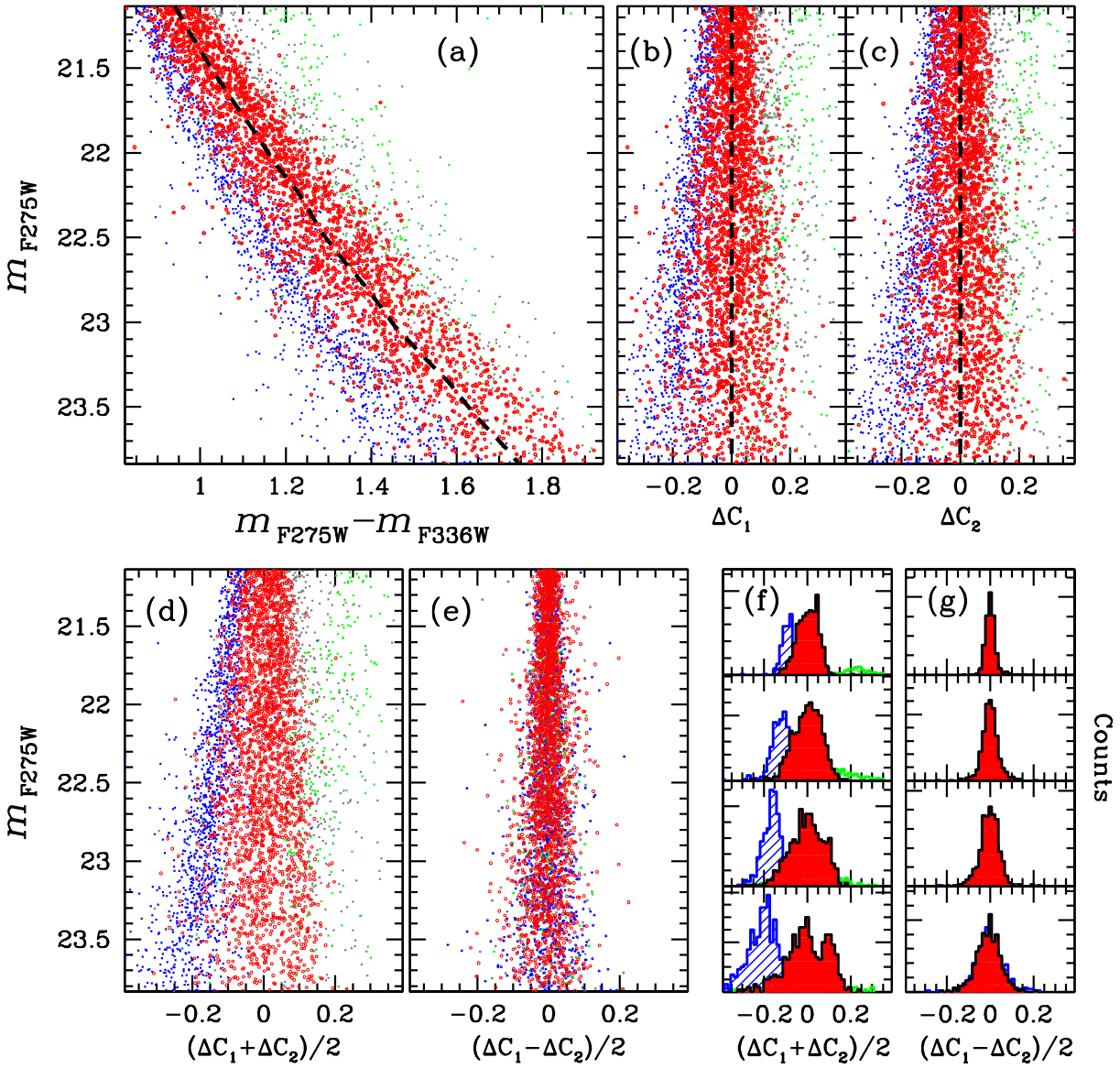

FIGURE 8.8— Evidence of the intrinsic broadening of the rMS (see the text for details).

8.3.3 The MS-a.

The accurate CMDs presented in the previous sections also impose a more detailed investigation for the MS-a.

Among all color combinations, the $m_{F336W} - m_{F435W}$ color is the one which provides us with the best separation between MS-a stars and the other MSs of ω Cen. The reason could be that the MS-a has a somewhat peculiar CNO content with respect to the other populations. As outlined above, filters centered in the blue-ultraviolet region, between ~3200 and ~4300 Å, are the most affected by CN and CH features (see Marino et al. 2008, their Fig. 14).

Moreover, the He content must affect the position of the different MSs, as discussed in previous sections.

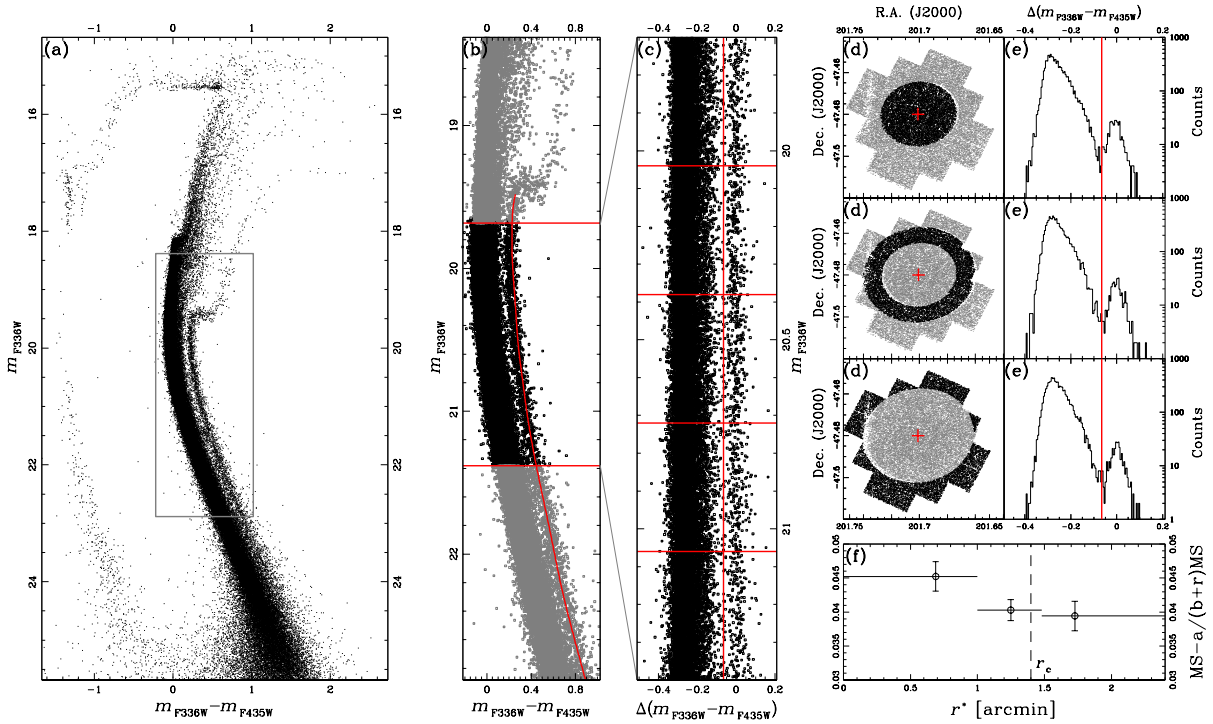

FIGURE 8.9— Panel (a) shows the m_{F336W} vs. $m_{F336W} - m_{F435W}$ CMD. The region highlighted with the grey rectangle is zoomed-in in panel (b). The red fit marks the MS-a fiducial line. In panel (c) we show the rectified MSs in the magnitude interval 19.7<m_{F336W}<21.4. The vertical red line separates MS-a members (on the right) from the rest of MS stars (on the left). We defined 3 radial bins [panels (d)], each one containing the same number of selected stars. For each radial bin we derived a color-distribution histogram [panels (e)]. The radial distribution of the MS-a/(b+r)MS star-count ratio is shown in panel (f). The dashed line marks the core radius (Harris 1996).

Panel (a) of Fig. 8.9 shows the m_{F336W} vs. $m_{F336W} - m_{F435W}$ CMD of ω Cen. The MS-a fiducial sequence (drawn by hand) is plotted in red in panel (b). We subtracted the color of this fiducial sequence from the color of all the stars at the same magnitude. The rectified MSs are presented in panel (c) of Fig. 8.9. We restricted our analysis to the magnitude interval 19.7<m_{F336W}<21.4, where MS-a can easily be separated from the other MSs. We drew a vertical line, located at $\Delta(m_{F336W} - m_{F435W}) = -0.065$ to isolate MS-a members (on the right) from the rest of the MSs [on the left, hereafter called (b+r)MS for simplicity]. We defined three radial intervals in such a way that each radial bin contains the same amount of selected stars [panels (d)]. For each of the three radial intervals, using a logarithmic scale to emphasize MS-a counts, panel (e) plots the distribution of the rectified colors. The ratios of the star counts of MS-a/(b+r)MS are plotted in panel (f) as a function of the angular distance from the cluster center. Errors are calculated as in Bellini et al. (2009): for each radial interval, we derived the MS-a/(b+r)MS ratio in 5 magnitude bins [as defined by the red horizontal lines in panel (c)], and we used the corresponding number of stars as weight to compute a weighted mean for the MS-a/(b+r)MS ratio in each of the 5 bins. Finally, we derived an error for the entire radial interval from the residuals of the individual ratio values from their mean, using the same weights as we had used for the mean. The radial trend shown in panel (f) of Fig. 8.9 is consistent, within the errors, with the flat radial distribution of RGB-a stars (the progeny of the MSa stars) with respect to (RGB-MInt+RGB-MP) ones (as found by Bellini et al. 2009) within the inner $\sim 2'$ from the cluster center.

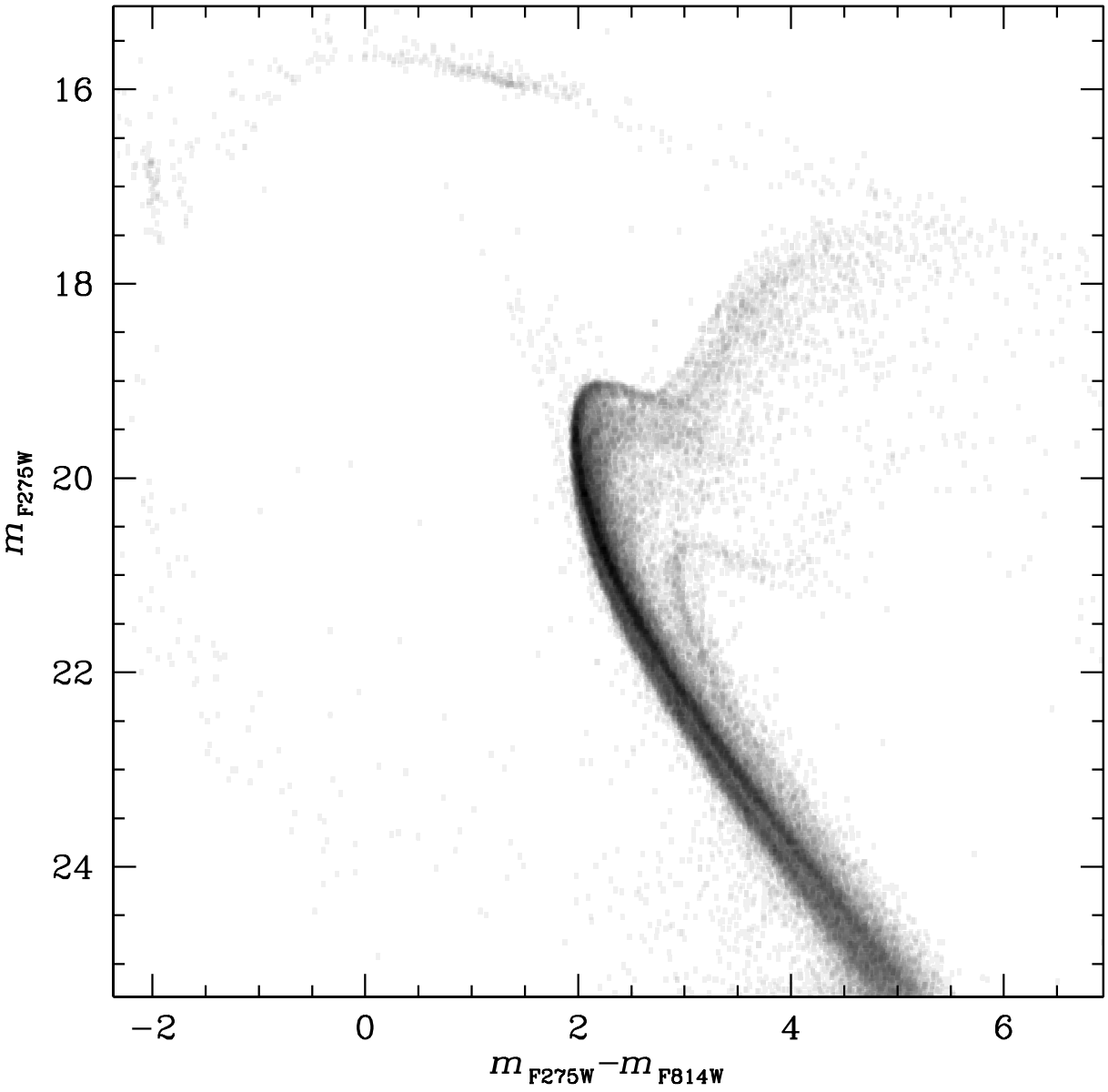

FIGURE 8.10— Hess diagram of the m_{F275W} vs. $m_{F275W} - m_{F814W}$ CMD showing the complexity of ω Cen.

8.3.4 The sub-giant and lower red giant branches

This region of the CMD was previously analyzed by Sollima et al. (2005) and by V07. The latter studied the m_{F435W} vs. $m_{F435W} - m_{F625W}$ ACS/WFC CMD. They identified four distinct stellar groups (named, from bright to faint magnitudes, A, B, C and D, see Fig. 8.2) corresponding to at least four distinct stellar populations, plus a broad distribution of stars, between groups C and D.

WFC3 photometry reveals a new, much-more-complex picture of the SGB region. In the m_{F275W} vs. $m_{F275W} - m_{F814W}$ CMD of Fig. 8.10 and 8.11, stars of the original B and C components of V07 are widely spread in the

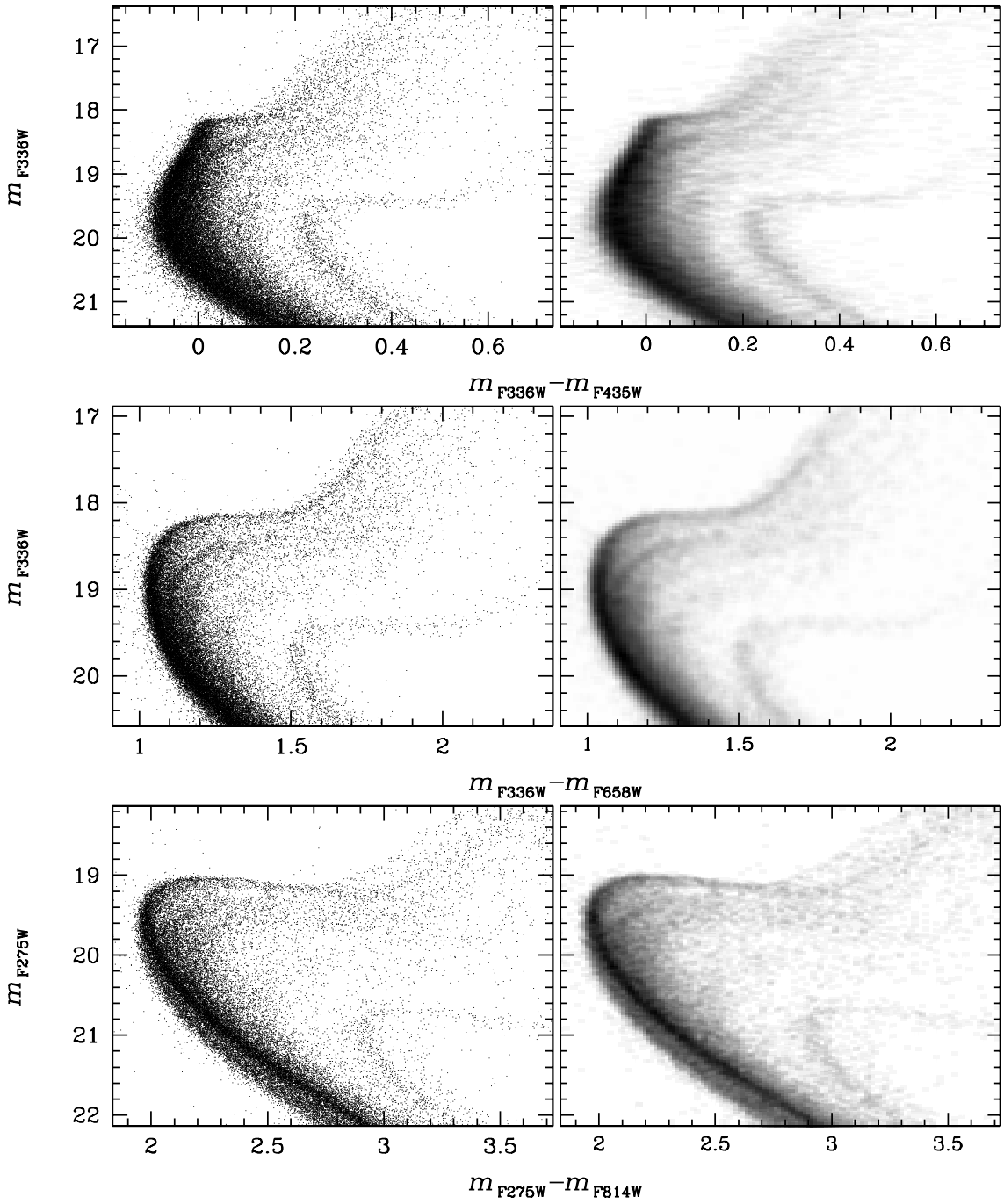

FIGURE 8.11— CMDs and corresponding Hess diagrams in different bands, focused around the SGBs region.

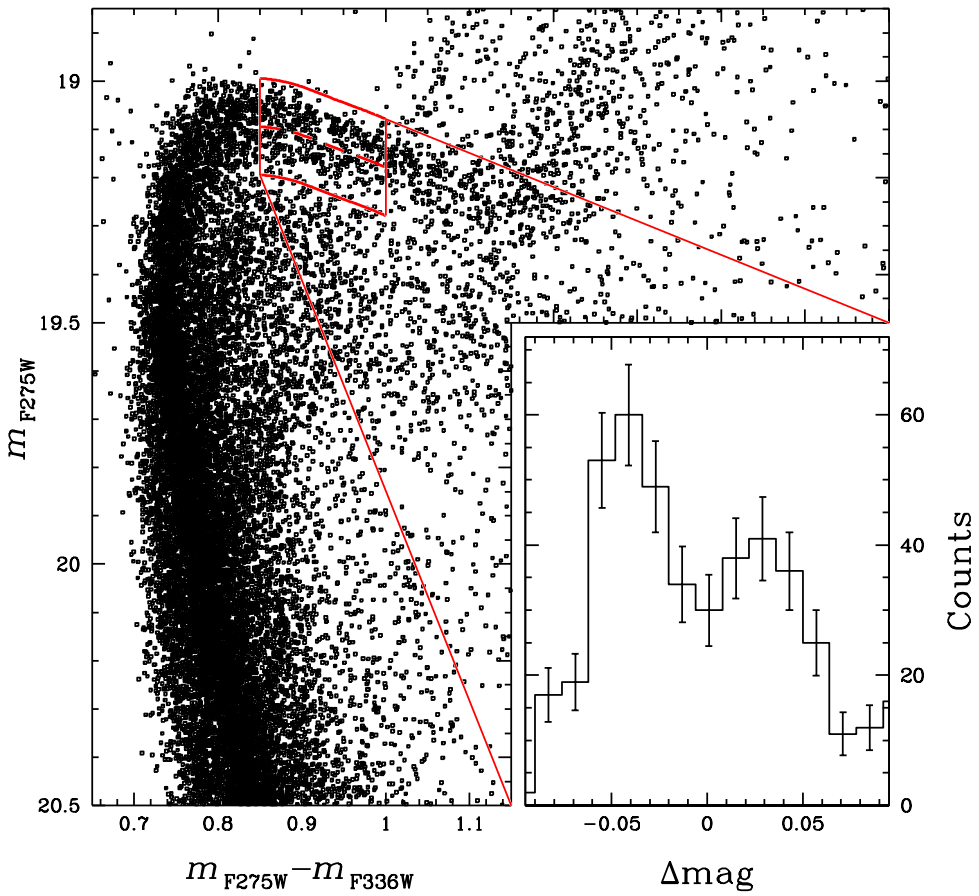

FIGURE 8.12— Zoom-in of the SGB in the m_{F275W} vs. $m_{F275W} - m_{F336W}$ CMD. On the lower right, is the histogram of the magnitude difference between the stars inside the red box and the magnitude of the dashed line, at the same color as the stars (see the text for more details).

F275W band, without any apparent substructure, while the brightest SGB component (A) is split into two branches. Figure 8.12 shows a more quantitative analysis of the split of SGB-A. The dashed red line has been traced (by hand) between the two branches of SGB-A. For each star in the red box which includes the dashed line, we calculated the difference between the star magnitude and the magnitude of the dashed line at the same color as the star. The bimodal distribution of these magnitude differences shown by the histogram in the lower part of Fig. 8.12 confirms the presence of two distinct branches.

It is not clear how the two SGB-A sequences evolve into the RGB, though in the middle panels of Fig. 8.11 they seem to run parallel up to the bright part of the RGB. In particular, the origin of the bluest RGB is not obvious: is it coming from SGB-B or from the faintest SGB of SGB-A? The bluest RGB could also be something similar to the broadened RGB of M4 visible in Fig. 11 of Marino et al. (2008), where the broadening has been related to a spread in CNO affecting the *U*-band. Only chemical abundance measurements will allow us to answer this question. Interestingly enough, the separation of the different RGB sequences becomes more visible in the CMD m_{F275W} vs. $m_{F275W} - m_{F814W}$ (see Fig. 8.11).

There is another feature of the SGB which is visible for the first time in the CMDs presented in this work. The

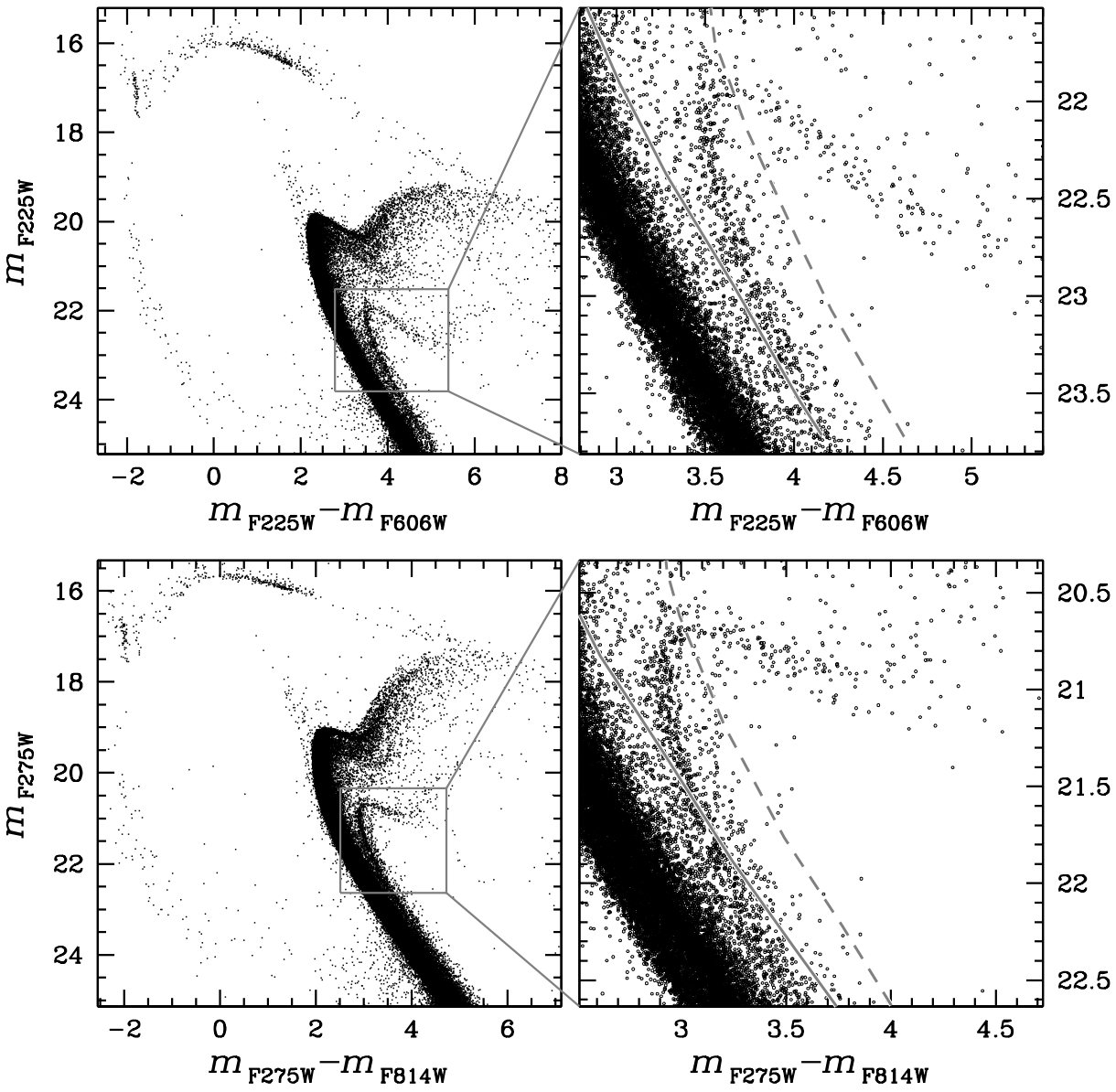

FIGURE 8.13— Zoom-in of two CMDs around the SGB-D region showing hints of two sub-groups.

SGB-D of V07 (which corresponds to the SGB-a Ferraro et al. 2004) is also broadened, as shown in Fig. 8.10, 8.11 and, in more details, in Fig. 8.13. It is not clear whether this broadening corresponds to two distinct populations. A visual inspection of all these figures suggests that the faintest part of SGB-D could be associated with a poorly populated MS which runs on the red side of the MS-a. The sequence on the red side of the MS-a cannot be a sequence of binaries, which would evolve into a brighter (not fainter) SGB.

In summary, the new WFC3 photometry shows that the SGB of ω Cen is even more complex than thought so far. There are at least *six* distinct sequences, plus the broad distribution of stars between SGB-C and SGB-D

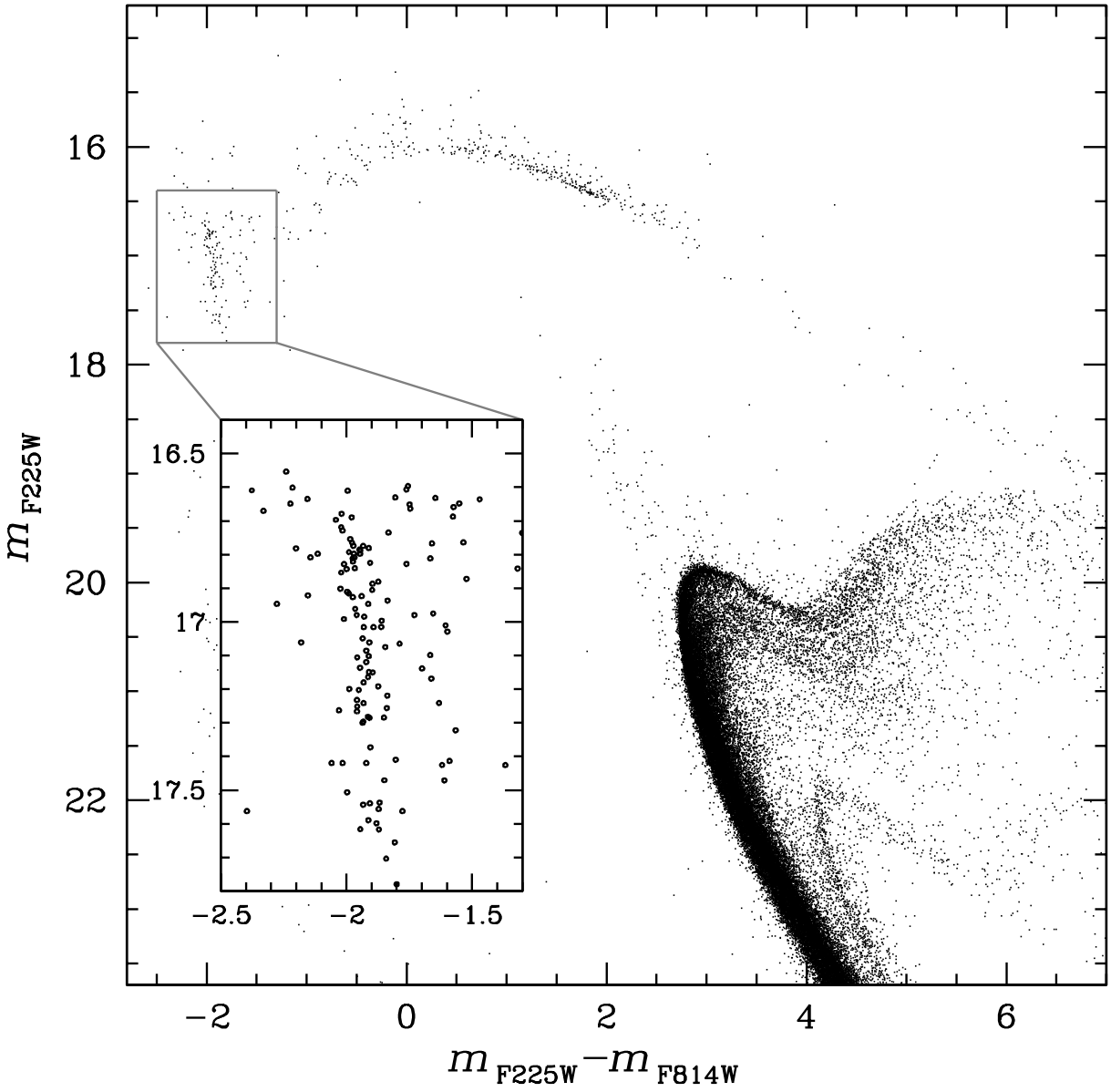

FIGURE 8.14— The m_{F225W} vs. $m_{F225W} - m_{F814W}$ CMD best highlights the complex morphology of the HB. The inset shows a zoom-in of the blue hook section of the HB. Two distinct and almost parallel features are visible.

already identified by V07.

8.3.5 The horizontal branch

Typically, the horizontal branch (HB) amplifies all the complexities of a stellar population, and it is no different for ω Cen. Indeed, the HB shown in Fig. 8.14 shows a multiplicity of features and, in particular, a well-known, very-extended HB, with a pronounced blue hook (D'Cruz et al. 2000). In this section we want to focus our attention on

TABLE 8.3— First lines of the electronically-available catalog.

ID	R.A. (J2000.0)	Dec. (J2000.0)	X	Y	m_{F225W}	m_{F275W}	m_{F336}	m_{F435W}	m_{F606W}	m_{F625W}	m_{F658N}	m_{F814W}
(1)	(2)	(3)	(4)	(5)	(6)	(7)	(8)	(9)	(10)	(11)	(12)	(13)
1	201.7162676	−47.5126489	1781.197	426.673	23.421	22.291	21.088	20.971	19.990	19.760	19.526	19.311
2	201.7156870	−47.5123958	1809.429	444.904	20.674	19.843	19.095	19.166	18.436	18.248	18.056	17.886
3	201.7142821	−47.5123325	1877.748	449.480	21.045	20.157	19.368	19.426	18.650	18.468	18.271	18.092
4	201.7150112	−47.5122876	1842.291	452.709	24.545	22.899	21.604	21.380	20.289	20.133	19.908	19.579
5	201.7138235	−47.5122802	1900.054	453.253	23.926	22.485	21.130	21.040	20.033	19.801	19.578	19.333
6	201.7158384	−47.5122430	1802.055	455.906	21.261	20.377	19.555	19.596	18.831	18.625	18.421	18.248
7	201.7153042	−47.5121646	1828.040	461.554	21.184	20.318	19.513	19.597	18.803	18.633	18.426	18.202
8	201.7150457	−47.5121237	1840.615	464.507	21.843	20.906	20.033	20.095	19.282	19.092	18.866	18.681
9	201.7166455	−47.5121043	1762.811	465.879	21.047	20.206	19.413	19.500	18.726	18.548	18.340	18.132
10	201.7164538	−47.5120773	1772.129	467.827	21.519	20.593	19.773	19.820	19.058	18.870	18.676	18.444
[...]	[...]	[...]	[...]	[...]	[...]	[...]	[...]	[...]	[...]	[...]	[...]	[...]

the blue hook.

The blue hook has a complex morphology, and it has been already studied by Cassisi et al. (2009) and D'Antona, Caloi, & Ventura (2010), using the current ACS/WFC data set from O-9442. The interesting new feature displayed by the WFC3/UVIS data set, and clearly shown in the inset of Fig. 8.14, is that the blue hook is split into two distinct, well-defined, separated – and almost vertical – sequences. The bluer blue-hook sequence contains 80±5% of the total blue hook population, while the remaining 20±5% of blue hook stars populate a redder parallel sequence shifted by about 0.3 magnitudes in the $m_{F275W} - m_{F814W}$ color.

We also note that, on the red side of the two blue hooks (see Fig. 8.14), the HB seems to be separated into a fainter (more populated) and a brighter component, up to at least $m_{F275W} - m_{F814W} = 0.4$.

8.4 Electronic catalog

The astro-photometric catalog will be available at the SIMBAD on-line database[2]. Table 8.3 shows the first entries of the catalog. Description of the catalog: column (1) contains stars ID; columns (2) and (3) give the J2000.0 equatorial coordinates in decimal degrees; columns (4) and (5) provide the pixel coordinates x and y of the distortion-corrected reference meta-chip. Columns (6) through (13) contain photometric measurements. Note that the public catalog gives the original photometry. The reddening and photometric zero point spatial variation corrected photometry is available upon request from the authors[3].

Bibliography

Anderson, J., Ph.D. thesis, Univ. of California, Berkeley, 1997
Anderson, J., Bedin, L. R., Piotto, G., Yadav, R. S., & Bellini, A. 2006, A&A, 454, 1029
Anderson, J., et al. 2008, AJ, 135, 2055
Anderson, J., Piotto, G., King, I. R., Bedin, L. R., & Guhathakurta, P. 2009, ApJL, 697, L58
Bedin, L. R., Piotto, G., Anderson, J., Cassisi, S., King, I. R., Momany, Y., & Carraro, G. 2004, ApJL, 605, L125

[2] `http://simbad.u-strasbg.fr/simbad/`

[3] Note that this work is based on images taken in July 2009. New WFC3/UVIS epochs have been (and others will soon be) collected for the same field of ω Cen analyzed here.

Bedin, l. R., et al. 2005, MNRAS, 357, 1038
Bekki, K., & Freeman, K. C. 2003, MNRAS, 346, L11
Bellini, A., Piotto, G., Bedin, L. R., King, I. R., Anderson, J., Milone, A. P., & Momany, Y. 2009, A&A, 507, 1393
Bellini, A., & Bedin, L. R. 2009, PASP, 121, 1419
Bellini, A., Bedin L., R., Piotto, G., Milone A., P., Marino A., F., & Villanova, S. 2010, AJ in press, arXiv:1006.4157
Cannon, R. D., & Stobie, R. S. 1973, MNRAS, 162, 207
Cassisi, S., Salaris, M., Anderson, J., Piotto, G., Pietrinferni, A., Milone, A., Bellini, A., & Bedin, L. R. 2009, ApJ, 702, 1530
D'Cruz, N. L., et al. 2000, ApJ, 530, 352
Ferraro, F. R., Sollima, A., Pancino, E., Bellazzini, M., Straniero, O., Origlia, L., & Cool, A. M. 2004, ApJL, 603, L81
Freeman, K. C., & Rodgers, A. W. 1975, ApJL, 201, L71
Harris, W. E. 1996, AJ, 112, 1487, as updated in February, 2003.
Johnson, C. I., Pilachowski, C. A., Rich, R. M., & Fulbright, C. P. 2009, ApJ, 698, 2048
Lee, Y.-W., Joo, J.-M., Sohn, Y.-J., Rey, S.-C., Lee, H.-C., & Walker, A. R. 1999, Nature, 402, 55
Lee, Y.-W., et al. 2005, ApJL, 621, L57
Lee, J.-W., Kang, Y.-W., Lee, J., & Lee, Y.-W. 2009, Nature, 462, 480
Marino, A. F., Villanova, S., Piotto, G., Milone, A. P., Momany, Y., Bedin, L. R., & Medling, A. M. 2008, A&A, 490, 625
Milone, A. P., et al. 2008, ApJ, 673, 241
Milone, A. P., Bedin, L. R., Piotto, G., & Anderson, J. 2009, A&A, 497, 755
Milone, A. P., et al. 2010, ApJ, 709, 1183
Norris, J. E. 2004, ApJL, 612, L25
Pancino, E., Ferraro, F. R., Bellazzini, M., Piotto, G., & Zoccali, M. 2000, ApJL, 534, L83
Pancino, E., Pasquini, L., Hill, V., Ferraro, F. R., & Bellazzini, M. 2002, ApJL, 568, L101
Piotto, G., et al. 2005, ApJ, 621, 777
Sarajedini, A., et al. 2007, AJ, 133, 1658
Sollima, A., Pancino, E., Ferraro, F. R., Bellazzini, M., Straniero, O., & Pasquini, L. 2005, ApJ, 634, 332
Sollima, A., Ferraro, F. R., Bellazzini, M., Origlia, L., Straniero, O., & Pancino, E. 2007, ApJ, 654, 915
Villanova, S., et al. 2007, ApJ, 663, 296

Future projects

9

Future projects

In this final Chapter we will describe our projects for the immediate future, some of which have already begun.

9.1 The VISTA VVV survey

Our group is involved in the VISTA (Visible and Infrared Survey Telescope for Astronomy) Variables in the Via Lactea (VVV): the public ESO near-IR variability survey of the Milky Way (MW, Minniti et al. 2010).

9.1.1 The telescope+camera system

VISTA is a 4-m class wide-field survey telescope for the Southern hemisphere, located at ESO Cerro Paranal Observatory in Chile. The telescope has a fast f/1 primary mirror, giving a f/3.25 focal ratio at the Cassengrain focus. It is equipped with the near-infrared (NIR) camera VIRCAM, with a 1.65 degree diameter field of view (FoV) at VISTA nominal pixel size, containing 67 million pixels of mean size $0\farcs339$ (see left panel of Fig. 9.1 for a comparison of the VIRCAM FoV with the size of the Moon and other detectors FoVs).

There are four broad band filters (Z, Y, H, Ks), and one narrow band filter at 1.18 μm. The point spread function (PSF) of the telescope+camera system provides a full width at half maximum of $\sim 0\farcs51$ (without seeing effects). Each night an average of 315 GB of raw data will be collected. Each individual rae image will have a size of 256 MB.

9.1.2 The survey

The bulk of the stars, gas and dust in the MW are confined to its bulge and plane. As a result, in these directions both extinction and crowding are high. The main goal of the VISTA VVV survey is to know how the stellar populations are distributed within the Galaxy in order to study the inner structure of the Galaxy itself.

Traditional distance indicators have been used with various success in the past. The approach was to concentrate on unobscured windows, where optical surveys can be carried out (e.g., MACHO, OGLE, EROS). The VISTA survey, instead, planned to cover a very wide area around the MW bulge, and an adjacent section of the mid-plane where star-formation activity is high, for a total FoV of 520°. The survey already started acquiring data, and it will conclude in 2014, after having mapped the whole bulge systematically for multiple ($\gtrsim$ 100) epochs, with almost 2000 hours of guaranteed observing time (see right panels of Fig. 9.1). The variability survey in the bulge will be carried out in the Ks band down to $\sim$ 18 mag (signal-to-noise $\simeq$ 3). The observing strategy employs about 30 deg^2

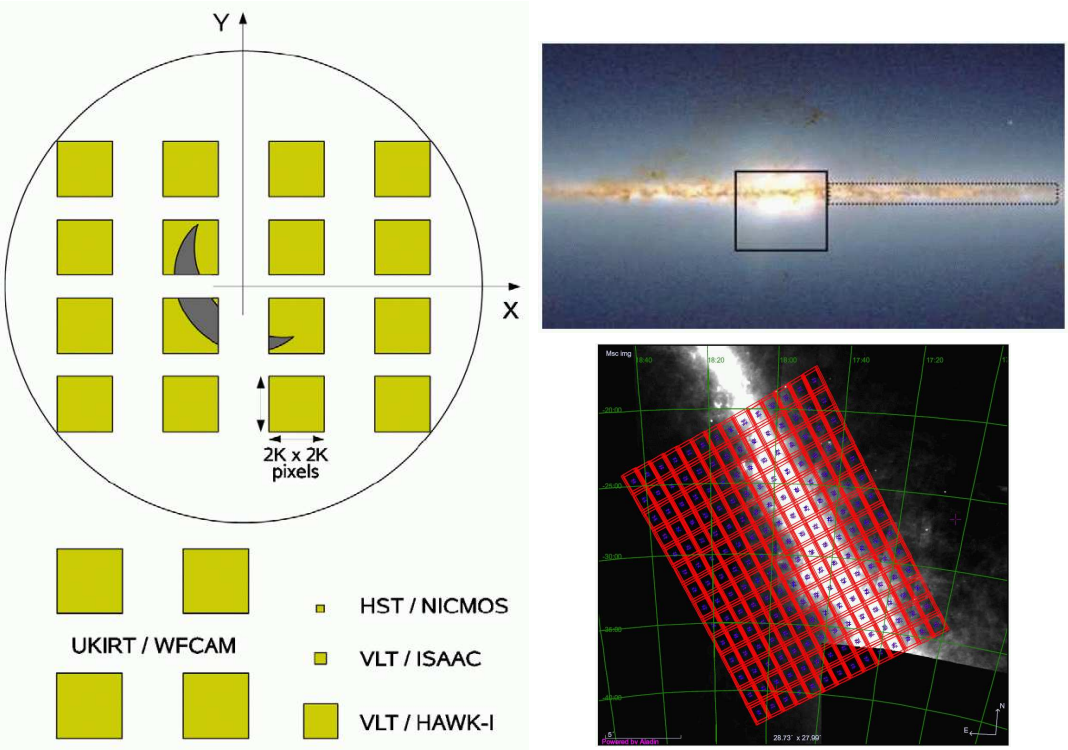

FIGURE 9.1— *(Left:)* Array of the 16 VIRCAM detectors. For comparison a crescent Moon over the VISTA camera is shown and the FoVs of WFCAM@UKIRT, NICMOS@HST, ISAAC@VLT, and HAWK-I@VLT. *(Top right:)* 2MASS map of the inner Milky Way (MW) the VVV bulge (solid box, $-10° < l < +10°$ and $-10° < b < +5°$) and the plane survey area (dotted box, $-65° < l < -10°$ and $-2° < b < +2°$). *(Bottom right:)* Coverage of the Galactic center overlaid on a mid-IR map. Red boxes show the dithern pattern. (From Minniti et al. 2010.)

per hour, or 300 deg^2 per night. The combined epochs will reach $Ks = 20$ mag, which is three magnitudes fainter than the unreddened bulge main-sequence turn-off, although the densest fields will be confusion-limited.

Previously, all-sky 2-dimensional maps in NIR wavelengths have been done with one epoch data only. Otherwise, multi-epochs observations have been carried out for specific small-FoV targets on the bulge and disk. The VVV survey will perform multi-epoch and wide-FoV observations of the Galaxy's bulge and part of the disk, providing the astronomical community with a high-resolution 3-D (or 4-D if you include the time dimension) map of the bulge.

9.1.3 Our science with VISTA

Besides the main project of the VVV survey, there are many other important scientific investigations than can exploit the huge amount of data offered by VVV. We are of course more interested in the ones involving wide field astrometry and proper motions. The VVV survey, indeed, will include in its FoV 33 bulge known globular clusters (GCs) and ~ 350 known open clusters (OCs, see Fig. 9.2 for the map of the known star cluster in the VVV FoV). This will give us the possibility to:

- obtain high-precision astrometry and photometry for ~ 10^9 stars;
- measure proper motions of metal-poor bulge GCs and OCs;

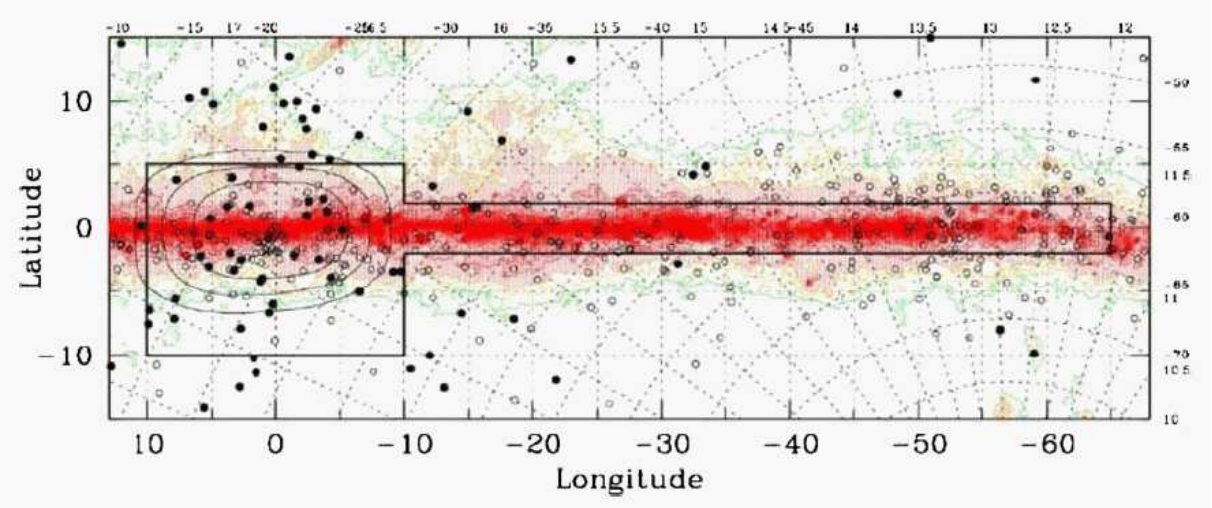

FIGURE 9.2— Map of the globular and open cluster positions (full and open circles, respectively) included in the VVV area. (From Minniti et al. 2010.)

- search for new GCs towards the inner MW;
- study IR color-magnitude diagrams (CMDs) of the 33 bulge GCs and 314 bulge OCs;
- search for new OCs towards the inner MW;
- derive IR CMDs of known OB associations towards the inner MW and search for new OB Associations;
- search for variable stars in the NIR in the field of the imaged GCs and OCs;
- search for high-proper-motion objects in the VVV data;
- analyze the Sagittarius dwarf galaxy in the VVV data;
- search for binary OCs;
- study the CMD of fossil OCs;
- trace the stellar populations of the MW bulge;
- search for red, faint, angularly distant companions of nearby stars.

9.2 Tidal tails of Galactic globular clusters

Recent extensive campaigns conducted to directly measure the GC tidal radius using their radial surface density profiles, have lead to the discovery of large tidal tails of stars around GCs (Grillmair et al. 1995; Zaggia et al. 1995; Zaggia, Piotto, & Capaccioli 1997; Kharcenko, Scholz, & Lehman 1997). These tidal tails are present as departures in the surface density profiles at large radii, with a break from a King profile (King 1666) at the tidal radius, followed by a power law decline which varies from cluster to cluster. Evidence of tidal tails has been found in 16 Galactic GCs out of 21 analyzed (Grillmair 1997), which means that tidal tails are a common feature among GCs. Recently tidal tails have been discovered thanks to SDSS data in the GC NGC 5466 (Grillmair & Johnson 2006; Belorukov et al. 2006) and, using wide-field imagers, in Palomar 5 (Koch et al. 2004) and NGC 7492 (Lee

et al. 2004). [Interestingly enough, tidal tails have recently been detected also in four GCs in M31 (Grillmair et al. 1996)].

Composed of unbound cluster stars that have escaped from the cluster, tidal tails have a complex morphology that depends strongly on the tidal field of the Galaxy, on Disk and Bulge tidal shocks, and on the rate of stellar evaporation from the cluster (see for a review Meylan & Heggie 1997). They are potentially very useful tools for understanding the complex dynamical evolution of GCs.

The existence of tidal tails is directly connected to the level of dark matter present in GCs. Indeed, Moore (1996) showed that if tidal tails are present in GCs, this would rule out the existence of dark matter halos around GCs, implying a global mass-to-light ratio $M/L = 2.5$, typical of an old stellar population. In principle, from the morphology of the tail it should be possible to obtain the shape of the orbit of the relative GC (Grillmair et al. 1997). Such an approach needs, for a correct interpretation of the observations, careful dynamical modelings, carried out with modern extensive and time consuming N-body simulations (Moore et al. 2006).

As a complementary approach, the study of the tidal-tail's stellar populations can be directly used to gather information on the internally- and externally-induced dynamical evolution of a GC. In the last few years, observational evidences have been collected by our group (and others) that, due to the evaporation of stars and the interaction with the gravitational potential of the Galaxy, GCs loose stars (Capaccioli, Piotto, & Stiavelli 1993; Piotto, Cool, & King 1997, and references therein). This star loss is enhanced by the tidal shocks experienced by the cluster when it passes through the disk and/or the bulge of the Galaxy. In combination with the internal mass segregation, and as a consequence of the fact that the stars closer to the tidal radius are preferentially lost, the star loss is selective, in the sense that it is easier for low-mass stars to escape from the cluster (Capaccioli, Piotto, & Stiavelli 1993). This in turn modifies the mass function and, unless we know how the stars are lost, there is no hope to have information on the initial mass function (which is what we would like to have) from the present-day mass function.

Modeling these dynamical effects is almost hopeless (Vesperini & Heggie 1997). However wide-field imagers (in particular the WFI@2.2m because of its huge archive, which can be combined with recent VISTA data) offer a unique opportunity to directly investigate both the internal mass segregation and the star-loss rate as a function of the stellar mass of GCs. A classic limitation in the study of GC tidal tails is the derivation of accurate membership, which is needed to discriminate between stars actually belonging to the cluster and field stars.

At larger distances from the cluster center there is another problem, due to the fact that the population of faint stars become larger as a consequence of the dynamical evolution, and reflects in the mass segregation. Kinematic membership (proper motion and radial velocity) is unfortunately available only for few nearby clusters, and does not reach very faint magnitudes on a wide coverage. One solution adopted in the past was to use the color-selection technique, which consists of selecting stars on the fiducial sequence of the observed GCs in order to discriminate and remove non-cluster members (Zaggia, Piotto, & Capaccioli 1997). Our astrometric techniques (Anderson et al. 2006) will allow us to seriously address, for the first time, the problem of the membership determination in the GC outskirts, and to directly investigate tidal tail stars. The WFI@2.2m archive is plenty of observations of GCs, sometimes with first- and second-epoch images suitable for accurate proper-motion derivations. In case a data set is missing from the archive, we will submit an ESO proposal to get time for it, which will also serve as a pilot experiment for future usage of the WFI archive. Other instrument/camera combinations will be useful as well, first of all LBC@LBT (and UH8K@CFHT) for GCs in the North hemisphere.

9.3 Absolute motion of Galactic globular clusters

Our group is involved in the Treasury program on Galactic globular clusters (P.I. Ata Sarajedini, GO-10775). Among the many scientific researches that can be (and have already been) undertaken (e.g., multiple populations, (Milone et al. 2008); stellar evolution tracks and isochrones (Dotter et al. 2007); relative GC ages (Marín-Franch et al. 2009), just to mention the most cited), this data set offers the unique opportunity to measure the absolute motions of 64 Galactic GCs, using the Galaxy spread function (Mahmud & Anderson 2008).

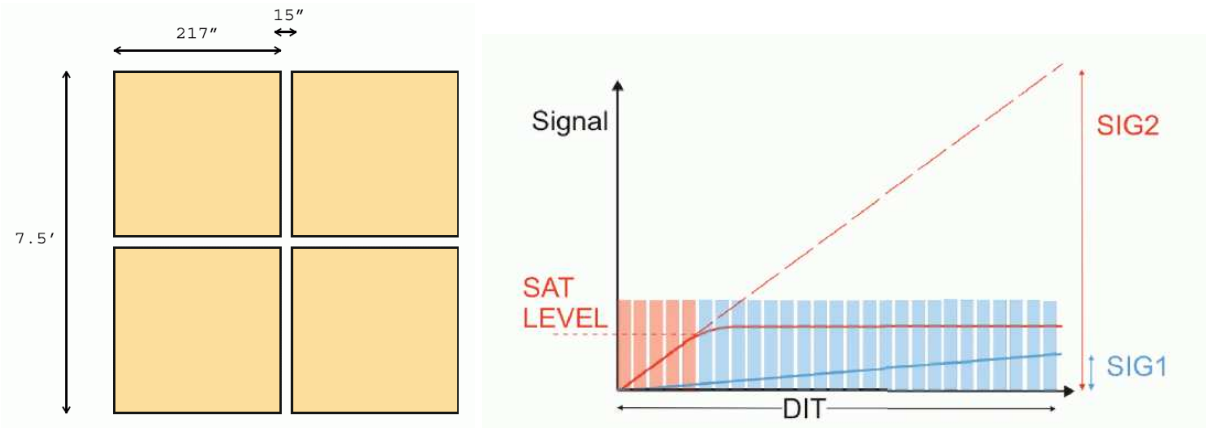

FIGURE 9.3— *(Left:)* HAWK-I field-of-view coverage by the detector mosaic. *(Right:)* HAWK-I's Threshold Limited Integration mode. Only pixel values below SATLEVEL are taken into account for calculation of the slope of pixels with high flux (red line). For low flux pixels (blue line) all non-destructive readouts indicated by rectangles are used. The final FITS file contains the value SIG1 and SIG2, allowing to overtake the saturation level of the detector. (From Kissler-Patig et al. 2008.)

All the required images are already available from the archive: the first-epoch, coming from a snapshot program (P.I. Giampaolo Piotto, GO-8118), will give us an adequate time base-line (1997–2002) and, more importantly, the second-epoch, coming from the Treasury program G0-10775, has produced photometry for stars from the red-giant branch to the faint main sequence with S/N $\geq$ 10 (Anderson et al. 2008), therefore precise proper motions will be achieved for stars in a wide range of magnitudes.

The use of background galaxies as an absolute reference frame will allow us to obtain absolute proper motions, and to provide better constraints on the Galactic potential in the inner regions of the Galaxy, which are dominated by the thick disk and bulge (Dinescu et al. 2003). These regions are poorly constrained at present; better constraints on the Galactic potential would also allow us to have an insight into GC orbits and dynamical destruction in the inner regions of the Galaxy.

Moreover, this data set will allow us to obtain, for most of the clusters, relative proper motions accurate enough to remove field stars and therefore clean the CMDs, improving resolution of the principal cluster sequences (Feltzing & Jhonson 2002; Richer et al. 2002). With more precise membership and better defined CMD ridge lines, it will be possible to provide better constraints on cluster age/distance, and possibly identify multiple populations (Piotto et al. 2007; Villanova et al. 2007; Milone et al. 2008) or unusual photometric sequences.

9.4 Exporting our techniques to other wide-field imagers

A growing number of wide-field imagers are installed at the focus of 4–8 m class telescopes (e.g., HAWK-I@VLT, PAN-STARR, Suprime-Cam@SUBARU, MEGAPRIME@CFHT, LSST, WFCAM@UKIRT, NEWFIRM@KPNO, WIRCAM@CFHT, ...), and many others, now dismissed (e.g., UH12K@CFHT), can provide precious first-epoch observations, thanks to the huge data base contained in their archives. The software we developed for high-precision astrometry and photometry is easily adjustable to many different telescope/camera combinations.

We have already started to fine-tune our techniques on the HAWK-I camera. The next section will give some information on what we have done so far and what we plan to do in the near future with this detector.

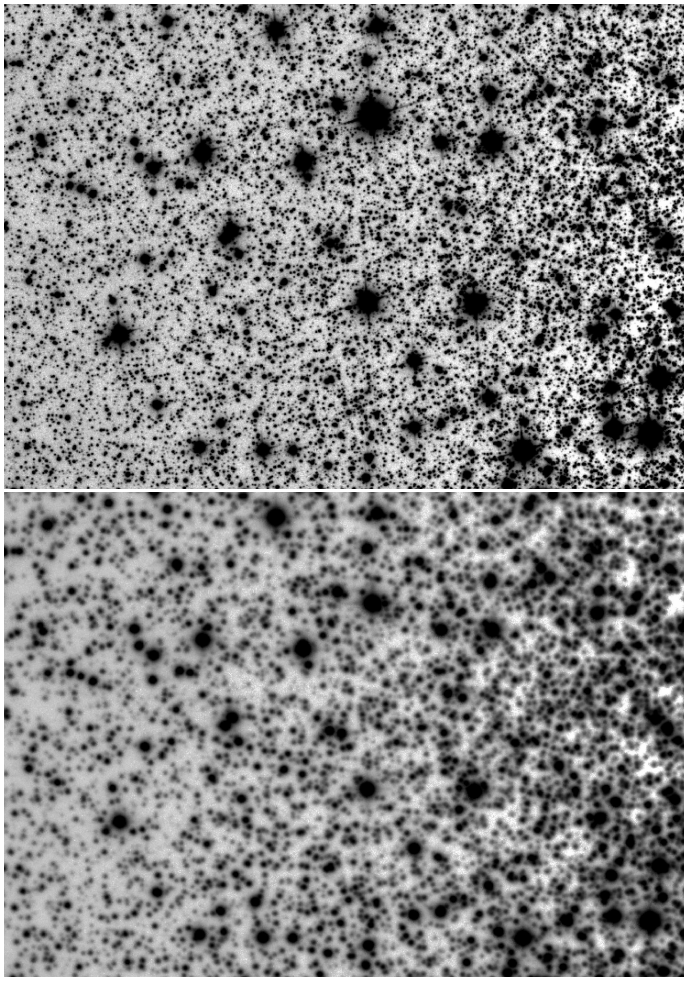

FIGURE 9.4— Stacked images of a patch of sky close to the center of the globular cluster M 22 as seen with HAWK-I@VLT (*K*s band, on the top), and with WFI@2.2m (*V* band, on the bottom). Note the sharpness of the HAWK-I stacked image.

9.4.1 HAWK-I@VLT

HAWK-I is a cryogenic wide-field imager installed at the Nasmyth A focus of UT4, at the VLT. The on-sky FoV is $7\farcm5 \times 7\farcm5$, with a cross-shaped gap of $15''$ between the four HAWAII 2RG 2048×2048 pixels detectors, with a pixel scale of $0\farcs106$ (left panel of Fig. 9.3). The instrument is offered with 10 observing filters, placed in two filter wheels: 4 broad-band filters ($Y(Z)$, J, H & Ks), and 6 narrow-band filters (Br γ, CH4, H2, 1.061 μm, 1.187 μm & 2.090 μm). The image quality is seeing-limited down to at least $0\farcs4$ seeing (i.e., $0\farcs3$ measured in Ks).

The telescope on which HAWK-I is mounted (UT4) is expected to be soon upgraded into an Adaptive-Optics Facility, comprising a deformable secondary mirror, four laser-guide stars and wavefront-sensor units for HAWK-I. This will provide ground-layer adaptive-optics correction over its full FoV, bringing improved seeing for longer periods and further enhancing its imaging capability and point source sensitivity. The HAWK-I detector is operated by default in a non-destructive read-out mode, using the so-called Threshold Limited Integration (TLI, see the right panel of Fig. 9.3 for more a detailed description). Until the availability of the James Webb Space Telescope (JWST)

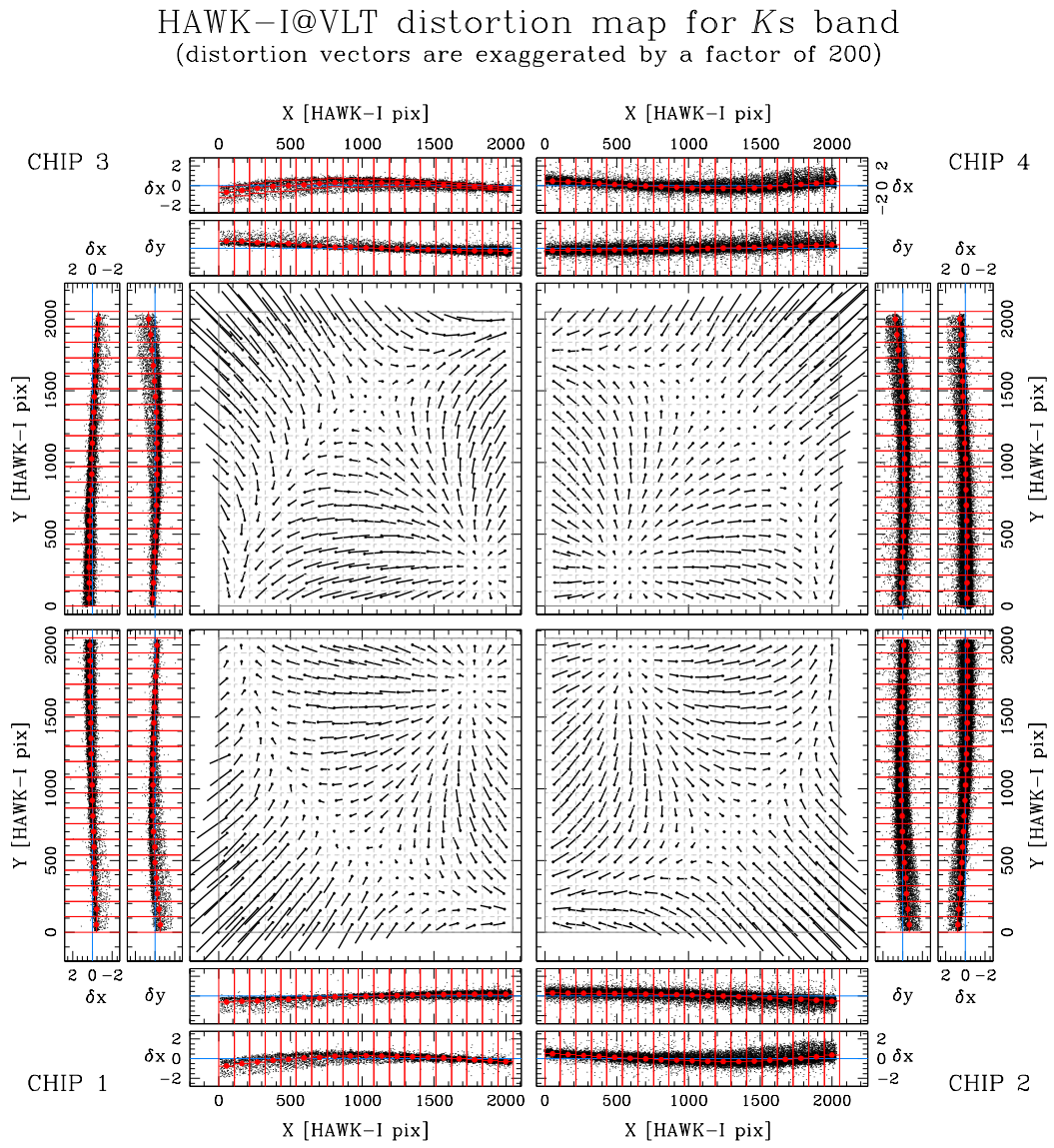

FIGURE 9.5— Predicted vs. uncorrected positions. The size of the residual vectors is magnified by a factor of 200. For each chip we plot also individual residuals as function of X and Y axes. Units are expressed HAWK-I pixels.

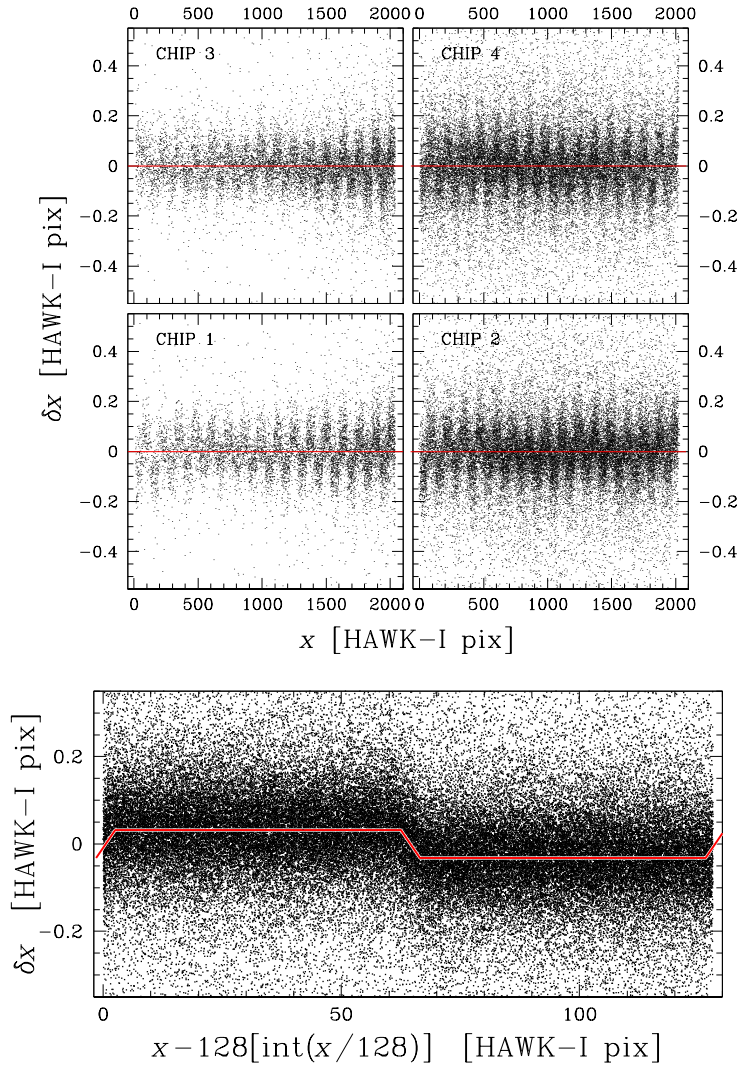

FIGURE 9.6— *(Top panels:)* distortion residuals δx versus their x location on the detector (for each chip), in units of HAWK-I pixels. A clear periodic trend in the residuals is present. *(Bottom panel:)* the periodogram with a period of 128 columns containing all the points plotted in the top panels.

in the next years, it is clear that 8-m class telescopes (in particular HAWK-I) will provide the best sensitivity achievable in the near-infrared below 3 μm. (See Kissler-Patig et al. 2008 for more details about the HAWK-I camera).

Luigi Bedin has been involved in the commissioning activities for the HAWK-I camera. Being responsible for the astrometric calibration, he decided to make use of an astrometric standard field that has been developed to calibrate JWST. The JWST Astrometric Calibration Field is a field near the center of the Large Magellanic Cloud that has a relatively flat distribution of stars. The field was chosen to have a good number of medium-brightness stars (~2 arcsec^{-2}) that will each give us positions good to about 1 mas. At the same time, the field was chosen to have a minimum of extremely bright stars that will be saturated in reasonable exposures. We have already found

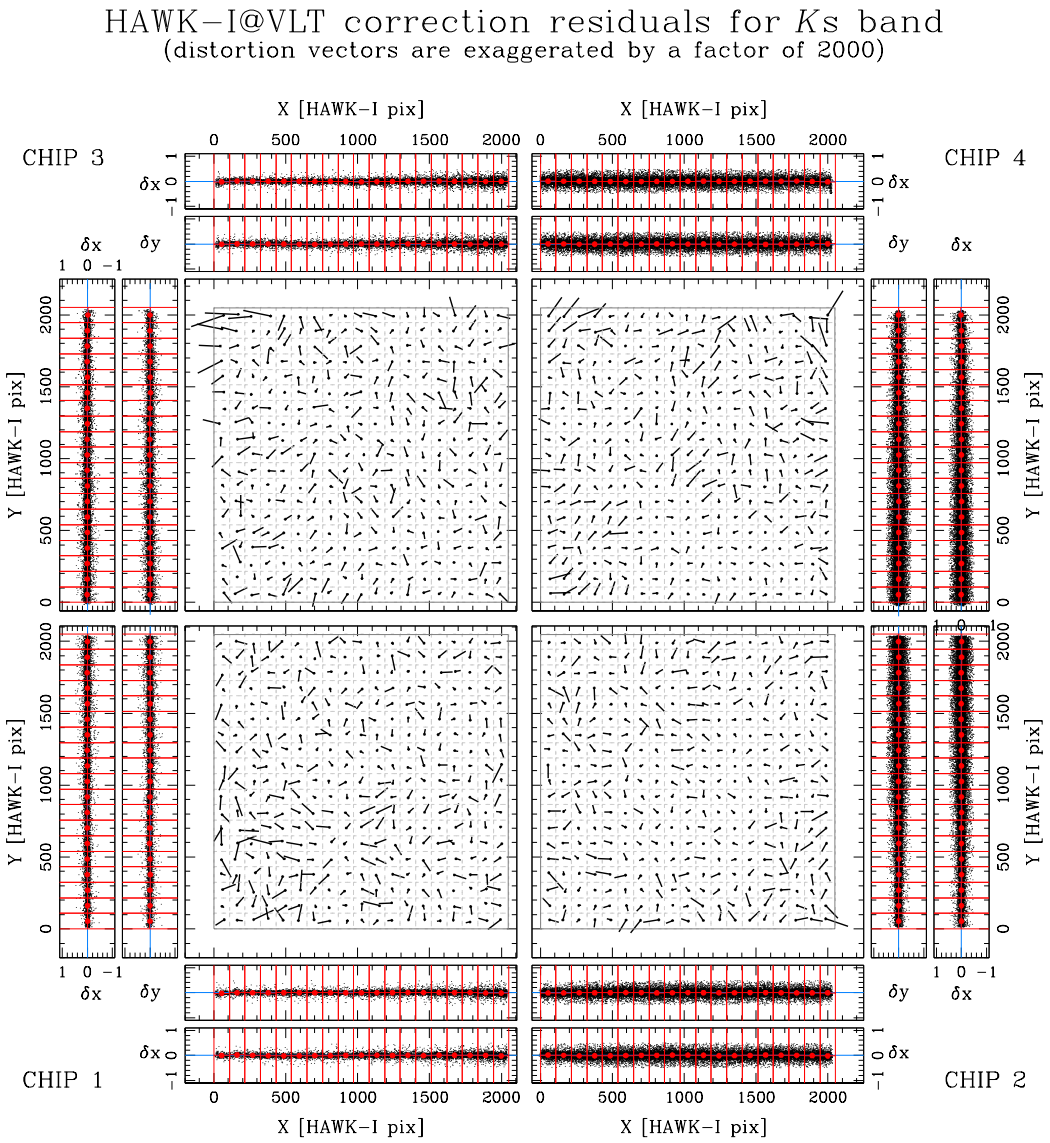

FIGURE 9.7— Same as Fig. 9.5 after the correction is applied. The size of the residuals is now magnified by a factor of 2000.

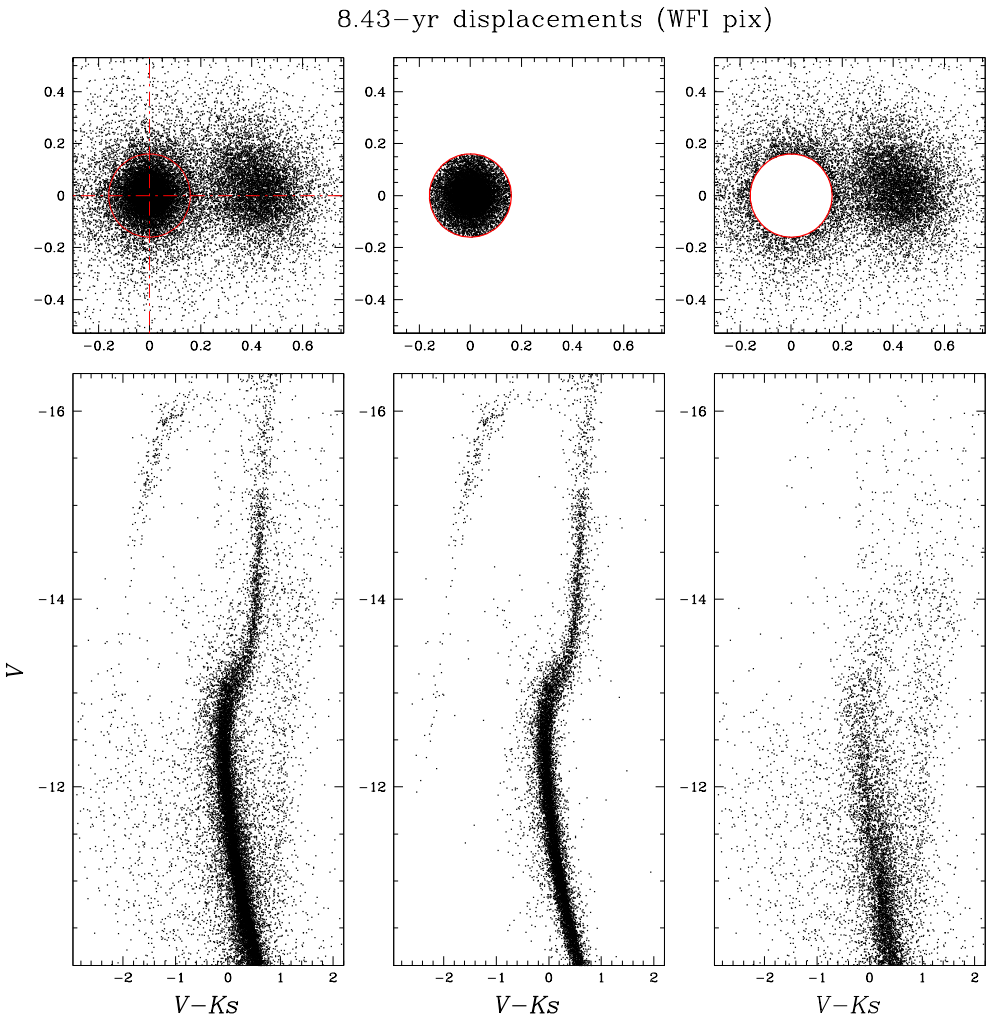

FIGURE 9.8— *(Top-panels:)* proper-motion vector-point diagrams. Zero point in VPD is the mean motion of cluster stars. *(Bottom panels)* uncalibrated V, $(B-V)$ CMDs *(Left:)* the entire sample. (*Center*): selected cluster members. *(Right:)* Objects with a proper motion larger than our membership-selection criterion (red circle).

a preliminary geometric-distortion (GD) solution for the four chips, by means of the same technique we used for LBC@LBT (Chapter 2) and for WFC3@*HST* (Chapter 3) cameras, so we pass over all the details here. We used the calibration field to solve for GD for J, H, Ks and Y bandpasses (more details below).

We also have a set of 5×5-dithered HAWK-I Ks and Y observations (6 DITs of 10 s each) of the globular cluster (GC) M 22 (NGC 6656), taken in October 2007. This very peculiar object has a double sub-giant branch (SGB) and a bimodal [Fe/H] distribution (Marino et al. 2009); the only other GCs with this characteristic are ω Cen, M 54 (Carretta et al. 2009), and Terzan 5 (Ferraro et al. 2009). Our aim is to analyze the relative radial distribution of the two SGB populations (as done in Bellini et al. 2009, for main sequence and red-giant branch in ω Cen, and in Milone et al. 2009, for the SGB of NGC 1851), looking for fossil signatures of radial gradients

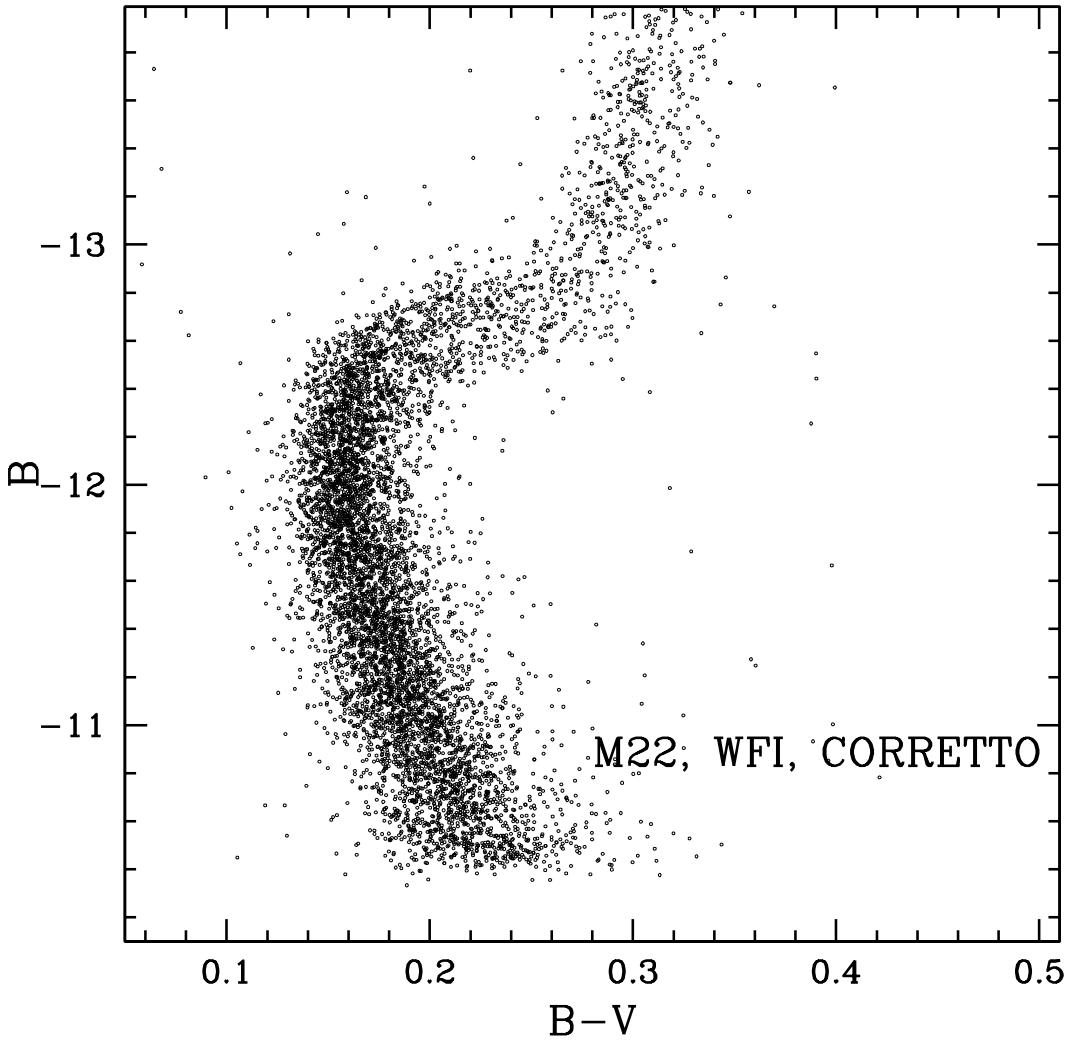

FIGURE 9.9— Differential-reddening corrected, proper-motion selected V vs. ($B - K$s) CMD of stars around the SGB region, which appears to be clearly split into two sub-branches.

(D'Ercole et al. 2008; Decressin et al. 2008). We retrieved in the WFI@2.2m archive a set of 2×240 s B and 2×240 s V images of M 22 taken in May 1999, to be used to measure proper motions for all objects in our sample and clean our CMD from foreground and background contamination. As an example, in Fig. 9.4 we show the same region of sky, located at 5′ east to M 22 center, as seen from our HAWK-I Ks stacked image (top), and from our WFI V stacked image (bottom).

Figure 9.5 shows, for each HAWK-I chip, the map of the geometric distortion (GD) affected by the detector+Ks filter combination, with the same fashion as for Figs. 2.4 and 3.3. Top panels of Fig. 9.6 show, for each chip, the distortion residuals δx versus x after GD correction is applied[1]. There is clearly some periodic striping in these panels. It does look like a problem similar to the one suffered by WFPC2 and WFC detectors on board *HST* (see

[1]Note that M 22 center is in general closer to CHIP # 2 and 4, this is why there are far more points in these two chips.

e.g., Anderson & King 1999 for the WFPC2). We found this period to be of 128 columns (i.e., 16 total periods per chip). On the bottom panel of Fig. 9.6 we plot collected δx versus x residuals coming from the four chips in a periodogram with a period of 128 columns. To correct this detector feature, we modeled it with a square wave of amplitude 0.0325 pixels ($\sim$ 3.5 mas, highlighted in red in the Figure).

Figure 9.7 shows distortion residuals after GD and periodic corrections are applied. Our preliminary solution works well in general (the rms of the residuals is ~5–7 hundreths of pixel), but areas close to the detectors corners need to be improved. There are also high-frequency components to the spatial distortion that remain to be removed. We will eventually correct them with a table of residuals, as done in Anderson et al. (2006) for the WFI@2.2m.

We developed a PSF-fitting procedure analogous to the one for LBC@LBT (see Chapter 4) to measure star positions and fluxes for the HAWK-I images. First-epoch WFI exposures were reduced with the same procedures described in Chapter 6. Preliminary proper-motion measurements, performed using a local sample of network of M 22 reference members (the local-transformation approach, see Chapters 4, 6) are shown in Fig. 9.8 (note that magnitudes are instrumental, and no differential-reddening correction is applied). From left to right, we show all stars, likely cluster members, and likely field objects, respectively. The top panels present the vector-point diagrams of all stars plotted underneath in the CMDs.

Finally, a preliminary differential-reddening correction (following prescriptions given in Sarajedini et al. 2007) of the proper-motion-selected B vs. $(B - V)$ CMD is shown in Fig. 9.9. The split in the SGB is evident in this Figure. The next step will be to study the relative radial distribution of the two SGB populations.

Bibliography

Anderson, J., & King, I. R. 1999, PASP, 111, 1095
Anderson, J., Bedin, L. R., Piotto, G., Yadav, R. S., & Bellini, A. 2006, A&A, 454, 1029
Anderson, J., et al. 2008, AJ, 135, 2055
Bellini, A., Piotto, G., Bedin, L. R., King, I. R., Anderson, J., Milone, A. P., & Momany, Y. 2009, A&A, 507, 1393
Belokurov, V., Evans, N. W., Irwin, M. J., Hewett, P. C., & Wilkinson, M. I. 2006, ApJL, 637, L29
Capaccioli, M., Piotto, G., & Stiavelli, M. 1993, MNRAS, 261, 819
Carretta, E., et al. 2009, A&A, 505, 117
D'Ercole, A., Vesperini, E., D'Antona, F., McMillan, S. L. W., & Recchi, S. 2008, MNRAS, 391, 825
Decressin, T., Baumgardt, H., & Kroupa, P. 2008, A&A, 492, 101
Dinescu, D. I., Girard, T. M., van Altena, W. F., & López, C. E. 2003, AJ, 125, 1373
Dotter, A., Chaboyer, B., Jevremović, D., Baron, E., Ferguson, J. W., Sarajedini, A., & Anderson, J. 2007, AJ, 134, 376
Feltzing, S., & Johnson, R. A. 2002, A&A, 385, 67
Ferraro, F. R., et al. 2009, Nature, 462, 483
Grillmair, C. J., Freeman, K. C., Irwin, M., & Quinn, P. J. 1995, AJ, 109, 2553
Grillmair, C. J., Ajhar, E. A., Faber, S. M., Baum, W. A., Holtzman, J. A., Lauer, T. R., Lynds, C. R., & O'Neil, E. J., Jr. 1996, AJ, 111, 2293
Grillmair C. J. 1997, Proc. of the UC Santa Cruz Workshop on Galactic Halos (ed. D. Zaritsky), astro-ph/9711223v1
Grillmair, C. J., & Johnson, R. 2006, ApJL, 639, L17
Kharchenko, N., Scholz, R.-D., & Lehmann, I. 1997, A&AS, 121, 439
King, I. R. 1966, AJ, 71, 64
Kissler-Patig, M., et al. 2008, A&A, 491, 941
Koch, A., Grebel, E. K., Odenkirchen, M., Martínez-Delgado, D., & Caldwell, J. A. R. 2004, AJ, 128, 2274
Lee, K. H., Lee, H. M., Fahlman, G. G., & Sung, H. 2004, AJ, 128, 2838
Mahmud, N., & Anderson, J. 2008, PASP, 120, 907
Marín-Franch, A., et al. 2009, ApJ, 694, 1498
Marino, A. F., Milone, A. P., Piotto, G., Villanova, S., Bedin, L. R., Bellini, A., & Renzini, A. 2009, A&A, 505,

1099
Meylan, G., & Heggie, D. C. 1997, A&A Rev., 8, 1
Milone, A. P., et al. 2008, ApJ, 673, 241
Milone, A. P., Stetson, P. B., Piotto, G., Bedin, L. R., Anderson, J., Cassisi, S., & Salaris, M. 2009, A&A, 503, 755
Minniti, D., et al. 2010, New Astronomy, 15, 433
Moore, B. 1996, ApJL, 461, L13
Moore, B., Diemand, J., Madau, P., Zemp, M., & Stadel, J. 2006, MNRAS, 368, 563
Piotto, G., Cool, A. M., & King, I. R. 1997, AJ, 113, 1345
Piotto, G., et al. 2007, ApJL, 661, L53
Sarajedini, A., et al. 2007, AJ, 133, 1658
Vesperini, E., & Heggie, D. C. 1997, MNRAS, 289, 898
Villanova, S., et al. 2007, ApJ, 663, 296
Zaggia, S. R., Piotto, G., & Capaccioli, M. 1995, IAU Symp., Stellar Populations (ed. P. C. van der Kruit & G. Gilmore), 164, 409
Zaggia, S. R., Piotto, G., & Capaccioli, M. 1997, A&A, 327, 1004